Co-deformation of metallic and intermetallic phases in Mg-Al-Ca alloys

from the Faculty of Georesources and Materials Engineering of the
RWTH Aachen University

to obtain the academic degree of

Doctor of Engineering Science

approved thesis

submitted by

Muhammad Zubair, M.Sc.

Advisors: Univ.-Prof. Dr. Sandra Korte-Kerzel
Prof. Dr. Cemal Cem Tasan

Date of the oral examination: 12.01.2022

This thesis is available in electronic format on the university library's website

D 82 (Diss. RWTH Aachen University, 2022)

Declarations on Publications

This thesis includes the following articles that have been published in international peer-reviewed journals:

Publication 1 (Chapter 5)

M. Zubair, S. Sandlöbes, M.A. Wollenweber, C.F.Kusche, W.Hildebrandt, C.Broeckmann, S. Korte-Kerzel, On the role of Laves phases on the mechanical properties of Mg-Al-Ca alloys, Materials Science and Engineering: A, 756 (2019) 272-283.

Publication 2 (Chapter 6)

M. Zubair, S. Sandlöbes-Haut, M.A. Wollenweber, K. Bugelnig, C.F. Kusche, G. Requena, S. Korte-Kerzel, Strain heterogeneity and micro-damage nucleation under tensile stresses in an Mg–5Al–3Ca alloy with an intermetallic skeleton, Materials Science and Engineering: A, 767 (2019) 138414.

Publication 3 (Chapter 7)

J. Guénolé, **M. Zubair,** S. Roy, Zhuocheng Xie, M. Lipińska-Chwałek, S. Sandlöbes-Haut, S. Korte-Kerzel, Exploring the transfer of plasticity across Laves phase interfaces in a dual phase magnesium alloy, Materials and Design, 202 (2021) 109572.

Publication 4 (Chapter 8)

M. Zubair, S. Sandlöbes-Haut, M. Lipińska-Chwałek, M. A. Wollenweber, C. Zehnder, S. Schröders, J. Mayer, J.S.K-L. Gibson, S. Korte-Kerzel, Co-deformation Between the Metallic Matrix and Intermetallic Phases in a Creep-Resistant Mg-3.68Al-3.8Ca Alloy, Materials and Design, 210 (2021) 110113.

Contributions of the candidate to the publications listed above

The candidate primarily conceptualised the experimental setup of these studies, planned and performed most of the experiments and wrote the initial draft of the manuscripts with the exception of publication 3, for which the candidate has performed the experimental work, and wrote and revised the experimental section of the manuscript. Furthermore, he revised the manuscripts according to the co-authors' and reviewers' feedback and is the corresponding author of all the publications except for publication 3. Detailed descriptions of the contributions of the candidate are listed below:

Publication 1

Metallographic preparation of samples, tensile tests, hardness tests, SEM imaging and EBSD analysis, DIC, were done by the candidate. All data evaluation and its complete analysis was done by him.

Publication 2

SEM imaging, tensile tests, high temperature quasi in-situ deformation and strain mapping experiments and EBSD were primarily done by the candidate. All data evaluation except Euler number analysis was done by the candidate.

Publication 3

All the quasi in-situ deformation experiments in SEM and their evaluation were done by the candidate and he also wrote bulk of the relevant experimental section in the manuscript. TEM sample was also prepared by him.

Publication 4

Most of the SEM images and EBSD maps presented in the article were taken by the candidate. In addition to that, TEM sample preparation (for one sample), room and high temperature nano-indentation experiments were also conducted by him. Nearly all data analysis except that from TEM was done by the candidate.

Acknowledgment

Throughout my Journey of PhD and in the compilation of this thesis, I have received enormous academic, technical, administrative, mental, and personal support.

I would like to start by saying a big thank you to my two supervisors, Prof. Dr. Sandra Korte-Kerzel and Dr. Stefanie Sandlöbes-Haut first for giving me an opportunity to become part of their research team at IMM, RWTH Aachen and then for their continuous guidance throughout this dissertation. Moreover, their help in formulating my research questions, their guidance in polishing my academic work and publications, their assistance and feedback in my conference talks and poster sessions are truly and greatly acknowledged. I would also like to thank Prof. Korte-Kerzel for showing faith in me and providing me an opportunity to also work in Collaborative Research Centre (CRC 1394). The interaction with several other leading researchers within the framework of CRC 1394 has also helped me to develop my research skills. I am also very grateful for Prof. C. Cem Tasan's time and effort in evaluating my thesis. In my interactions with him, I have gained a new perspective on research problems.

I would also express my sincere gratitude to

- Dr. James S.K.L. Gibson for his endless support in performing and analysing data generated from nanoindentation at room and elevated temperatures, and his significant help in revising my latest manuscript.
- Dr. Marta Lipinska-Chwalek for her substantial assistance with the transmission electron microscopy, for the energy and motivation she has shown in our joint collaborative work, and for her feedback in my recent work.
- Dr. Risheng Pei for his significant help in dealing with EBSD data, for stimulating and long research discussions and his contribution in revising various Matlab codes according to this work needs. The knowledge exchanged with him on using innovative solutions for imaging in SEM and various sample polishing procedures was also very fruitful.
- Mr. Maximilian Aeneas Wollenweber for his help in polishing and imaging huge number of samples in last three years of my PhD.
- Dr. Julien Guénolé and Dr. Zhuocheng Xie, for their useful co-operation and atomistic simulations.
- Dr. Wei Luo for fruitful discussions on numerous research aspects.

- Dr. Sebastian Schröders and Martin Heller for their help in FIB usage.
- Dr. Talal Al-Samman for his help and support in administrative and technical matters.

I would also like to thank Mr. David Beckers, Mr. Loeck Mathias, Mr. Gerd Schütz, Mr. Laiko Sergej, and Mr. Arndt Ziemons for their significant help and guidance at several stages of this work.

Besides them, I would also like to thank all my colleagues at IMM, Pakistan Students Association-Aachen, and International Office at RWTH who have helped me initially in finding my feet in Aachen, adjusting into a new environment and dealing with bureaucratic works throughout my stay.

I am also very thankful to the encouragement and motivation I got from my family: loving parents, co-operative wife and two kids. The sacrifices and contributions they made for me during this period are unmatched.

In the end, I would also like to thank UET Lahore Pakistan and DFG Germany for funding my research at IMM, RWTH Aachen. I also thank God for giving me strength and resources to carry out this research.

List of Abbreviations

Mg	Magnesium
AZ	Aluminium-Zinc
AM	Aluminium-Manganese
Y	Yttrium
La	Lanthanum
Gd	Gadolinium
Ca	Calcium
Al	Aluminium
CRSS	Critical resolved shear stress
S.F	Schmid factor
ET	Extension twinning
L-S-L	Large-small-large
Sr	Strontium
Mn	Manganese
Zn	Zinc
TEM	Transmission Electron Microscopy
TA	Thermal Analysis
SEM	Scanning Electron Microscopy
XRD	X-ray Diffraction
AZX	Aluminium-Zinc-Calcium
Sr	Strontium
MPa	Mega Pascal
AXJ	Aluminium-Calcium-Strontium
DIC	Digital Image Correlation
GNDs	Geometrically Necessary Dislocations
LRB	Lee-Robertson-Birnbaum
RT	Room Temperature

List of Figures

List of Tables

Abstract

Mg-Al-Ca alloys have a dual phase microstructure comprising a soft α-Mg phase reinforced with a hard intermetallic interconnected Laves phase skeleton. The excellent creep properties of these alloys are attributed to the presence of Laves phases in the microstructure. However, it is not entirely clear how the amount, type, and morphology of the Laves phases can affect the elevated temperature tensile and creep properties of these alloys. Furthermore, the two mechanically and crystallographically different phases (α-Mg and Laves phases) provide an opportunity to study the co-deformation behaviour of such heterogeneous materials. This thesis, therefore, focuses on the two main aspects: i) effect of Laves phases on the mechanical properties of Mg-Al-Ca alloys and ii) co-deformation of metallic and intermetallic phases.

The Ca/Al ratio can be used to manipulate the amount, type, and morphology of Laves phases. Therefore, three different Mg-Al-Ca alloys with varying Ca/Al ratio (Ca/Al: 0.32, 0.62 and 1.03) were produced. The alloys were microscopically and mechanically investigated using SEM, EDS, EBSD, micro-hardness, tensile and creep testing. The results show that an increase in Ca/Al ratio from 0.32 to 1.03 results in a higher volume fraction of Laves phase in the as-cast microstructure, higher yield strength, UTS and better creep properties at a temperature of 170 °C. However, the alloy with the highest Ca/Al ratio exhibits lowest ductility.

The co-deformation mechanisms of the same Mg-Al-Ca alloys were studied using DIC, quasi in-situ tensile deformation in SEM (at 170 °C), EBSD, and TEM. The strain maps obtained from DIC experiments showed that the strain is highly heterogeneous at the microstructural level and tends to concentrate along slip lines and twins in the α-Mg phase and along the α-Mg/Laves phase interfaces. Moreover, it was found that cracks preferentially nucleate in the Laves phase at the intersections of slip in the α-Mg and Mg-Laves phase interfaces as well as at the intersections of twins in the matrix and Mg-Laves phase interfaces. Consequently, cracks in the Laves phase were mainly observed in microstructural regions that underwent significant basal slip and tensile twinning. Euler number analysis also confirmed that the interconnectivity of the Laves phase decreases with deformation because of cracking. In addition to cracks in the Laves phase, slip transfer was also observed in the $(Mg,Al)_2Ca$ phase at strain concentration points.

Atomistic simulations of the Mg/Mg_2Ca system confirmed that dislocation slip in the Mg_2Ca phase was triggered by the interaction of basal dislocation of the Mg matrix with the interface.

However, the slip transfer mechanisms across the Mg/Mg_2Ca interface were affected by temperature and orientation relationship between both phases. In line with atomistic simulations, basal slip lines in the $(Mg,Al)_2Ca$ phase were also observed at strain concentration points in deformed alloys investigated using SEM and TEM. The co-deformation mechanism based on experimental results is proposed within this thesis.

Finally, nanoindentation with constant and variable strain rate was conducted to determine the mechanical properties and thermally activated deformation mechanisms of the individual phases in Mg-Al-Ca alloys. It was observed that the hardness of the α-Mg phase decreases with temperature while that of the Laves phases stays constant until 200 °C. The strain rate sensitivity, m, was nearly the same for α-Mg and α-Mg/Laves interfaces while the activation volume was lower for indents made across interfaces. Nanoindentation creep tests indicated that the creep resistance of the Mg_2Ca phase is higher than that of the α-Mg phase.

The findings of this thesis provide valuable insights for the design of creep resistant Mg-Al-Ca alloys by manipulating the Ca/Al ratio. Additionally, the methods involved in this thesis are generally applicable to study the co-deformation of multiphase alloys with mechanically heterogeneous microstructural components. They may, therefore, be of interest to researchers working on other multi-phase alloys such as dual-phase steels or titanium alloys.

Kurzfassung

Mg-Al-Ca-Legierungen haben eine zweiphasige Mikrostruktur, die aus einer weichen α-Mg-Phase besteht, die durch ein hartes intermetallisches, miteinander verbundenes Skelett aus Laves-Phasen verstärkt wird. Die hervorragenden Kriecheigenschaften dieser Legierungen werden auf das Vorhandensein der Laves-Phasen im Gefüge zurückgeführt. Es ist jedoch nicht klar, wie der Volumenanteil, der Typ und die Morphologie der Laves-Phasen die Zug- und Kriecheigenschaften dieser Legierungen bei erhöhter Temperatur beeinflussen können. Dazwei mechanisch und kristallographisch sehr unterschiedliche Phasen das Gefüge bilden, besteht darüber hinaus die Möglichkeit, das Co-Verformungsverhalten solcher heterogenen Werkstoffe zu untersuchen. Diese Arbeit konzentriert sich daher auf die beiden Hauptaspekte: i) Wirkung der Laves-Phasen auf die mechanischen Eigenschaften von Mg-Al-Ca-Legierungen und ii) Co-Verformung von metallischen und intermetallischen Phasen.

Das Ca/Al-Verhältnis kann verwendet werden, um den Anteil, den Typ und die Morphologie der Laves-Phasen zu beeinflussen. Daher wurden drei verschiedene Mg-Al-Ca-Legierungen mit unterschiedlichen Ca/Al-Verhältnissen (Ca/Al: 0,32, 0,62 und 1,03) hergestellt. Die Legierungen wurden mikroskopisch und mechanisch mittels REM, EDS, EBSD, Mikrohärte, Zug- und Kriechversuchen untersucht. Die Ergebnisse zeigen, dass die Erhöhung des Ca/Al-Verhältnisses von 0,32 auf 1,03 zu einem höheren Anteil an Laves-Phasen im Gefüge im Gusszustand führt und eine höhere Streckgrenze, UTS und verbesserte Kriecheigenschaften bei einer Temperatur von 170 °C bewirkt. Die Legierung mit dem höchsten Ca/Al-Verhältnis wies jedoch die geringste Duktilität auf.

Die Co-Verformungsmechanismen wurden mit DIC, Quasi-In-Situ-Zugverformung im REM (bei 170 °C), EBSD und TEM untersucht. Die Dehnungskarten aus DIC-Experimenten zeigten, dass die Dehnung auf mikrostruktureller Ebene sehr heterogen ist und dazu neigt, sich entlang von Gleitlinien und Zwillingen in der α-Mg-Phase und entlang der α-Mg/Laves-Phasengrenzflächen zu konzentrieren. Darüber hinaus wurde festgestellt, dass sich die Risse in der Laves-Phase bevorzugt an den Schnittpunkten von basalen Gleitlinien und Verformungszwillingen in der α-Mg-Matrix mit der Laves-Phase ausbilden. Folglich konzentrierten sich die Risse in der Laves-Phase in Gefügebereichen, die signifikante basale Gleitung und die Bildung von Zugzwillinge aufwiesen. Die Eulerzahl-Analyse bestätigte auch, dass die (Inter-)Konnektivität der Laves-Phase mit der Verformung aufgrund von Rissbildung abnimmt. Zusätzlich zu den Rissen in der Laves-Phase wurde auch Versetzungsgleiten in der $(Mg,Al)_2Ca$-Phase an Dehnungskonzentrationsbereichen in der Mikrostruktur beobachtet.

Atomistische Simulationen (am Mg/Mg_2Ca-System) bestätigten, dass Versetzungsgleuten in der Mg_2Ca-Phase an Stellen ausgelöst wird, an denen die basalen Mg-Gleitlinien mit der Grenzfläche interagieren. Die Übertragungsmechanismen von Versetzungsgleiten über die Mg/Mg_2Ca-Grenzfläche wurden jedoch von der Temperatur und der Orientierungsbeziehung zwischen den beiden Phasen beeinflusst. In Übereinstimmung mit atomistischen Simulationen wurden basale Gleitlinien in der $(Mg,Al)_2Ca$-Phase auch an Dehnungskonzentrationspunkten in verformten Legierungen beobachtet, die mit REM und TEM untersucht wurden. Ein auf experimentellen Ergebnissen basierende Co-Deformationsmechanismus wird in dieser Studie ebenfalls vorgeschlagen.

Schließlich wurden mit Hilfe von Nanoindentationstests mit konstanter und variabler Dehnungsrate die mechanischen Eigenschaften und thermisch aktivierten Verformungsmechanismen der einzelnen Phasen bestimmt. Diese Arbeit berichtet, dass die Härte der α-Mg-Phase mit der Temperatur abnahm, während die der Laves-Phase zumindest bis 200 °C gleich blieb. Die Dehnratenempfindlichkeit, m, war für die α-Mg- und α-Mg/Laves-Grenzflächen nahezu gleich, während das Aktivierungsvolumen bei Eindrücken über Grenzflächen geringer war. Nanoindentations-Kriechversuche zeigten, dass die Kriecheigenschaften der Mg_2Ca-Phase viel besser waren als die der α-Mg-Phase.

Die Ergebnisse dieser Studie liefern somit wertvolle Erkenntnisse für das Design von kriechfesten Mg-Al-Ca-Legierungen durch Manipulation des Ca/Al-Verhältnisses. Darüber hinaus sind die Methoden dieser Studie allgemein auf die Untersuchung der Co-Verformung in mehrphasigen Legierungen mit mechanisch heterogenen Gefügekomponenten anwendbar. Sie können daher auch für Forscher interessant sein, die in anderen metallurgischen Bereichen arbeiten, wie z. B. in Dualphasenstählen oder Titanlegierungen.

Contents

1. Introduction and Motivation

Improving the fuel economy and reducing harmful greenhouse gas emissions are two of the most important challenges that the automotive industry encounters today. Mg, being the lightest structural metal has a density of ~1.74 g/cm^3 [1], thus has enormous potential for usage in automotive sector. This is because the reduction of the vehicle weight is one way to efficiently reduce harmful emission [2].

The AZ or AM series are among the most widely used Mg alloys in the automotive industry and, therefore, a lot of research has been done to explore and improve their microstructure, recrystallisation and mechanical behaviour [3-8]. However, the application temperature of these alloys is limited to 125 °C [1]. This is because the $Mg_{17}Al_{12}$ intermetallic phase, that acts as a reinforcement phase in these alloys, softens at elevated temperatures (~ > 130 °C) and thus results in inferior creep properties [9, 10].

Rare earth (RE, like Y, La, Gd) element or Ca addition to conventional Mg-Al alloys can improve the creep behaviour since the formation of the $Mg_{17}Al_{12}$ phase fraction is reduced and the formation of more thermally stable intermetallics is enhanced [10-15]. Particularly Ca is favoured because of its availability and cost effectiveness as compared to RE based additives. Addition of about 2 wt. % calcium to AM60 results in a complete suppression of the $Mg_{17}Al_{12}$ phase and the formation of only Al_2Ca as reinforcement phase in the as-cast alloy [10]. Al_2Ca belongs to the class of Laves phases, which are known for their high temperature properties. There are two other Laves phases present in the Mg-Al-Ca alloy system, the $(Mg,Al)_2Ca$ and Mg_2Ca Laves phase [16]. These intermetallic Laves phases are much harder [17, 18] and stronger than the α-Mg matrix [19]. These phases also have high melting points, i.e. Mg_2Ca: 715 °C and Al_2Ca: 1079 °C [17] and high thermal stability [10] when compared to the $Mg_{17}Al_{12}$ phase present in commercial Mg-Al alloys. However, the excellent mechanical and physical properties of these phases are accompanied by ab inherent brittleness at the bulk scale. This inherent brittleness of the Laves phases limits the possibility of studying the deformation mechanisms at the bulk scale, especially at low temperatures or below their ductile to brittle transition temperatures. In contrast to bulk scale investigations, plasticity is reported and observed for small-scale testing of several Laves phases [20-22] even at room temperature. The strut thickness of the Laves phases in the Mg-Al-Ca alloys is within the range of a few micrometres (sometimes a few hundred nm's only). Therefore, from the deformation point of view, it is of high importance to understand the co-deformation behaviour of these Laves phases with the α-Mg matrix. The present work is therefore dedicated to study the deformation behaviour of ternary Mg-Al-Ca alloys.

1.1 Objectives and research questions

The main objective of the present work is to study the co-deformation behaviour of the metallic and intermetallic phases present in the Mg-Al-Ca alloys. To address this aim, the following research questions were explored and addressed in this study.

1. What are the effects of different Laves phases, their volume fraction, morphology, and distribution on the mechanical properties of Mg-Al-Ca alloys? **Publication 1**
2. How is the strain distributed at the microstructural scale in Mg-Al-Ca alloys during elevated temperature tensile deformation? **Publication 2**
3. How do micro cracks nucleate in the Laves phase and how does the matrix orientation influence the crack nucleation in the Laves phase? **Publication 2**
4. How does the Laves phase deform plastically in the Mg-Al-Ca alloys and which slip transfer mechanisms occur from the soft α-Mg matrix to the hard Laves phase? **Publications 3 and 4**
5. What is the effect of the orientation relationship between the α-Mg matrix and the Laves phase on the slip transfer mechanisms? **Publications 3 and 4**
6. How does temperature affect the mechanical properties of the individual phases present in Mg-Al-Ca alloys? **Publication 4**

Table 1 contains the list of publications addressing the above-mentioned research questions.

Table 1. Publications included in the thesis

	Publication title	**Journal**	**Chapter No.**
Publication 1	On the role of Laves phases on the mechanical properties of Mg-Al-Ca alloys	Materials Science and Engineering: A	5
Publication 2	Strain heterogeneity and micro-damage nucleation under tensile stresses in an Mg–5Al–3Ca alloy with an intermetallic skeleton	Materials Science and Engineering: A	6
Publication 3	Exploring the transfer of plasticity across Laves phase interfaces in a dual phase magnesium alloy	Materials and Design	7

Publication 4	Co-deformation Between the Metallic Matrix and Intermetallic Phases in a Creep-Resistant Mg-3.68Al-3.8Ca Alloy	Materials and Design	8

The topics/research questions addressed in each publication are presented in Figure 1 and Figure 2.

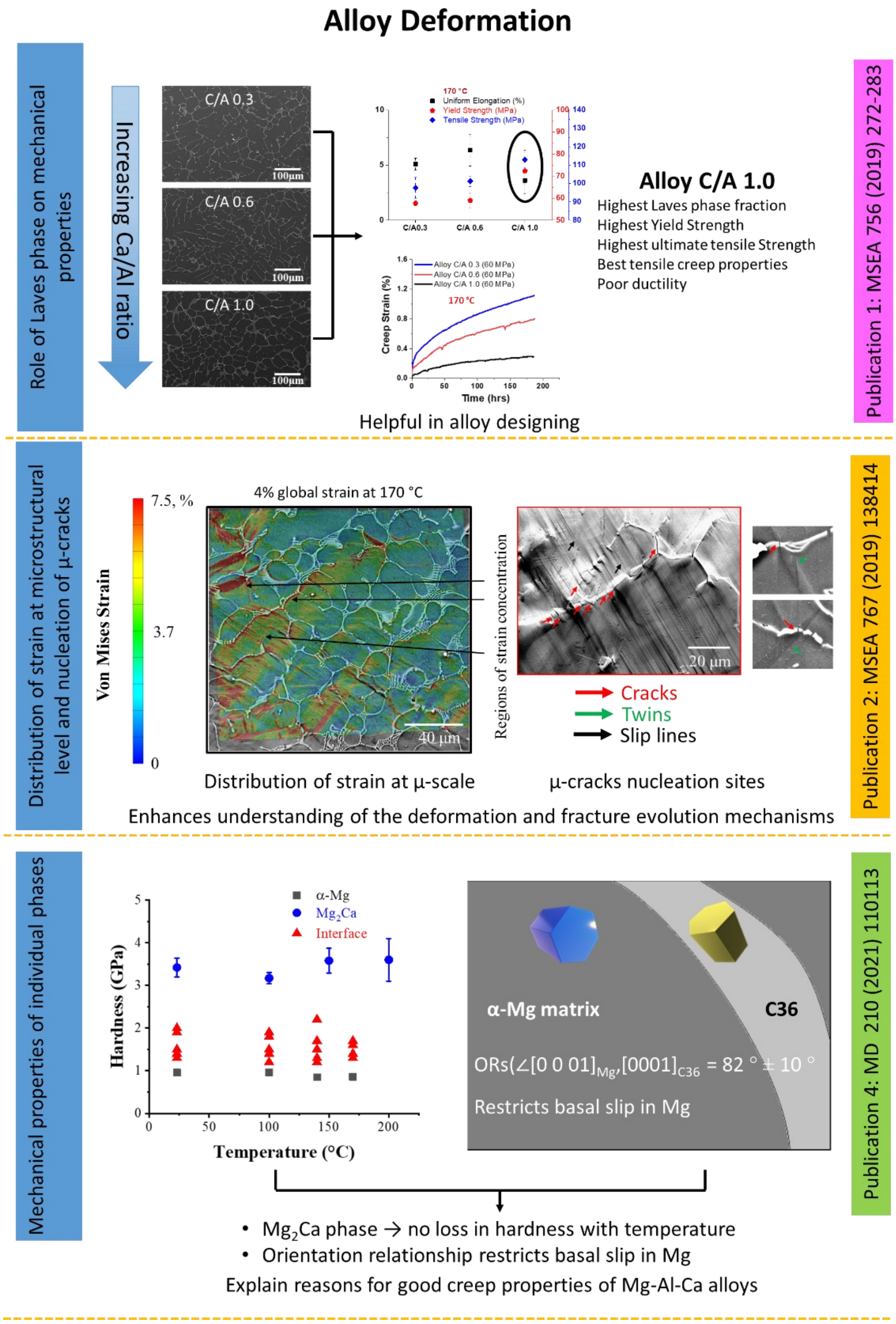

Figure 1. The deformation behaviour and mechanical properties of Mg-Al-Ca alloys at macro and microscopic scale.

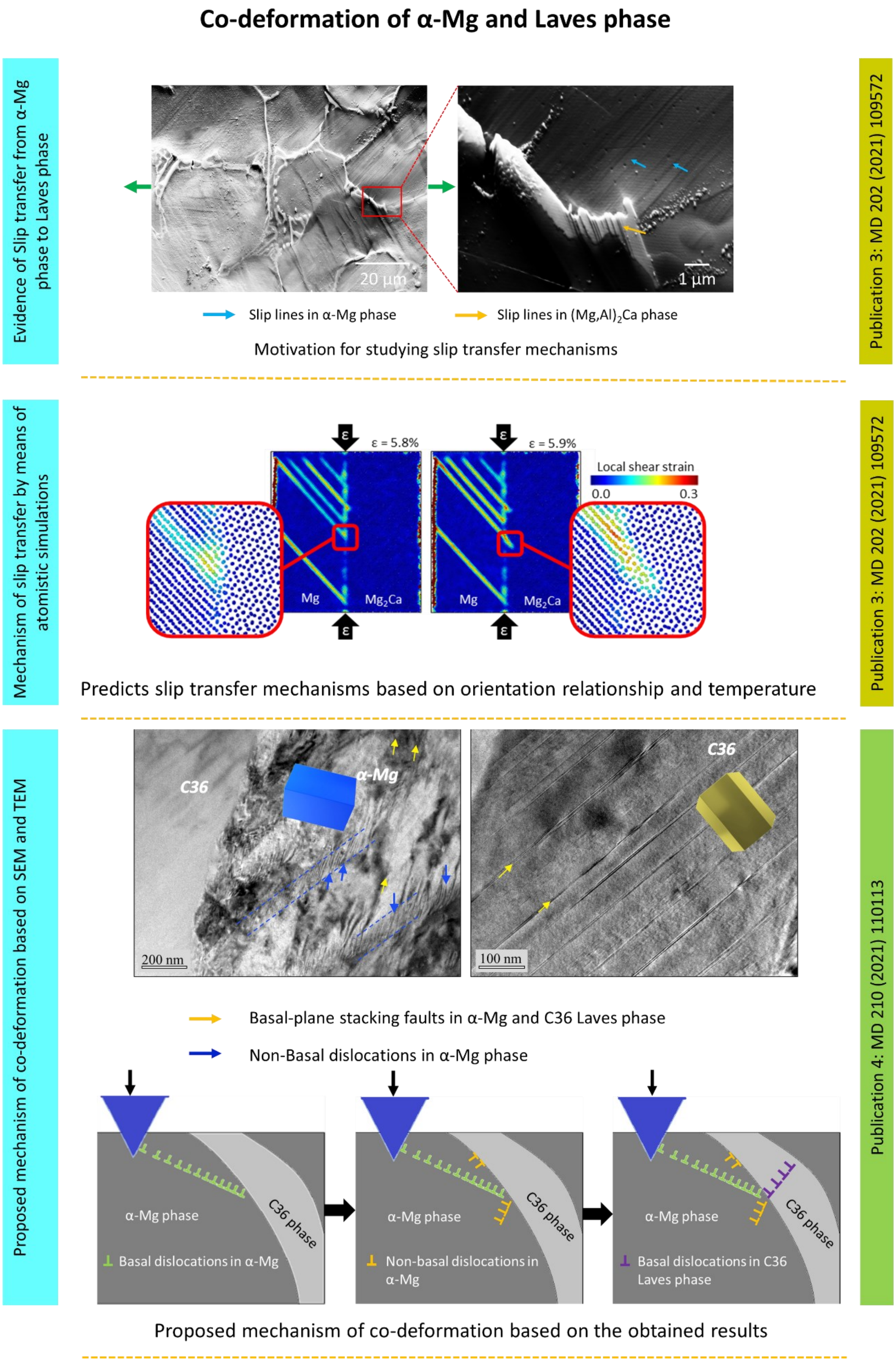

Figure 2. Co-deformation of α-Mg matrix and Laves phase in Mg-Al-Ca alloys.

2. Fundamentals

The microstructure of Mg-Al-Ca alloys consists of the α-Mg matrix and an interconnected Laves phase skeleton. As both phases have very different crystal structure and mechanical properties, they will be described separately before explaining in detail the microstructure, deformation mechanisms and peculiar characteristics of Mg-Al-Ca alloys.

2.1. Mg-Introduction

Mg has a hexagonal lattice and deforms mainly by basal slip $\{0001\}$<$11\bar{2}0$> and tensile twinning $\{10\bar{1}2\}$<$10\bar{1}1$>. In addition, the following deformation mechanisms have been reported: i) prismatic slip $\{10\bar{1}0\}$<$11\bar{2}0$> , ii) first order pyramidal slip $\{10\bar{1}1\}$<$11\bar{2}0$>, $\{10\bar{1}1\}$<$11\bar{2}3$>, iii) second order pyramidal slip $\{112\bar{2}\}$<$11\bar{2}3$>, and iv) compression twinning $\{10\bar{1}1\}$<$10\bar{1}2$>.

The activation of a particular glide system depends on several factors such as the direction of the applied load, slip plane, slip direction and the CRSS value. In terms of tensile or compressive loading, this relationship is best expressed in terms of Schmid's law, which relates the resolved shear stress to the applied stress via Equation 1:

$$\tau = \sigma \cdot \cos\Phi \cdot \cos\lambda \qquad \text{Equation 1}$$

With τ being the resolved shear stress, σ the applied tensile stress, Φ the angle between the tensile force and the normal to the slip plane and λ the angle between the tensile force and the slip direction.

The product of cosine Φ and cosine λ is termed as Schmid factor, m_S, and varies between 0 and 0.5. A higher value of m_S indicates a favourable orientation for the activation of a particular slip system. The plastic deformation on a particular slip system commences when τ approaches a critical value on that slip system. This τ_{crit} is known as CRSS.

The CRSS required to activate basal slip and tensile twinning at room temperature in Mg and Mg alloys is very low when compared to the other modes of deformation, Figure 3:.

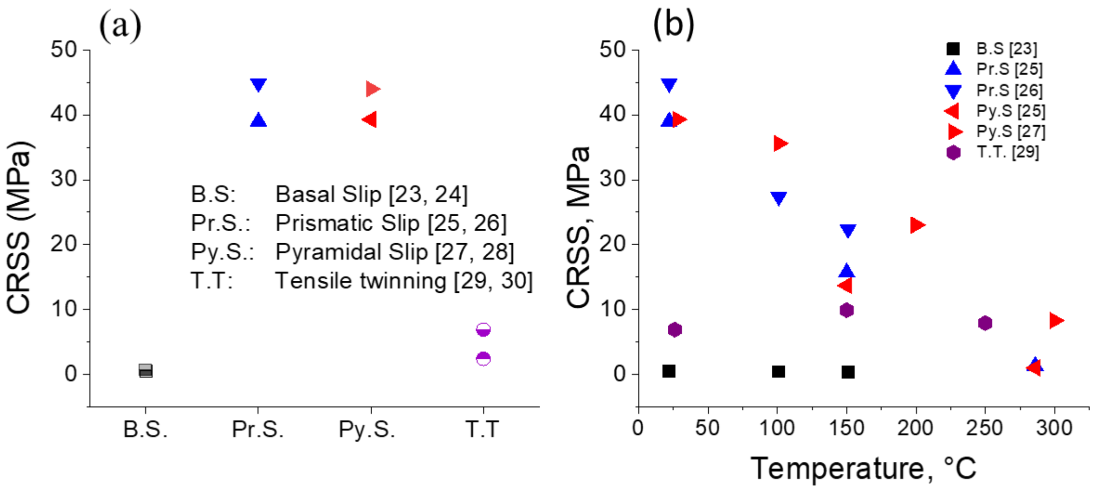

Figure 3. (a) CRSS for various slip system at room temperature for pure Mg, (b) variation of CRSS with temperature. Values of basal slip were extracted from [23, 24], prismatic slip from [25, 26], pyramidal slip from [25, 27, 28], tensile twinning from [29, 30].

It can be seen in Figure 3 (a) that the CRSS for prismatic and pyramidal slip is nearly two orders of magnitude higher than that for basal slip and a few times higher than that for tensile twinning. This renders basal slip and tensile twinning the mainly activated slip systems in Mg and its alloys at room temperature. The CRSS values are affected by temperature and the CRSS values of prismatic and pyramidal slip decreases considerably with temperature (see Figure 3 (b)). Further, the CRSS values are also affected by the composition [23, 26, 31, 32].

2.1.1. Basal slip in Mg

It can be seen from Figure 3 that basal slip is the easiest deformation mechanism in magnesium. There are three slip directions on the {0001} basal planes. The Burgers vector of these dislocations is $\frac{1}{3} < 11\bar{2}0 >$ also named <a> type. These perfect basal <a> dislocations can also dissociate into two Shockley partials with the Burgers vector $\frac{1}{3} < 10\bar{1}0 >$. These partial dislocations bound a stacking fault with ABC (FCC) stacking sequence. Values for the stacking fault energy, γ, (for the I_2* type basal fault) in Mg are in the range of 30 to 40 mJm^{-2} [33, 34]. However, basal <a> slip offers only two independent basal slip systems not fulfilling the minimum requirement of activating five independent slip systems for any arbitrary shape change [34].

*There are different types of stacking faults in Mg, i.e., two intrinsic labelled as I_1 and I_2, while one extrinsic commonly called as E. Further details are available in [33].

2.1.2. Non-basal slip of <a> type dislocations

Screw dislocations with an <a> Burgers vector can cross-slip from the basal to the prismatic planes [35] and in some cases to the first order pyramidal planes. Prismatic and pyramidal slip with <a> type dislocations can provide two and four independent slip systems, respectively, in addition to the two independent basal slip systems. However, no strain along the c-axis can be accommodated by <a> type dislocations [34].

It should also be noted that the CRSS for prismatic <a> slip is significantly higher than basal <a> slip at room temperature (see Figure 3 (a)). This is because <a> dislocations in Mg are dissociated, hence, hindering the cross-slip of screw dislocations from the basal to prismatic planes. The difference decreases with temperature (Figure 3 (b)). In case of polycrystals, the plastic anisotropy can create compatibility effects that can promote prismatic <a> slip [36]. Prismatic <a> slip was observed in several Mg alloys at room temperature and the activation of prismatic slip appears to be easier than for single crystals [37, 38].

2.1.3. Non-basal slip of <c+a> type dislocations

Slip on pyramidal planes with <c+a> dislocations was reported by several researchers [39-46]. <c+a> dislocation and deformation twinning are the only deformation mechanisms that can accommodate deformation along the c axis. Therefore, the activation of <c+a> dislocation slip is considered as one of the most effective ways to increase the ductility of Mg alloys [39, 40, 44, 45, 47]. <c+a> dislocations can be activated by decreasing the grain size where c+a> dislocations can be activated due to high stress concentrations at the grain boundaries [43, 45]. Another assumption how <c+a> dislocations can be activated lies in the manipulation of stacking fault energies (I_1 in particular but also I_2 type faults) by suitable alloying additions like rare earth (Y, Gd etc) and Ca [39-42, 44, 47].

2.1.4. Deformation twinning

Deformation twinning is a shear deformation process in which a part of the crystal is shifted into a mirror-symmetry with the matrix phase. Twinning generally occurs in one direction and mostly not in the opposite direction. $\{10\bar{1}2\}<\bar{1}011>$ twinning is usually activated under tensile stresses but is restricted under compressive stresses along the <c> direction or c-axis. It is also called extension twinning (ET) since it results in an extension along the c-axis. $\{10\bar{1}1\}<10\bar{1}\bar{2}>$ compression twinning on the other hand is activated under the action of compressive stresses along the c-axis [48]. In Mg and its alloys, extension twinning is easily activated because of its low CRSS (see Figure 3). In ET, the angle between <11$\bar{2}$0> of the parent and twinned crystal amounts to ~86.2°. This is schematically shown in the Figure 4. K_1 is the first invariant (shear) plane and K_2 is the second invariant (or conjugate) plane. This is the plane that changes its orientation during shearing and the displacement of the K_2 plane after twinning defines the shear which occurs during twinning [34].

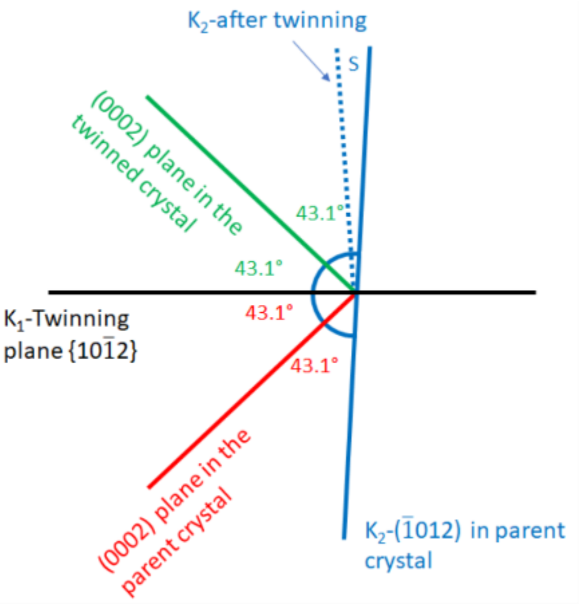

Figure 4. {10$\bar{1}$2} twin in Mg along the plane twinning K_1. K_2 is the (conjugate) twinning plane. The figure is reproduced from [49].

Compression twinning generally requires high stresses to be activated. In the as-cast Mg-Al-Ca alloys investigated in this thesis, predominantly extension twinning is observed, therefore, compression twinning will not be discussed in detail. In polycrystals, twins tend to nucleate at grain boundaries triggered by stress concentrations [50-52]. In permanent mould cast Mg-Al-Ca alloys, an intragranular (in addition to intergranular) Laves phase skeleton is present throughout the α-Mg matrix. This Laves phase skeleton is considered to block dislocation motion in the α-Mg matrix and the interfaces can act as sources for twin nucleation in the Mg matrix similar to grain boundaries. Once a twin is nucleated, a considerable redistribution of stresses occurs. Specifically, forward stresses are induced at the twin tip and backward stresses in the interior of the twin [34, 52-54]. The back stresses are lower in the middle of the twin than at the ends leading to lenticular shaped twins. Crack nucleation was also observed at locations where twins were intersecting with the grain/phase boundaries or at twin boundaries

[55-58]. Lenticular shaped twins formed in the α-Mg matrix in a Mg-Al-Ca alloy are highlighted in Figure 5. Crack nucleation in the Laves phase at the twin intersection points can be seen in the Figure 5.

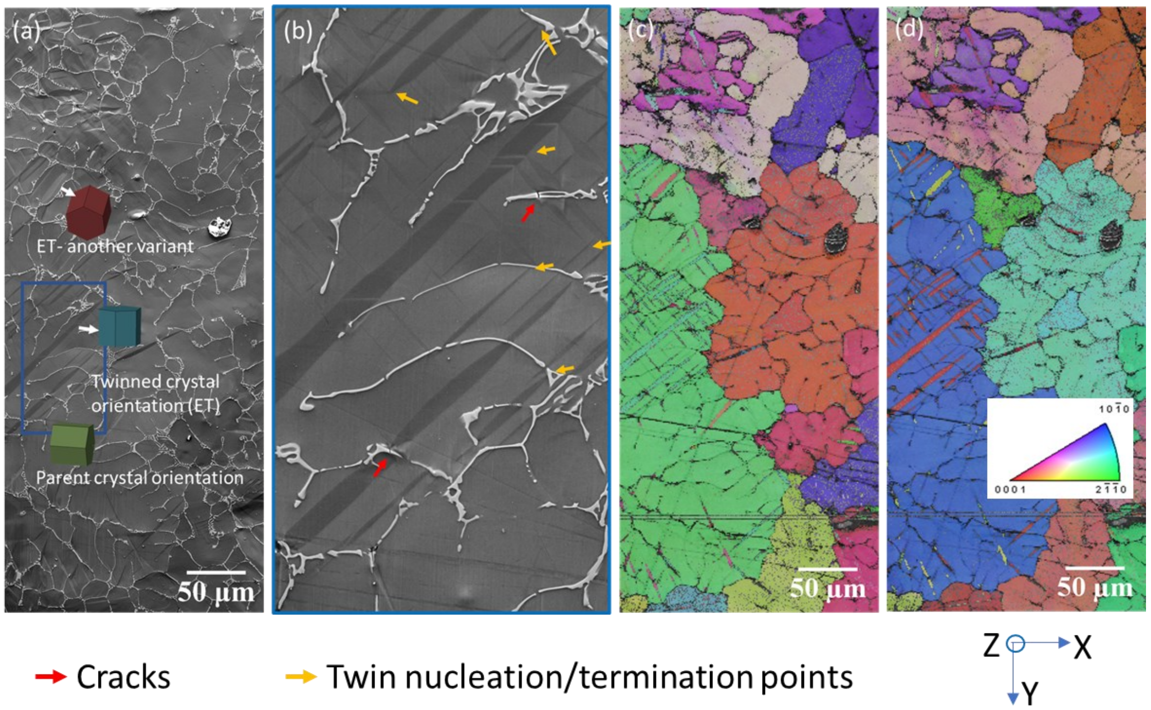

Figure 5. (a) SE micrographs of the Mg-4.65Al-2.82Ca alloy after 5 % deformation at 170 °C, unit cells in (a) show the orientation of parent and twinned crystal, (b) is the magnified view of the microstructural region highlighted by a blue rectangle in (a), (c) and (d) show the inverse pole figure (IPF) maps from normal direction (Z) and from the Y axis respectively.

2.2. Laves Phases

Laves phases are one of the most prominent classes of intermetallic compounds with AB_2 stoichiometry. Combinations of metals spanning over nearly the complete periodic table can form Laves phases [21, 59-61]. These phases usually have three different structure types, i.e. C14, C15, and C36 [59].

2.2.1. Stacking sequences of Laves phases

The close packing of all types of Laves phases is attained from the formation of quadruple layers. These quadruple layers consist of alternating layers of single and triple layers. The single layers are comprised of small atoms forming a Kagome net. The Kagome net (a two-dimensional structure comprised of alternating hexagons and triangles) is shown in Figure 6 (a) and (b) [62, 63].

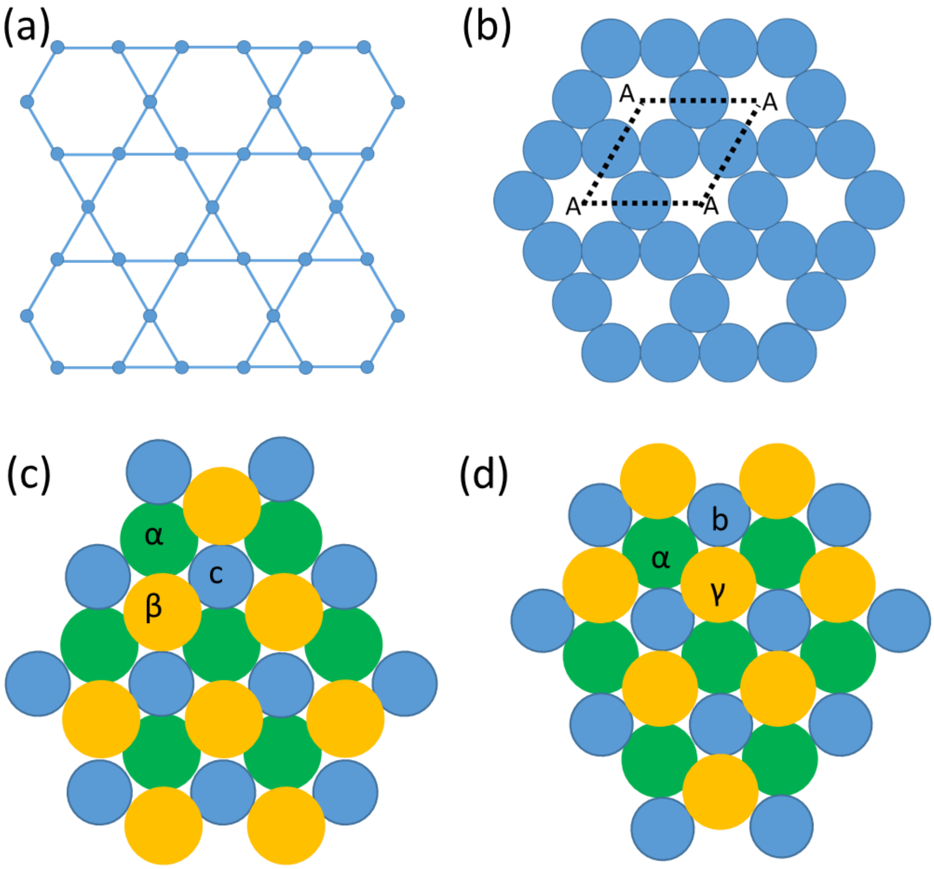

Figure 6. (a) and (b) Kagome net formed by small atoms in a Laves phase, (c) triple (t) layer with a stacking sequence of αcβ, (d) triple (t´) layer with a stacking sequence of αbγ. The images are recreated using data presented in [62, 63].

The triple layers consist of L-S-L (denoting large-small-large atoms) sandwiches that are formed above the single layers in such a way that the large atoms fill the A lattice points (Figure 6 (b)) shown by α in Figure 6 (c). The small atoms (denoted by c) take the c positions followed by the large atoms denoted β in Figure 6 (c). Such type of stacking sequence is conventionally termed as X and if a triple layer of t´ variant is present at point A the quadruple layer stacking sequence is termed X´. The next quadruple layer can then be Y or Y´ having the stacking sequence of Bβaγ or Bβcα. Depending on the repetition of these quadruple layers the three variants of Laves phases are

1) XY´XY´….. -2H- C14
2) XYZXYZ... -3C-C15
3) XY´X´Z…. -4H-C36

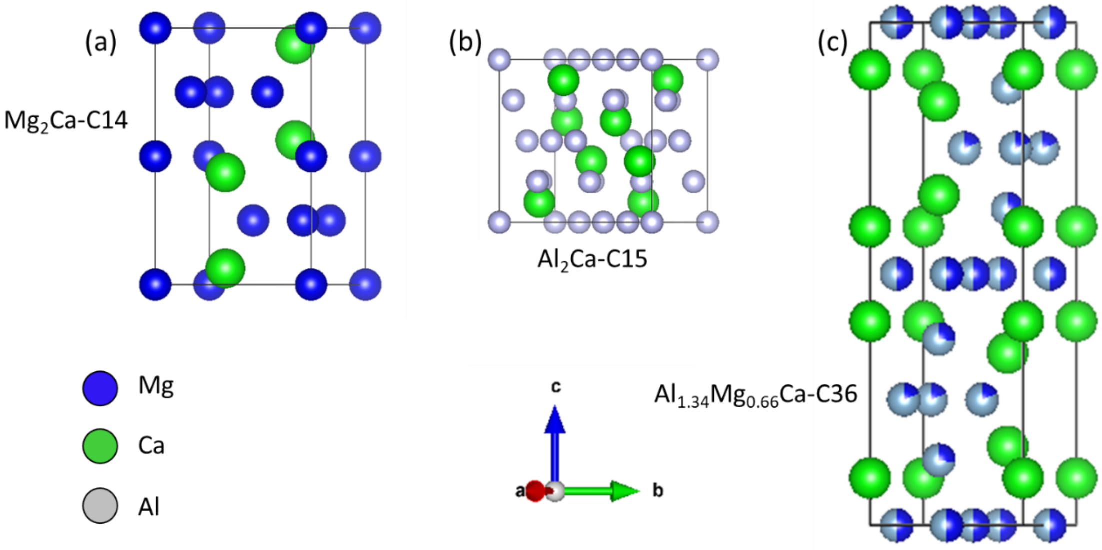

Figure 7. Unit cells of (a) Mg_2Ca phase (C14), b) Al_2Ca phase (C15) and c) $Al_{1.34}Mg_{0.66}Ca$ phase (C36). The legends show the colours of the atoms and crystallographic directions. The images were created using VESTA [64].

The respective unit cells of these Laves phases are presented in Figure 7 using the system Mg-Al-Ca as example. The unit cell of the C36 phase is nearly twice as large as the C14 phase in c direction.

A more extended view of the Laves phase type is given in Figure 8. The triple layer of L-S-L atoms in C14 and C36 Laves phases are highlighted using red oval shapes.

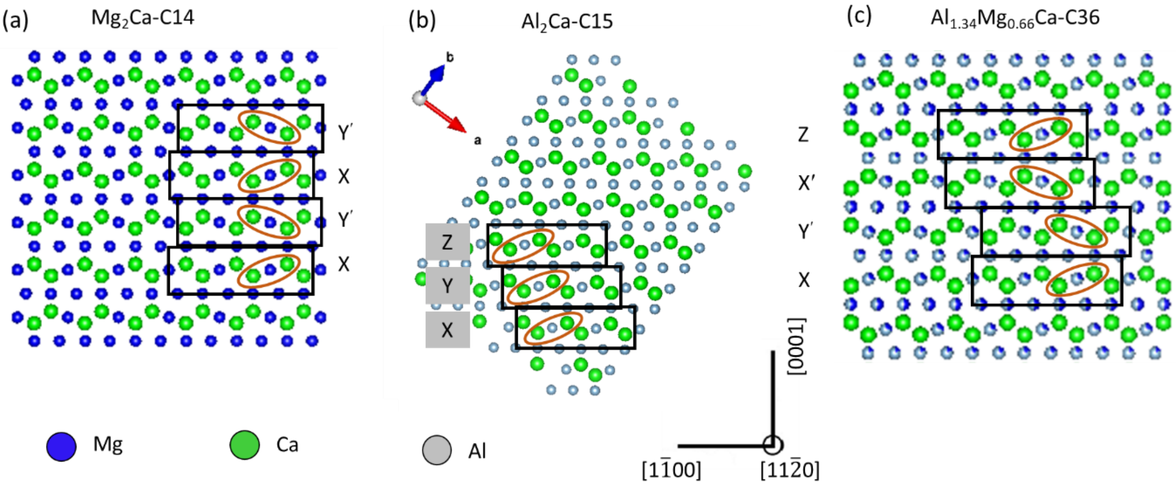

Figure 8. Stacking sequences of (a) C14, (b) C15 and (c) C36 Laves phases. The c axis is pointing upwards in vertical direction. Please note that the black and white direction legend is for the C14 and C36 phases. The C15 phase is cubic and to accurately demonstrate the triple layers, it is presented along the direction represented by the coloured legend. The images were created using VESTA [64].

Further details related to these the structure of Laves phases can be found in [63].

2.2.2. Deformation mechanisms and mechanical properties of Laves phases

The deformation mechanisms and mechanical properties of Laves phases were first studied in detail by a group of scientists around Paufler and Schulze in Dresden, Germany [18]. The work of this group has been summarised rather recently by Paufler et al. [18, 65]. In Laves phases, plastic deformation occurs by dislocation slip and deformation twinning. The most common and widely reported mechanism of slip in Laves phase is via the synchroshear process [66].

2.2.2.1. Synchroshear deformation or transformation mechanism

Within the triple layers, the planes of large and small atoms are closely spaced by a distance of around ~0.05 nm, which is much smaller than the atom size. However, as can be seen in Figure 8, none of the planes are closely packed. Therefore, the shear of one plane over another occurs via double shear or the so called synchroshear mechanism [63, 66] which is explained in the following.

Synchroshear deformation occurs within the triple layer. If the lower layer of large atoms within the triple layer is stationary, the small atoms (see Figure 9) can only move along either of the directions: $-b_1$,$-b_2$ or $-b_3$. However, this is only possible if the large atoms also move synchronously along their respective $-b_1$,$-b_2$ or $-b_3$ direction, relative to the small atoms. This means for synchroshear, the c and β atoms must move together. This type of synchroshear movement within the triple layer thus converts a t type layer into a t′ layer [63]. These synchronised movements of small and large atoms can be conveniently explained by the movement of two Shockley partial dislocations on two adjacent planes. These two Shockley partials are closely coupled due to energetic reasons. Thus, the pair of Shockley dislocations, is considered as a single synchro-Shockley partial dislocation having its core spread on two adjacent planes [66, 67]. The movement of this synchro-Shockley partial dislocations is responsible for phase transformations (shear and stress induced), slip and twinning in the Laves phases [63, 66, 68].

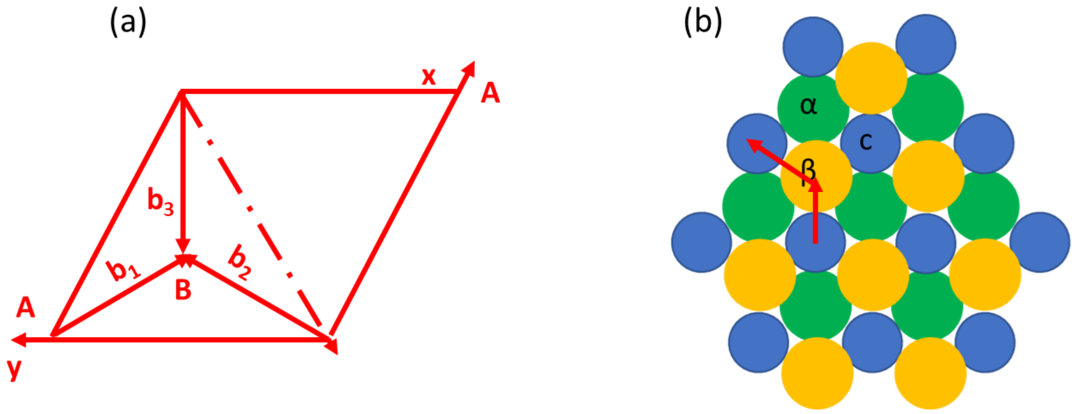

Figure 9. (a) Unit cell projected on (0001) for the C14 and C36 phases and on (111) for the C15 phase, (b) stacking sequence in the triple layer, t. The images were recreated using data presented in [63].

2.2.2.2. Deformation behaviour of Mg based Laves phases

The inherent brittleness of Laves phases limits the possibility to study the bulk mechanical behaviour of Laves phases at temperature below ~$0.6T_m$ (ductile-brittle transition temperature) [69]. A way to study the deformation mechanisms at temperatures below $0.6T_m$ is possible using micro-pillar compression [20], nanoindentation or hardness testing [17, 70]. Since the application temperature of Laves phase containing Mg-Al-Ca alloys is limited to around 200 °C, it is important to understand their deformation behaviour at temperatures below $0.6T_m$. Kirsten et al. [70] studied the deformation behaviour and mechanical properties of $MgZn_2$ and Mg_2Ca Laves phases using Brinell hardness tests. They found that the hardness of the $MgZn_2$ phase is nearly unaffected by temperature below the transition temperature ($0.61T_m$), while the hardness of the Mg_2Ca phase was only mildly affected until $0.59T_m$. After the transition temperature the hardness abruptly dropped for both phases. They [70] also reported deformation by prismatic slip at room temperature for the Mg_2Ca phase and by basal slip for the $MgZn_2$ Laves phase below the transition temperature. Further, the anisotropy of the hardness for various orientations of hexagonal based Laves phases was also reported by Kirsten et al. [18, 71]. The variation of microhardness with crystal orientation for Mg_2Ca is summarised in Table 2.

Table 2. Microhardness variation with orientation [18, 71].

Compound	**Planes**	**H_M, GPa**
Mg_2Ca	(0001)	2.23 ± 0.06
	$(10\bar{1}0)$	2.13 ± 0.06

	$(11\bar{2}2)$	1.96 ± 0.06
	$(10\bar{1}1)$	1.87 ± 0.06

Moreover, data pertaining to the mechanical properties of Laves phases present in Mg-Al-Ca alloys is very limited i.e., Brinell hardness variation with temperature [70] or microhardness variation with orientation [18, 71]. Further, there is one more study by Rokhlin et al. [17], who reported variation in the microhardness with temperature for Mg_2Ca and Al_2Ca Laves phases after different holding times. The data is shown schematically in Figure 10. There is almost no data on the CRSS at low temperatures for various slip systems except one recent study by Zehnder et al. [20] on Mg_2Ca (see section 2.3.5 and Figure 14).

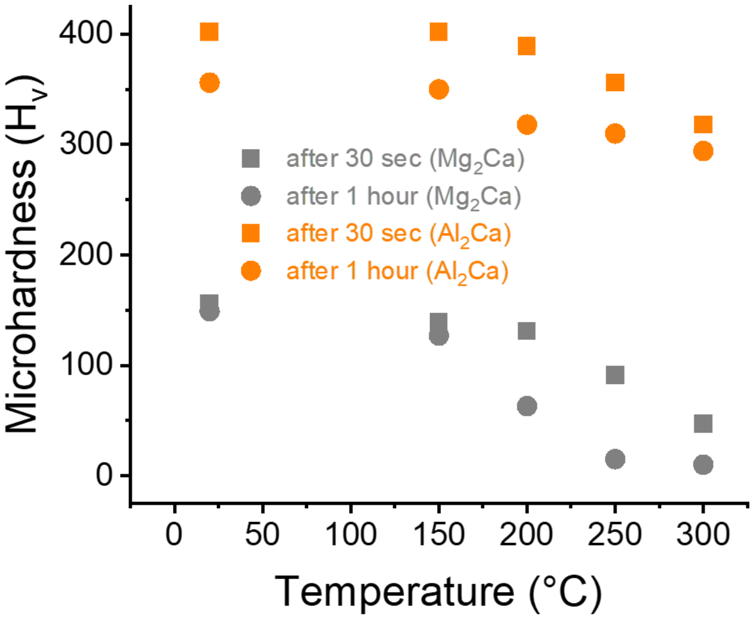

Figure 10. Variation of hardness with temperature and holding time for Mg_2Ca and Al_2Ca Laves phases as reported by Rokhlin et al. [17].

Also, no data on the mechanical properties of the C36 phase present in Mg-Al-Ca alloys are available to the author's best knowledge. However, the determination of the mechanical properties of each Laves phase over a range of temperature (from RT to 200 °C) is vital in completely understanding the deformation behaviour of these alloys and requires more research in the future.

2.3. Mg-Al-Ca alloys

2.3.1. Solidification behaviour of Ca containing Mg-Al alloys

Suzuki et al [72] studied a very wide range of Mg-Al-Ca alloys and found that the liquidus temperature of these alloys decreases with the additions of Ca and Al. In alloys having relatively low Al and Ca contents (for example in alloys with nominal compositions of Mg-3.6Al-3.7Ca, Mg-5Al-3Ca, Mg-8Al-3Ca), the α-Mg phase solidifies first as the primary phase. The actual liquidus temperature varies with alloy composition. Solidification is terminated by the formation of either C36, C14 or A12 ($Mg_{17}Al_{12}$) phase through a eutectic reaction depending on the composition, i.e., the content of Al and Ca and the Ca/Al ratio. Liang et al. [73] also studied the solidification behaviour of AZ91 and AM50 alloys with different Ca additions. They also reported that with increasing Ca/Al ratio, the Ca containing intermetallic Laves phases change from C15 to C36 and C14.

2.3.2. Microstructure of as-cast Mg-Al-Ca alloys

The evolution of phases in the microstructure of ternary Mg-Al-Ca alloys is determined by the i) Al content [74-76], ii) Ca content [10, 12] and iii) Ca/Al ratio [74, 77]. In addition to that, the contents of the alloying elements as well as the Ca/Al ratio determines the amount (volume fraction), type (C14, C15 or C36), distribution and morphology (discontinuous, partially connected or fully connected skeleton) of the intermetallic reinforcing Laves phase. The effect of alloying elements on the type of reinforcing intermetallic Laves phase present in Mg-Al-Ca alloys is reported in Table 3.

Table 3. Effect of alloying elements and Ca/Al ratio on the type of secondary phase/s formed.

Alloy composition						**Method of phase determination**	**Secondary Phase/s**
Al	**Ca**	**Sr/Zn**	**Mn**	**Mg**	**Ca/Al**		
4.52	2.98	0.14	0.25	Balance	0.66	TEM	C36 [78]
2	3	-	-	Balance	1.5	SEM, TEM, TA*	C14 [72]
5	3	-	-	Balance	0.6	SEM, TEM, TA*	C36 & C14 [72]
8	3	-	-	Balance	0.38	SEM, TEM, TA*	C36 [72]
9.05	-	1.08	0.41	Balance	0	TA*, SEM	$Mg_{17}Al_{12}$ [73]
9.09	2.05	1.0	0.32	Balance	0.23	TA*, SEM	$Mg_{17}Al_{12}$ and C15 [73]

5.1	-	-	0.3	Balance	0	TA*, SEM	$Mg_{17}Al_{12}$ [73]
5.32	0.62	-	0.28	Balance	0.12	TA*, SEM	$Mg_{17}Al_{12}$ and C15 [73]
5.11	1.63	-	0.32	Balance	0.32	TA*, SEM	C36 [73]
5.37	2.89	-	0.3	Balance	0.54	TA*, SEM	C14 and C36 [73]
3.68	3.99	-	0.02	Balance	1.08	SE, TEM	C14 and C36 [79]
6	0.5	-	0.3	Balance	0.08	XRD, SEM	$Mg_{17}Al_{12}$ [10]
6	1.2	-	0.3	Balance	0.2	XRD, SEM	$Mg_{17}Al_{12}$ and C15 [10]
6	2	-	0.3	Balance	0.33	XRD, SEM	C15 [10]
4.4	1.1	-	0.4	Balance	0.25	SEM	C36 [80]
2.7	3.5	-	0.4	Balance	1.3	SEM	C14 [80]

*TA: Thermal analysis

Further it can be seen that when the Ca/Al ratio increases from 0 to 1, the type of intermetallic phase changes according to: A12 → C15 → C36 → C14. The effect of the Ca/Al ratio on the microstructure of as-cast Mg-Al-Ca alloys is summarised schematically in Figure 11.

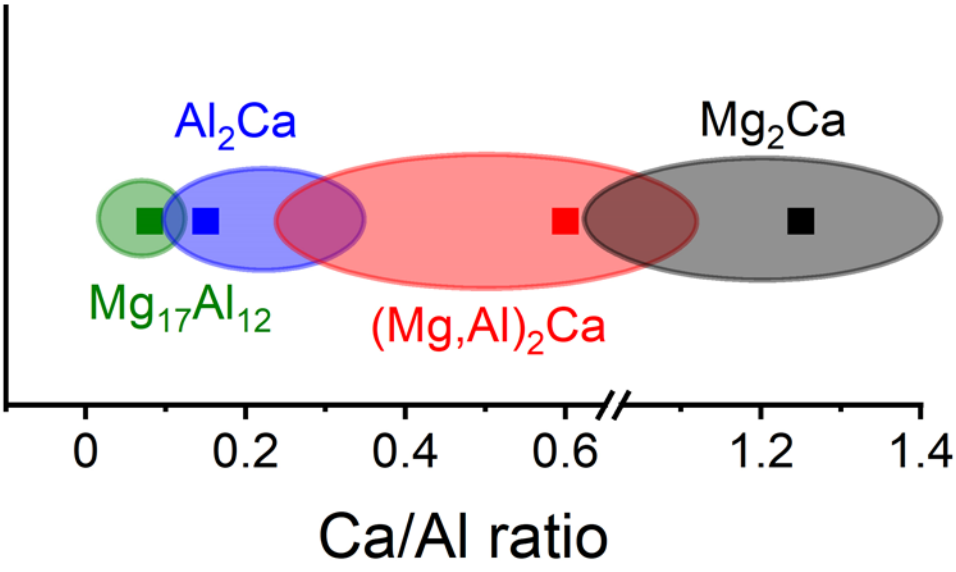

Figure 11. Effect of the Ca/Al ratio on the type of intermetallic phase formed reported in Mg-Al-Ca alloys.

2.3.3. Mechanical properties of Mg-Al-Ca alloys and the influence of the Ca/Al ratio

The yield and tensile strength of as-cast Mg-Al-Ca alloys are comparable to commercial cast Mg-Al alloys [1], however, these (Mg-Al-Ca) alloys exhibit significantly better creep properties than commercial AM or AZ series Mg alloys at temperatures > 125 °C. [12-14, 81-83]. An increase in Ca leads to a significant reduction in the minimum creep rates of Mg-Al alloys as visible in Figure 12. There is a nearly three orders of magnitude reduction in minimum creep rate for alloy AZX951 (AZ91 + 5 wt.% Ca) when compared to the commercial AZ91 as reported by Amberger et al. [13]. Similar results can be seen for AM50 (Figure 12). The better creep properties of Ca containing Mg-Al alloys are attributed to the interconnected, intermetallic skeleton of high strength Laves phases, commonly observed in these alloys. The precipitates in AM50 and AZ91 alloys are discontinuous $Mg_{17}Al_{12}$ phase precipitates. The Laves phase skeleton is an effective obstacle against plastic deformation carriers in this alloy [13].

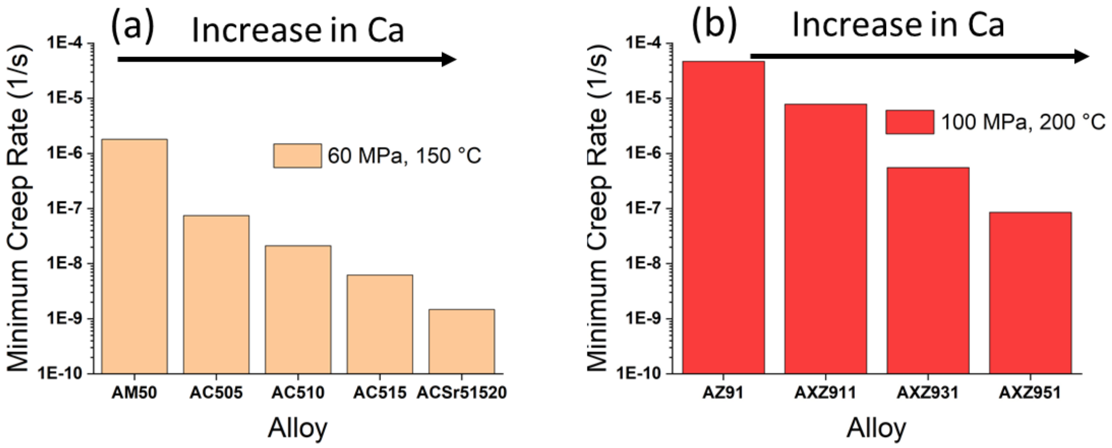

Figure 12. An increasing amount of Ca leads to a reduction in the minimum creep rate in a) AM50 alloy [83] and b) AZ91 alloy [13].

2.3.3.1. Effect of casting on mechanical properties

The yield and ultimate strength of the as-cast alloys in tension and compression are dependent on the casting method, e.g., Nakaura et al. [83] reported a yield strength of about 150 MPa for die-cast Mg-5.16Al-1.45Ca-0.11Sr-0.22 and Mg-5.26Al-1.63Ca-0.22Sr-0.27Mn alloys at room temperature. The tensile strength was also ~200 MPa and >200 MPa for both alloys, respectively. On the contrary, sand-cast Mg-6.3Al-3.7-Ca-0.3Mn and Mg-4.5-Al-2.0-Ca-0.5Mn alloys exhibited yield strength of 79 ± 6 and 81 ± 5 MPa, respectively, while the tensile strength amounted to 116 ± 15 and 111 ± 18 MPa for the two alloys, respectively [84]. In a similar way, the creep properties of die-cast Mg-Al-Ca with small amounts of Sr, were much better than that of a permanent mould cast alloy with a similar composition (see Figure 13) [85]. Die-cast alloys exhibited smaller grain size and lower minimum creep rates at all stress levels as compared to their coarse-grained counterparts [85].

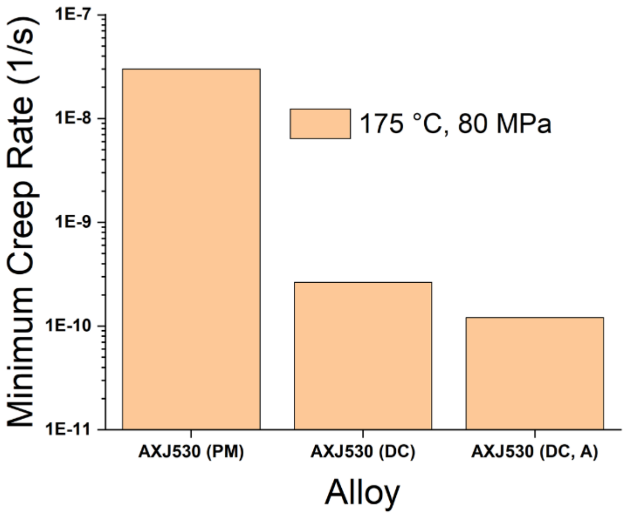

Figure 13. Comparison of the creep properties of permanent and die-cast Mg-5.3Al-2.6Ca-0.17Sr-0.3Mn (AXJ530) alloys [85]. PM stands for permanent mould cast and DC stands for die-cast alloy while A stands for aging.

Further, it can be seen that the creep properties of die-cast AXJ530 alloy slightly improve with aging. This is because the aging at 573K results in the formation of needle like Al_2Ca precipitates within the Mg matrix. These precipitates share a definite orientation relationship with the matrix of $(111)_{C15}||(0001)_{\alpha-Mg}$, $[01\bar{1}]_{C15}||$ $[0\bar{1}10]_{\alpha\text{-Mg}}$ and are parallel to the basal planes of the matrix. Thus, they cannot not hinder the movement of basal dislocations. Basal slip is by far the most common and abundant deformation mechanism for Mg and, therefore, the precipitates result in only slight improvement of the creep properties of the aged AXJ530 alloy (Figure 13).

2.3.4. Strain distribution during deformation

Digital image correlation (DIC) is a powerful, advanced, and relatively simple method to quantify the strain localisation in complex stress states during macro and microscopic loading [86-99]. In DIC, images before and after deformation are recorded and correlated, by measuring and quantifying the relative displacement of two images of the same region. The amount of deformation varies with position in the image because of microstructural heterogeneities like grain or phase boundaries, inclusions etc. In order to quantify displacement and consequently strain, the individual images are subdivided into smaller facets and these small facets are then individually correlated for the deformed and un-deformed image [87]. Among the most important parameters controlling the resolution of DIC strain maps are the speckle size, the facet size and the facet step size. Their role and importance in strain mapping have already been reported elsewhere [87, 100]. The microstructure of Mg-Al-Ca alloys is highly heterogeneous and consists of the soft α-Mg matrix reinforced with hard interconnected intermetallic Laves phase skeleton (see Figure 5). So, due to the highly heterogeneous microstructure, strain is also expected to be non-uniform in certain microstructural regions of the alloys. Although strain maps for samples deformed in creep loading have been shown and discussed by Saddock et al. [85], the strain maps presented in this thesis are at higher resolution, correlated with crystal orientation and thus provide additional information. In this thesis, the DIC was done for samples deformed at ~170 °C in tensile loading.

2.3.5. Co-deformation of metallic and intermetallic phases

The CRSS values of different slip systems are much higher in the Mg_2Ca Laves phase than in Mg (see Figure 14), i.e., specifically, the difference amounts to three orders of magnitude for basal slip.

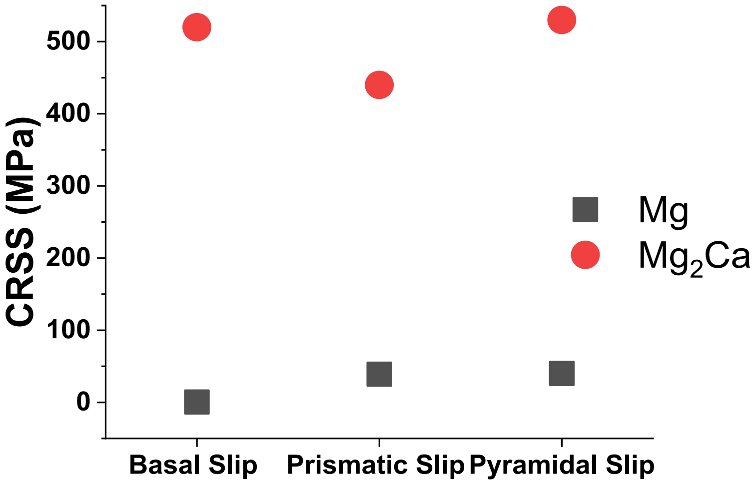

Figure 14. Difference between the CRSS values for basal slip, prismatic slip and pyramidal slip for Mg and the Mg_2Ca Laves phase. The values shown are extracted from [20, 24, 25, 27].

However, it should be considered that the slip behaviour from experiments on single crystals cannot truly account for polycrystalline Mg alloys, for example, in case of Mg, the CRSS for basal slip is around 1/80 to that reported for prismatic or pyramidal slip systems from single crystal experiments. However, in polycrystalline alloys, the presence of grain boundaries [36, 101], alloying elements [102] and precipitates [35, 103] significantly affects the deformation behaviour and activation of non-basal slip systems in alloys. In line with this description, the reported CRSS ratio between non-basal and basal slip systems in polycrystalline Mg alloys, is quite low (~2-3) when compared to the values obtained from testing single crystals (~80-100)

(Figure 14). Therefore, non-basal slip (in addition to basal slip) is readily observed in several Mg alloys [37, 38, 104].

The strong microstructural and mechanical heterogeneity of Mg-Al-Ca alloys requires an in depth understanding of slip transfer mechanisms to understand the co-deformation behaviour of these alloys. Slip transfer can occur due to backstress hardening in the Mg matrix and the induced forward stresses on the interfaces.

2.3.5.1. Back stress hardening and forward stresses

If a dual phase material, like Mg-Al-Ca alloys, is subjected to tensile loading, a dislocation source S_1 in the softer matrix is activated once the CRSS of the corresponding slip system is exceeded. In the case of the α-Mg phase, the initial dislocation slip is assumed to be basal slip. The emitted dislocations then move under the influence of the resolved shear stress, τ_a, and pile up at the phase boundaries. This pile up of dislocations creates back stresses, τ_b, on the dislocation source (Figure 15). The effective stress (τ_e) on the dislocation source S_1 can then be described via Equation 2 [105]:

$$\tau_e = \tau_a - \tau_b \qquad \text{Equation 2}$$

The source emits dislocations as long as τ_e is higher than the critical stress required to emit dislocations. This means with an increasing number of dislocations in the pile-up, more stress is needed to emit further dislocations, this is known as back-stress hardening. Moreover, this pile-up of dislocations creates a strain and stress gradient within the matrix [105]. The stress is highest concentrated at the interface.

The induced forward stresses on the interface are many times larger than the applied stress, τ_a, and depends on the number of dislocations in the pile up, as described by Equation 3 [106, 107]:

$$\tau_i = n\tau_a \qquad \text{Equation 3}$$

where τ_i is the stress concentration at the interface and n is the number of dislocations.

2.3.5.2. Activation of secondary slip systems

As mentioned in the previous section, pile ups of dislocations are associated with stress and strain gradients. The strain gradient will be highest at the interface and must be accommodated by the nucleation of geometrically necessary dislocations (GNDs) [105]. Non-basal (<c+a> dislocations) GNDs around non-shearable Al_2Ca precipitates in a Mg-6Al-1Ca alloy were observed by Zhu et al. [103]. In addition to these non-basal GNDs at the interfaces, the back stress work hardening in the soft α-Mg matrix can also activate non-basal dislocations sources in the matrix (see Figure 15 and chapter 8 for further details).

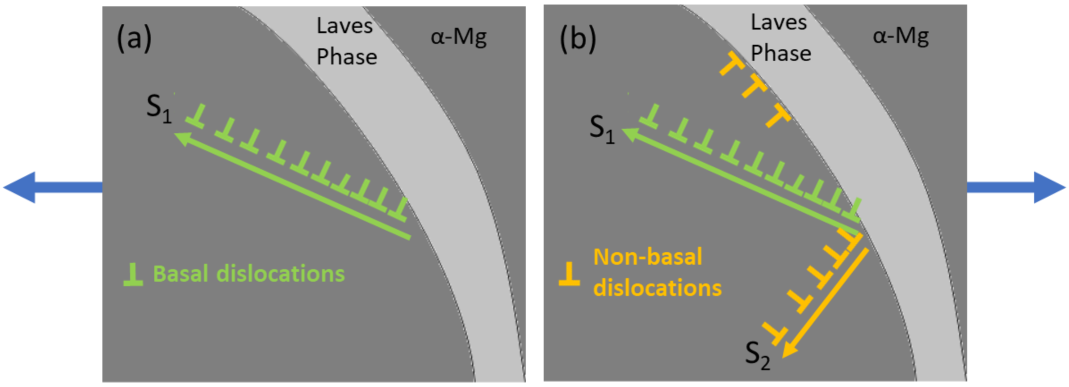

Figure 15. (a) Activation of basal slip. The direction of green arrow represents the direction of the back stress on the dislocation source, S_1, (b) activation of non-basal dislocations in the α-Mg matrix and at the α-Mg/Laves phase interface. The direction of the forward stresses on the Laves phase by basal and non-basal dislocations is opposite to that of the green and orange arrows. Blue arrows show the direction of tensile loading.

Under the influence of the stress concentration induced by basal and non-basal dislocations at the interface, the Laves phase can behave in three different ways.

i) Cracks may develop in the intermetallic phase (Figure 16a).
ii) Dislocations may transfer from the metallic to the intermetallic phase (Figure 16a).
iii) The strain may be accommodated by interface (α-Mg/Laves phase) sliding or interface cracking/decohesion.

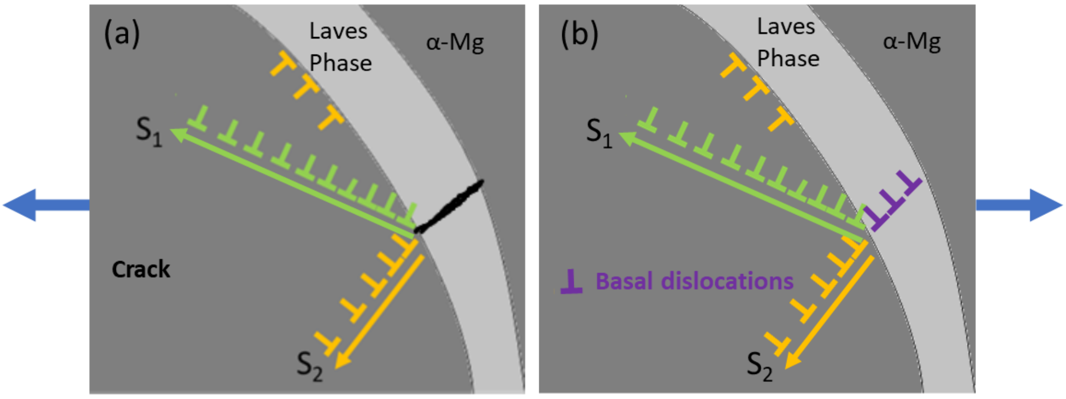

Figure 16. (a) Micro-crack nucleation in Laves phase because of stress induced by dislocations pile up in α-Mg phase, (b) slip in the Laves phase activated by dislocation pile up in α-Mg phase.

2.3.5.3. Nucleation of micro-cracks

The formation of cracks at stress concentration points like slip band or twin-grain/phase boundaries intersections was widely reported in the literature [56, 57, 108, 109]. Huang et al. [108], in their work on a Ti-6Al extra low interstitial (ELI) alloy, proposed that the cracks nucleate along grain boundaries where no slip transmission occurs or at grain boundaries that are geometrically incompatible. Significant stress concentrations along such boundaries provides preferential micro-cracks nucleation sites. This means an easier slip transfer results in more homogeneous plastic flow while difficult configurations for slip transfer lead to micro-crack initiation [108, 110, 111]. In many alloys, hard second phases or the interfaces between hard and soft phases were found to be dominant crack nucleation sites [14, 79, 112-116].

2.3.5.4. Slip transfer mechanisms at grain boundaries

Various types of slip transfer mechanisms across grain boundaries have been reported in the literature [117].

a. Direct transfer occurs when the slip planes in both grains have a common line of intersection in the grain boundary plane. Moreover, the Burgers vectors of the dislocations in both grains must be equal and collinear.
b. Dislocations may be absorbed at the grain boundaries, which can induce the nucleation of a dislocation in the adjacent grain leaving behind a residual dislocation at the grain or phase boundary. The dislocation nucleation occurs either at the same point where the dislocations of the primary grain are intersecting with the grain boundary, but can also be away from the point of intersection [117-119].

Consequently, dislocation-grain boundaries interactions can be divided into four stages: i) pile up of dislocations at the boundary, ii) absorption of dislocations into the interface, iii) nucleation of dislocation from the boundary, and iv) propagation of the dislocations from the boundary. At all stages, conservation of the Burgers vector of the system is mandatory. The piled-up dislocations can also be dissociated in the grain boundaries without subsequent re-emission or these can also be reflected into the parent grain [117, 118]. The slip transfer from one grain to another is governed by certain rules, i.e., as per the Lee-Robertson-Birnbaum (LRB) criteria, the slip is easier [117, 119, 120] if:

1. the angle between the lines of intersection by the slip plane and the grain boundary plane is minimum.

2. the magnitude of residual dislocations at the grain boundary is small. The ejection of a dislocation in the grain where slip is transmitted, generally requires the creation of residual dislocations.
3. the resolved shear stress acting on the outgoing slip system from the piled-up dislocations is high.

Out of these three, the second criteria is believed to be the most important one [121]. The compatibility of slip transfer is also expressed by an geometric compatibility factor, m', parameter first suggested by Luster and Morris [122], Equation 4.

$$m' = \cos\Phi \,.\, \cos\kappa \qquad \text{Equation 4}$$

where, Φ and κ are the angles between the slip planes normals and the slip directions in two adjacent grains or phases, respectively. Values of m' close to 1 indicate that the slip systems are aligned and highly favourable for slip transmission, while m'= 0 means that the slip systems are completely incompatible.

2.3.5.5. Slip transfer across phase boundaries

Similar to grain boundaries, slip transfer across phase boundaries is also affected by the alignment or deviation of slip systems of both phases [123].

a. Interfaces between two metallic phases

Dislocation transfer across interfaces between two metallic phases was extensively studied in Ti alloys [124-126]. Dislocation transfer is easier if the misorientation between the slip systems of the two phases is small [123, 126, 127]. Savage et al. [127] reported that a small misorientation (~0.25 °) between the slip systems of the α and β phases in Ti-6242 alloy resulted in easier slip transfer, lower strength and lower work hardening. On the contrary, misorientations of ~11 ° between the primary slip systems of both phases resulted in an increased difficulty in slip transmission, higher stresses, more work hardening and a higher number of dislocation pile ups at the α/β interfaces. Similarly, Zhang et al. [126] also proposed that slip transfer across α/β interfaces is favoured if the slip plane normals of both phases are aligned.

b. Interfaces between metallic and non-metallic phases

Dislocation transfer across such interfaces between metallic and non-metallic phases is much more complex than that across interfaces between metallic phases [123]. Pearlitic steel (containing ferrite and cementite) is one alloy group in which dislocation transfer mechanisms were extensively studied [123, 128]. Cold wire drawing of such steels results in an enormous increase in the flow stress, decreasing thickness of the cementite lamellas and reduction in the inter-lamellar spacing between ferrite and cementite [128, 129]. Under the application of an external stress, plasticity is first induced in the ferrite lamella [130] and then the slip proceeds into the cementite lamella [131]. Slip transfer occurs by $\frac{1}{2}\{110\}\langle 111\rangle$ and $\frac{1}{2}\{112\}\langle 111\rangle$ in the ferrite [130, 132, 133]. These feasibility of slip transfer has been studied using the LRB criteria [133] suggesting that slip transfer can only occur along 2 {110}<111> slip systems and 1 {112}<111> slip system of the ferrite.

2.3.5.6. Slip transfer in Mg-Al-Ca alloys

Zhu et al. [103] recently reported a co-deformation mechanism for a homogenised and extruded Mg–6Al–1Ca (wt%) alloy (AX61). The alloy exhibited appreciable formability and a reasonably high work hardening capacity. According to them [103], basal slip was first activated in the Mg matrix when loaded in tension. Then, the dislocations piled-up at the intermetallic (Al_2Ca)/metallic (Mg) interfaces generating non-basal geometrically necessary dislocations in the matrix. The induced stresses then caused deformation of the Al_2Ca by dislocation slip on the {111} plane. They related the difficulty to deform the Al_2Ca phase, along with the enhanced non-basal dislocation activity to the large work hardening and tensile elongation of the respective material system.

3. General Conclusions

The focus of this thesis is to contribute to a better Mg-Al-Ca alloy for elevated temperature applications and to gain an in depth understanding of the co-deformation mechanisms of Mg-Al-Ca alloys. The following general conclusions can be drawn from this thesis.

1. Effect of the Ca/Al ratio on the microstructure of Mg-Al-Ca alloys

An increase in the Ca/Al ratio leads to

i) an increase in the volume fraction of the Laves phases,
ii) a change in the Laves phase morphology: from a loosely connected (at Ca/Al=0.32) to a fully interconnected skeleton (at Ca/Al=1.03),
iii) reduced dissolution of Al in the α-Mg phase,
iv) a change in the type of Laves phase changes from a combination of C15 and C36 phase at low Ca/Al to C14 and C36 at higher Ca/Al ratio.

2. Effect of the Ca/Al ratio on the mechanical properties of Mg-Al-Ca alloys

With an increase in the Ca/Al ratio, the

i) microhardness and yield stress increase at the expense of ductility.
ii) minimum creep rate and stress exponents, determined at 170 °C and within 50–70 MPa, are reduced.

3. Strain partitioning and study of µ-cracks nucleation

The high-resolution strain maps reveal that during tensile deformation at 170 °C, the strain is mainly carried by the α-Mg phase. Further, the strain is localised along slip lines, deformation twins, and at α-Mg/Laves phase interfaces. Moreover, cracks in the Laves phase form at strain concentration points. The Euler number depicting connectivity of Laves phase also decreases with increasing deformation.

Further, from quasi in-situ and bulk material analysis, it was observed that micro-damage nucleates in the Laves phase at locations where basal slip lines and tensile twins in the α-Mg phase intersect the Laves phase. Basal slip and tensile twinning were more localised in grains with higher respective Schmid factors. In line with this observation, cracks in the Laves phase were more concentrated in grains with higher Schmid factors for basal slip and tensile twinning.

4. Slip transfer from Mg to the Laves phase

In addition to cracking, slip transmission into the Laves phase and also interfacial sliding triggered by slip and twinning in the Mg phase, were also observed in experiments and in atomistic simulations (performed by Dr. Julien Guenole). SEM and TEM analysis revealed that deformation of the $(Mg,Al)_2Ca$ Laves phase occurred via basal slip. The simulations on the Mg/Mg_2Ca system revealed that deformation of the Mg_2Ca (C14) phase occurred along basal and prismatic planes. Moreover, simulations indicated that the slip transfer mechanism from Mg to the Mg_2Ca phase depends on temperature and orientation relationship between both phases.

5. Effect of the orientation relationship on the mechanism of slip transfer

Atomistic simulations considered two different orientation relationships.

i) Parallel basal planes in Mg and the Mg_2Ca phase:

For such an OR, basal slip in the Mg_2Ca phase was triggered from the interface at the point where basal <a> dislocations were impinging from the Mg matrix. This is considered as direct slip transfer

ii) Perpendicular basal planes in Mg and the Mg_2Ca phase:

For such an OR, stress concentrations at the interface initiated prismatic slip via a non-dissociated <a> dislocations in the Mg_2Ca phase. This is considered as indirect slip transfer. TEM (performed by Dr. Lipińska-Chwałek) revealed that the basal planes of α-Mg and the $(Mg,Al)_2Ca$ phase were nearly perpendicular to each other. However, unlike prismatic slip, the C36 phase deformed via basal slip. Moreover, in addition to basal slip, non-basal dislocations were also observed in the vicinity of α-Mg/C36 Laves phase interface. These non-basal dislocations are supposed to create favourable stress concentration to trigger basal slip in the C36 Laves phase.

6. Mechanical properties of the individual phases

Nanoindentation short interval constant strain rate tests demonstrated that the hardness of the α-Mg phase decreases with temperature while the hardness of the C14 Laves phase stays constant at least until 200 °C. In line with these results, the hardness at α-Mg/C14 and α-Mg/C36 interfaces was also higher than that of the α-Mg matrix at all testing temperatures. The hardness-depth curves of the indents made close to the interfaces revealed noticeable hardening after a certain depth. This showed that dislocations pile-ups at interfaces can create back stress work hardening of the matrix.

Nanoindentation creep tests at 170 °C on the other hand showed that the hardness of both, the α-Mg and the Mg_2Ca phase, decreases noticeably during creep loading, especially at strain rates below 0.01/s.

7. Thermally activated mechanisms in α-Mg matrix

The strain rate sensitivity of both, the α-Mg phase and Mg-Laves phase interfaces increased with temperature. The activation volume determined from strain rate jump tests suggests the possibility of dislocation cross-slip as predominant thermally activated deformation mechanism especially in the temperature range of 100–170 °C in the α-Mg matrix. The activation volume at interfaces was lower than that of the α-Mg matrix at all testing temperatures. This may be attributed to the interfacial sliding occurring at the α-Mg/Laves phase interfaces.

4. Outlook and Future Work

The present work demonstrates that the Laves phase can deform plastically in the Mg-Al-Ca alloys and its strut thickness in the α-Mg matrix can be used as a tool to design alloys with appreciable ductility without sacrificing creep properties. However, the following experiments can be carried out in direct extension of this work to gain more insights into the deformation behaviour of these dual phase alloys.

1. More post mortem TEM and in-situ deformation in TEM

The presented TEM results are sufficient to propose a first suggestion for a mechanism of co-deformation. However, slip transfer across metallic to intermetallic phase is complex, therefore, more work (more post mortem TEM and if possible in-situ deformation inside TEM) is needed to fully understand and verify the mechanism of slip transfer.

2. Micro-pillar compression tests

The grain size of Mg-Al-Ca alloys is much larger (above 150 µm in most cases) than the area bounded by intermetallic struts (~30 µm, see chapter 5 to 8). Therefore, it offers a possibility to mill several micro-pillars in selected orientations both in the matrix and at the α-Mg/Laves phase interfaces. These experiments will be able to i) explain the strengthening effect induced by the Laves phases in α-Mg phase and ii) present the possibility to observe co-deformation as a function of matrix and Laves phase orientation. These experiments can be done over a range of temperature since it is known that non-basal slip is more favourable at elevated temperatures (Figure 3 b) and its seems critical in activating basal slip in C36 Laves phase (see chapter 8).

3. Quasi in-situ deformation inside SEM

The tensile specimen can be deformed over a range of strain rates and temperatures. Large scale panoramas can be captured inside SEM and the effect of temperature and strain rates on cracking of Laves phase and slip transfer from α-Mg to Laves phase samples could be observed using machine learning techniques.

References

1. Powell, B.R., P.E. Krajewski, and A.A. Luo, *Magnesium alloys for lightweight powertrains and automotive structures*, in *Materials, Design and Manufacturing for Lightweight Vehicles*. 2021. p. 125-186.
2. Mallick, P.K., *Overview*, in *Materials, Design and Manufacturing for Lightweight Vehicles*, P.K. Mallick, Editor. 2021, Woodhead Publishing. p. 1-36.
3. Lee, J.H., et al., *Improved tensile properties of AZ31 Mg alloy subjected to various caliber-rolling strains.* Journal of Magnesium and Alloys, 2019. **7**(3): p. 381-387.
4. Fu, Y., et al., *Deformation mechanisms and differential work hardening behavior of AZ31 magnesium alloy during biaxial deformation.* Journal of Magnesium and Alloys, 2020.
5. Dinaharan, I., et al., *Assessment of Ti-6Al-4V particles as a reinforcement for AZ31 magnesium alloy-based composites to boost ductility incorporated through friction stir processing.* Journal of Magnesium and Alloys, 2021.
6. Zhang, K., Z. Shao, and J. Jiang, *Effects of twin-twin interactions and deformation bands on the nucleation of recrystallization in AZ31 magnesium alloy.* Materials & Design, 2020. **194**: p. 108936.
7. Barker, E.I., et al., *Microstructure based modeling of beta phase influence on mechanical response of cast AM series Mg alloys.* Computational Materials Science, 2014. **92**: p. 353-361.
8. Afsharnaderi, A., et al., *Enhanced mechanical properties of as-cast AZ91 magnesium alloy by combined RE-Sr addition and hot extrusion.* Materials Science and Engineering: A, 2020. **792**: p. 139817.
9. Mathur, H.N., V. Maier-Kiener, and S. Korte-Kerzel, *Deformation in the* γ*-*$Mg_{17}Al_{12}$ *phase at 25–278 °C.* Acta Materialia, 2016. **113**: p. 221-229.
10. Kondori, B. and R. Mahmudi, *Effect of Ca additions on the microstructure, thermal stability and mechanical properties of a cast AM60 magnesium alloy.* Materials Science and Engineering: A, 2010. **527**(7): p. 2014-2021.
11. Ashrafizadeh, S.M., R. Mahmudi, and A.R. Geranmayeh, *A comparative study on the effects of Gd, Y and La rare-earth elements on the microstructure and creep behavior of AZ81 Mg alloy.* Materials Science and Engineering: A, 2020. **790**: p. 139712.
12. Kondori, B. and R. Mahmudi, *Effect of Ca additions on the microstructure and creep properties of a cast Mg–Al–Mn magnesium alloy.* Materials Science and Engineering: A, 2017. **700**: p. 438-447.
13. Amberger, D., P. Eisenlohr, and M. Göken, *Microstructural evolution during creep of Ca-containing AZ91.* Materials Science and Engineering: A, 2009. **510-511**: p. 398-402.
14. Amberger, D., P. Eisenlohr, and M. Goken, *On the importance of a connected hard-phase skeleton for the creep resistance of Mg alloys.* Acta Materialia, 2012. **60**(5): p. 2277-2289.
15. Sakai, T., et al., *Tensile creep behavior of a die-cast Mg–6Al-0.2Mn–2Ca-0.3Si (wt.%) alloy.* Materials Science and Engineering: A, 2020. **774**: p. 138841.
16. Amerioun, S., S.I. Simak, and U. Häussermann, *Laves-Phase Structural Changes in the System* $CaAl_{2-x}Mg_x$. Inorganic Chemistry, 2003. **42**(5): p. 1467-1474.
17. Rokhlin, L.L., et al., *Calcium-alloyed magnesium alloys.* Metal Science and Heat Treatment, 2009. **51**(3): p. 164.
18. Paufler, P., *Early work on Laves phases in East Germany.* Intermetallics, 2011. **19**(4): p. 599-612.
19. Wei-chao, Z., L.I. Shuang-shou, and T. Bin, *Microstructure and properties of Mg-Al binary alloys.* China Foundry, 2006. **3**(4): p. 270-274.
20. Zehnder, C., et al., *Plastic deformation of single crystalline C14* Mg_2Ca *Laves phase at room temperature.* Materials Science and Engineering: A, 2019. **759**: p. 754-761.
21. Takata, N., et al., *Plastic deformation of the C14 Laves phase* $(Fe,Ni)_2Nb$. Scripta Materialia, 2013. **68**(8): p. 615-618.
22. Luo, W., et al., *Crystal structure and composition dependence of mechanical properties of single-crystalline* $NbCo_2$ *Laves phase.* Acta Materialia, 2020. **184**: p. 151-163.

23. Akhtar, A. and E. Teghtsoonian, *Solid solution strengthening of magnesium single crystals—I alloying behaviour in basal slip.* Acta Metallurgica, 1969. **17**(11): p. 1339-1349.
24. Conrad, H. and W.D. Robertson, *Effect of temperature on the flow stress and strain-hardening coefficient of magnesium single crystals.* JOM, 1957. **9**(4): p. 503-512.
25. Reed-Hill, R.E. and W.D. Robertson, *Deformation of magnesium single crystals by nonbasal slip.* JOM, 1957. **9**(4): p. 496-502.
26. Akhtar, A. and E. Teghtsoonian, *Solid solution strengthening of magnesium single crystals—ii the effect of solute on the ease of prismatic slip.* Acta Metallurgica, 1969. **17**(11): p. 1351-1356.
27. Obara, T., H. Yoshinga, and S. Morozumi, $\{11\bar{2}2\}$ $\langle\bar{1}\bar{1}23\rangle$ *Slip system in magnesium.* Acta Metallurgica, 1973. **21**(7): p. 845-853.
28. Byer, C.M., et al., *Microcompression of single-crystal magnesium.* Scripta Materialia, 2010. **62**(8): p. 536-539.
29. Chapuis, A. and J.H. Driver, *Temperature dependency of slip and twinning in plane strain compressed magnesium single crystals.* Acta Materialia, 2011. **59**(5): p. 1986-1994.
30. Yu, Q., J. Zhang, and Y. Jiang, *Direct observation of twinning–detwinning–retwinning on magnesium single crystal subjected to strain-controlled cyclic tension–compression in [0 0 0 1] direction.* Philosophical Magazine Letters, 2011. **91**(12): p. 757-765.
31. Akhtar, A. and E. Teghtsoonian, *Substitutional solution hardening of magnesium single crystals.* The Philosophical Magazine: A Journal of Theoretical Experimental and Applied Physics, 1972. **25**(4): p. 897-916.
32. Stanford, N. and M.R. Barnett, *Solute strengthening of prismatic slip, basal slip and twinning in Mg and Mg–Zn binary alloys.* International Journal of Plasticity, 2013. **47**: p. 165-181.
33. Hull, D. and D.J. Bacon, *Chapter 6 - Dislocations in Other Crystal Structures*, in *Introduction to Dislocations (Fifth Edition)*, D. Hull and D.J. Bacon, Editors. 2011, Butterworth-Heinemann: Oxford. p. 109-136.
34. Agnew, S.R., *2 - Deformation mechanisms of magnesium alloys*, in *Advances in Wrought Magnesium Alloys*, C. Bettles and M. Barnett, Editors. 2012, Woodhead Publishing. p. 63-104.
35. Huang, Z., et al., *Dislocation cross-slip in precipitation hardened Mg–Nd alloys.* Journal of Alloys and Compounds, 2021. **859**: p. 157858.
36. Koike, J., *Enhanced deformation mechanisms by anisotropic plasticity in polycrystalline Mg alloys at room temperature.* Metallurgical and Materials Transactions A, 2005. **36**(7): p. 1689-1696.
37. Koike, J. and R. Ohyama, *Geometrical criterion for the activation of prismatic slip in AZ61 Mg alloy sheets deformed at room temperature.* Acta Materialia, 2005. **53**(7): p. 1963-1972.
38. Zhu, G., et al., *Improving ductility of a Mg alloy via non-basal <a> slip induced by Ca addition.* International Journal of Plasticity, 2019. **120**: p. 164-179.
39. Sandlöbes, S., et al., *The relation between ductility and stacking fault energies in Mg and Mg–Y alloys.* Acta Materialia, 2012. **60**(6): p. 3011-3021.
40. Sandlöbes, S., et al., *On the role of non-basal deformation mechanisms for the ductility of Mg and Mg–Y alloys.* Acta Materialia, 2011. **59**(2): p. 429-439.
41. Sandlöbes, S., et al., *Basal and non-basal dislocation slip in Mg–Y.* Materials Science and Engineering: A, 2013. **576**: p. 61-68.
42. Guan, L., et al., *Activation of <c+a> slip and enhanced ductility in as-extruded Mg-Gd-Y-Nd alloys through Si addition.* Materials Science and Engineering: A, 2021. **804**: p. 140736.
43. Liu, B.-Y., et al., *Large plasticity in magnesium mediated by pyramidal dislocations.* Science, 2019. **365**(6448): p. 73.
44. Wei, K., et al., *Enhancing the strain hardening and ductility of Mg-Y alloy by introducing stacking faults.* Journal of Magnesium and Alloys, 2020. **8**(4): p. 1221-1227.
45. Wei, K., et al., *Grain size effect on tensile properties and slip systems of pure magnesium.* Acta Materialia, 2021. **206**: p. 116604.
46. Buey, D. and M. Ghazisaeidi, *Atomistic simulation of <c+a>screw dislocation cross-slip in Mg.* Scripta Materialia, 2016. **117**: p. 51-54.
47. Sandlöbes, S., et al., *A rare-earth free magnesium alloy with improved intrinsic ductility.* Scientific Reports, 2017. **7**(1): p. 10458.

48. Guo, C., et al., *Observation and analysis of the coexistence of two "opposite" twin modes in a Mg-Al-Zn alloy.* Materials & Design, 2016. **102**: p. 196-201.
49. Reza Abbaschian, L.A., Rober E. Reed-Hill, *Deformation Twinning and Martensite Reactions*, in *Physical Metallurgy Principles*. 2010, Cengage Learning.
50. Khosravani, A., et al., *Nucleation and propagation of {101¯2} twins in AZ31 magnesium alloy.* Acta Materialia, 2015. **100**: p. 202-214.
51. Wang, J., I.J. Beyerlein, and C.N. Tomé, *An atomic and probabilistic perspective on twin nucleation in Mg.* Scripta Materialia, 2010. **63**(7): p. 741-746.
52. Arul Kumar, M., et al., *Characterizing the role of adjoining twins at grain boundaries in hexagonal close packed materials.* Scientific Reports, 2019. **9**(1): p. 3846.
53. Arul Kumar, M., et al., *Grain neighbour effects on twin transmission in hexagonal close-packed materials.* Nature Communications, 2016. **7**(1): p. 13826.
54. Zhang, R.Y., M.R. Daymond, and R.A. Holt, *A finite element model of deformation twinning in zirconium.* Materials Science and Engineering: A, 2008. **473**(1): p. 139-146.
55. Yang, F., et al., *Crack initiation mechanism of extruded AZ31 magnesium alloy in the very high cycle fatigue regime.* Materials Science and Engineering: A, 2008. **491**(1-2): p. 131-136.
56. Bieler, T.R., et al., *Strain heterogeneity and damage nucleation at grain boundaries during monotonic deformation in commercial purity titanium.* JOM, 2009. **61**(12): p. 45-52.
57. Ng, B.C., et al., *The role of mechanical twinning on microcrack nucleation and crack propagation in a near-γ TiAl alloy.* Intermetallics, 2004. **12**(12): p. 1317-1323.
58. Zubair, M., et al., *Strain heterogeneity and micro-damage nucleation under tensile stresses in an Mg–5Al–3Ca alloy with an intermetallic skeleton.* Materials Science and Engineering: A, 2019. **767**.
59. Stein, F. and A. Leineweber, *Laves phases: a review of their functional and structural applications and an improved fundamental understanding of stability and properties.* Journal of Materials Science, 2020. **56**(9): p. 5321-5427.
60. Rabadia, C.D., et al., *Laves phase precipitation in Ti-Zr-Fe-Cr alloys with high strength and large plasticity.* Materials & Design, 2018. **154**: p. 228-238.
61. Zubair, M., et al., *On the role of Laves phases on the mechanical properties of Mg-Al-Ca alloys.* Materials Science and Engineering: A, 2019. **756**: p. 272-283.
62. Johnston, R.L. and R. Hoffmann, *The Kagome Net - Band Theoretical and Topological Aspects.* Polyhedron, 1990. **9**(15-16): p. 1901-1911.
63. Kumar, K.S. and P.M. Hazzledine, *Polytypic transformations in Laves phases.* Intermetallics, 2004. **12**(7-9): p. 763-770.
64. Momma, K. and F. Izumi, *VESTA 3 for three-dimensional visualization of crystal, volumetric and morphology data.* Journal of Applied Crystallography, 2011. **44**(6): p. 1272-1276.
65. Paufler, P., *Gustav E. R. Schulze's pioneering work on Laves phases.* Zeitschrift für Kristallographie - Crystalline Materials, 2006. **221**(5-7): p. 311-318.
66. Chisholm, M.F., S. Kumar, and P. Hazzledine, *Dislocations in Complex Materials.* Science, 2005. **307**(5710): p. 701.
67. Hazzledine, P.M. and P. Pirouz, *Synchroshear transformations in Laves phases.* Scripta Metallurgica et Materialia, 1993. **28**(10): p. 1277-1282.
68. Guénolé, J., et al., *Basal slip in Laves phases: The synchroshear dislocation.* Scripta Materialia, 2019. **166**: p. 134-138.
69. Müllerr, T.H. and P. Paufler, *Yield strength of the monocrystalline intermetallic compound* $MgZn_2$. 1977. **40**(2): p. 471-477.
70. Kirsten, C., P. Paufler, and G.E.R. Schulze, *Zur plastischen Verformung intermetallischer Verbindungen.* Monatsberichte der Deutschen Akademie der Wissenschaften, 1964. **6 (2)**: p. 140-147.
71. C., K., *Über Festigkeitseigenschaften intermetallischer Verbindungen*. 1963, TU Dresden.
72. Suzuki, A., et al., *Solidification paths and eutectic intermetallic phases in Mg–Al–Ca ternary alloys.* Acta Materialia, 2005. **53**: p. 2823-2834.
73. Liang, S.M., et al., *Thermal analysis and solidification pathways of Mg–Al–Ca system alloys.* Materials Science and Engineering: A, 2008. **480**(1): p. 365-372.

74. Zhang, L., et al., *Microstructures and mechanical properties of Mg–Al–Ca alloys affected by Ca/Al ratio.* Materials Science and Engineering: A, 2015. **636**: p. 279-288.
75. Li, Z.T., et al., *Ultrahigh strength Mg-Al-Ca-Mn extrusion alloys with various aluminum contents.* Journal of Alloys and Compounds, 2019. **792**: p. 130-141.
76. Chai, Y., et al., *Role of Al content on the microstructure, texture and mechanical properties of Mg-3.5Ca based alloys.* Materials Science and Engineering: A, 2018. **730**: p. 303-316.
77. Sanyal, S., et al., *Evolution of microstructure, phases and mechanical properties in lean as-cast Mg–Al–Ca–Mn alloys under the influence of a wide range of Ca/Al ratio.* Materials Science and Engineering: A, 2021. **800**.
78. Suzuki, A., et al., *Structure and transition of eutectic (Mg,Al)$_2$Ca Laves phase in a die-cast Mg–Al–Ca base alloy.* Scripta Materialia, 2004. **51**(10): p. 1005-1010.
79. Xu, S.W., et al., *High temperature tensile properties of as-cast Mg–Al–Ca alloys.* Materials Science and Engineering: A, 2009. **509**(1): p. 105-110.
80. Li, Z.T., et al., *Effect of Ca/Al ratio on microstructure and mechanical properties of Mg-Al-Ca-Mn alloys.* Materials Science and Engineering: A, 2017. **682**: p. 423-432.
81. Jing, B., et al., *Microstructure and tensile creep behavior of Mg–4Al based magnesium alloys with alkaline-earth elements Sr and Ca additions.* Materials Science and Engineering: A, 2006. **419**(1): p. 181-188.
82. Terada, Y., et al., *A thousandfold creep strengthening by Ca addition in die-cast AM50 magnesium alloy.* Metallurgical and Materials Transactions A, 2004. **35**(9): p. 3029-3032.
83. Nakaura, Y., A. Watanabe, and K. Ohori, *Effects of Ca,Sr Additions on Properties of Mg-Al Based Alloys.* MATERIALS TRANSACTIONS, 2006. **47**(4): p. 1031-1039.
84. Koltygin, A.V., et al., *Development of a magnesium alloy with good casting characteristics on the basis of Mg–Al–Ca–Mn system, having Mg–Al$_2$Ca structure.* Journal of Magnesium and Alloys, 2013. **1**(3): p. 224-229.
85. Saddock, N.D., et al., *Grain-scale creep processes in Mg–Al–Ca base alloys: Implications for alloy design.* Scripta Materialia, 2010. **63**(7): p. 692-697.
86. Polatidis, E., et al., *Deformation mechanisms in a superelastic NiTi alloy: An in-situ high resolution digital image correlation study.* Materials & Design, 2020. **191**: p. 108622.
87. Quinta Da Fonseca, J., P.M. Mummery, and P.J. Withers, *Full-field strain mapping by optical correlation of micrographs acquired during deformation.* Journal of Microscopy, 2005. **218**(1): p. 9-21.
88. Di Gioacchino, F. and J. Quinta da Fonseca, *Plastic Strain Mapping with Sub-micron Resolution Using Digital Image Correlation.* Experimental Mechanics, 2013. **53**(5): p. 743-754.
89. Pan, B., et al., *Two-dimensional digital image correlation for in-plane displacement and strain measurement: a review.* Measurement Science and Technology, 2009. **20**(6).
90. Yan, D., C.C. Tasan, and D. Raabe, *High resolution in situ mapping of microstrain and microstructure evolution reveals damage resistance criteria in dual phase steels.* Acta Materialia, 2015. **96**: p. 399-409.
91. Tasan, C.C., et al., *Integrated experimental–simulation analysis of stress and strain partitioning in multiphase alloys.* Acta Materialia, 2014. **81**: p. 386-400.
92. Tschopp, M.A., et al., *Microstructure-Dependent Local Strain Behavior in Polycrystals through In-Situ Scanning Electron Microscope Tensile Experiments.* Metallurgical and Materials Transactions A, 2009. **40**(10): p. 2363-2368.
93. Di Gioacchino, F. and J. Quinta da Fonseca, *An experimental study of the polycrystalline plasticity of austenitic stainless steel.* International Journal of Plasticity, 2015. **74**: p. 92-109.
94. Edwards, T.E.J., et al., *Longitudinal twinning in a TiAl alloy at high temperature by in situ microcompression.* Acta Materialia, 2018. **148**: p. 202-215.
95. Wu, Z., et al., *Local mechanical properties and plasticity mechanisms in a Zn-Al eutectic alloy.* Materials & Design, 2018. **157**: p. 337-350.
96. Dutta, A., et al., *Strain partitioning and strain localization in medium manganese steels measured by in situ microscopic digital image correlation.* Materialia, 2019. **5**.

97. Edwards, T.E.J., F. Di Gioacchino, and W.J. Clegg, *High resolution digital image correlation mapping of strain localization upon room and high temperature, high cycle fatigue of a TiAl intermetallic alloy.* International Journal of Fatigue, 2021. **142**: p. 105905.
98. Lee, S.-Y., et al., *Macroscopic and microscopic characterizations of Portevin-LeChatelier effect in austenitic stainless steel using high-temperature digital image correlation analysis.* Acta Materialia, 2021. **205**: p. 116560.
99. Yuzbekova, D., et al., *On the mechanisms of nucleation and subsequent development of the PLC bands in an AlMg alloy.* Journal of Alloys and Compounds, 2021. **868**: p. 159135.
100. Amini, S. and R.S. Kumar, *A high-fidelity strain-mapping framework using digital image correlation.* Materials Science and Engineering: A, 2014. **594**: p. 394-403.
101. Koike, J., et al., *The activity of non-basal slip systems and dynamic recovery at room temperature in fine-grained AZ31B magnesium alloys.* Acta Materialia, 2003. **51**(7): p. 2055-2065.
102. Somekawa, H., et al., *Non-Basal Dislocation Nucleation Site of Solid Solution Magnesium Alloy.* MATERIALS TRANSACTIONS, 2020. **61**(6): p. 1172-1175.
103. Zhu, G., et al., *Highly deformable Mg–Al–Ca alloy with Al_2Ca precipitates.* Acta Materialia, 2020. **200**: p. 236-245.
104. Agnew, S.R. and Ö. Duygulu, *Plastic anisotropy and the role of non-basal slip in magnesium alloy AZ31B.* International Journal of Plasticity, 2005. **21**(6): p. 1161-1193.
105. Wu, X. and Y. Zhu, *Heterogeneous materials: a new class of materials with unprecedented mechanical properties.* Materials Research Letters, 2017. **5**(8): p. 527-532.
106. Zhu, Y. and X. Wu, *Perspective on hetero-deformation induced (HDI) hardening and back stress.* Materials Research Letters, 2019. **7**(10): p. 393-398.
107. Hull, D. and D.J. Bacon, *Chapter 9 - Dislocation Arrays and Crystal Boundaries*, in *Introduction to Dislocations (Fifth Edition)*, D. Hull and D.J. Bacon, Editors. 2011, Butterworth-Heinemann: Oxford. p. 171-204.
108. Huang, S., et al., *In-situ investigation of tensile behaviors of Ti–6Al alloy with extra low interstitial.* Materials Science and Engineering: A, 2021. **809**: p. 140958.
109. Joseph, S., T.C. Lindley, and D. Dye, *Dislocation interactions and crack nucleation in a fatigued near-alpha titanium alloy.* International Journal of Plasticity, 2018. **110**: p. 38-56.
110. Joseph, S., et al., *Slip transfer and deformation structures resulting from the low cycle fatigue of near-alpha titanium alloy Ti-6242Si.* International Journal of Plasticity, 2018. **100**: p. 90-103.
111. Bieler, T.R., et al., *Grain Boundary Responses to Heterogeneous Deformation in Tantalum Polycrystals.* JOM, 2014. **66**(1): p. 121-128.
112. Sanyal, S., et al., *Evolution of microstructure, phases and mechanical properties in lean as-cast Mg–Al–Ca–Mn alloys under the influence of a wide range of Ca/Al ratio.* Materials Science and Engineering: A, 2021. **800**: p. 140322.
113. Lai, Q., et al., *Damage and fracture of dual-phase steels: Influence of martensite volume fraction.* Materials Science and Engineering: A, 2015. **646**: p. 322-331.
114. Tang, A., et al., *Mesoscopic origin of damage nucleation in dual-phase steels.* International Journal of Plasticity, 2021. **137**: p. 102920.
115. Avramovic-Cingara, G., et al., *Void Nucleation and Growth in Dual-Phase Steel 600 during Uniaxial Tensile Testing.* Metallurgical and Materials Transactions A, 2009. **40**(13): p. 3117-3127.
116. Kusche, C., et al., *Large-area, high-resolution characterisation and classification of damage mechanisms in dual-phase steel using deep learning.* PLOS ONE, 2019. **14**(5): p. e0216493.
117. Lee, T.C., I.M. Robertson, and H.K. Birnbaum, *AnIn Situ transmission electron microscope deformation study of the slip transfer mechanisms in metals.* Metallurgical Transactions A, 1990. **21**(9): p. 2437-2447.
118. Bayerschen, E., et al., *Review on slip transmission criteria in experiments and crystal plasticity models.* Journal of Materials Science, 2016. **51**(5): p. 2243-2258.
119. Shen, Z., R.H. Wagoner, and W.A.T. Clark, *Dislocation and grain boundary interactions in metals.* Acta Metallurgica, 1988. **36**(12): p. 3231-3242.

120. Lee, T.C., I.M. Robertson, and H.K. Birnbaum, *TEM in situ deformation study of the interaction of lattice dislocations with grain boundaries in metals.* Philosophical Magazine A, 1990. **62**(1): p. 131-153.
121. Kacher, J., B.P. Eftink, and I.M. Robertson, *In Situ Transmission Electron Microscopy Investigation of Dislocation Interactions*, in *Handbook of Mechanics of Materials*, S. Schmauder, et al., Editors. 2019, Springer Singapore: Singapore. p. 131-166.
122. Luster, J. and M.A. Morris, *Compatibility of deformation in two-phase Ti-Al alloys: Dependence on microstructure and orientation relationships.* Metallurgical and Materials Transactions A, 1995. **26**(7): p. 1745-1756.
123. Pan, H., Y. He, and X. Zhang, *Interactions between Dislocations and Boundaries during Deformation.* Materials (Basel, Switzerland), 2021. **14**(4): p. 1012.
124. Suri, S., et al., *Room temperature deformation and mechanisms of slip transmission in oriented single-colony crystals of an α/β titanium alloy.* Acta Materialia, 1999. **47**(3): p. 1019-1034.
125. Savage, M.F., et al., *Deformation mechanisms and microtensile behavior of single colony Ti–6242Si.* Materials Science and Engineering: A, 2001. **319-321**: p. 398-403.
126. Zhang, Z., et al., *Determination of Ti-6242 α and β slip properties using micro-pillar test and computational crystal plasticity.* Journal of the Mechanics and Physics of Solids, 2016. **95**: p. 393-410.
127. Savage, M.F., J. Tatalovich, and M.J. Mills, *Anisotropy in the room-temperature deformation of α–β colonies in titanium alloys: role of the α–β interface.* Philosophical Magazine, 2004. **84**(11): p. 1127-1154.
128. Zhang, X., et al., *Microstructure and strengthening mechanisms in cold-drawn pearlitic steel wire.* Acta Materialia, 2011. **59**(9): p. 3422-3430.
129. Toribio, J. and E. Ovejero, *Effect of cumulative cold drawing on the pearlite interlamellar spacing in eutectoid steel.* Scripta Materialia, 1998. **39**(3): p. 323-328.
130. Guziewski, M., S.P. Coleman, and C.R. Weinberger, *Atomistic investigation into interfacial effects on the plastic response and deformation mechanisms of the pearlitic microstructure.* Acta Materialia, 2019. **180**: p. 287-300.
131. Liang, L.-W., et al., *Dislocation nucleation and evolution at the ferrite-cementite interface under cyclic loadings.* Acta Materialia, 2020. **186**: p. 267-277.
132. Karkina, L.E., et al., *Crystallographic analysis of slip transfer mechanisms across the ferrite/cementite interface in carbon steels with fine lamellar structure.* Journal of Applied Crystallography, 2015. **48**(1): p. 97-106.
133. Kar'kina, L.E., I.G. Kabanova, and I.N. Kar'kin, *Strain Transfer across the Ferrite/Cementite Interface in Carbon Steels with Coarse Lamellar Pearlite.* Physics of Metals and Metallography, 2018. **119**(11): p. 1114-1119.

5. Research Publication 1 – On the role of Laves Phases on the mechanical properties of Mg-Al-Ca alloys

M. Zubair, S. Sandlöbes, M.A. Wollenweber, C.F.Kusche, W.Hildebrandt, C.Broeckmann, S. Korte-Kerzel, On the role of Laves phases on the mechanical properties of Mg-Al-Ca alloys, Materials Science and Engineering: A, 756 (2019) 272-283.

The paper discusses the effect of Ca/Al ratio on the mechanical properties of Mg-Al-Ca alloys. Ca/Al ratio alters, the amount, type, and morphology of the Laves phases in the microstructure and thus significantly effects the mechanical properties of Mg-Al-Ca alloys. Therefore, this publication explicitly addresses the first research question laid down in section 1.1.

Materials Science & Engineering A 756 (2019) 272–283

Contents lists available at ScienceDirect

Materials Science & Engineering A

journal homepage: www.elsevier.com/locate/msea

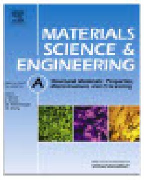

On the role of Laves phases on the mechanical properties of Mg-Al-Ca alloys

M. Zubair[a,b,*], S. Sandlöbes[a], M.A. Wollenweber[a], C.F. Kusche[a], W. Hildebrandt[c], C. Broeckmann[c], S. Korte-Kerzel[a]

[a] Institut für Metallkunde und Metallphysik, Kopernikusstr. 14, RWTH Aachen University, 52074, Aachen, Germany
[b] Department of Metallurgical and Materials Engineering, G.T Road, UET Lahore, Pakistan
[c] Institut für Werkstoffanwendungen im Maschinenbau, Augustinerbach 4, 52062, Aachen, Germany

ARTICLE INFO

Keywords:
Mg alloys
Ca/Al ratio
Creep properties
Digital Image Correlation
Microstructure characterisation

ABSTRACT

As-cast Mg-Al-Ca alloys are among the most promising alloys for elevated temperature applications (≤200 °C) due to their superior creep properties when compared to conventional AZ or AM series Mg alloys. The microstructures of Mg-Al-Ca alloys consist of a soft α-Mg phase reinforced with hard interconnected Laves phases. These interconnected Laves phases are the main reason for the good creep resistance of these alloys as they impede creep deformation. The volume fraction, type and morphology of Laves phases can be controlled through the Ca/Al ratio. Consequently, the Ca/Al ratio can be used to manipulate the mechanical properties of this alloy system in order to achieve optimum creep resistance. We show here that a higher Ca/Al ratio results in i) higher volume fraction of intermetallic Laves phases in the microstructure, ii) improvement in the yield strength (YS), and iii) enhancement in creep resistance at a stress level of 50–70 MPa and a temperature of 170 °C of the as-cast alloys. Moreover, the local strain distribution and partitioning at the microstructural level occurring during high temperature tensile deformation (at ~170 °C) was measured using quasi in-situ DIC in SEM revealing stress localisation at the α-Mg Laves phase interfaces.

1. Introduction

Weight reduction in the automobile and aerospace industries is one of the key elements to improve fuel efficiency and reduce harmful emissions. Mg is promising over other materials due to its low density of about 1.7 g cm^{-3}. The most widely used Mg alloys used in vehicles contain Al as one of the major alloying elements (AZ or AM series). However, the operating temperature of these alloys is limited to below 125 °C due to the rapid deterioration of their creep strength at elevated temperatures [1–3]. This is because the main strengthening phase present in Al-based Mg alloys is the $Mg_{17}Al_{12}$ intermetallic phase, which softens at temperatures above 150 °C [4,5] rendering these alloys unsuitable for high temperature applications like powertrains and transmission cases.

Most Mg alloys for high temperature applications (125 °C-200 °C) are Mg–Al-based alloys with single or combined additions of Ca, Sr, Mn, Zn, RE (RE: rare earth elements) [3,6–8]. Ca is one of the most promising alloying elements as it is cheap and causes the formation of a continuous network of Laves phases instead of discontinuous $Mg_{17}Al_{12}$ precipitation in Mg-Al alloys. This continuous Laves phase network has been reported to improve the creep resistance [8–11]. It is also pertinent to mention here that the Laves phases also have significantly higher melting points, T_m, ($Mg_2Ca \approx 715$ °C and $Al_2Ca \approx 1079$ °C) [12,13] than $Mg_{17}Al_{12}$ ($T_m \approx 460$ °C) [14]. Terada et al. [10] have compared the creep properties of commercial die-cast AM50 with AM50 containing 1.72 wt% Ca. They [10] have reported, that the addition of 1.72 wt% Ca reduces the minimum creep rate of AM50 by about three orders of magnitude at an application temperature of 423 K and stress levels below 120 MPa. Similarly, Amberger et al. [9] have studied the effects of the addition of 1, 3 and 5 wt% Ca on the properties of AZ91 revealing that the minimum creep rate of the alloy containing 5 wt% Ca was also three orders of magnitude lower than in the alloy containing no Ca at 200 °C and stress levels of 100 MPa.

The microstructure of cast Mg-Al-Ca alloys resembles that of composites in which the soft α-Mg phase is reinforced with hard and brittle interconnected intermetallic Laves phases. The mechanical properties of this alloy system can thus be controlled by altering amount and distribution of Laves phases in the α-Mg matrix. The Ca/Al ratio is one important factor which determines the volume fraction, distribution and type of Laves phases in the Mg-Al-Ca alloy system. It has been reported that an increase of the Ca/Al ratio from 0.4 to 1 results in a change of the Laves phase type from Al_2Ca (low Ca/Al ratio) to

---

[*] Corresponding author. Institut für Metallkunde und Metallphysik, Kopernikusstr. 14, RWTH Aachen University, 52074, Aachen, Germany.
E-mail address: zubair@imm.rwth-aachen.de (M. Zubair).

https://doi.org/10.1016/j.msea.2019.04.048
Received 6 September 2018; Received in revised form 9 April 2019; Accepted 11 April 2019
Available online 12 April 2019
0921-5093/ © 2019 Elsevier B.V. All rights reserved.

$(Mg,Al)_2Ca$ (intermediate Ca/Al ratio) and to Mg_2Ca (high Ca/Al ratio) [15]. Several recent publications focus on the effects of the Ca/Al ratio on the microstructure and mechanical properties of this alloy system [15–18], however, these studies mainly concentrate on the evolution of the mechanical properties and texture after hot extrusion. Further studies have been performed on the tensile and compressive creep properties of different Mg-Al-Ca alloys [8–11,19–21].

However, the effects of different Ca/Al ratios on the creep properties of cast Mg-Al-Ca alloys are not yet fully understood and require further investigation in order to design Mg-Al-Ca alloys with improved creep properties. Therefore, we systematically vary the Ca/Al ratio in Mg-Al-Ca alloys and study the microstructure formation, tensile and creep properties of different Mg-Al-Ca alloys. Further, we use quasi in-situ μ-digital image correlation (μ-DIC) [22–31] to investigate the strain partitioning at the microstructural level during high temperature tensile deformation of as-cast Mg-Al-Ca alloys.

2. Experimental methods

Pure Mg (99.95 wt%), Al (99.99 wt%) and an Mg-30Ca master alloy were used to synthesise alloys with different Ca/Al ratios. The raw materials were molten in an induction furnace under protective atmosphere of Ar and CO_2 using a graphite crucible. The melt was then poured into a boron nitride coated Cu mold and cooled down to room temperature. The chemical compositions of the as-cast alloys were measured using inductively coupled plasma optical emission spectrometry (ICP-OES), Table 1.

Samples for microstructure analysis were mechanically ground using 4000 SiC emery paper, followed by mechanical polishing using 3, 1, 0.25 μm diamond suspension and 0.04 μm Al_2O_3 powder suspension. Samples for EBSD were electro-polished after a 1 μm diamond suspension polishing step using the electrolyte AC2 (Struers). The temperature, voltage and time used for electro-polishing were −20 °C, 15V and 50s, respectively. The microstructures of the as-cast and deformed samples were observed using scanning electron microscopy (SEM) (LEO1530 and a FEI Helios Nanolab 600i). An accelerating voltage of 20 kV was used for secondary electron (SE) imaging, back-scattered electron (BSE) imaging and electron back scattered diffraction (EBSD). An accelerating voltage of 10 kV was used for energy dispersive X-ray spectroscopy (EDS) to reduce the electron-sample interaction volume. The images and EBSD data were analysed using ImageJ, Channel 5 and OIM.

Micro hardness tests were performed using a Vickers hardness tester at a load of 1 kg at room temperature for all samples. The holding time at maximum load amounted to 15 s for all indents. Tensile tests at room temperature and 170 °C were done using an electromechanical testing machine (DZM) equipped with a heater. The strain rate during tensile testing at room temperature and 170 °C was $5 \times 10^{-4}\ s^{-1}$. The extension of the specimens during tensile testing was measured using a linear variable differential transformer (LVDT) extensometer. The specimens for tensile testing were standard dog bone shaped with a gauge length of 10 mm. Quasi in-situ μ-DIC experiments were performed in an SEM (LEO1530) to examine the strain partitioning occurring at the microstructural level during high temperature tensile deformation. Digital image correlation (DIC) is a powerful technique to measure the local strain distribution in complex stress conditions at macroscopic and microscopic scales [32–34]. For DIC, Al_2O_3 particles were deposited on the sample surface during the final polishing step using a concentrated OPA suspension and a polishing time of ~4 min to generate a suitable pattern on the sample surface. These samples were stepwise deformed at 170 °C in an electromechanical testing machine and in between subsequent deformation steps monitored using SEM. The software ARAMIS GOM Correlate was used to determine the local strain. The creep properties of the different alloys were measured through constant stress experiments using a lever-arm creep testing machine. Standard dog bone shaped specimens with a gauge length of 40 mm were used for the tensile creep studies. The extension of the specimens during creep deformation was measured using a LVDT based tube-rod extensometer.

Table 1
Composition of the as-cast alloys C/A 0.3, C/A 0.6 and C/A 1.0.

	Al (wt %)	Ca (wt %)	Al + Ca (wt %)	Mg (wt %)	Ca/Al ratio
Alloy C/A 0.3	5.44	1.73	7.17	Balance	0.32
Alloy C/A 0.6	4.7	2.93	7.63	Balance	0.62
Alloy C/A 1.0	3.68	3.8	7.48	Balance	1.03

3. Results

3.1. Microstructures of the as-cast alloys

Fig. 1(a–c) shows the microstructures of the as-cast alloys, which contain α-Mg and intermetallic Laves phases. The volume fraction and distribution of Laves phases vary considerably when the Ca/Al ratio is increased from 0.32 in alloy C/A 0.3 to 1.03 in alloy C/A 1.0. In alloy C/A 0.3, the amount of intermetallic phases amounts to 5.5% and the average dendrite cell size (mean free path as determined by the linear intercept method according to ASTM E 112–12) is 41.9 ± 3.8 μm (see Table 2). The amount of intermetallic phase increases to 8.7% and the average dendrite cell size decreases to 32.5 ± 4.2 μm in alloy C/A 1.0. In alloy C/A 1.0 parts of the intermetallic phases are present as fine eutectic regions (see Fig. 1 (e and f)) containing alternating lamallae of intermetallic Laves phase and soft α-Mg phase. The average dendrite cell size in alloy C/A 0.6 amounts to 31.9 ± 5.8 μm, where most of the intermetallic phase is present as single intermetallic lamellae.

EDS analysis was performed for the different microstructure constituents at the points marked by characters in Fig. 1 (b, d and f). Table 3 lists the obtained local compositions and the intermetallic phases corresponding to these chemical compositions [15,17,35,36].

Amerion et al. [35] have reported that the most stable phase in the $CaAl_{2-x}Mg_x$ system is Al_2Ca when x is in the range of 0–0.24, $(Mg,Al)_2Ca$ when x lies between 0.66 and 1.07 and Mg_2Ca when x is in the range of 1.5–2. The EDS analysis in our study shows that the predominant intermetallic phases in alloy C/A 0.3 are Al_2Ca and $(Mg,Al)_2Ca$, in alloy C/A 0.6 $(Mg,Al)_2Ca$ and in alloy C/A 1.0 $(Mg,Al)_2Ca$ and Mg_2Ca. This is further confirmed by the BSE images shown in Fig. 1 (b, d and f), where the intermetallic phases present in alloy C/A 1.0 (Fig. 1 f)) give clear contrast of two different intermetallic phases: fine lamellar Mg_2Ca Laves phase with C14 structure and coarse lamellar $(Mg,Al)_2Ca$ Laves phase with C36 structure, as revealed from EDS analysis.

EDS analysis of the α-Mg matrix reveales that the Al content in the α-Mg matrix decreases from 1.6 at% to 0.6 at% when the global Ca/Al ratio is increased from 0.32 to 1.03 wt% (see Table 3). This is in agreement to the work by Eibisch et al. [37] who also reported that the solute Al concentration in the α-Mg phase is reduced when the Ca content is increased in Mg-Al-Ca alloys. The Ca concentration in the α-Mg matrix is negligible due to its very low solubility in Mg [37,38]. With increasing Ca/Al ratio fine disc-shaped intermetallic phase precipitates were formed within the α-Mg matrix, Fig. 2(a–c). However, quantitative analysis of the composition of the precipitates was not possible using EDS due to their fine size with respect to the interaction volume of the electron beam with the sample when generating the EDS signal.

Similarly, fine intermetallic phase precipitates in the α-Mg matrix have also been observed in permanent mold cast and also aged die cast AXJ 530 [39,40]. Suzuki et al. [39] and Saddock et al. [40] have further concluded that the fine intermetallic phase is C15 Al_2Ca Laves phase. The fine intermetallic precipitates observed in our study form parallel to the basal plane of the α-Mg matrix, Fig. 3 (a and b), similar to the observations reported in Refs. [39,40]. It is therefore assumed that the

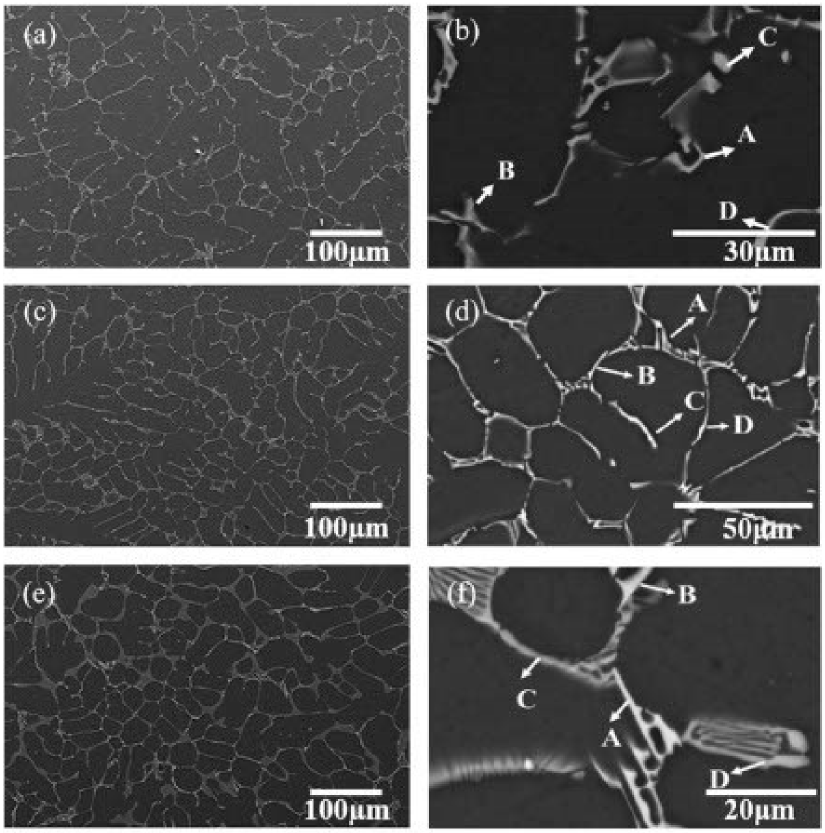

Fig. 1. Secondary electron (SE) micrographs of the microstructures of as-cast a) alloy C/A 0.3, c) alloy C/A 0.6 and e) alloy C/A 1.0. High resolution back-scattered electron (BSE) micrographs of the microstructures of b) alloy C/A 0.3, d) alloy C/A 0.6 and f) alloy C/A 1.0. Characters A, B, C and D highlight the points at which EDS compositional analysis of intermetallic phase was done, Table 3.

Table 2
Variation of the amount of intermetallic phase and cell size with Ca/Al ratio.

Alloy	Area fraction of intermetallic phase, %	Cell size, µm
Alloy C/A 0.3	5.5	41.9 ± 3.8
Alloy C/A 0.6	6.8	31.9 ± 5.8
Alloy C/A 1.0	8.7	32.5 ± 4.2

Table 3
EDS analysis of the different microstructural constituents and corresponding phases [15,17,35,36] in alloys C/A 0.3, C/A 0.6 and C/A 1.0.

		Mg (at. %)	Al (at. %)	Ca (at. %)	Corresponding phases
Alloy C/A 0.3	Spot A	24.4	50.2	25.4	$(Mg, Al)_2Ca$
	Spot B	23.3	50.2	26.5	
	Spot C	10.6	59.9	29.5	Al_2Ca
	Spot D	14.5	57.6	27.9	
	Matrix (α-Mg)	Balance	1.6	–	
Alloy C/A 0.6	Spot A	39.8	38.5	21.7	$(Mg, Al)_2Ca$
	Spot B	41.8	36.5	21.7	
	Spot C	30.4	40.2	29.4	
	Spot D	25.6	45.0	29.4	
	Matrix (α-Mg)	Balance	1.0	–	–
Alloy C/A 1.0	Spot A	32.4	37.7	29.9	$(Mg, Al)_2Ca$
	Spot B	31.0	38.6	30.4	
	Spot C	55.5	18.5	26.0	Mg_2Ca
	Spot D	59.0	17.6	23.4	
	Matrix (α-Mg)	Balance	0.6	–	–

intermetallic precipitates present in the α-Mg matrix of alloys C/A 0.6 and C/A 1.0 are C15 Al_2Ca Laves phase precipitates.

Fig. 4 shows EBSD inverse pole figure (IPF) maps of the as-cast alloys revealing that the α-Mg dendrite cells form large grains or colonies consisting of finer α-Mg dendrite cells and Laves phase of the same crystallographic orientation.

3.2. *Mechanical properties*

3.2.1. *Microhardness*

The microhardness of alloys C/A 0.3, C/A 0.6 and C/A 1.0 (Table 4) show an increase in microhardness with increasing Ca/Al ratio from 50.5 HV in alloy C/A 0.3 to 58.4 HV in C/A 1.0. This increase in hardness with higher Ca/Al ratio is assumed to be caused by a higher volume fraction of Laves phases in alloys with higher Ca/Al ratio. Cracking of the Laves phase skeleton during microhardness testing at room temperature is observed in all alloys and is shown in Fig. 5 (a and b) for alloy C/A 1.0.

3.2.2. *Tensile properties*

Fig. 6 (a and b) shows the YS (yield stress, $\sigma_{0.2}$), UTS (ultimate tensile strength) and UE (uniform elongation) of alloys C/A 0.3, C/A 0.6 and C/A 1.0 at room temperature and 170 °C, respectively. The values of the YS, UTS and UE for each alloy at both temperatures are averaged over at least 3 tests. With increasing Ca/Al ratio, the YS increases both at room temperature and at 170 °C, Fig. 6 (a and b). Alloy C/A 1.0 has a YS of 80 MPa and a uniform elongation of 0.7% at room temperature while alloy C/A 0.3 exhibits a YS of 61 MPa and a uniform elongation of 3.9% at room temperature. Alloy C/A 0.6 exhibits intermediate YS, UTS and UE values in between those of alloys C/A 0.3 and C/A 1.0. A similar trend was obeserved at 170 °C, where the YS of alloy C/A 1.0 amounts

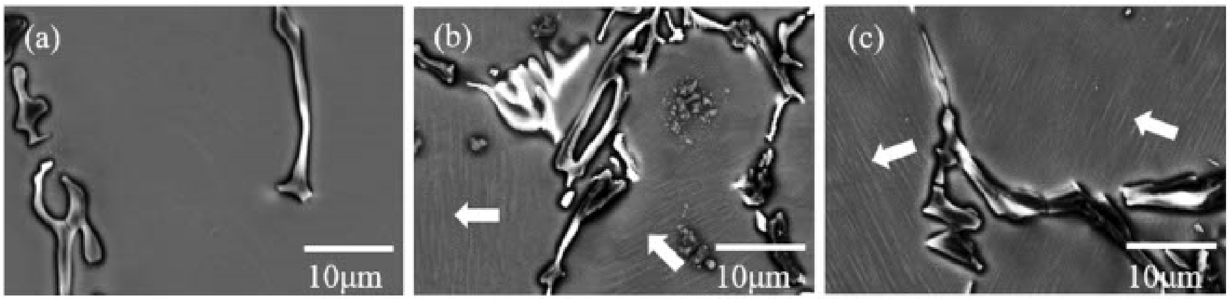

Fig. 2. As-cast microstructures of a) alloy C/A 0.3, b) alloy C/A 0.6, and c) alloy C/A 1.0 after electro-polishing. Arrows indicate the presence of fine disc-shaped intermetallic phases within the α-Mg matrix.

to 72.3 MPa and 57.6 MPa for alloy C/A 0.3, Fig. 6 b). However, alloy C/A 0.6 exhibits the highest UE values of the three alloys investigated, alloy C/A 0.3 displays an intermediate and alloy C/A 1.0 the lowest UE. Further, the variation of the UTS with Ca/Al ratio was different at room temperature and 170 °C. Specifically, alloy C/A 1.0 has the lowest UTS at room temperature, while C/A 0.6 has an intermediate and C/A 0.3 the highest UTS. However, at 170 °C the UTS increases with increasing Ca/Al ratio: Alloy C/A exhibits the highest UTS followed by alloy C/A 0.6 and C/A 0.3, Fig. 6 b).

The true stress-strain curves further show that alloys C/A 0.6 and C/A 0.3 exhibit a considerable decrease in flow stress with increasing temperature while alloy C/A 1.0 shows only a marginal decrease, Fig. 7(a–c).

3.2.3. *Local strain distribution and strain partitioning*

The microstructure of the Mg-Al-Ca alloys investigated is composed of two different phases: a soft α-Mg matrix and a hard intermetallic skeleton. The hard intermetallic skeleton is generally considered as reinforcement phase which acts as obstacle against dislocation motion [9]. Therefore, we have used μ-DIC to study the local strain distribution at the microscopic scale during tensile deformation at 170 °C in alloy C/A 0.6 as this alloy exhibits an intermediately interconnected Laves phase network and the highest uniform elongation. Fig. 8 a) shows an SE micrograph of the un-deformed material. The white speckles visible on the sample surface are Al_2O_3 particles which were deposited on the sample surface to measure the local displacements and, hence, strain. Fig. 8b) and c) show the same sample area after deformation to 4% global strain at 170 °C and the corresponding local von Mises strain map. Most strain localisation is observed at α-Mg-Laves phase interfaces, as highlighted in the enlarged local von Mises strain map in Fig. 8 d). Additionally, strain concentration occurs along bands inclined by ~45° and ~70° to the tensile axis. Further, cracks in the Laves phases are observed in the regions of high local von Mises strain (red and yellow arrows in Fig. 8 b) and by red, yellow and black arrows in Fig. 8 d)).

3.2.4. *Creep properties*

Tensile creep tests were performed on all three alloys at stress levels of 50, 60 and 70 MPa at a temperature of 170 °C. The temperature and stresses were selected according to the stress and temperature levels required for elevated temperature automotive applications such as in powertrains [7,20,41].

Fig. 9 shows the creep strain-time curves of alloys C/A 0.3, C/A 0.6 and C/A 1.0 obtained at a creep stress of 50 MPa (a)), 60 MPa (b)) and 70 MPa (c)). At a creep stress of 50 MPa all three alloys show a similar creep response with maximum creep strains of 0.19, 0.18 and 0.15% for alloys C/A 0.3, C/A 0.6 and C/A 1.0, respectively, after 100 h, Fig. 9 a).

However, when the stress level is increased to 60 MPa, alloy C/A 1.0 exhibits the lowest creep rate and creep strain, while alloy C/A 0.3 displays the highest values, Fig. 9 b). A similar creep behaviour is observed at a stress level of 70 MPa, Fig. 9 c).

Further, the minimum or secondary creep rate was also lowest for alloy C/A 1.0 at all stress levels investigated. The relationship between the secondary creep rate and the stress level for the alloys C/A 0.3, C/A 0.6 and C/A 1.0 is given in Fig. 9 d). The values of the minimum creep rate were calculated from the slope of stage 2 creep in the creep strain-time curves. The value of the stress exponent, n, decreases with incresing Ca/Al ratio and is lowest for alloy C/A 1.0 (5.4) and highest for alloy C/A 0.3 (11.1).

4. Discussion

4.1. *Microstructure of the as-cast Mg alloys*

The Ca/Al ratio has a considerable effect on the composition, morphology and distribution of Laves phases in the Mg-Al-Ca alloys investigated, Fig. 1, Tables 2 and 3. The type of Laves phases formed during casting changes from Al_2Ca and $(Mg,Al)_2Ca$ in alloy C/A 0.3 to $(Mg,Al)_2Ca$ in alloy C/A 0.6 and finally to Mg_2Ca and $(Mg,Al)_2Ca$ in alloy C/A 1.0.

The formation of the different Laves phases during solidification of

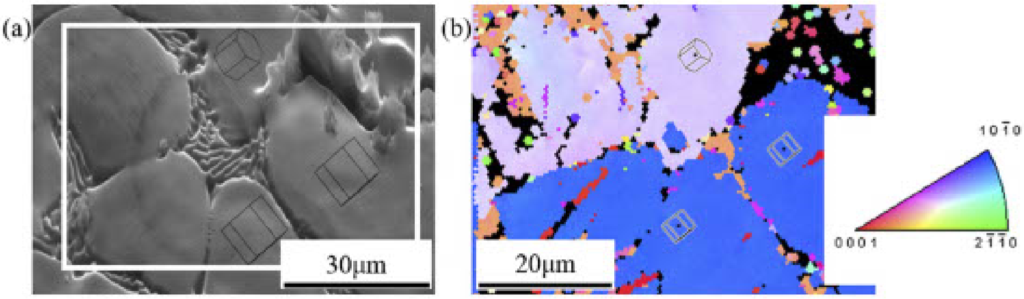

Fig. 3. a) Microstructure of alloy C/A 1.0 after electro-polishing b) IPF map of the rectangular (white) region in (a). Unit cells indicate the crystal orientation of the α-Mg phase.

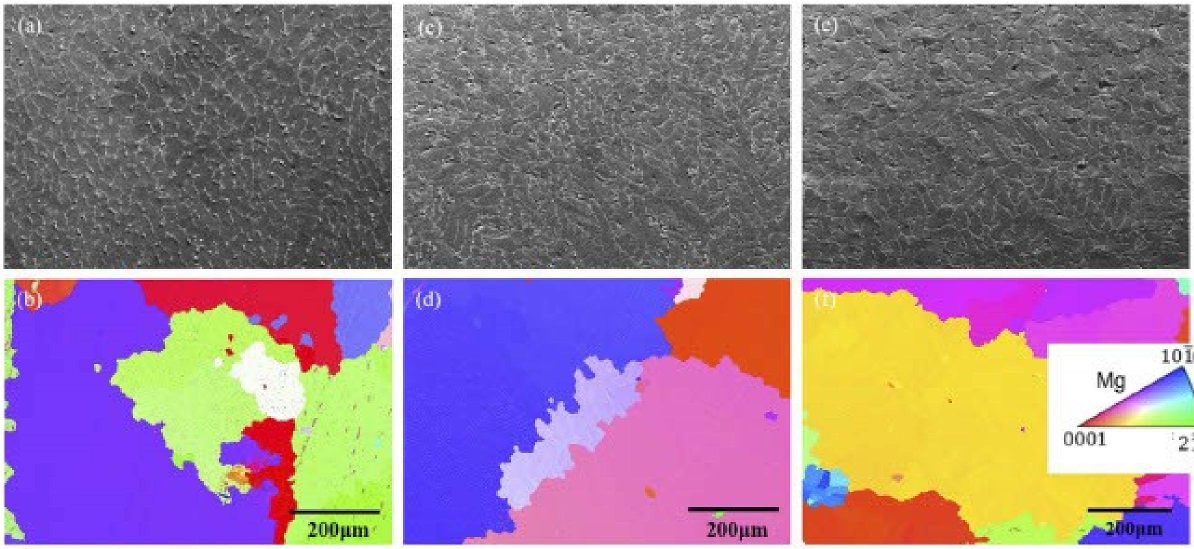

Fig. 4. SE micrographs and IPF maps of the as-cast alloys showing large grain/colony sizes present in the as-cast alloys. a), c) and e) show the microstructural area on which EBSD scans were performed for alloys C/A 0.3 (a), C/A 0.6 (c) and C/A 1.0 (e). b), d) and f) show the corresponding IPF maps.

Table 4
Microhardness of as-cast alloys at room temperature.

Alloy	Microhardness (HV)
C/A 0.3	50.5 ± 4.4
C/A 0.6	53.3 ± 2.0
C/A 1.0	58.4 ± 3.1

Mg-Al-Ca alloys with different Al and Ca contents has been studied by Ozturk et al., Suzuki et al. and Liang et al. [12,42,43]. Liang et al. [43] have reported that in Ca modified AM50 alloys with a Ca content of 0.62 wt% $Mg_{17}Al_{12}$, Al_2Ca and α-Mg form during solidification. They [43] have further observed that in Ca modified AM50 with a higher Ca content of 1.63 wt%, the formation of $Mg_{17}Al_{12}$ was completely suppressed and the eutectic reaction L→ α-Mg + $(Mg,Al)_2Ca$ was the last step during solidification resulting in a microstructure consisting of α-Mg and $(Mg,Al)_2Ca$ phase. Kondori et al. [38] observed in their work the formation of Al_2Ca Laves phase in an AM60 alloy containing 2 wt% Ca. Suzuki et al. [42] have observed the presence of $(Mg,Al)_2Ca$ Laves phase embedded in the α-Mg matrix in Mg-3.9Al-1.9Ca and Mg-8Al-3Ca alloys. These studies [38,42,43] are consistent with the present work, where in alloy C/A 0.3 no $Mg_{17}Al_{12}$ precipitates were observed and the microstructure consisted of α-Mg + Al_2Ca+ $(Mg,Al)_2Ca$ phase at room temperature. Similarly, $(Mg,Al)_2Ca$ Laves phase was present in alloy C/A 0.6.

Further, it has been reported that in alloys with a Ca/Al ratio ≥0.75 the Mg_2Ca phase can also form during solidification [42]. Suzuki et al. [42] have observed that the room temperature microstructure of Mg-3.9Al-3.8Ca and Mg-8Al-6Al alloys consisted of the three phases α-Mg + $(Mg,Al)_2Ca$ + Mg_2Ca [42]. In the same study [42], it was also reported that in these alloys $(Mg,Al)_2Ca$ forms first during solidification as a result of the reaction L → α-Mg + $(Mg,Al)_2Ca$ (in the temperature range of 807-789 K) and Mg_2Ca forms later as a result of the eutectic reaction L → α-Mg + Mg_2Ca (787 K). However, when considering the small differences in the eutectic temperatures, they [42] have further concluded that a ternary eutectic transformation following L → α-Mg + $(Mg,Al)_2Ca$ + Mg_2Ca might be possibile in some Mg-Al-Ca alloys. A similar microstructure consisting of the three phases α-Mg + $(Mg,Al)_2Ca$ + Mg_2Ca is also observed in alloy C/A 1.0 in the present study, in line with the above mentioned study.

In the present study we further observed that the volume fraction of Laves phase increases with increasing Ca/Al ratio. This is attributed to the types of Laves phases present in the different alloys. In alloy C/A 0.3 (Mg, $Al)_2Ca$ and Al_2Ca Laves phases were observed (Table 3) which both contain less Mg than Mg_2Ca. The Laves phases present in alloys C/A 0.6 and C/A 1.0 are (Mg, $Al)_2Ca$ Laves phase and (Mg, $Al)_2Ca$ + Mg_2Ca, respectively, hence, the amount of Mg incorporated in the Laves phases increases with increasing Ca/Al ratio in the alloys investigated.

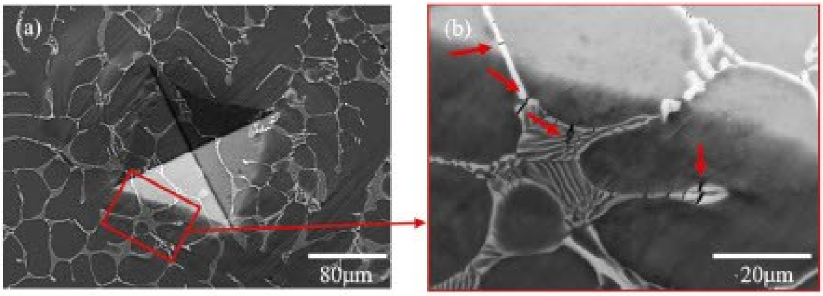

Fig. 5. a) and b) Micro-indent in the alloy C/A 1.0 revealing cracks in the Laves phase.

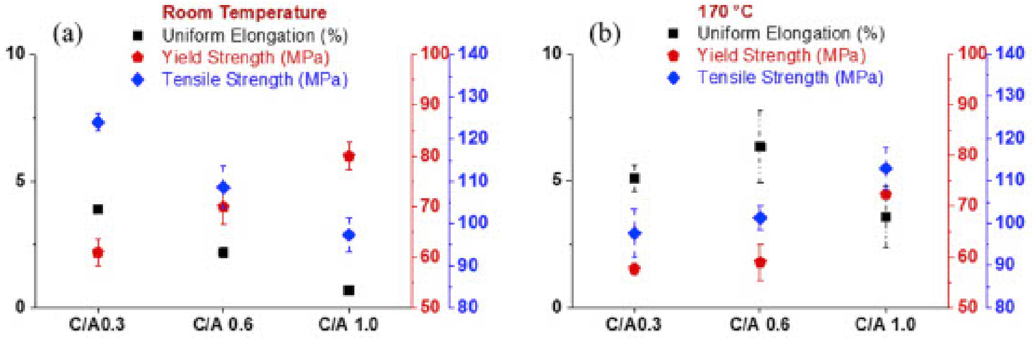

Fig. 6. Variation of Yield Strength, Tensile Strength and Uniform Elongation with Ca/Al ratio a) at room temperature, b) at 170 °C.

4.2. Mechanical properties

4.2.1. Microhardness

The microhardness increases with increasing Ca/Al ratio, Table 4. Similarly, Elamami et al. [44] have observed an increase in the microhardness with increasing Ca/Al ratio in Mg-Al-Ca alloys. This increase in hardness with increasing Ca/Al ratio is assumed to be due to the higher volume fraction of Laves phases formed, as intermetallic Laves phases have a much higher hardness than the soft α-Mg phase. The hardness of pure Mg amounts to 36.3 HV, while the addition of Al has been reported to increase the hardness to 44.5 HV in as-cast Mg-3Al and slightly above 46 HV in as-cast Mg-6Al [45]. The as-cast alloys C/A 0.3, C/A 0.6 and C/A 1.0 investigated in the present study contain similar amounts of Al (C/A 0.3: 5.44 wt%, C/A 0.6: 4.7 wt%, C/A 1.0: 3.68 wt%) but higher hardness values (Table 4) indicating that the strengthening effects induced by solute Al atoms and $Mg_{17}Al_{12}$ precipitates is less than that induced by solid solution and Laves phase strengthening in the present study.

4.2.2. Tensile properties

Consistent with the trend observed for the hardness values, the YS of the alloys investigated increases with increasing Ca/Al ratio as evident from the tensile test results at room temperature and 170 °C, Fig. 6 (a and b). On the other hand, the UE and UTS decrease with increasing Ca/Al ratio at room temperature. These results are in agreement to those reported by Nakaura et al. [46] who similarly observed an increase in YS concomitant with a decrease in UE and UTS with increasing amount of Ca in Ca modified AM50. This is interpreted by the

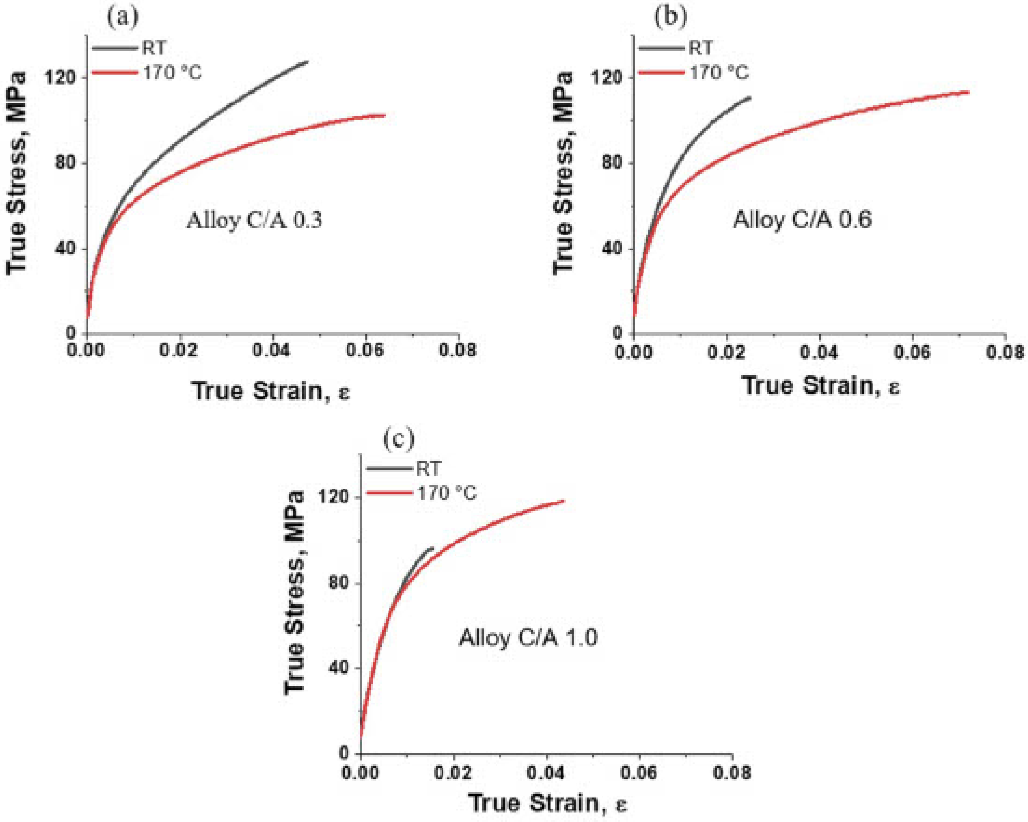

Fig. 7. True stress-strain curves at room temperature and 170 °C a) of alloy C/A 0.3, b) of alloy C/A 0.6 and c) of alloy C/A 1.0.

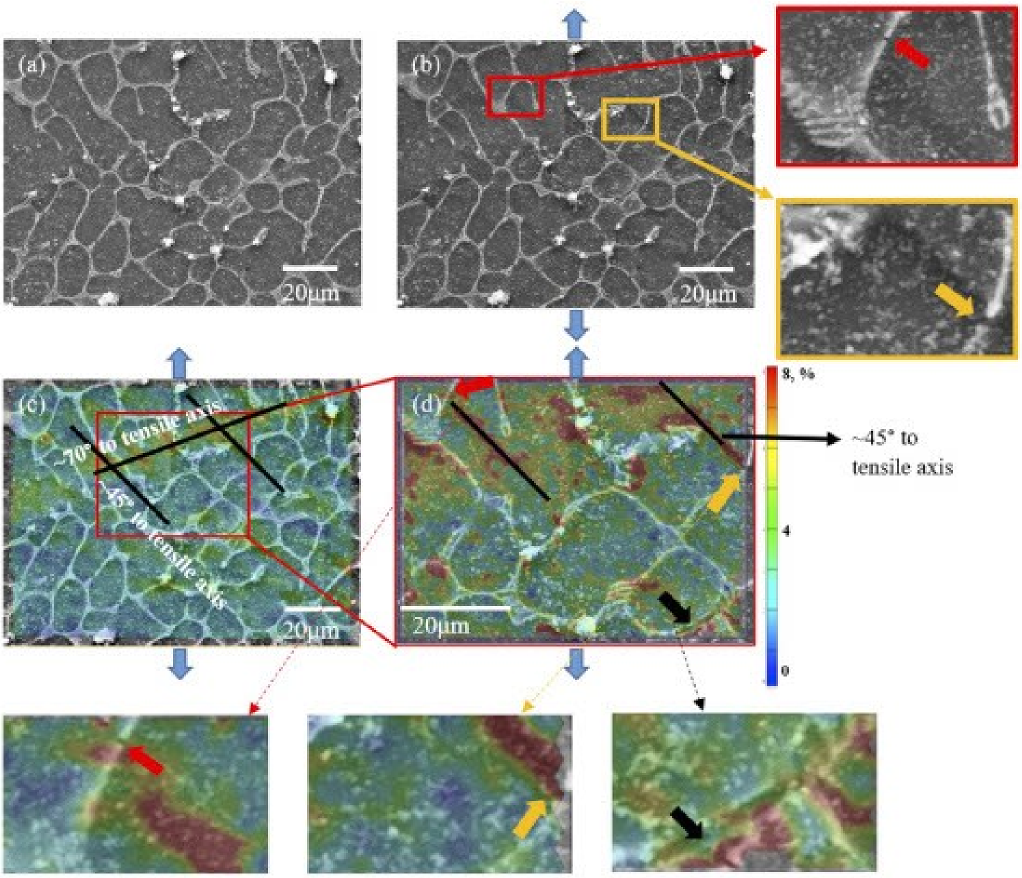

Fig. 8. a) SE micrograph of Un-deformed C/A 0.6 sample (white particles are Al_2O_3), b) SE micrograph after 4% global tensile strain at 170 °C. Blue arrows represent the tensile loading direction while red and yellow arrows show the cracks in the Laves phases, c) and d) von Mises technical strain map for the strained microstructure shown in b). Cracks in the Laves phase are highlighted on the strain map in d) by red, yellow and black arrows. (For interpretation of the references to colour in this figure legend, the reader is referred to the Web version of this article.)

change in the volume fraction and interconnectivity of Laves phase in the different alloys in this study.

Further, Fig. 10 (a, c and d) shows that cracks prefer to nucleate and grow along the intermetallic phase during tensile deformation. Furthermore, cracks were also observed inside the Al_2Ca intermetallic needle-shaped precipitates within the α-Mg phase, as evident from the fracture micrograph of alloy C/A 0.6 (Fig. 10 c)). It is therefore concluded that alloy C/A 0.3, which contains the least amount of intermetallic phase shows the highest elongation to fracture as the α-Mg matrix might impede growth of cracks formed in the Laves phases. This is further evident from the fracture micrograph of alloy C/A 0.3 where cracks propagate through the soft and more ductile α-Mg phase due to the low interconnectivity of the Laves phase network in this alloy (see Fig. 10 b)). In contrast, alloy C/A 1.0 exhibits the lowest UE as cracks can easily propagate through the interconnected Laves phase network, Fig. 10 d).

The fracture micrograph of alloy C/A 1.0 after tensile test at 170 °C (Fig. 10 d)) shows that cracks prefer to propagate through the Laves phase even at elevated temperature, which explains why the tensile elongation of alloy C/A 1.0 is lower than those of alloys C/A 0.3 and C/A 0.6 at 170 °C. Xu et al. [48] have also observed that during high temperature tensile testing cracks nucleate and grow preferentially in the intermetallic phase. However, the UE of alloy C/A 0.6 was higher than that of alloy C/A 0.3 at 170 °C. This is assumed to be caused by the activation of additional interfacial deformation modes, i.e. grain and phase boundary sliding. For example, Zhang et al. [47] have observed interfacial (α-Mg/eutectic intermetallic phase) cracking and sliding during high temperature creep studies of an as-cast Mg-5Al-5Ca-2Sn alloy. Similarly, in our work the formation of cracks in the Laves phase and interfacial sliding is observed in alloy C/A 0.6 after tensile deformation to 5% global strain at 170 °C, Fig. 10 (e and f). This interface sliding is assumed to contribute to the accommodation of shape changes of the matrix phase in case of an intermediately connected Laves phase network. In contrast, in alloy C/A 1.0 a fully interconnected, and consequently intrinsically rigid, Laves phase network is present. Consequently, the eutectic regions tend to stay rigid and interfacial sliding might even induce cracks due to this intrinsic rigidity of the fully interconnected skeleton. In alloy C/A 0.3 on the other hand, which contains only a disconnected Laves phase network, the potential contribution of interfacial sliding is thought not to become substantial enough to be macroscopically measurable. This is assumed to be the reason why alloy C/A 0.6 possesses a higher uniform elongation at elevated temperature (170 °C) than alloys C/A 0.3 and C/A 1.0.

The quasi in-situ µ-DIC results of alloy C/A 0.6 at 170 °C have further revealed bands of localized strain at an angle of 45° to the tensile axis (i.e. geometrically highest shear stress) and at the interfaces between α-Mg and Laves phase, Fig. 8(a–d). Additionally, cracks were observed in regions of high strain concentrations in the Laves phases and these cracks grow further with deformation and eventually cause material failure along the Laves phase network.

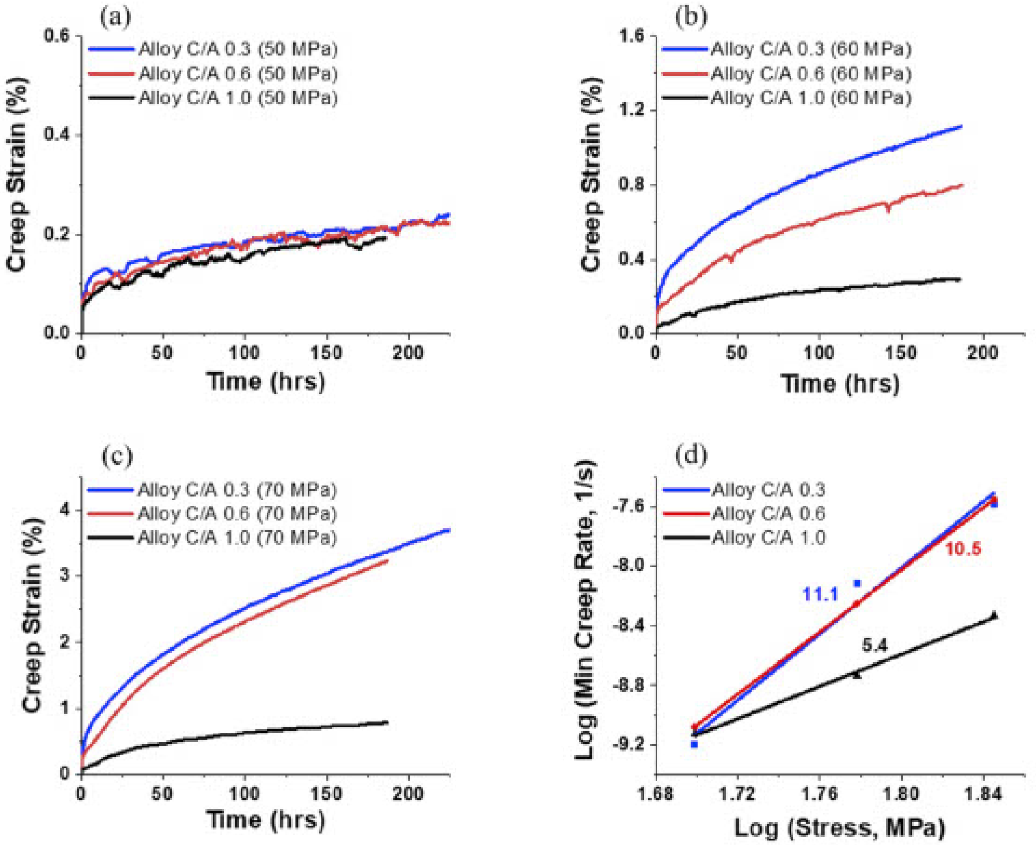

Fig. 9. Creep curves for the three alloys investigated at 170 °C a) at 50 MPa, b) 60 MPa, c) 70 MPa. d) Relationship between minimum creep rate and applied stress with stress exponent, n.

Hence, it is concluded that because of a higher amount and interconnectivity of Laves phases, the stress is carried more efficiently by the intermetallic skeleton, resulting in higher shielding of the α-Mg matrix and, consequently, higher YS, UTS and creep properties at a temperature of 170 °C (see section 4.3 for further details).

4.2.3. Creep properties

The minimum creep rate, $\dot{\varepsilon}$, of Mg-Al-Ca based alloys is related to the stress and temperature via a power law equation [8,20]:

$$\dot{\varepsilon} = A\sigma^{n}e^{\frac{-Q}{RT}} \tag{1}$$

where σ is the stress, A is a material constant, n is the stress exponent, Q is the activation energy, R is the general gas constant and T is the temperature.

The n and Q values can be used to estimate the active creep mechanisms. For most of the Mg-Al alloys, n values close to 2 are associated with grain boundary sliding, while n values of 3–6 are associated with dislocation creep and higher n values (> 8) are associated with power law breakdown creep [8,20,46,49,50]. A Q value of 30 kJ/mol is associated with grain boundary sliding in conjunction with discontinuous precipitation of $Mg_{17}Al_{12}$ phase in Mg-Al alloys, while Q values close to 80 kJ/mol are associated with grain boundary diffusion [7,8,20,46,51]. A Q value of 100 kJ/mol has been attributed to thermally activated cross-slip and a Q value of 135 kJ/mol to dislocation climb (135 kJ/mol is also the activation energy of self-diffusion of Mg) [7,8,16,20,46,49,52]. Table 5 summarizes n and Q values and the related predominant creep mechanisms of various Mg alloys published in the literature.

The stress exponents, n, obtained in the present study amount to 11.1 for alloy C/A 0.3, 10.5 for alloy C/A 0.6, and 5.4 for alloy C/A 1.0. A general trend is, that n decreases with increasing Ca/Al ratio. This is in agreement to the work of Nakaura et al. [46], although the absolute n values measured in the present study are a bit higher. The stress exponents measured in the present study indicate that the active creep mechanism in alloy C/A 1.0 is predominantly dislocation climb controlled creep (n = 5.4) while power law breakdown (PLB) occurred predominantly in alloys C/A 0.6 (n = 10.4) and C/A 0.3 (11.1). It is relevant to mention here that the possibility of dislocation climb even in the PLB regime cannot be excluded [53,54]. Terada et al. [53] have suggested this mechanism for an AX52 Mg alloy which exhibited similar stress exponents as alloys C/A 0.3 and C/A 0.6 in the present study. The activation energy in the PLB regime has been computed to be either very close to or slightly higher than the activation energy required for self-diffusion of Mg atoms (135 kJ/mol) [7] and inter-diffusion of Mg-Al solid solutions (143 kJ/mol) [7,16,53]. Relatively high stress exponents in precipitation or dispersion strengthened materials have also been observed previously and were often related to dislocation climb as it has been assumed that in such alloys the actual stress on dislocations is decreased due to interaction of dislocations with obstacles [55–59].

Post-creep microstructure analysis of specimens tested at 70 MPa reveals fewer cracks in the Laves phases in alloy C/A 1.0 than in alloy C/A 0.6 where several cracks are visible in the intermetallic phase, Fig. 11 (a and b). Alloy C/A 0.3 also exhibited small cracks in the intermetallic phase, similar to alloy C/A 0.6. The higher creep strain present in alloys C/A 0.3 and C/A 0.6 is assumed to be possibly the main reason for the higher crack density in the intermetallic phase

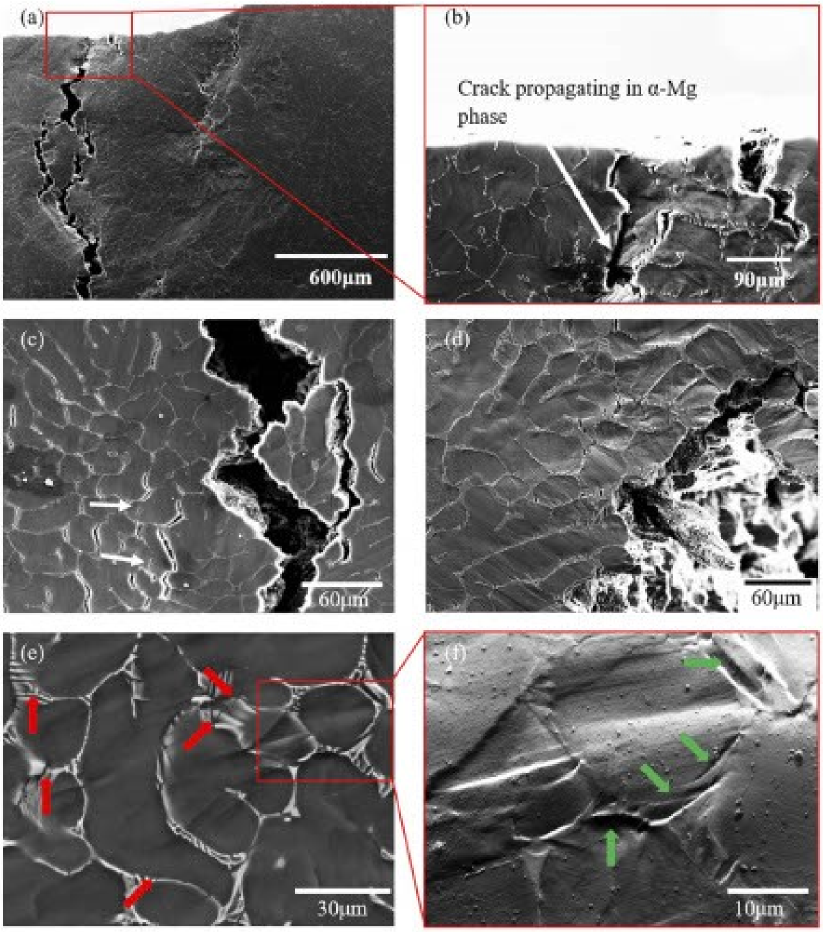

Fig. 10. a) and b) Fracture surface of alloy C/A 0.3 after tensile test at room temperature, c) microstructure after fracture (cracks within the Al_2Ca Laves phase in the α-Mg matrix are highlighted by the white arrows), d) fracture surface of alloy C/A 1.0 after tensile test at 170 °C, e) microstructure of alloy C/A 0.6 in-situ deformed to 5% global strain at 170 °C (red arrows highlight the cracks in the Laves phase), and f) SE image at 70° tilt (green arrows indicate interfacial sliding). (For interpretation of the references to colour in this figure legend, the reader is referred to the Web version of this article.)

Table 5
Creep data of high temperature Mg alloys.

	Al	Ca	Mn	Sr	Temp (°C)	Stress (MPa)	n	Q (kJ/mol)	Creep Mechanism
AC52[a] [8]	4.5	1.9	0.27	–	100–200	42–70	1.5	40	Grain boundary sliding
AC52[a] [8]	4.5	1.9	0.27	–	100–200	70–97	8.5	120	Dislocation creep
AM50[a] [46]	4.98	–	0.22	–	150–200	25–70	5.6	–	Dislocation creep
AC510[a] [46]	5.2	0.89	0.22	–	150–200	25–70	3.2	–	Dislocation creep
AC515[a] [46]	5.03	1.5	0.22	–	150–200	25–70	2.3	41	Grain boundary sliding
ACSr51520[a] [46]	5.26	1.63	0.27	0.22	150–200	25–70	1.7	60	Grain boundry diffusion
AJ42[c] [20]	4.1	–	0.27	2.17	150–200	50–60	5.12	–	Dislocation creep
AJ42[c] [20]	4.1	–	0.27	2.17	150–200	60–80	12.39	123.3	Power-law breakdown
AJ43[c] [20]	4.05	–	0.26	3.1	150–200	50–65	5.17	–	Dislocation creep
AJ43[c] [20]	4.05	–	0.26	3.1	150–200	65–80	17.41	91.8	Power-law breakdown
AJC411[c] [20]	3.87	0.86	0.28	0.84	150–200	50–80	3.75	83.2	Dilocation creep + Grain boundary sliding
AJC421[c] [20]	3.79	1.01	0.31	2.22	150–200	50–80	3.35	69.9	Dilocation creep + Grain boundary sliding
AX52[a] [53]	4.98	1.72	0.29	–	150–225	40–100	16–9	231–164	Dislocation climb
AX44[b] [40]	3.8	3.5	0.01	–	100–175	< 90	14.7	–	Power law creep
AJ44[b] [40]	3.8	–	0.02	4.2	100–175	< 80	17.5	–	Power law creep
AXJ530[b] [40]	5.3	2.6	0.30	0.17	100–175	60–90	14.9	–	Power law creep
AXJ530[a] [40]	5.3	2.6	0.30	0.17	100–175	80–100	6.7	–	Power law creep

[a] die cast.
[b] permanent mold cast.
[c] water cooled permanent mold cast.

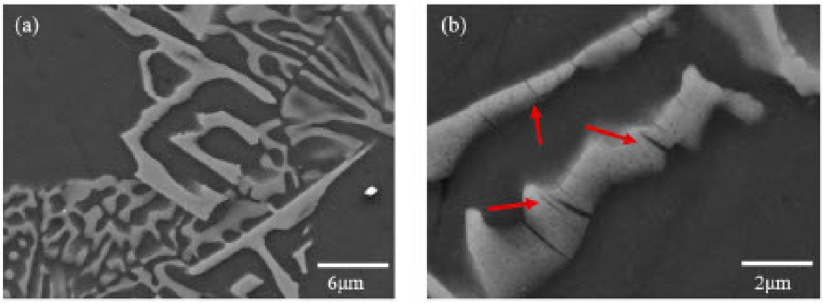

Fig. 11. a) Microstructure of alloy C/A 1.0 after creep at 70 MPa, b) microstructure of alloy C/A 0.6 after creep at 70 MPa. Red arrows indicate cracks in the Laves phases. (For interpretation of the references to colour in this figure legend, the reader is referred to the Web version of this article.)

compared to alloy C/A 1.0, Fig. 9 c). In line with our observations, it has been reported before that the collapse of eutectic intermetallic phases can cause a deterioration of the creep properties [9,53].

The high creep strain, minimum creep rate and n values of alloys C/A 0.3 and C/A 0.6 when compared to alloy C/A 1.0 are assumed to be related to their lower YS. Both, low YS and high creep strain and creep rate are likely to be caused by the lower volume fraction and interconnectivity of Laves phases in alloys C/A 0.3 and C/A 0.6 than in alloy C/A 1.0. During creep many dislocations are thought to be introduced during the instantaneous plastic strain since the stress level of 60 and 70 MPa is above the tensile YS of alloys C/A 0.3 and C/A 0.6 (Fig. 6 b)). Further, it has been reported previously that the n value increases considerably if the creep stress level is above the tensile YS [53]. The relation between the YS and the creep strain and rate is further evident when the creep strain of all three alloys investigated are compared at a similar stress level with respect to their YS at 170 °C, e.g. at $\sim 0.85\sigma_{0.2}$ and at $\sim 1.0\sigma_{0.2}$, Fig. 12. When comparing the creep properties of alloy C/A 1.0 with those of alloys C/A 0.3 and C/A 0.6 at a similar stress level with respect to their YS, Fig. 12 (a and b), the creep properties of alloy C/A 1.0 are indeed comparable to the other two alloys. This indicates that the lower creep strain and rate observed for alloy C/A 1.0 is related to its higher YS, presumably caused by the higher volume fraction and interconnectivity of Laves phases in this alloy.

Generally, higher minimum creep rates were measured in the present study when compared to literature data on die-cast Mg-Al-Ca alloys [8,19,40,46]. This is likely to be due to the large grain size of the permanent mold cast alloys investigated in the present study, Fig. 4. A similar phenomenon has been reported by Refs. [19,40] where it has been shown that die-cast Mg-Al-Ca-Sr alloys with a small grain size exhibit lower minimum creep rates than permanent mold cast Mg-Al-Ca-Sr alloys with a large grain size [19,40].

4.3. *Significance of the Ca/Al ratio in designing Mg-Al-Ca alloys*

It has been observed in the present work that during tensile testing cracks prefer to initiate and propagate in the Laves phases as evident in Fig. 10 (a, c, d and e). Crack formation in Laves phases was also observed in the region underneath a micro-indent and in post-creep microstructures. The fact that the cracks initiated inside Laves phases and not at the interfaces of Laves phases with the α-Mg matrix indicates that efficient stress transfer is occurring from the soft and more ductile α-Mg matrix to the hard and strong (but brittle) Laves phases in these alloys and that the Laves phases also undergo strain (at least to some extent). Otherwise the strain concentrations at Laves phase/α-Mg interfaces (Fig. 8) would have caused de-cohesion/cracking at the interfaces and not inside the Laves phases (some amount of interfacial sliding occurs at 170 °C (Fig. 10 f))) Amberger et al. [11] observed that the load carried by the intermetallic phase rises with increasing Ca content in Mg-Al-Ca alloys primarily because of the increase in the interconnectivity of the Laves phases as the interconnected skeleton carries more load than only loosely connected intermetallic phases. This explains also why in the present work the flow stress increases with increasing Ca/Al ratio, both at room and elevated temperatures, along with creep resistance. So, for designing Mg-Al-Ca alloys with superior creep resistance, a higher Ca/Al ratio is favorable but a compromise has to be made in terms of ductility. The optimum combination between creep resistance and ductility might lie anywhere between a Ca/Al ratio of 0.6 and 1.0.

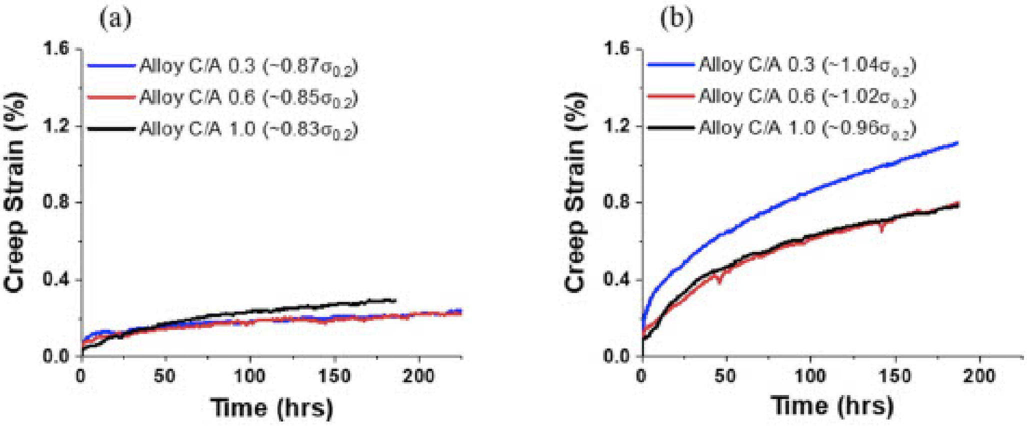

Fig. 12. Creep curves at 170 °C of all alloys at stress levels relative to their YS of a) $\sim 0.85\sigma_{0.2}$ and b) $\sim 1.0\sigma_{0.2}$.

5. Conclusions

We investigated the effects of the Ca/Al ratio on the microstructure formation, tensile and creep properties of as-cast Mg-Al-Ca alloys at room temperature and 170 °C using mechanical testing, μ-DIC, SEM and EBSD. The following conclusions are drawn:

- With an increase in the Ca/Al ratio, the volume fraction of Laves phases increases concomitant with a change in their morphology: from a disconnected network (at Ca/Al = 0.32) to a fully interconnected skeleton (at Ca/Al = 1.03).
- The Ca/Al ratio is an effective tool to control the types of Laves phases formed in Mg-Al-Ca alloys: from Al_2Ca and $(Mg,Al)_2Ca$ Laves phases at low to $(Mg,Al)_2Ca$ and Mg_2Ca Laves phases at higher Ca/Al ratio.
- The amount of Al dissolved in the α-Mg matrix decreases with an increase in the Ca/Al ratio. Additionally, needle-shaped Al_2Ca precipitates parallel to the basal plane of the α-Mg matrix were observed in alloys with Ca/Al = 0.62 and 1.03.
- The microhardness and YS of the alloys increase with increasing Ca/Al ratio as the volume fraction and network interconnectivity of the Laves phases increases.
- With increasing Ca/Al ratio, the flow stress of the alloys increases and the UE decreases. The higher volume fraction of interconnected Laves phases with increasing Ca/Al ratio carry a higher load resulting in higher flow stresses. On the other hand, the UE decreases with increasing Ca/Al ratio as cracks tend to nucleate and propagate in the Laves phases.
- Strain maps generated from quasi in-situ μ-DIC measurements in the SEM show that the strain concentrates within the α-Mg grains at an angle of 45° (in regions experiencing the highest shear stress) and at the interfaces of α-Mg and $(Mg,Al)_2Ca$ Laves phases. Cracks were formed in the Laves phases at points of high strain localisation in the microstructure. These cracks grow and propagate in the Laves phases until the material breaks.
- Within stress levels of 50–70 MPa, the alloy with the highest Ca/Al ratio exhibited the best creep properties at 170 °C. With increasing Ca/Al ratio, the stress exponent, n, and minimum creep rate decrease. This is related to the higher YS with increasing Ca/Al ratio.

5.1. Outlook

The present study demonstrates that there is a huge potential for manipulating the mechanical properties of as-cast Mg-Al-Ca alloys by controlling the amount, type and distribution of Laves phases. However, the role of the individual microstructural components (α-Mg, Laves phase, interfaces of both phases) during plastic deformation of this alloy system at various temperatures is still not fully clear and requires further investigation in future studies.

Acknowledgments

M. Zubair acknowledges funding from the University of Engineering and Technology, Lahore Pakistan. S. Korte-Kerzel and C. F. Kusche gratefully acknowledge the German Research Foundation (DFG) for funding project B2 within the Collaborative Research Centre TRR 188 and the use of the in-situ device. Further, we would also like to extend our gratitude to our colleagues, Ms. Doreen Andre, Mr. Risheng Pei and the highly skilled technicians, especially Mr. David Beckers, Mr. Thomas Burlet, Mr. Gerhard Schütz and Mr. Arndt Ziemons (both in alphabetic order) at our Institute (Institut für Metallkunde und Metallphysik, RWTH Aachen) in helping at various steps of this study.

Data Availability

The raw/processed data required to reproduce these findings cannot be shared at this time as the data also forms part of an ongoing study.

References

[1] P.K. Mallick, Advanced materials for automotive applications: an overview, in: J. Rowe (Ed.), Advanced Materials in Automotive Engineering, Woodhead Publishing Limited, 2012, pp. 5–27.
[2] A.P. Mouritz, Magnesium alloys for aerospace structures, in: A.P. Mouritz (Ed.), Introduction to Aerospace Materials, Woodhead Publishing Limited, 2012, pp. 224–231.
[3] B.R. Powell, P.E. Krajewski, A.A. Luo, Magnesium alloys for lightweight powertrains and automotive structures, in: P.K. Mallick (Ed.), Materials, Design and Manufacturing for Lightweight Vehicles, Woodhead Publishing Limited, 2010, pp. 114–173.
[4] A.A. Kaya, Physical metallurgy of magnesium, in: K.U.K.a.A.A.K. Mihriban, O. Pekguleryuz (Eds.), Fundamentals of Magnesium Alloy Metallurgy, Woodhead Publishing Limited, 2013, pp. 33–84.
[5] H.N. Mathur, V. Maier-Kiener, S. Korte-Kerzel, Deformation in the γ-$Mg_{17}Al_{12}$ phase at 25–278 °C, Acta Mater. 113 (2016) 221–229.
[6] A. Suzuki, et al., Effect of Sr additions on the microstructure and strength of a Mg-Al-Ca ternary alloy, Metall. Mater. Trans. 38 (2) (2007) 420–427.
[7] M.O. Pekguleryuz, A.A. Kaya, Creep resistant magnesium alloys for powertrain applications, Adv. Eng. Mater. 5 (12) (2003) 866–878.
[8] A.A. Luo, M.P. Balogh, B.R. Powell, Creep and microstructure of magnesium-aluminum-calcium based alloys, Metallurgic. Mater. Trans. Phys. Metallurgy Mater. Sci. 33 (3) (2002) 567–574.
[9] D. Amberger, P. Eisenlohr, M. Goken, Microstructural evolution during creep of Ca-containing AZ91, Mater. Sci. Eng. Struct. Materi. Propert. Microstruct. Process. 510–11 (2009) 398–402.
[10] Y. Terada, et al., A thousandfold creep strengthening by Ca addition in die-cast AM50 magnesium alloy, Metall. Mater. Trans. 35A (2004) 4.
[11] D. Amberger, P. Eisenlohr, M. Goken, On the importance of a connected hard-phase skeleton for the creep resistance of Mg alloys, Acta Mater. 60 (5) (2012) 2277–2289.
[12] K. Ozturk, et al., Creep resistant Mg-Al-Ca alloys: computational thermodynamics and experimental investigation, Jom-J. Mineral Metal Mater. Soc. 55 (11) (2003) A40–A44.
[13] L.L. Rokhlin, et al., Calcium-alloyed magnesium alloys, Met. Sci. Heat Treat. 51 (3–4) (2009) 164–169.
[14] A.V. Koltygin, et al., Development of a magnesium alloy with good casting characteristics on the basis of Mg–Al–Ca–Mn system, having Mg–Al2Ca structure, J. Magnesium Alloys 1 (3) (2013) 224–229.
[15] L. Zhang, et al., Microstructures and mechanical properties of Mg–Al–Ca alloysaffected by Ca/Al ratio, Mater. Sci. Eng. 636 (2015) 279–288.
[16] B. Kondori, R. Mahmudi, Effect of Ca additions on the microstructure and creep properties of a cast Mg–Al–Mn magnesium alloy, Mater. Sci. Eng. 700 (2017) 438–447.
[17] Z.T. Li, et al., Effect of Ca/Al ratio on microstructure and mechanical properties of Mg-Al-Ca-Mn alloys, Mater. Sci. Eng. Struct. Materi. Propert. Microstruct. Process. 682 (2017) 423–432.
[18] Y. Chai, et al., Role of Al content on the microstructure, texture and mechanical properties of Mg-3.5Ca based alloys, Mater. Sci. Eng. 730 (2018) 303–316.
[19] S.M. Zhu, B.L. Mordike, J.F. Nie, Creep properties of a Mg–Al–Ca alloy produced by different casting technologies, Mater. Sci. Eng. 483–484 (2008) 583–586.
[20] B. Jing, et al., Microstructure and tensile creep behavior of Mg–4Al based magnesium alloys with alkaline-earth elements Sr and Ca additions, Mater. Sci. Eng. 419 (2006) 181–188.
[21] D. Xiao, et al., Microstructure, mechanical and creep properties of high Ca/Al ratio Mg-Al-Ca alloy, Mater. Sci. Eng. 660 (2016) 166–171.
[22] F. Di Gioacchino, J. Quinta da Fonseca, Plastic strain mapping with sub-micron resolution using digital image correlation, Exp. Mech. 53 (5) (2013) 743–754.
[23] B. Pan, et al., Two-dimensional digital image correlation for in-plane displacement and strain measurement: a review, Meas. Sci. Technol. 20 (6) (2009).
[24] D.A.F.J. Quinta, P.M. Mummery, P.J. Withers, Full-field strain mapping by optical correlation of micrographs acquired during deformation, J. Microsc. 218 (Pt 1) (2005) 9–21.
[25] D. Yan, C.C. Tasan, D. Raabe, High resolution in situ mapping of microstrain and microstructure evolution reveals damage resistance criteria in dual phase steels, Acta Mater. 96 (2015) 399–409.
[26] C.C. Tasan, et al., Integrated experimental–simulation analysis of stress and strain partitioning in multiphase alloys, Acta Mater. 81 (2014) 386–400.
[27] M.A. Tschopp, et al., Microstructure-dependent local strain behavior in polycrystals through in-situ scanning electron microscope tensile experiments, Metall. Mater. Trans. 40 (10) (2009) 2363–2368.
[28] A.D. Kammers, S. Daly, Self-assembled nanoparticle surface patterning for improved digital image correlation in a scanning electron microscope, Exp. Mech. 53 (8) (2013) 1333–1341.
[29] F. Di Gioacchino, J. Quinta da Fonseca, An experimental study of the polycrystalline plasticity of austenitic stainless steel, Int. J. Plast. 74 (2015) 92–109.
[30] T.E.J. Edwards, et al., Longitudinal twinning in a TiAl alloy at high temperature by in situ microcompression, Acta Mater. 148 (2018) 202–215.
[31] Z. Wu, et al., Local mechanical properties and plasticity mechanisms in a Zn-Al eutectic alloy, Mater. Des. 157 (2018) 337–350.
[32] S. Amini, R.S. Kumar, A high-fidelity strain-mapping framework using digital image correlation, Mater. Sci. Eng. 594 (2014) 394–403.

[33] Z. Li, et al., Damage investigation in A319 aluminum alloy by digital image correlation during in-situ tensile tests, Procedia Structural Integrity 2 (2016) 3415–3422.

[34] H. Halim, D. Wilkinson, M. Niewczas, The Portevin–Le Chatelier (PLC) effect and shear band formation in an AA5754 alloy, Acta Mater. 55 (12) (2007) 4151–4160.

[35] S. Amerioun, S.I. Simak, H.U., Laves-phase structural changes in the system CaAl2-xMgx, Inorg. Chem. 42 (5) (2003) 1467–1474.

[36] S.W. Xu, et al., High temperature tensile properties of as-cast Mg–Al–Ca alloys, Mater. Sci. Eng. 509 (2009) 105–110.

[37] H. Eibisch, et al., Effect of solidification microstructure and Ca additions on creep strength of magnesium alloy AZ91 processed by Thixomolding, Int. J. Mater. Res. 99 (1) (2008) 56–66.

[38] B. Kondori, R. Mahmudi, Effect of Ca additions on the microstructure, thermal stability and mechanical properties of a cast AM60 magnesium alloy, Mater. Sci. Eng. Struct. Materi. Propert. Microstruct. Process. 527 (7–8) (2010) 2014–2021.

[39] A. Suzuki, et al., Precipitation strengthening of a Mg-Al-Ca–based AXJ530 die-cast alloy, Metall. Mater. Trans. 39 (3) (2008) 696–702.

[40] N.D. Saddock, et al., Grain-scale creep processes in Mg–Al–Ca base alloys: implications for alloy design, Scripta Mater. 63 (7) (2010) 692–697.

[41] A.A. Luo, Recent magnesium alloy development for elevated temperature applications, Int. Mater. Rev. 49 (1) (2013) 13–30.

[42] A. Suzuki, et al., Solidification paths and eutectic intermetallic phases in Mg–Al–Ca ternary alloys, Acta Mater. 53 (2005) 2823–2834.

[43] S.M. Liang, et al., Thermal analysis and solidification pathways of Mg–Al–Ca system alloys, Mater. Sci. Eng. 480 (2008) 365–372.

[44] H.A. Elamami, et al., Phase selection and mechanical properties of permanent-mold cast Mg-Al-Ca-Mn alloys and the role of Ca/Al ratio, J. Alloy. Comp. 764 (2018) 216–225.

[45] Z. Wei-chao, L.I. Shuang-shou, T. Bin, Microstructure and properties of Mg-Al binary alloys, China Foundry 3 (4) (2006) 270–274.

[46] Y. Nakaura, A. Watanabe, K. Ohori, Effects of Ca,Sr additions on properties of Mg-Al based alloys, Mater. Trans. 47 (4) (2006) 1031–1039.

[47] G. Zhang, et al., Creep resistance of as-cast Mg-5Al-5Ca-2Sn alloy, China Foundry 14 (4) (2017) 265–271.

[48] S.W. Xu, et al., High temperature tensile properties of as-cast Mg–Al–Ca alloys, Mater. Sci. Eng. 509 (1–2) (2009) 105–110.

[49] D. Zhang, et al., Effects of minor Sr addition on the microstructure, mechanical properties and creep behavior of high pressure die casting AZ91-0.5RE based alloy, Mater. Sci. Eng. 693 (2017) 51–59.

[50] D.H. Kang, S.S. Park, N.J. Kim, Development of creep resistant die cast Mg–Sn–Al–Si alloy, Mater. Sci. Eng. 413–414 (2005) 555–560.

[51] H. Uchida, T. Shinya, Estimation of creep deformation behavior in Mg-Al alloys by using .THETA. projection method, J. Jpn. Inst. Light Metals 45 (10) (1995) 572–577.

[52] H. Somekawa, et al., Dislocation creep behavior in Mg–Al–Zn alloys, Mater. Sci. Eng. 407 (1) (2005) 53–61.

[53] Y. Terada, N. Ishimatsu, T. Sato, Creep parameters in a die-cast Mg-Al-Ca alloy, Mater. Trans. 48 (9) (2007) 2329–2335.

[54] M.E. Kassner, Chapter 2 - five-power-law creep, in: M.E. Kassner (Ed.), Fundamentals of Creep in Metals and Alloys, third ed., Butterworth-Heinemann, Boston, 2015, pp. 7–102.

[55] O.D. Sherby, P.M. Burke, Mechanical behavior of crystalline solids at elevated temperature, Prog. Mater. Sci. 13 (1968) 323–390.

[56] S.C. Tjong, Z.Y. Ma, Steady state creep deformation behaviour of SiC particle reinforced 2618 aluminium alloy based composites, Mater. Sci. Technol. 15 (4) (2013) 429–436.

[57] H. Dieringa, N. Hort, K.U. Kainer, Investigation of minimum creep rates and stress exponents calculated from tensile and compressive creep data of magnesium alloy AE42, Mater. Sci. Eng. 510–511 (2009) 382–386.

[58] P. Jain, K.S. Kumar, Tensile creep of Mo–Si–B alloys, Acta Mater. 58 (6) (2010) 2124–2142.

[59] Z. Wu, et al., Creep behaviour of eutectic Zn-Al-Cu-Mg alloys, Mater. Sci. Eng. 724 (2018) 80–94.

6. Research Publication 2 – Strain heterogeneity and micro-damage nucleation under tensile stresses in an Mg-5Al-3Ca alloy with an intermetallic skeleton

M. Zubair, S. Sandlöbes-Haut, M.A. Wollenweber, K. Bugelnig, C.F. Kusche, G. Requena, S. Korte-Kerzel, Strain heterogeneity and micro-damage nucleation under tensile stresses in an Mg–5Al–3Ca alloy with an intermetallic skeleton, Materials Science and Engineering: A, 767 (2019) 138414.

This publication discusses the distribution of strain at microstructural level and summarises the micro-damage nucleation behaviour in Mg-5Al-3Ca alloy. Quasi in-situ DIC and deformation analysis in SEM in combination with EBSD were used to study for this purpose. The paper addresses the 2nd and 3rd research question laid down in the section 1.1.

Materials Science & Engineering A 767 (2019) 138414

Contents lists available at ScienceDirect

Materials Science & Engineering A

journal homepage: www.elsevier.com/locate/msea

Strain heterogeneity and micro-damage nucleation under tensile stresses in an Mg–5Al–3Ca alloy with an intermetallic skeleton

M. Zubair[a,b,*], S. Sandlöbes-Haut[a], M.A. Wollenweber[a], K. Bugelnig[c], C.F. Kusche[a], G. Requena[c], S. Korte-Kerzel[a]

[a] *Institute for Physical Metallurgy and Materials Physics, RWTH Aachen University, Kopernikusstr. 14, 52074, Aachen, Germany*
[b] *Department of Metallurgical and Materials Engineering, G.T Road, UET Lahore, Lahore, Pakistan*
[c] *German Aerospace Centre, Linder Höhe, 51147, Cologne, Germany*

ARTICLE INFO

Keywords:
µ-DIC
Strain heterogeneity
Euler number
µ-Cracks
Dual phase Mg–Al–Ca alloy
High temperature tensile behavior

ABSTRACT

Strain heterogeneity at the microstructural level plays a vital role in the deformation and fracture behaviour of dual or multi-phase materials. In the present work, the strain heterogeneity, localisation and partitioning arising at the sub-micron scale during elevated temperature (170 °C) tensile deformation of an Mg–5Al–3Ca alloy was investigated using quasi in-situ µ-DIC experiments. The results reveal that the strain is mainly carried by the α-Mg phase, while the intermetallic Laves phase plays a critical role in that strain concentrations build up at the α-Mg matrix and Laves phase interfaces, hence, reducing the overall deformability of the alloy. In quasi in-situ and bulk material analysis at elevated temperature, cracks were observed to nucleate in the Laves phase, at i) the intersection points of slip lines in the α-Mg matrix with the Laves phase and ii) the twin intersections with α-Mg/Laves phase interfaces and iii) twin transmissions across α-Mg/Laves phase interfaces. Euler number analysis has shown that the (inter-)connectivity of the Laves phase decreases with deformation. Finally, cracks grow preferentially along the Laves phases until the material fractures.

1. Introduction

During the last years, Mg-based alloys have attracted attention of many researchers around the globe, particularly due to their low density, low cost and high availability [1,2]. Al is the main alloying element of most commercial Mg alloys (Al–Zn or Al–Mn) as it enhances the strength and hardness and also the corrosion resistance and castability [2,3]. However, the high temperature mechanical properties of Mg–Al alloys are poor, mainly because of the presence of $Mg_{17}Al_{12}$ as intermetallic precipitate phase in the microstructure. $Mg_{17}Al_{12}$ has a low thermal stability and readily softens at temperatures above 130 °C [4–6].

Ca addition to Mg–Al alloys can considerably enhance the elevated temperature mechanical properties like yield strength [7], tensile strength, creep properties [8–11] and thermal stability [4]. This is because Ca addition suppresses the formation of the $Mg_{17}Al_{12}$ phase with a low thermal stability and promotes the formation of harder Laves phases with a higher thermal stability. At low concentrations, Ca tends to dissolve in the matrix and in the second phase ($Mg_{17}Al_{12}$), thereby, enhancing its thermal stability [4]. Once the Ca concentration exceeds a critical value, the Laves phase starts to appear in the microstructure. Specifically, Kondori et al. [4] observed i) only $Mg_{17}Al_{12}$ as second phase in AM60 and modified AM60 containing 0.5 wt% Ca, ii) a combination of $Mg_{17}Al_{12}$ and Al_2Ca Laves phase in modified AM60 with 1.2 wt% Ca addition, and iii) only Al_2Ca Laves phase when the Ca content was 2.0 wt%. The two other Laves phases of the Mg–Al–Ca system, namely, $(Mg,Al)_2Ca$ and Mg_2Ca, were also reported to form in Mg–Al–Ca alloys [12–15]. It was reported that the Ca/Al ratio controls which Laves phases form: the type of Laves phase changes from Al_2Ca (C15) to $(Mg,Al)_2Ca$ (C36) and Mg_2Ca (C14) with variation of the Ca/Al ratio from 0.3 to 1.0 [12,16].

The alloy Mg–5Al–3Ca (in wt.%) (from here onwards referred to as AX53) has a dual phase microstructure, containing a hard intermetallic skeleton of $(Mg,Al)_2Ca$ Laves phase embedded in a soft α-Mg matrix [16]. Due to significantly different intrinsic mechanical properties of the different phases (α-Mg matrix and Laves phases) [17–19], a highly heterogeneous strain distribution was reported for Mg–Al–Ca alloys [16,20]. In addition, the volume fraction, morphology, distribution, and orientation relationship between matrix and second phase can affect the strain heterogeneity. Strain heterogeneity usually results in strain partitioning, localisation and shear band formation, thus significantly affecting the mechanical and fracture behaviour of dual or

---

[*] Corresponding author. Institute for Physical Metallurgy and Materials Physics, RWTH Aachen University, Kopernikusstr. 14, 52074, Aachen, Germany
E-mail address: zubair@imm.rwth-aachen.de (M. Zubair).

https://doi.org/10.1016/j.msea.2019.138414
Received 22 August 2019; Received in revised form 9 September 2019; Accepted 10 September 2019
Available online 11 September 2019
0921-5093/ © 2019 Elsevier B.V. All rights reserved.

multi-phase materials [21–23]. Analysis of the strain distribution and partitioning from the grain level down to the sub-micrometer scale can provide valuable insights regarding the mechanical and fracture behaviour of multi-phase Mg–Al–Ca alloys.

Several recent studies focused on the evaluation of grain level strain heterogeneities in multi-phase materials [21,23,24]. Digital Image Correlation (DIC) is an advanced method to quantitatively measure the strain partitioning occurring at macroscopic and microscopic scales under complex stress states [22,24–35]. In DIC, images of the same sample area before and after straining are correlated by measuring and quantifying the local relative displacements before and after deformation. In order to quantify the relative displacements, speckles or small particles are deposited on the sample surface and the relative displacement of the speckles are correlated for the deformed and un-deformed image [28]. The local relative displacements are commonly considered to result from strain in the microstructure. A small speckle size or use of nanoparticles such as SiO_2 or Al_2O_3 enables to measure the local strain at a sub-micrometer scale using scanning electron microscopy (SEM) as demonstrated e.g. by Dutta et al. [21] for a medium Mn steel and Zubair et al. [16] for Mg–Al–Ca alloys.

In the present work, the strain distribution and partitioning between the α-Mg matrix and the $(Mg,Al)_2Ca$ Laves phase evolving during deformation in the dual phase AX53 alloy was investigated using high resolution sub-micrometer scale quasi in-situ experiments coupled with DIC and electron backscatter diffraction (EBSD). The tensile and fracture behaviour of alloy AX53 was also studied using quasi in-situ and ex-situ deformation experiments in SEM. To evaluate any changes in the connectivity of the Laves phase network during deformation, the Euler number was used as a mathematical method to express the connectivity of objects and to measure the effect of deformation on the (loss of) connectivity [36].

2. Experimental methods

Pure Mg, Al and Ca were molten and solidified in an induction furnace with a pressure of 15 bar argon using a steel crucible. The global chemical composition of the as-cast alloy was measured using wet chemical analysis, Table 1.

Samples for microstructure analysis were metallographically prepared by mechanical grinding and polishing, electrolytic polishing and a subsequent final mechanical polishing step. First, the samples were mechanically ground down to 4000 SiC emery paper and then mechanically polished using 3 μm and 1 μm diamond suspension. Subsequently, the samples were electro-polished using the AC2 (Struers) electrolyte (electro-polishing was needed to prepare good surfaces for EBSD analysis). The temperature, time and voltage of electro-polishing were $\leq -20\,^{\circ}C$, 60 s and 15 V, respectively. Due to the different electrochemical behaviour of Mg and the Laves phase, electro-polishing produced a waviness at the sample surface. Finally, this waviness was removed via mechanical polishing using OPU (~40 nm SiO_2 colloidal suspension) followed by cleaning in an ultrasonic bath and softly rotating on a clean cloth using ethanol as a cleaning agent. For μ-DIC, the sample was not cleaned and the residual nano-sized SiO_2 particles acted as speckles (a necessary prerequisite for strain partitioning analyses using DIC). An acceleration voltage of 10–20 kV was used to characterize the as-cast and deformed microstructures as described in detail in [16]. Energy dispersive X-ray spectroscopy (EDS) was carried out at the lower voltage of 10 kV and the higher voltage of 20 kV was selected for secondary electron (SE) imaging, back-scattered electron (BSE) imaging and electron backscatter diffraction (EBSD). Image J, OIM and Channel 5 were used to analyse the images and EBSD data. In order to investigate large microstructural areas at a sub-micrometer scale resolution, panoramic imaging was extensively used within this study for μ-DIC and fracture analysis. The software used for image stitching was Image Composite Editor (ICE) [37].

Table 1
Composition of the as cast alloy.

Alloy	Al (wt. %)	Ca (wt. %)	Fe (wt.%)	Mg (wt.%)
AX53	5.21	3.18	0.008	balance

For the evaluation of the change in local connectivity of the 2D Laves phase network as a function of composition and deformation, SEM images of the same sample positions before and after tensile deformation were used. Images taken on the sample prepared in this work were further compared with samples possessing different Ca/Al ratios produced in the same way and discussed in terms of their mechanical properties in our previous work [16]. Images were smoothed with a bilateral filter and the 2D networks were segmented using global gray value thresholds. The segmented networks were then labeled so that a different color was assigned to each individual Laves phase segment. Afterwards, the local connectivity of the 2D segmented Laves networks, i.e. the amount of connecting branches of the network, was quantitatively evaluated using the software Avizo Fire 9.5 by means of the Euler number, χ, as a topological parameter [36,38]. This parameter reveals changes in local connectivity in complex network structures. In two dimensions, the Euler number can be calculated as follows:

$$\chi = b_0 - b_1 \tag{1}$$

where b_0 is the number of objects and b_1 the number of holes within the object [39]. Variations in the Euler number indicate a change in local connectivity. More specifically, a decreasing Euler number indicates an increase of local connectivity and vice versa [36,38].

An electromechanical testing machine (ETM) was used to carry out tensile deformation of standard dog bone shaped specimens having a gauge length of 10 mm at room temperature (RT) and 170 °C. This temperature was selected based on the temperatures required for applications like automotive powertrains [40,41] and was also used in a previous study [16]. At least three tests were carried out at both temperatures. An initial strain rate of $5 \times 10^{-4} s^{-1}$ was selected for tensile testing at RT and 170 °C. A linear variable differential transformer (LVDT) extensometer was used to measure the elongation of the specimens during tensile deformation. Quasi in-situ μ-DIC experiments were done using SEM (Zeiss LEO1530) to study the distribution of strain at the sub-micrometer level during tensile deformation at 170 °C. The sample was deformed stepwise at 170 °C in an ETM and monitored using SEM after certain pre-defined deformation steps of 3, 4 and 5% global strain. The local strain was determined using the ARAMIS GOM Correlate software. For deformation and fracture analysis, the samples were deformed both, quasi in-situ and ex-situ.

3. Results

3.1. Microstructure analysis

The microstructure of as-cast AX53 is shown in Fig. 1 (a). EDS point analysis of the Laves phases was performed as highlighted by the characters A – D in Fig. 1 (b) and the corresponding compositions are listed in Table 2.

The area fraction of intermetallic phase amounts to around 7.3% and the mean dendrite cell size (as calculated using the linear intercept method, ASTM E 112–12) is 28.5 ± 3.4 μm in the as cast alloy. The grain size of the α-Mg matrix is much larger than the dendrite cell size as can be seen from the inverse pole figure (IPF) map in Fig. 2. The average grain size of the α-Mg matrix is 183.5 ± 72.5 μm (determined using the same procedure i.e. according to ASTM E 112–12).

3.2. Tensile properties

Fig. 3 (a) represents the true stress-strain curve of the as-cast alloy at

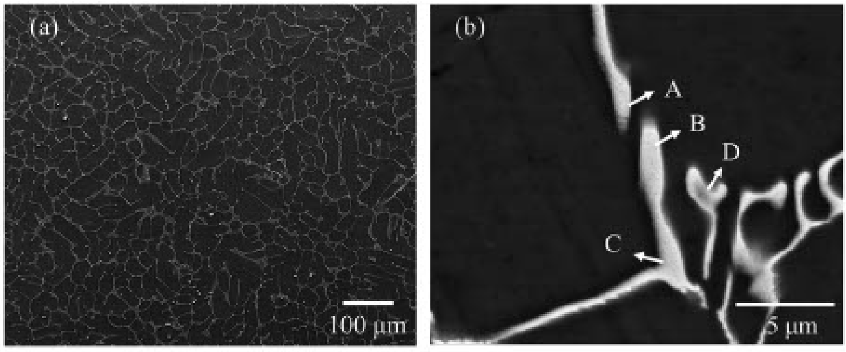

Fig. 1. (a): SE micrograph of the microstructure of as-cast alloy AX53, (b) high resolution BSE image of the alloy. Compositional analysis of the Laves phases via EDS was performed on the points marked by the characters A, B, C and D, see Table 2.

Table 2
Compositional analysis of the Laves phases in alloy AX53 using EDS.

Spots	Mg (at. %)	Al (at. %)	Ca (at. %)	Corresponding Phase
A	55.3	27.7	17.1	$(Mg,Al)_2Ca$
B	33.6	40.3	26.2	$(Mg,Al)_2Ca$
C	32.7	40.6	26.7	$(Mg,Al)_2Ca$
D	64.9	22.6	12.5	$(Mg,Al)_2Ca$
Matrix (α-Mg)	98.3	1.7	–	–

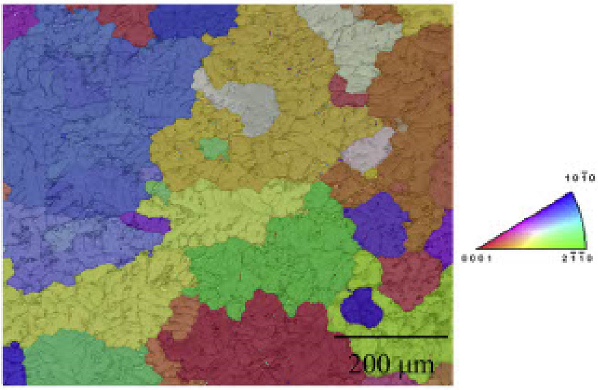

Fig. 2. Superimposed IPF (inverse pole figure) and band contrast (BC) maps of the as-cast alloy showing that the dendrite cell size is much smaller than the α-Mg grain size.

RT and 170 °C. With increasing temperature from RT to 170 °C, the yield strength ($\sigma_{0.2}$) drops from 92 ± 2 MPa to 74 ± 2 MPa, the uniform elongation (UE) increases from 1.2 ± 0.5 to 6.2 ± 1.3%, and the ultimate tensile strength (UTS) stays nearly constant (≈123 ± 11 MPa at RT and ≈122 ± 5 at 170 °C), Fig. 3 (b).

3.3. *Strain partitioning*

As shown in Fig. 1, the microstructure of the as-cast alloy contains two phases: a soft α-Mg phase reinforced with a hard interconnected Laves phase (predominant network of $(Mg,Al)_2Ca$). In order to understand the deformation behaviour of alloy AX53, it is of prime interest to investigate how strain is distributed at the sub-micrometer level. For that purpose, quasi in situ µ-DIC in conjunction with EBSD mapping was performed. In order to achieve a high resolution DIC map of a statistically relevant large sample area, panoramic imaging was used. For panoramic imaging, 56 individual images of 33.0µm by 24.8 µm and a magnification of 3.46 KX (7(rows) x 8(columns), with 20% overlap each) were captured and stitched together.

Fig. 4 (a) depicts the stitched panoramic image of the undeformed specimen. One of the individual images of which the panorama is composed of, is shown in Fig. 4(b) and (c) displays the SiO_2 nanoparticle speckles on the sample surface.

The deformed microstructure of the same sample area as shown in Fig. 4 (a) after 4% global straining at 170 °C is shown in Fig. 5(a) and (b). The unit cells in Fig. 5 (a) indicate the orientation of the α-Mg matrix. Basal slip lines (highlighted by white arrows in Fig. 5 (b)) and tensile deformation twins (highlighted by yellow arrows in Fig. 5 (b)) are observed in the deformed microstructure.

Fig. 6 shows a 2D von Mises strain map of the microstructural region given in Fig. 4 and Fig. 5. The map reveals highly heterogeneous strain at the sub-micron level in the microstructure. The strain tends to concentrate (i) along basal slip traces (white arrows in Fig. 6), (ii) at deformation twins (yellow arrows), (iii) along α-Mg/Laves phase interfaces (black arrows), and (iv) in between the eutectic Laves phase lamellas (orange arrows). In the Laves phase, cracks are visible in the

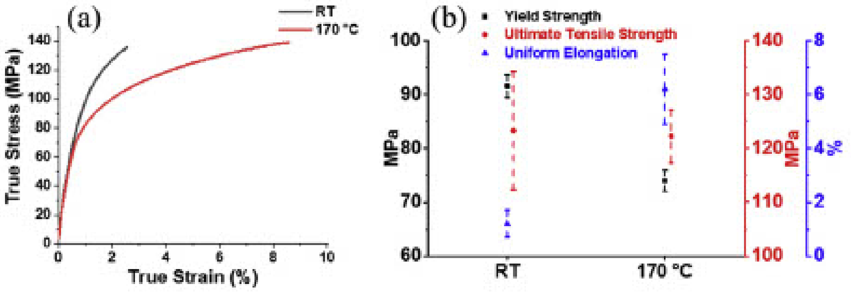

Fig. 3. (a) True stress-strain curve of the as-cast alloy deformed at RT and 170 °C, (b) Comparison of yield strength ($\sigma_{0.2}$), ultimate tensile strength and uniform elongation at RT and 170 °C.

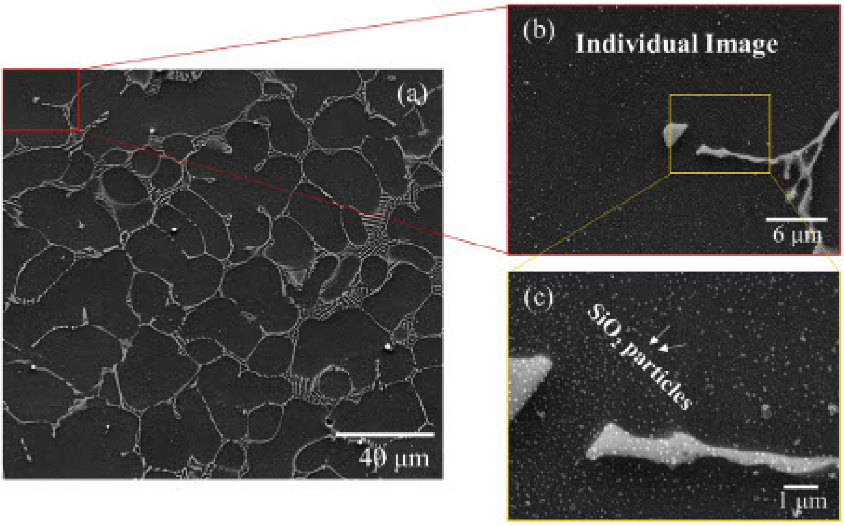

Fig. 4. (a) Un-deformed panoramic image, (b) one individual image of magnification 3.46 KX and (c) high magnification image showing the speckle patterns on the sample surface.

regions of high strain concentrations and intersections of slip traces and deformation twins with α-Mg/Laves phase interfaces (red arrows in Fig. 6). Subsequently, the sample was also deformed to 5.5% global strain, however, the strain map was similar to the one after 4% global strain with an increased surface topography limiting detailed microstructure observations and is therefore not shown.

The Euler number was used to describe the evolution of the connectivity of the Laves phase skeleton during deformation. For this purpose, the Laves phase network before and after deformation was first segmented, where each segment represents an interconnected Laves phase structure, Fig. 7. The different colours correspond to different Laves phase segments.

From Fig. 7 it is evident that deformation leads to fragmentation of the Laves phase network visible as an increased number of Laves phase segments in the deformed microstructure and correspondingly quantified by an increased Euler number.

3.4. *Deformation and fracture behavior*

Fig. 8 (a) reveals the microstructure of the alloy after quasi in-situ deformation at 170 °C to 3% global strain. Fig. 8(b) and (c) depict magnified micrographs of a region undergoing basal slip and tensile twinning. Basal slip lines are highlighted by white arrows in Fig. 8(b and c). In addition to basal slip, traces of $(10\bar{1}1)$ pyramidal slip are observed and highlighted by blue arrows. Further, it can be seen that at the intersection points of basal slip traces in the α-Mg matrix with α-Mg/Laves phase interfaces, small cracks are formed. Some cracks are also visible at intersections of deformation twins with α-Mg/Laves phase interfaces. Fig. 8(d), (e) and (f) show the IPF and Schmid factor maps for basal slip and tensile twinning superimposed on BC maps. Basal slip and tensile twinning is indeed observed in grains with high Schmid factors for the corresponding deformation mechanisms, viz. basal slip and tensile twinning.

To verify that the formation of cracks observed at the sample surface during quasi in-situ deformation (Fig. 6 and Fig. 8) is not an artifact induced by the free surface of the sample, characterisation of the bulk of deformed samples was performed in addition to the quasi in-situ tests. As the sample was metallographically prepared after deformation, no slip traces are visible, but only deformation twins. Specifically, Fig. 9 (a) shows superimposed BC and IPF maps of the microstructure after deformation to 4% global strain at 170 °C and (b) shows cracks nucleating in the Laves phase at twin – α-Mg/Laves phase interfaces intersection points.

Micrographs of samples quasi in-situ deformed at 170 °C to 5% global strain are given in Fig. 10 (a) and (b). Cracks were observed to form at the intersection points of basal slip traces in the Mg matrix with α-Mg/Laves phase interfaces (Fig. 10 (c)) and at points where deformation twins transfer from the Mg matrix through the Laves phase (Fig. 10 (b)).

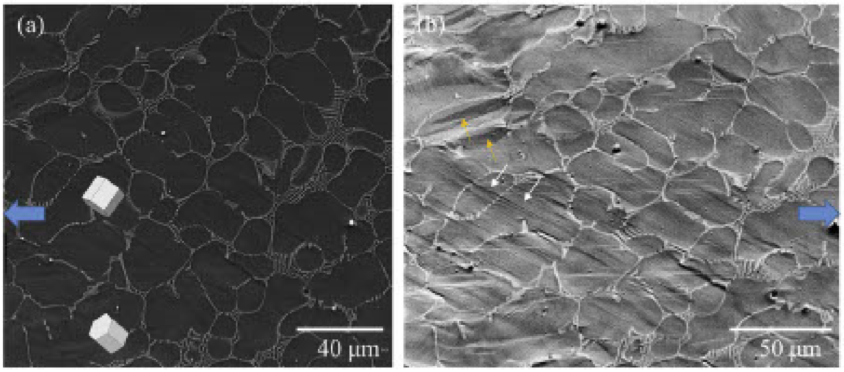

Fig. 5. (a) SE panoramic image of the same sample surface region (as shown in Fig. 4 (a)) after quasi in-situ straining to a global strain of 4% at 170 °C and (b) deformed image at a stage tilt of 70°. The blue arrows indicate the tensile direction, white arrows show slip lines and yellow arrows highlight twins. The unit cells in (a) show the orientation of the α-Mg matrix (determined from EBSD of deformed microstructural regions). (For interpretation of the references to colour in this figure legend, the reader is referred to the Web version of this article.)

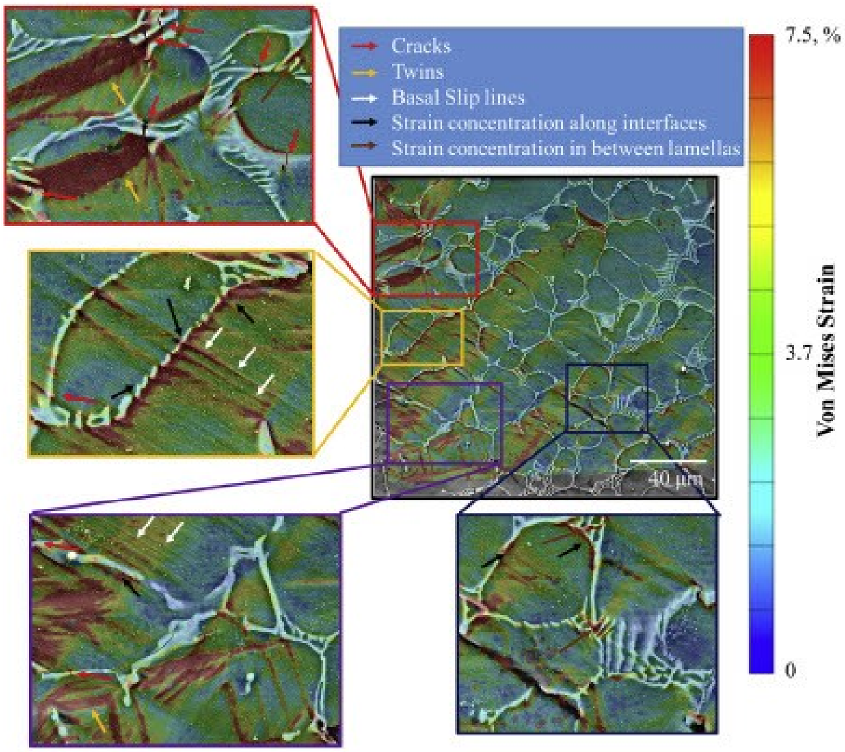

Fig. 6. Von Mises strain map (facet size: 0.55 μm, step size: 0.44 μm) of the deformed microstructure region depicted in Fig. 4. Laves phase cracks are marked in the insets with red arrows, twinned regions with yellow arrows, basal slip lines with white arrows, strain concentrations along α-Mg/Laves phase interfaces with black arrows and strain concentration in between the eutectic Laves lamellas with orange arrows. (For interpretation of the references to colour in this figure legend, the reader is referred to the Web version of this article.)

4. Discussion

4.1. Microstructure and mechanical properties

The microstructure of as-cast AX53 consists of the two phases α-Mg and $(Mg,Al)_2Ca$ Laves phase. Luo et al. [42] have shown that these commonly share an orientation relationship of (001)Mg//(001)$(Mg,Al)_2Ca$ and [010]Mg//[110]$(Mg,Al)_2Ca$. Similar microstructures were also observed before in other Mg–Al–Ca alloys [16,20,42]. The average dendrite cell is slightly lower and the area fraction of Laves phase slightly higher than the values reported for a similar Mg–Al–Ca alloy (with a Ca/Al ratio of 0.6) in our previous work [16]. On the other hand, the $\sigma_{0.2}$ and UTS of the present alloy at both temperatures (RT and 170 °C) are significantly higher. Specifically, the $\sigma_{0.2}$ at RT of the present alloy is 30% higher and the $\sigma_{0.2}$ at 170 °C is 26.5% higher, while the corresponding UTS values are 13.5% higher at RT and 21.7% higher at 170 °C. This is assumed to be due to different melting and casting conditions: the alloy investigated in the current study was molten and cast under 15 bar Ar pressure, whereas the one studied in [16] was molten and cast under ambient conditions. Melting and casting under 15 bar Ar pressure is assumed to cause a lower number of casting defects than at ambient conditions resulting in better mechanical properties.

4.2. Strain partitioning and localisation

As shown in Fig. 6, it is generally observed that the α-Mg grains carry most of the imposed strain, while the Laves phase does not

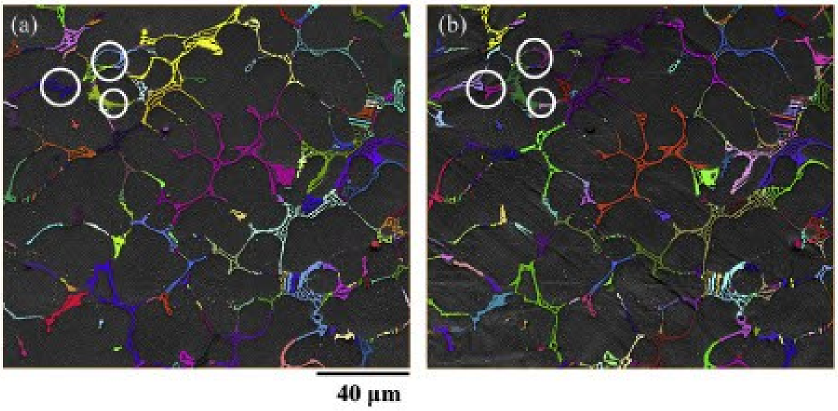

Fig. 7. Segmented Laves phase network (a) before deformation, Euler number: -1363, (b) after 4% global strain at 170 °C, Euler number: -594. White circles indicate fragmentation of the Laves phase network during deformation.

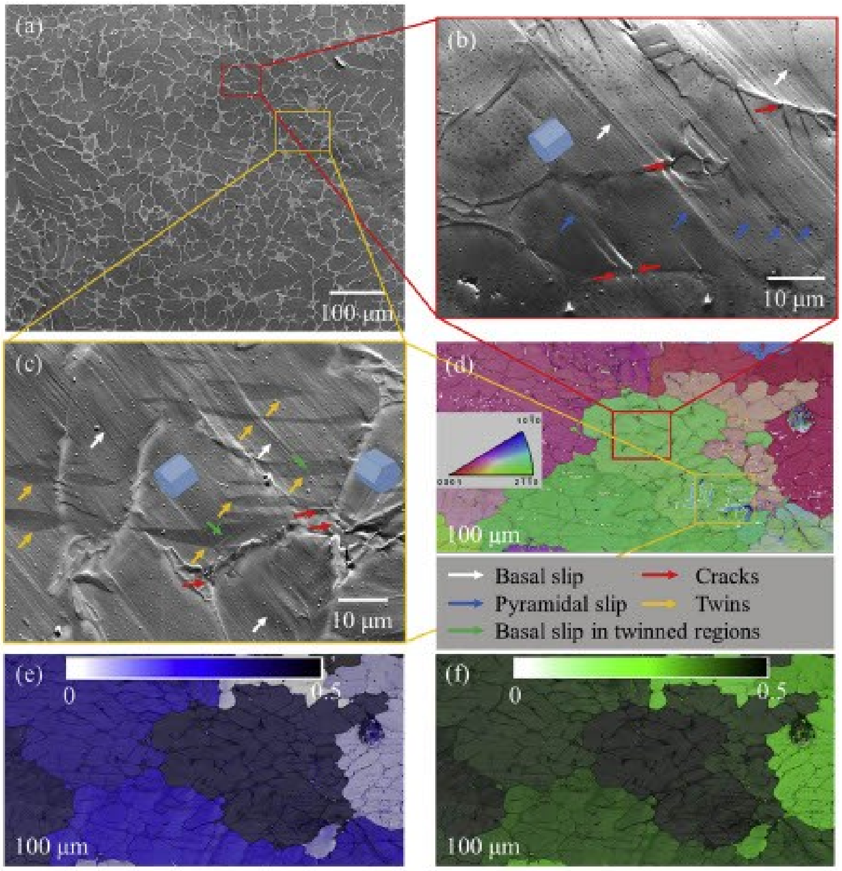

Fig. 8. (a) SE image of a sample after 3% global strain (quasi in-situ deformation) at 170 °C, (b) and (c) SE images of the regions highlighted by yellow and red boxes in (a) at a stage tilt of 70°. The α-Mg matrix orientation is depicted by the unit cells, white arrows highlight basal slip traces, red arrows cracks in the Laves phase, blue arrows $(10\bar{1}1)$ pyramidal slip, yellow arrows tensile deformation twins and green arrows basal slip lines in the twinned regions. (d) Superimposed IPF and BC maps, tensile twins are highlighted by white lines. (e) Schmid factor map for basal slip and (f) Schmid factor map for tensile twinning; the area shown in (e) and (f) is identical to the IPF map shown in (d). (For interpretation of the references to colour in this figure legend, the reader is referred to the Web version of this article.)

undergo a significant amount of plastic deformation. Specifically, von Mises strains of about 0.5–1.5% were observed, considerably lower than the applied global strain of 4%, Fig. 6. Further, strain localisation was observed i) along basal slip traces, ii) at deformation twins, iii) at α-Mg/Laves phase interfaces, and iv) in between the eutectic Laves phase lamellas. These can be categorized into two distinct types of strain localisation:

4.2.1. Type 1: Strain partitioning and localisation in the α-Mg matrix

The α-Mg matrix deforms mainly by basal slip and tensile twinning, Figs. 5, 8–10. It can be further seen in Fig. 6, that some grains carry high strain while other grains exhibit only relatively low strain levels.

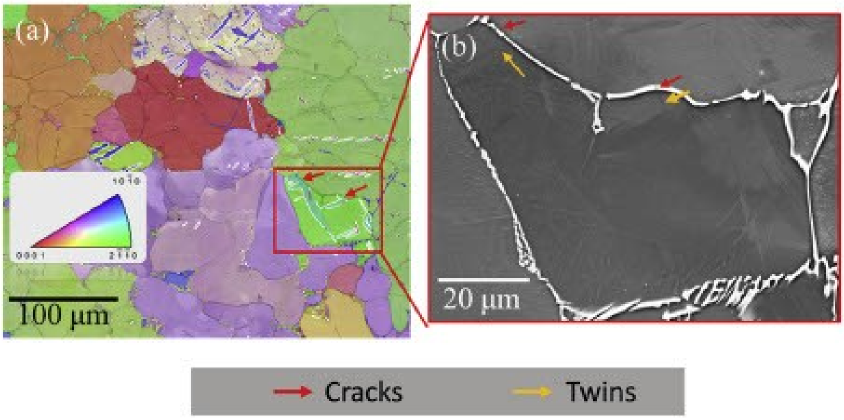

Fig. 9. (a) Superimposed IPF and BC maps from the bulk of a sample after 4% deformation at 170 °C, (b) SE image highlighting cracks at twin intersection points (red arrows) in the Laves phases of the sample shown in (a). (For interpretation of the references to colour in this figure legend, the reader is referred to the Web version of this article.)

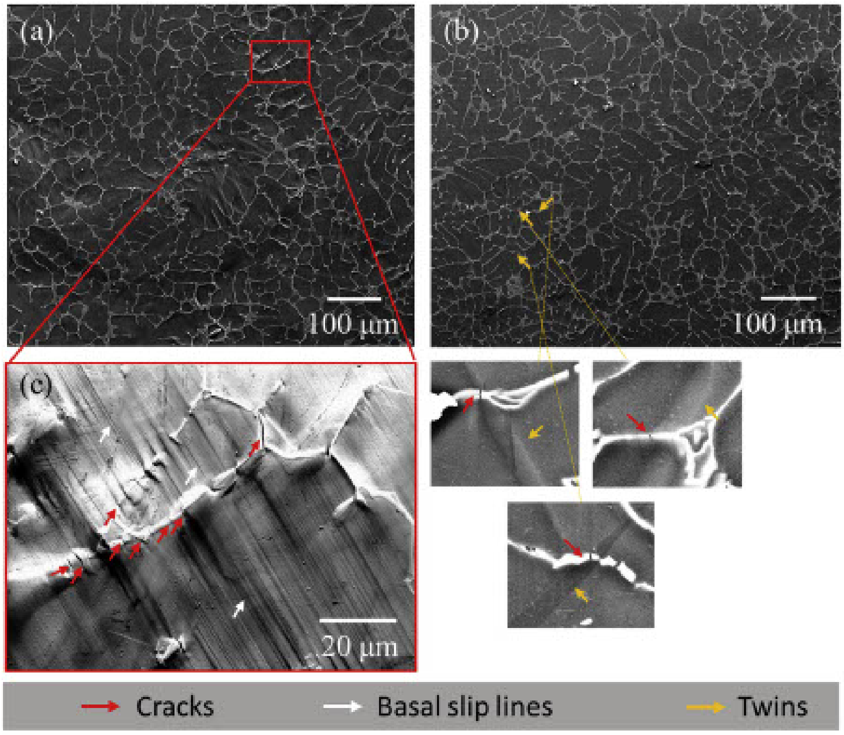

Fig. 10. (a) and (b) SE images of the sample at 5% global strain (quasi in-situ) at 170 °C, (c) depicts the SE image of the region in inset in (c) with stage tilted at 70° to the electron beam. Crack nucleation points in the Laves phase are shown by red arrows, basal slip lines as white arrows, yellow arrows in the magnified portion of (b) represent twins and red arrows depict cracks in the Laves phase. (For interpretation of the references to colour in this figure legend, the reader is referred to the Web version of this article.)

Strain localisation in those grains which carry high strain levels occurs preferentially along basal slip traces and tensile twins. This is assumed to be due to the different grain orientations and the plastic anisotropy of Mg. Specifically, in pure Mg, the critical resolved shear stresses (CRSS) for basal slip (~0.52 MPa [43]) and tensile twinning (2.4 MPa [44]) are low when compared to prismatic slip (≈20–39 MPa [45–47]) and pyramidal slip (≈44 MPa [46,48]). Although the exact CRSS values depend on temperature and composition, the trend of low CRSS for basal slip and tensile twinning and high CRSS for prismatic and pyramidal slip was reported for a huge number of Mg alloys in the temperature range RT-170 °C [47,49–51]. Consequently, only grains with a high Schmid factor for either basal < a > slip or tensile twinning, undergo significant amounts of deformation through slip and twinning (see Fig. 8). Therefore, strain localisation in α-Mg is proposed to be primarily dependent on the crystallographic orientations of the grains.

4.2.2. Type 2: Strain localisation along the α-Mg/Laves phase interface

In addition to strain concentrations in the α-Mg grains, strain localisation was observed along the α-Mg/Laves phase interfaces and in between the eutectic Laves phase lamellas, Fig. 6. As no preference regarding the crystallographic orientation and misorientation is observed, it is assumed that these strain localisations are caused by grain/phase boundary sliding during deformation at 170 °C. The occurrence of grain and phase boundary sliding during elevated temperature deformation and creep in Mg–Al–Ca alloys was also reported in our own previous work and by several other researchers [7,16,42,52]. This type of strain partitioning and localisation does not seem to have any geometrical or orientation dependence. However, higher strain accumulation are observed at interfaces adjacent to α-Mg grains that carry high strain, which is proposed to be caused by the higher amount of strain induced on the interface through larger deformation of the respective α-Mg grains.

4.3. Cracks and micro damage

In line with our previous work and the reports of other groups [10,16,53], crack nucleation was observed in the Laves phase in the present study. More detailed analysis based on quasi in-situ deformation experiments in the present study showed that these crack nucleation sites are not random but correspond to strain concentration sites, Fig. 6, mainly at the intersection points of basal slip traces and deformation twins with α-Mg/Laves phase interfaces. Similarly, Bieler et al. [54] showed that, in single phase materials, damage tends to nucleate at grain boundaries that are unfavorable for slip transmission. In many alloys, hard second phases or interfaces (between hard and soft phase) were reported to act as preferential damage nucleation sites [10,52,53,55–57]. The observation of preferred crack nucleation at slip band intersections with α-Mg/Laves phase interfaces, Fig. 8 (b) and Fig. 10 (c), indicate that stress concentrations are generated at the intersections due to the pile-up of dislocations. Dislocation pile-ups at the α-Mg/Laves phase interfaces are assumed to be prevalent as the hard Laves phase skeleton is considered as an effective obstacle to dislocation movement [9,19]. A more detailed large-scale analysis of the crack nucleation sites revealed that those microstructural regions where the α-Mg matrix carries a considerable amount of strain induced by dislocation slip and/or twinning contain also a high amount of cracks in the Laves phase. In contrast, those α-Mg grains that do not carry much strain, exhibit far fewer cracks. In Fig. 11 (a), cracks that developed during successive deformation are highlighted by yellow (slip intersections points), blue (twin intersection points) and orange circles (where no distinction between slip or twin intersection can be made). Fig. 11(b), (c) and (d) represent the IPF map and the Schmid factor maps for basal slip and tensile twinning superimposed on BC maps. It is evident from these micrographs that the α-Mg orientation determines the amount of cracks that formed during deformation. Specifically, grains with a high Schmid factor for basal slip or tensile twinning contain also a high number of cracks predominantly at intersections of slip lines and twins with α-Mg/Laves phase interfaces. Fig. 11 (e) also

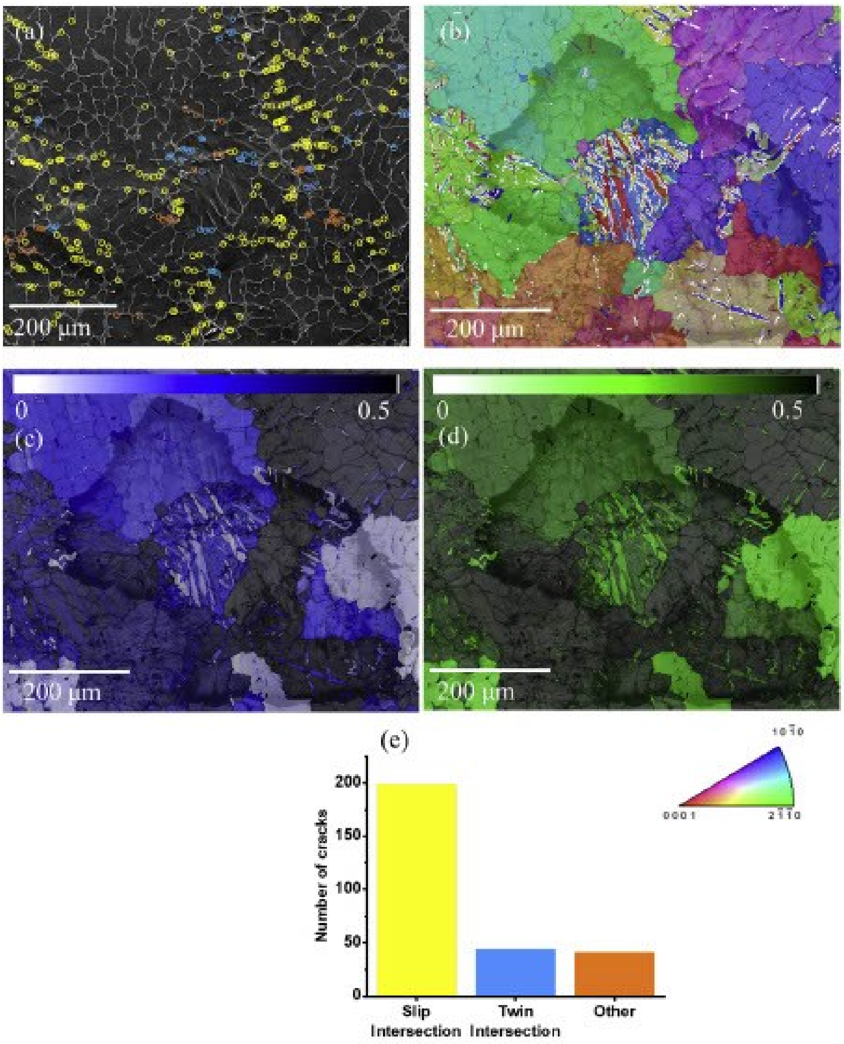

Fig. 11. (a) SE image of deformed microstructure after 5% global deformation at 170 °C, cracks at slip intersection points are highlighted by yellow circles, those at twin intersections by blue circles and others by orange circles, (b) Superimposed IPF and BC maps of approximately the same region shown in (a), tensile twin boundaries are highlighted by white lines. (c) Schmid factor map for basal slip and (d) Schmid factor map for tensile twinning; the area shown in (c) and (d) is identical to the IPF map shown in (b). (e) depicts the fraction of cracks appearing at slip band intersection (SI) and twin intersection (TI) with α-Mg/Laves phase interfaces, "others" are cracks which could not be related to a slip band – interface or twin – interface intersection. (For interpretation of the references to colour in this figure legend, the reader is referred to the Web version of this article.)

indicates that the number of cracks appearing at slip intersection points are much more than twin intersection points with α-Mg/Laves phase interfaces. This is primarily because the number of slip lines intersections is significantly higher than twin intersections as basal slip is the predominant deformation mechanism observed.

Similarly, crack nucleation at intersections of twins with grain boundaries and at twin boundaries was reported before for Mg and Ti alloys [58–60]. With continued straining, some of these cracks eventually grow preferentially along the Laves phase network and cause fracture of the material. Fig. 12 shows a micrograph of a sample deformed at 170 °C until fracture in which the crack causing failure propagated preferentially along the Laves phase network.

This means that a high connectivity of the Laves phase network provides a preferential crack growth path, while the α-Mg grains in loosely connected networks might cause crack blunting causing increased deformability. This is in agreement to our earlier work [16] where we showed that an Mg–Al–Ca alloy with a loosely connected Laves phase network (C/A 0.3) has a higher tensile elongation of 5.1% at 170 °C than an Mg–Al–Ca alloy with a highly connected Laves phase network (C/A 1.0) (tensile elongation of 3.6% at 170 °C). However, the $\sigma_{0.2}$ and the UTS of the alloy with the highly connected Laves phase network ($\sigma_{0.2} \approx 72$ MPa and UTS ≈ 113 MPa for alloy C/A 1.0) were

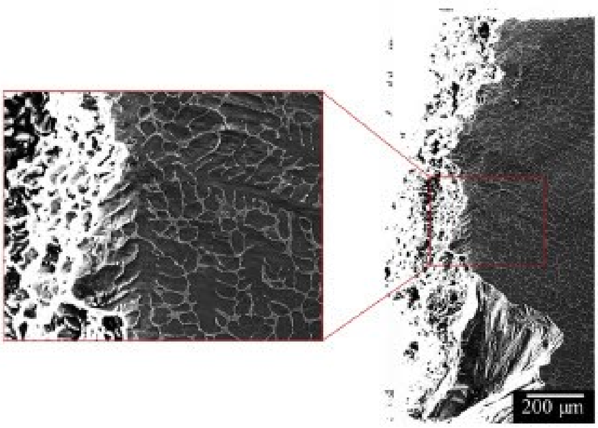

Fig. 12. Sample fracture surface (deformed at 170 °C), crack growth is observed to follow the Laves phase network.

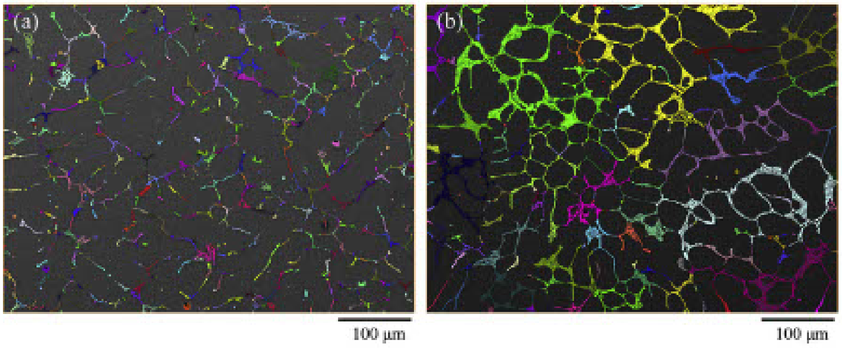

Fig. 13. (a) Segmented Laves phases of an Mg–Al–Ca alloy with a Ca/Al ratio of 0.3, Euler Number: 681 and (b) an Mg–Al–Ca alloy with a Ca/Al ratio of 1.0, Euler Number: -2811.

higher than those of the alloy with a loosely connected Laves phase network ($\sigma_{0.2} \approx 58$ and UTS ≈ 98 MPa for alloy C/A 0.3). Fig. 13 shows the Euler numbers of these two alloys revealing indeed the Euler number is lower for alloy C/A 1.0 than for alloy C/A 0.3. Similarly, it was shown in previous work that the Euler number of structures with high connectivity decreases and vice versa [36]. Kruglova et al. [36] showed for Al–Si alloys, that the Euler number can be effectively used to represent the connectivity of microstructural elements and reported that the strength of Al–Si alloys increased with decreasing Euler number, i.e. with higher connectivity of the intermetallic skeleton. Bugelnig et al. [61] showed that an increasing amount of Ni from 2 wt% to 3 wt% in an AlSi12Cu4Ni(2,3)Mg alloy increases the local connectivity, quantified by a more negative Euler number.

We therefore conclude that besides other microstructural parameters, such as crystal orientations, grain sizes, etc., the morphology and connectivity of the Laves phase network determines the mechanical properties of dual-phase Mg–Al–Ca alloys. Specifically, a highly connected Laves network is increasing the strength and also creep resistance on the one hand, but acts as preferential crack growth path reducing the formability of the alloy on the other hand. Therefore, for application of such alloys a compromise between (i) strength and creep resistance and (ii) ability to accommodate mechanical loads by plastic deformation has to be made. Further, as most of the cracks in the Laves phase are induced by strong slip localisation in the α-Mg phase, it is suggested that texture engineering to decrease the activation of basal slip might be used to design materials with a lower number of potential crack nucleation sites.

5. Conclusions

We draw the following conclusions from this study:

1. A considerable amount of strain partitioning and localisation was observed at the microstructure level during elevated temperature tensile deformation using quasi in-situ tests with µ-DIC and:
   a. the strain is mainly concentrated in α-Mg grains with a high Schmid factor for basal slip or tensile twinning.
   b. strain localisations are further observed at the intersections of basal slip lines and deformation twins with α-Mg/Laves phase interfaces.
2. Quasi in-situ and bulk material analysis showed the initiation of micro damage in the Laves phase at the sites of maximum strain localisations, namely:
   a. intersections of slip lines in the α-Mg matrix with α-Mg/Laves phase interfaces.
   b. intersections of deformation twins with α-Mg/Laves phase interfaces and where deformation twins transfer across α-Mg/Laves phase interfaces.
3. Crack growth at large strains occurs preferentially along the Laves phase network.
4. The morphology and connectivity of the Laves phase network in Mg–Al–Ca alloys affect the mechanical properties: a high Laves phase connectivity causes high strength and creep resistance, but a low tensile ductility. On the other hand, microstructures with loosely connected Laves phase networks display low strength and creep resistance but higher tensile deformability.

Data availability

The data used in this study is also a part of the ongoing research work and therefore we cannot share (at this time) the raw or processed data to reproduce the findings.

Acknowledgments

M. Zubair gratefully acknowledges the financial support from the University of Engineering and Technology, Lahore Pakistan. S. Korte-Kerzel and C. F. Kusche are grateful to the German Research Foundation (DFG) for funding project B2 within the Collaborative Research Center TRR 188. Further, we are also very thankful to our colleagues, Mr. David Beckers, Mr. Thomas Burlet, Mr. Risheng Pei, Mr. Gerhard Schutz and Mr. Arndt Ziemons (alphabetic order) at the Institute for Physical Metallurgy and Materials Physics, RWTH Aachen for their help at various steps in this study.

References

[1] A.P. Mouritz, Magnesium alloys for aerospace structures, in: A.P. Mouritz (Ed.), Introduction to Aerospace Materials, Woodhead Publishing Limited, 2012, pp. 224–231.
[2] B.R. Powell, P.E. Krajewski, A.A. Luo, Magnesium alloys for lightweight powertrains and automotive structures, in: P.K. Mallick (Ed.), Materials, Design and Manufacturing for Lightweight Vehicles, Woodhead Publishing Limited, 2010, pp. 114–173.
[3] Z. Wei-chao, L.I. Shuang-shou, T. Bin, Microstructure and properties of Mg-Al binary alloys, China Foundry 3 (4) (2006) 270–274.
[4] B. Kondori, R. Mahmudi, Effect of Ca additions on the microstructure, thermal stability and mechanical properties of a cast AM60 magnesium alloy, Mater. Sci. Eng. A Struct. Mater. Prop. Microstruct. Process. 527 (7–8) (2010) 2014–2021.
[5] A.A. Kaya, Physical metallurgy of magnesium, in: M.O. Pekguleryuz, K.U. Kainer, A.A. Kaya (Eds.), Fundamentals of Magnesium Alloy Metallurgy, Woodhead Publishing Limited, 2013, pp. 33–84.
[6] H.N. Mathur, V. Maier-Kiener, S. Korte-Kerzel, Deformation in the γ-$Mg_{17}Al_{12}$ phase at 25–278 °C, Acta Mater. 113 (2016) 221–229.
[7] Y. Nakaura, A. Watanabe, K. Ohori, Effects of Ca,Sr additions on properties of Mg-Al based alloys, Mater. Trans. 47 (4) (2006) 1031–1039.
[8] B. Kondori, R. Mahmudi, Effect of Ca additions on the microstructure and creep properties of a cast Mg–Al–Mn magnesium alloy, Mater. Sci. Eng. A 700 (2017) 438–447.
[9] D. Amberger, P. Eisenlohr, M. Goken, Microstructural evolution during creep of Ca-containing AZ91, Mater. Sci. Eng. A Struct. Mater. Prop. Microstruct. Process. 510–11 (2009) 398–402.

[10] D. Amberger, P. Eisenlohr, M. Goken, On the importance of a connected hard-phase skeleton for the creep resistance of Mg alloys, Acta Mater. 60 (5) (2012) 2277–2289.

[11] Y. Terada, et al., A thousandfold creep strengthening by Ca addition in die-cast AM50 magnesium alloy, Metall. Mater. Trans. A 35A (2004) 4.

[12] Z.T. Li, et al., Effect of Ca/Al ratio on microstructure and mechanical properties of Mg-Al-Ca-Mn alloys, Mater. Sci. Eng. A Struct. Mater. Prop. Microstruct. Process. 682 (2017) 423–432.

[13] Y. Chai, et al., Role of Al content on the microstructure, texture and mechanical properties of Mg-3.5Ca based alloys, Mater. Sci. Eng. A 730 (2018) 303–316.

[14] L. Zhang, et al., Microstructures and mechanical properties of Mg–Al–Ca alloysaffected by Ca/Al ratio, Mater. Sci. Eng. A 636 (2015) 279–288.

[15] A. Suzuki, et al., Solidification paths and eutectic intermetallic phases in Mg–Al–Ca ternary alloys, Acta Mater. 53 (2005) 2823–2834.

[16] M. Zubair, et al., On the role of Laves phases on the mechanical properties of Mg-Al-Ca alloys, Mater. Sci. Eng. A 756 (2019) 272–283.

[17] L.L. Rokhlin, et al., Calcium-alloyed magnesium alloys, Met. Sci. Heat Treat. 51 (3–4) (2009) 164–169.

[18] H.X. Wang, et al., Microstructure and properties of Mg-Al binary alloys, Rare Metal Mater. Eng. 37 (11) (2008) 2004–2007.

[19] C. Zehnder, et al., Plastic deformation of single crystalline C14 Mg_2Ca Laves phase at room temperature, Mater. Sci. Eng. A 759 (2019) 754–761.

[20] N.D. Saddock, et al., Grain-scale creep processes in Mg–Al–Ca base alloys: implications for alloy design, Scr. Mater. 63 (7) (2010) 692–697.

[21] A. Dutta, et al., Strain partitioning and strain localization in medium manganese steels measured by in situ microscopic digital image correlation, Materialia 5 (2019).

[22] C.C. Tasan, et al., Integrated experimental–simulation analysis of stress and strain partitioning in multiphase alloys, Acta Mater. 81 (2014) 386–400.

[23] P. Gao, et al., Characterization and analysis of strain heterogeneity at grain-scale of titanium alloy with tri-modal microstructure during tensile deformation, Materials 11 (11) (2018) 2194.

[24] D. Yan, C.C. Tasan, D. Raabe, High resolution in situ mapping of microstrain and microstructure evolution reveals damage resistance criteria in dual phase steels, Acta Mater. 96 (2015) 399–409.

[25] S. Amini, R.S. Kumar, A high-fidelity strain-mapping framework using digital image correlation, Mater. Sci. Eng. A 594 (2014) 394–403.

[26] Z. Li, et al., Damage investigation in A319 aluminum alloy by digital image correlation during in-situ tensile tests, Procedia Struct. Integr. 2 (2016) 3415–3422.

[27] H. Halim, D. Wilkinson, M. Niewczas, The Portevin–Le Chatelier (PLC) effect and shear band formation in an AA5754 alloy, Acta Mater. 55 (12) (2007) 4151–4160.

[28] D.A.F.J. Quinta, P.M. Mummery, P.J. Withers, Full-field strain mapping by optical correlation of micrographs acquired during deformation, J. Microsc. 218 (Pt 1) (2005) 9–21.

[29] F. Di Gioacchino, J. Quinta da Fonseca, Plastic strain mapping with sub-micron resolution using digital image correlation, Exp. Mech. 53 (5) (2013) 743–754.

[30] B. Pan, et al., Two-dimensional digital image correlation for in-plane displacement and strain measurement: a review, Meas. Sci. Technol. 20 (6) (2009).

[31] M.A. Tschopp, et al., Microstructure-dependent local strain behavior in polycrystals through in-situ scanning electron microscope tensile experiments, Metall. Mater. Trans. A 40 (10) (2009) 2363–2368.

[32] A.D. Kammers, S. Daly, Self-assembled nanoparticle surface patterning for improved digital image correlation in a scanning electron microscope, Exp. Mech. 53 (8) (2013) 1333–1341.

[33] F. Di Gioacchino, J. Quinta da Fonseca, An experimental study of the polycrystalline plasticity of austenitic stainless steel, Int. J. Plast. 74 (2015) 92–109.

[34] T.E.J. Edwards, et al., Longitudinal twinning in a TiAl alloy at high temperature by in situ microcompression, Acta Mater. 148 (2018) 202–215.

[35] Z. Wu, et al., Local mechanical properties and plasticity mechanisms in a Zn-Al eutectic alloy, Mater. Des. 157 (2018) 337–350.

[36] A. Kruglova, et al., 3D connectivity of eutectic Si as a key property defining strength of Al–Si alloys, Comput. Mater. Sci. 120 (2016) 99–107.

[37] **Image composite editor, Available from:** https://www.microsoft.com/en-us/research/product/computational-photography-applications/image-composite-editor/.

[38] D.B. Aydogan, J. Hyttinen, Characterization of microstructures using contour tree connectivity for fluid flow analysis, J. R. Soc. Interface 11 (95) (2014) 20131042.

[39] C.-N. Lee, T. Poston, Winding and Euler numbers for 2D and 3D digital images, Graph. Model. Image Process. 53 (6) (1991) 522–537.

[40] B. Jing, et al., Microstructure and tensile creep behavior of Mg–4Al based magnesium alloys with alkaline-earth elements Sr and Ca additions, Mater. Sci. Eng. A 419 (2006) 181–188.

[41] M.O. Pekguleryuz, A.A. Kaya, Creep resistant magnesium alloys for powertrain applications, Adv. Eng. Mater. 5 (12) (2003) 866–878.

[42] A.A. Luo, M.P. Balogh, B.R. Powell, Creep and microstructure of magnesium-aluminum-calcium based alloys, Metall. Mater. Trans. A Phys. Metall. Mater. Sci. 33 (3) (2002) 567–574.

[43] H. Conrad, W.D. Robertson, Effect of temperature on the flow stress and strain-hardening coefficient of magnesium single crystals, J. Occup. Med. 9 (4) (1957) 503–512.

[44] Q. Yu, J. Zhang, Y. Jiang, Direct observation of twinning–detwinning–retwinning on magnesium single crystal subjected to strain-controlled cyclic tension-compression in [0 0 0 1] direction, Philos. Mag. Lett. 91 (12) (2011) 757–765.

[45] R.E. Reed-Hill, W.D. Robertson, Deformation of magnesium single crystals by nonbasal slip, J. Occup. Med. 9 (4) (1957) 496–502.

[46] R. Sánchez-Martín, et al., Measuring the critical resolved shear stresses in Mg alloys by instrumented nanoindentation, Acta Mater. 71 (2014) 283–292.

[47] A. Chapuis, J.H. Driver, Temperature dependency of slip and twinning in plane strain compressed magnesium single crystals, Acta Mater. 59 (5) (2011) 1986–1994.

[48] C.M. Byer, et al., Microcompression of single-crystal magnesium, Scr. Mater. 62 (8) (2010) 536–539.

[49] S. Miura, et al., Deformation behavior of Mg alloy single crystals at various temperatures, Mater. Sci. Forum 350–351 (2000) 183–190.

[50] N. Stanford, M.R. Barnett, Solute strengthening of prismatic slip, basal slip and twinning in Mg and Mg–Zn binary alloys, Int. J. Plast. 47 (2013) 165–181.

[51] C.J. Boehlert, et al., In situ analysis of the tensile deformation mechanisms in extruded Mg–1Mn–1Nd (wt%), Philos. Mag. 93 (6) (2013) 598–617.

[52] G. Zhang, et al., Creep resistance of as-cast Mg-5Al-5Ca-2Sn alloy, China Foundry 14 (4) (2017) 265–271.

[53] S.W. Xu, et al., High temperature tensile properties of as-cast Mg–Al–Ca alloys, Mater. Sci. Eng. A 509 (2009) 105–110.

[54] T.R. Bieler, et al., The role of heterogeneous deformation on damage nucleation at grain boundaries in single phase metals, Int. J. Plast. 25 (9) (2009) 1655–1683.

[55] G. Avramovic-Cingara, et al., Void nucleation and growth in dual-phase steel 600 during uniaxial tensile testing, Metall. Mater. Trans. A 40 (13) (2009) 3117–3127.

[56] N. Pathak, et al., Damage evolution in complex-phase and dual-phase steels during edge stretching, Materials 10 (4) (2017).

[57] C. Kusche, et al., Large-area, high-resolution characterisation and classification of damage mechanisms in dual-phase steel using deep learning, PLoS One 14 (5) (2019) e0216493.

[58] F. Yang, et al., Crack initiation mechanism of extruded AZ31 magnesium alloy in the very high cycle fatigue regime, Mater. Sci. Eng. A 491 (1–2) (2008) 131–136.

[59] T.R. Bieler, et al., Strain heterogeneity and damage nucleation at grain boundaries during monotonic deformation in commercial purity titanium, J. Occup. Med. 61 (12) (2009) 45–52.

[60] B.C. Ng, et al., The role of mechanical twinning on microcrack nucleation and crack propagation in a near-γ TiAl alloy, Intermetallics 12 (12) (2004) 1317–1323.

[61] K. Bugelnig, et al., Revealing the effect of local connectivity of rigid phases during deformation at high temperature of cast AlSi12Cu4Ni(2,3)Mg alloys, Materials 11 (8) (2018).

7. Research Publication 3 – Exploring the transfer of plasticity across Laves phase interfaces in a dual phase magnesium alloy

J. Guénolé**, M. Zubair,** S. Roy**,** Z. Xie**,** M. Lipińska-Chwałek**,** S. Sandlöbes-Haut**,** S. Korte-Kerzel, Exploring the transfer of plasticity across Laves phase interfaces in a dual phase magnesium alloy, Materials and Design, 202 (2021) 109572.

The paper presents the experimental and theoretical evidence of the plastic deformation of Laves phase bounded in soft Mg matrix. Quasi in-situ deformation analysis in SEM, EBSD, site specific electron transparent specimen preparation and its analysis in TEM are used to unravel the deformation mechanisms of matrix and the Laves phase. Further, atomistic simulations are used in detail and provide suitable evidence of strain transfer from soft to hard phases across Mg/Mg_2Ca interfaces. The manuscript, therefore, address the 4th and 5th research question laid down in the section 1.1.

Materials and Design 202 (2021) 109572

Contents lists available at ScienceDirect

Materials and Design

journal homepage: www.elsevier.com/locate/matdes

Exploring the transfer of plasticity across Laves phase interfaces in a dual phase magnesium alloy

Julien Guénolé [a,b,c,*], Muhammad Zubair [a,d], Swagata Roy [a], Zhuocheng Xie [a], Marta Lipińska-Chwałek [e,f], Stefanie Sandlöbes-Haut [a], Sandra Korte-Kerzel [a]

[a] Institute of Physical Metallurgy and Materials Physics, RWTH Aachen University, 52056 Aachen, Germany
[b] Université de Lorraine, CNRS, Arts et Métiers ParisTech, LEM3, 57070 Metz, France
[c] Labex Damas, Université de Lorraine, 57070 Metz, France
[d] Department of Metallurgical and Materials Engineering, G.T Road, UET, Lahore, Pakistan
[e] Central Facility for Electron Microscopy, RWTH Aachen University, 52074 Aachen, Germany
[f] Ernst Ruska-Centre for Microscopy and Spectroscopy with Electrons, Forschungszentrum Jülich GmbH, 52425 Jülich, Germany

HIGHLIGHTS

- Co-deformation of Mg-Laves phase composites shows cracking, slip deformation and interfacial sliding.
- The active co-deformation mechanism depends on the interfacial orientation.
- Slip transfer into the Laves phase occurs on prismatic and basal planes.
- Interfacial sliding is favoured by matrix dislocations absorbed at the interface.

GRAPHICAL ABSTRACT

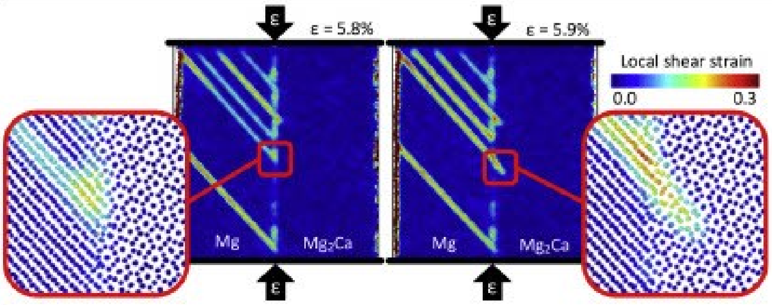

ARTICLE INFO

Article history:
Received 30 November 2020
Received in revised form 4 February 2021
Accepted 6 February 2021
Available online 09 February 2021

Keywords:
Dislocation
Intermetallic
Atomistic simulations
Indentation
Scanning electron microscopy

ABSTRACT

The mechanical behaviour of Mg—Al alloys can be largely improved by the formation of an intermetallic Laves phase skeleton, in particular the creep strength. Recent nanomechanical studies revealed plasticity by dislocation glide in the $(Mg,Al)_2Ca$ Laves phase, even at room temperature. As strengthening skeleton, this phase remains, however, brittle at low temperature. In this work, we present experimental evidence of slip transfer from the Mg matrix to the $(Mg,Al)_2Ca$ skeleton at room temperature and explore associated mechanisms by means of atomistic simulations. We identify two possible mechanisms for transferring Mg basal slip into Laves phases depending on the crystallographic orientation: a direct and an indirect slip transfer triggered by full and partial dislocations, respectively. Our experimental and numerical observations also highlight the importance of interfacial sliding that can prevent the transfer of the plasticity from one phase to the other.

© 2021 The Authors. Published by Elsevier Ltd. This is an open access article under the CC BY license (http://creativecommons.org/licenses/by/4.0/).

1. Introduction

The mechanical response of composite materials is dependent on the properties of their different phases individually, but also largely on the properties of their interfaces. Lightweight Mg-based composites with a controlled proportion of Al and Ca can be strengthened by the precipitation of a Laves phases skeleton [1]. The reinforcement potential

---

* Corresponding author at: Université de Lorraine, CNRS, Arts et Métiers ParisTech, LEM3, 57070 Metz, France.
E-mail address: julien.guenole@univ-lorraine.fr (J. Guénolé).

https://doi.org/10.1016/j.matdes.2021.109572
0264-1275/© 2021 The Authors. Published by Elsevier Ltd. This is an open access article under the CC BY license (http://creativecommons.org/licenses/by/4.0/).

of Laves phases in these alloys is primarily due to their high strength compared to the matrix phase [2]. Laves phases are hard intermetallic phases with a topologically close packed structure arranged in a cubic (C15) or hexagonal (C14 and C36) unit cell [3,4]. The mechanical response of such a dual phase microstructure typically shows plasticity in the Mg matrix and fracture in the hard-intermetallic phase [1,5]. While effectively strengthening the composite, the brittleness of the Laves phase limits the maximum strength and the formability of the composite.

Plasticity in hexagonal Mg-based Laves phases has been observed experimentally at room temperature by means of nano-mechanical testing [2]. In particular, Mg_2Ca (C14) micro-pillar compression revealed the activation of basal, prismatic and pyramidal slip systems [2]. Additionally, atomistic simulations with the same phase confirmed that synchroshear dislocations are activated for basal slip [6]. To our best knowledge, one study investigated the properties of interfaces in the similar Mg-Zn_2Mg composites [7], and none investigated the transfer of plasticity from the matrix to the Laves phase.

Different Laves phases exhibit different dislocation pinning characteristics as observed for Laves phase reinforced Ti alloys [8]. In case of Mg alloys, Laves phases and their interfaces are strong obstacles for dislocation motion, making Mg alloys containing Laves phases well suited for high temperature applications in which creep resistance is required [9]. However, a lack of slip transfer from α-Mg to Laves phases also results in limited plasticity as displayed by the low ductility of these alloys at room and elevated temperatures [1]. Easier slip transfer is usually associated with more homogenous plastic flow [10] and in case of Mg-Al-Ca alloys, this would presumably result in better bulk plasticity at the expense of creep resistance. The knowledge of slip transfer mechanisms may thus prove essential in designing alloys with a tailored balance between ductility, strength and creep resistance.

Here, we explore the co-defomation of Laves phases with an α-Mg matrix by the combination of experimental and numerical approaches. The surface morphology of a deformed composite is analysed by scanning electron microscopy. Cracks and slip traces are characterized in both, the matrix and the Laves phase skeleton. In parallel, atomistic simulations are performed for a similar composite and several possible orientation relationships are investigated. Numerical nano-mechanical tests and controlled dislocation-interface interactions at the atomic scale enlighten the experimental results. Finally, we show mechanisms of transfer of plasticity from the Mg matrix to the Laves phase skeleton across the interface.

2. Experiments

A cast Mg-5.21Al-3.18Ca (wt%) alloy was prepared from raw materials consisting of pure Mg, Ca and Al. The raw materials were molten in an induction furnace and solidified under 15 bar Ar pressure in a steel crucible. The chemical composition was determined through wet chemical analysis.

The samples for microstructural examination were first ground using 4000 SiC emery paper, followed by mechanical polishing using 3 and 1 μm diamond suspension. The mechanically polished samples were then subjected to electrolytic polishing using the AC-II (Struers) electrolyte. Electro-polishing was carried out at ≤−20 °C, 15 V and for 60 s. Different electrochemical behaviour of the metallic and intermetallic phases resulted in the appearance of a waviness on the sample surface which was then removed by fine polishing with OPU (≈40 nm SiO_2 colloidal suspension). After fine polishing, the samples were cleaned in an ultrasonic bath followed by light pressing on gently rotating cleaning cloth containing ethanol as a cleaning agent/lubricant. The composition of the α-Mg matrix and intermetallic phase was determined with the aid of energy dispersive X-ray spectroscopy (EDS) performed at an accelerating voltage of 10 kV in SEM. This relatively low voltage was selected to limit the interaction volume.

Standard dog-bone shaped specimens with a gauge length of 10 mm were deformed in an electromechanical testing machine (ETM) at 170 °C in tensile mode at a constant strain rate of $5 \times 10^{-4}\,s^{-1}$. The specimens were later characterized in a scanning electron microscope (SEM; Zeiss LEO1530) using secondary electron (SE) imaging and electron backscatter diffraction (EBSD) after pre-determined deformation steps of 3 and 5%. An acceleration voltage of 20 kV was used for EBSD and 10–20 kV for SE imaging. The EBSD data were analysed using Channel 5 and Matlab 2018b software. A step size in between 0.25 and 0.7 μm was used for EBSD depending on the scanned area. Focussed Ion beam (FIB) milling (in FEI Helios Nanolab 600i) was used to prepare the site-specific electron transparent samples (FIB lamella) for investigations in transmission electron microscope (TEM). The FIB lamella cut plane was selected to be perpendicular to the polished surface of the bulk sample and to the tensile direction, as shown in Fig. 2. The orientation relationship between matrix and intermetallic phase and EDS analysis of their chemical composition were performed by TEM (FEI Tecnai G2 F20 [11]) at an accelerating voltage of 200 kV.

2.1. Experimental results

Fig. 1 represents an SE image taken from a sample deformed to 3% global strain. It can be seen in the figure that the microstructure consists of two phases, i.e. α- matrix reinforced with an intermetallic Laves phase skeleton. Note that grains are much larger than the cell size or, in other words, phase boundaries are not necessarily grain boundaries (See Supplementary material, Fig. SM1). As a consequence, to a scale far beyond that studied and presented in Fig. 1, the sample is a single crystal (See Supplementary material, Fig. SM2). A comparative observation before and after deformation at 170 °C reveals no modification in the morphology of the Laves phase network induced by, for example, the temperature (See Supplementary material, Fig. SM3).

The composition of the intermetallic phase as determined from EDS point analysis performed on the intermetallic phase (at 8 points in SEM) is presented in the Table 1. The EDS point analysis confirms the presence of all three elements in significant quantities in the Laves phase and is considered to be C36 ($(Mg,Al)_2Ca$) phase. Similar compositions for C36 Laves phase via EDS have also been reported earlier [12,13]. The α-Mg matrix composition was measured at three (3) different points [22]. Further, EDS was also performed in TEM (to measure the Laves phase separately from the matrix) and the results for both phases present in TEM lamella (shown in Fig. 2) are given in Table 1.

Moreover, an EDS area scan was performed in the SEM on the same alloy and is presented in the supplementary data (Fig. SM4). From this figure, it is clear that the alloying elements are mainly concentrated in the intermetallic phase. There is negligible amount of Ca in the α-Mg matrix (Table 1) because of limited solubility of Ca in α-Mg [14].

As can be seen from the comparison of the compositions determined from EDS in SEM and TEM (see), the influence of the matrix is diminished in case of EDS in TEM. However, there still is a considerable amount of Mg present in the intermetallic phase showing that it is indeed C36 Laves phase. This argument is further validated from the respective SAED pattern shown in Fig. 2(e).

The same intermetallic phase was also reported by several other researchers in similar alloys, i.e. Suzuki et al. [15] in the Mg-5Al-3Ca alloy and by Luo et al. [16] in AC53 (Mg-4.5Al-3Ca-0.27Mn) alloy. They used TEM to confirm their results. In our results, slip lines in the matrix phase are clearly visible and highlighted by blue arrows. Using EBSD-assisted slip line analysis, these slip lines were identified as basal slip traces in the α-Mg matrix. At points where the slip lines interact with the $(Mg,Al)_2Ca$ (C36) Laves phase, cracks in the C36 phase can be observed. This is in agreement with our earlier work [1].

Fig. 2 reveal co-deformation of the α-Mg matrix and the intermetallic C36 Laves phase in the sample deformed to 5% global tensile strain at ≈170 °C. The slip lines in the α-Mg and C36 phases are highlighted with blue and orange arrows, respectively. Unfortunately, it was very difficult

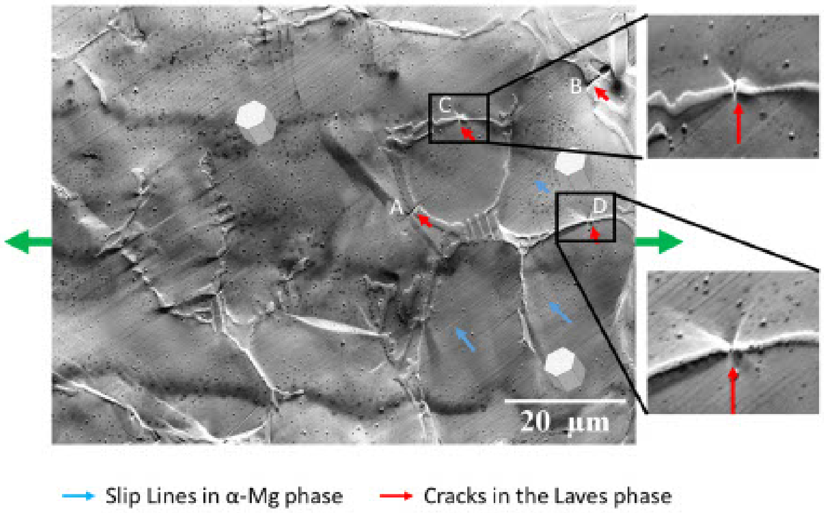

Fig. 1. SE image (with the stage tilted 70° towards the electron beam, image tilt-corrected) of a sample deformed to 3% at 170 °C. Green arrows represent the direction of the applied force, blue arrows show basal slip lines in the α-Mg phase and red arrows indicate cracks in the Laves phase. The insets show the magnified images of the cracks in the C36 phase which are perpendicular to the loading direction at points C and D. Unit cells depict the orientation of α-Mg matrix. (For interpretation of the references to colour in this figure legend, the reader is referred to the web version of this article.)

Table 1
Composition of intermetallic and matrix phases as determined from EDS in SEM and TEM.

Microscope		Mg (at. %)	Al (at. %)	Ca (at. %)	Remarks
SEM	Intermetallic phase	49.7 ± 11.3	31 ± 6.4	19.3 ± 4.9	C36 phase
SEM	α-Mg matrix	98.3	1.7	–	Solid solution
TEM	Intermetallic phase	25.5 ± 3.8	45.5 ± 4.1	29.0 ± 3.2	C36 phase
TEM	α-Mg matrix	98.2 ± 0.5	1.7 ± 0.4	0.14 ± 0.07	Solid solution

to analyse the orientation of the C36 Laves phase from EBSD data. This is primarily because of the small size of the intermetallic phase in comparison to the α-Mg matrix and also their structural similarity with the hexagonal Mg matrix. Therefore, a detailed TEM analysis was performed on the FIB lamella lifted out of the material volume indicated in Fig. 2(b) with white dotted rectangle. TEM investigations yielded information about the orientation relationship between the Mg matrix and the C36 Laves phase and confirmed the presence of a basal slip deformation mode in the Laves phase. Fig. 2(c–g) shows microstructure details of the deformed material, as observed with the aid of TEM. Planar defects corresponding to the basal slip events were observed in α-Mg matrix, as well as in the intermetallic phase. In particular, bright field (BF) TEM images in Fig. 2(d) and (f) show basal slip planar defects in either phase observed in edge-on orientation (i.e. slip plane is parallel to the viewing direction). Accordingly, planar defects have appearance of thin lines passing diagonally the BF images (indicated with blue arrows in α-Mg matrix (d) and with orange arrows in the Laves phase (f)). In either case, the observation direction is parallel to the respective $\left[2\,\bar{1}\,\bar{1}\,0\right]$ crystallographic direction. Corresponding SAED patterns are given in Fig. 2(e) and (g), respectively. It is worth to note, however, that different sample orientations were required for $\left[2\,\bar{1}\,\bar{1}\,0\right]$ zone orientations of each phase. A detailed analysis of the crystallographic orientation relationship between α-Mg matrix and the Laves phase revealed that basal planes of both phases are almost perpendicular to each other ($\measuredangle[0\ 0\ 0\ 1]_{Mg}, [0\ 0\ 0\ 1]_{C36} = 79^{\circ}$ and $\measuredangle\left[2\,\bar{1}\,\bar{1}\,0\right]_{Mg}, \left[1\,0\,\bar{1}\,0\right]_{C36} = 8^{\circ}$). Similar ORs ($\measuredangle[0\,0\,0\,1]_{Mg}, [0\,0\,0\,1]_{C36} = 82^{\circ} \pm 10^{\circ}$) were systematically observed also for different FIB lamellas cut out of other sample grains (not described here), indicating the tendency of the composite alloy to adopt a preferential crystallographic orientation relationship, with basal planes of constituent hexagonal phases being almost perpendicular to each other.

2.2. Discussion on the experiments

It can be observed in Fig. 1 that the cracks in the C36 Laves phase occur at points where slip lines in the α-Mg matrix interact with the Laves phase. Further, it can be seen in Fig. 1 that the cracks at points A and B are oriented around 45–50° to the globally applied tensile stress direction. Moreover, these cracks in the C36 phase are almost parallel to the basal slip lines in the α-Mg matrix. This indicates that the cracks are developed due to the shearing of the C36 Laves phase by basal slip in the α-Mg matrix. On the other hand, the cracks at points C and D (as can be seen enlarged in the insets of Fig. 1) are almost perpendicular to the applied stress direction and correspond probably to brittle fracture of the C36 phase. Fig. 2, on the other hand, shows an event where plastic flow is actually transmitted from the α-Mg matrix into the Laves phase. Basal defect structures are indeed observable in the BF TEM micrographs of both phases, represented in Fig. 2 (d and f). This suggests that in addition to α-Mg matrix, the intermetallic Laves phase (C36) is indeed plastically deformable at length scales present in the as-cast Mg-5.21Al-3.18Ca alloy. The α-Mg matrix offers significantly lower resistance to dislocations movement as compared to the Laves phases. Specifically, the critical resolved shear stress (CRSS) values for basal, prismatic and pyramidal slip in Mg amounts to ≈ 0.52 MPa [17], ≈ 39 MPa [18] and ≈44 MPa [19], respectively (as determined by macroscopic testing of pure Mg, except in case of [19] where the CRSS for

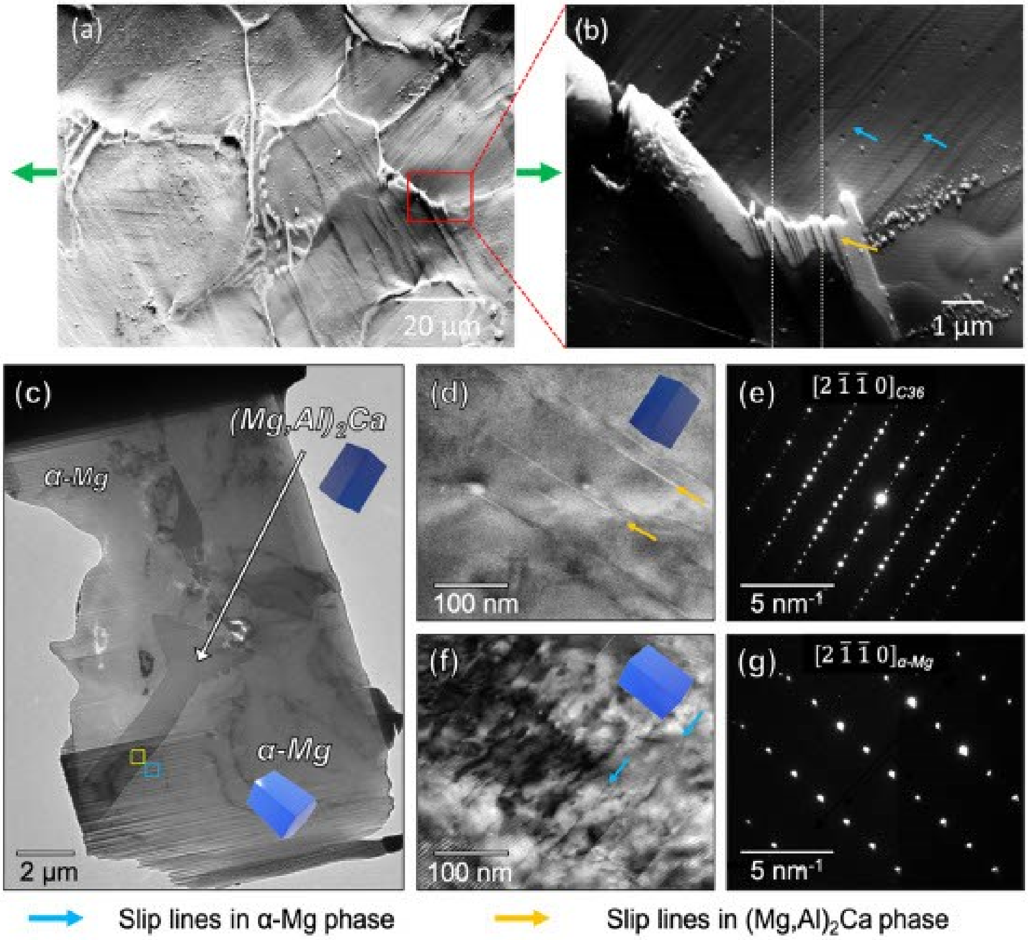

Fig. 2. Microstructure of the sample deformed to 5% at 170 °C: (a) SE SEM overview image (stage tilted 70° to the electron beam, image tilt-corrected) with green arrows indicating the direction of the tensile force applied in deformation test. (b) Magnified image (SE SEM) of the microstructure marked in (a) with red rectangle. The white dotted rectangle in (b) indicates, in top view, the position of the FIB cut. (c) Overview (BF TEM) image of the FIB lamella in the initial orientation (no sample tilt). Yellow and blue rectangles indicate sample areas shown in detail in (d) and (f), respectively. (d–g) BF images of the basal-slip structures observed in (Mg,Al)$_2$Ca (d) and α-Mg matrix (f), with corresponding $\left[2\,\bar{1}\,\bar{1}\,0\right]$ SAED patterns in (e) and (g). Unit cell projections in (c), (d) and (f) schematically indicate orientation of the hexagonal structures in the respective images (bright blue for α-Mg and dark blue for (Mg,Al)$_2$Ca). (For interpretation of the references to colour in this figure legend, the reader is referred to the web version of this article.)

pyramidal slip was determined through micropillar compression). The CRSS values for the Mg phase are much lower than the CRSS values reported for the same slip systems in the C14 Mg$_2$Ca Laves phase, which were determined as ≈520 MPa (basal slip), ≈440 MPa (prismatic slip) and ≈530 MPa (pyramidal slip) by micropillar compression [2] (NB: a direct comparison is impeded by the brittleness of the Laves phase and the size effect encountered in microcompression testing of Mg, resulting in a CRSS for basal slip of the order of ≈7 MPa as opposed to 0.52 MPa [17] measured macroscopically [20]). The other Laves phase (C15 Al$_2$Ca phase) in the Mg-Al-Ca system was reported to be even harder than the C14 Mg$_2$Ca Laves phase [21]. As the hexagonal C36 Laves phase is very closely related to the hexagonal C14 Laves phase, we assume here that plastic deformation follows the same mechanisms. Owing to this difference in CRSS; it appears likely that under the application of a tensile stress, slip in the α-Mg matrix is activated first and then at points of severe stress concentrations, for example where slip lines in the Mg phase interact with the Laves phase, plastic flow can be transmitted into the Laves phase. Further, it is possible that at those intersection points of slip in the Mg matrix with the Laves phase, where cracks were observed, some plastic flow has occurred prior to cracking. However, it is not possible to distinguish cracking with and without prior slip in the Laves phase by considering only post-mortem results.

As reported elsewhere, it is worth mentioning that considerable strengthening is induced by the Laves phases, i.e. the yield and tensile strength of this alloy in the as-cast state is 92 ± 2 MPa and 123 ± 11 MPa, respectively [22] at room temperature, whereas the same values for pure Mg in the as-cast state are 26.6 and 69.2 MPa, respectively [23].

3. Simulations

To explore the atomic-scale details of the slip transfer observed experimentally and to understand the underlying mechanisms, we performed atomistic simulations with semi-empirical potentials. As no reliable potential is available to date that correctly models the plasticity in the ternary Mg-Al-Ca intermetallic phase, we consider here the C14 Mg$_2$Ca Laves phase as surrogate for the C36 (Mg,Al)$_2$Ca Laves phase. Similar to previous experimental [16] and numerical work [7], two different orientation relationships (OR) have been considered in our numerical approach. One with both phases' basal planes parallel, $(0001)_\alpha \parallel (0001)_{Mg2Ca}$, the other with the basal plane of the Mg phase aligned with the prismatic plane of the Mg_2Ca, $(0001)_\alpha \parallel (11\bar{2}0)_{Mg_2Ca}$, close to the OR we observed by TEM.

3.1. Numerical methods

Atomistic simulations have been carried out with the classical molecular dynamics code LAMMPS [24]. Interatomic interactions were modelled by the recently developed potential of Kim et al. [25] based on the modified embedded atom method (MEAM). This potential has been specifically optimized to represent both, hexagonal Mg phase and the C14 Mg_2Ca Laves phase, and it has been used successfully to model the complex dislocation motion in the basal plane of the C14 Laves phase [6]. This work involves molecular static (MS) and molecular dynamic (MD) simulations. MS simulations were performed by using both conjugate gradient [26] and FIRE [27,28] algorithms, and the configurations were considered optimized for a norm of the global force vector below 10^{-8} eV/Å. MD simulations were performed within either the microcanonical (NVE, $T_0 = 0$ K) or the canonical (NVT, $T_0 > 0$ K) thermodynamic ensemble with a timestep $\Delta t = 1.0$ fs. In the NVT ensemble, the temperature was controlled by a Nosé-Hoover thermostat [29] with a damping parameter of 0.1 ps. The atomistic configurations were constructed using Atomsk [30], and visualized and analysed using OVITO [31]. The defects in both, Mg and Mg_2Ca phases were evidenced by calculating atomic-level strain tensors at each particle. More specifically, the von Mises local shear invariant, γ_{vM}, was estimated from the atomic deformation gradient tensor calculated based on atom displacements [32]. Note that the commonly used structural identification methods, like the common neighbours analysis (CNA) [33], are not adapted to the C14 structure and defects at complex interfaces have been already characterized by such shear invariant based method [34].

3.2. Numerical results

3.2.1. Parallel basal planes: $(0001)_\alpha \parallel (0001)_{Mg_2Ca}$

We first focus on the OR $(0001)_\alpha \parallel (0001)_{Mg2Ca}$, which forms a composite that exhibits coplanar basal planes. As the objective of the simulation is to study the transfer of slip at the interface from the Mg matrix, the onset of plasticity in the Mg phase is favoured by choosing an angle

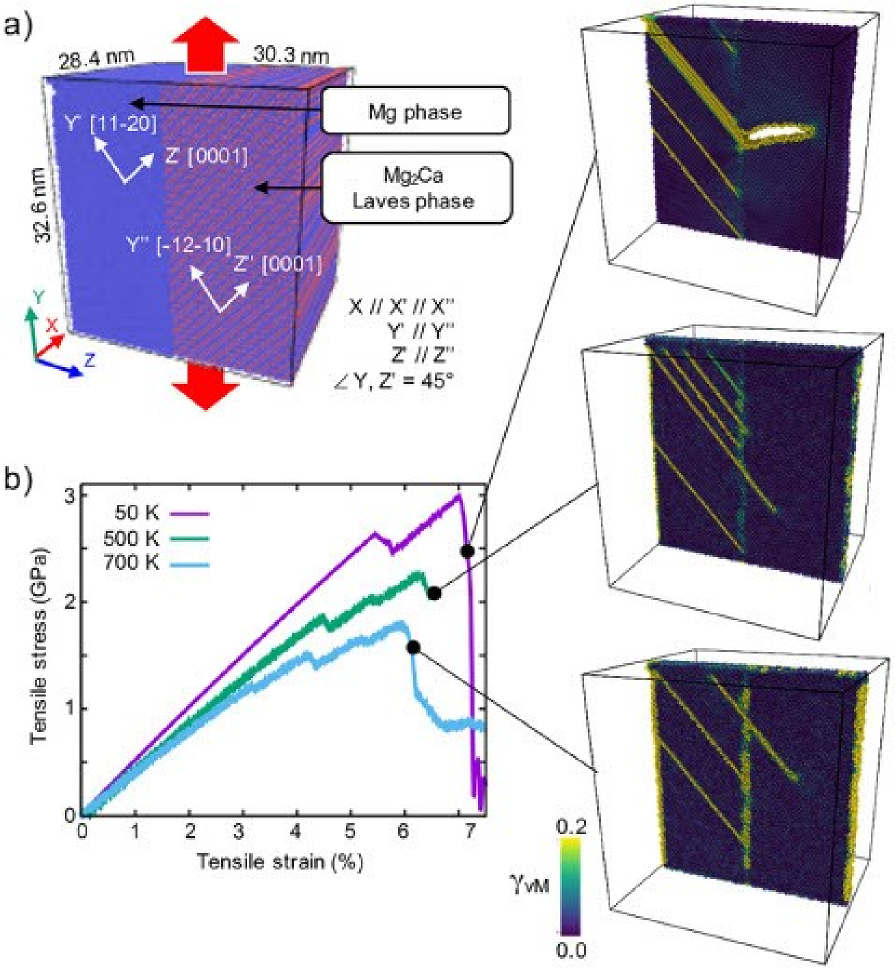

Fig. 3. Direct slip transfer at an Mg-Mg_2Ca interface during nanomechanical tensile tests. a) Simulation setup with the orientation relationship OR $(0001)_\alpha \parallel (0001)_{Mg2Ca}$. Red arrows indicate the pulling direction. Atoms in blue (red) are Mg (Ca). b) Stress-strain curves of the tensile tests at 50 K (purple), 500 K (green) and 700 K (blue). Insets show sliced snapshots of the first plastic event in the Mg_2Ca phase. Atoms are coloured according to their averaged local shear strain γ_{vM}. (For interpretation of the references to colour in this figure legend, the reader is referred to the web version of this article.)

of 45° with the deformation axis. This maximises the resolved shear stress on the primary (basal) slip planes. The corresponding atomistic sample shown in Fig. 3 is made of Mg and Mg_2Ca phases separated by an interface perpendicular to the Z-axis, and contains 996,941 atoms. The phases are oriented as follows: X′-$\left[\bar{1}100\right]$, Y′-$\left[11\bar{2}0\right]$, Z′-[0001] for Mg, and X″-$\left[2\bar{1}\bar{1}0\right]$, Y″-$\left[\bar{1}2\bar{1}0\right]$, Z″-[0001] for Mg_2Ca. The crystallographic directions X′ and X″ are aligned with the box axis X. The crystallographic directions Z′ and Z″ are parallel and have an angle of 45° with the Y axis. No periodic boundary conditions are used. Uniaxial deformation is dynamically applied along the Y-axis: the sample is homogeneously scaled at a strain rate of 10^8 s^{-1} and the deformation is maintained by means of 2D boundary conditions. The deformation was performed at $T \approx 50$ K within the microcanonical ensemble ($T_0 = 0$ K). In this case, the temperature T corresponds to the average temperature during the simulated deformation. Tests at 500 K and 700 K have been also performed within the canonical ensemble.

Fig. 3b shows the stress-strain curves of our numerical strain-controlled nanomechanical tensile tests at 50 K, 500 K and 700 K. Note, that we also performed compression tests on the same sample, and they produced comparable results. All three curves exhibit a similar profile. First, there is an initially purely elastic co-deformation regime: both phases deform with negligible plasticity limited to surfaces. Then small stress drops indicate the activation of plasticity in the Mg phase by means of dislocation nucleation and glide from the surface or from the interface. Finally, a large stress drop corresponds to the initiation of either fracture at low temperature or slip at high temperature in the Mg_2Ca phase, as illustrated by the simulation snapshots in Fig. 3b. In all cases, fracture or plasticity in the Mg_2Ca phase are initiated from locations where Mg basal slip lines interact with the interface. A closer look at the mechanism is provided in Fig. 4 (See also Movie S1), which shows a sequence of snapshots of the sample deformed at 500 K. The slip mechanisms are highlighted in both phases by the calculation of the local shear strain, or von Mises local shear invariant, as described above. At $\varepsilon = 3.08\%$, two slip traces are visible. The stronger one indicates that more than one dislocation has glided within the same glide plane. At $\varepsilon = 5.8\%$, 3 more slip traces are visible with a local shear strain concentration at the location of slip transfer, as highlighted in the inset. At $\varepsilon = 5.9\%$, no additional slip traces appear in the Mg phase, but the slip trace in the Mg phase highlighted in red shows a higher shear strain level indicating additional dislocation glide. As a consequence, a slip event in the Mg_2Ca phase is initiated as highlighted in the magnified views (Fig. 4). At $\varepsilon = 6.0\%$, it propagates further within the basal plane of the Mg_2Ca phase by showing similarities with the synchroshear mechanism, typical for basal slip in Laves phases [6,35].

Our simulation at low temperature (50 K) does not show any slip within the Mg_2Ca phase. We reduced the deformation rate up to 2 orders of magnitude without preventing the formation of a crack from the interface and through the Mg_2Ca phase.

3.2.2. *Non-parallel basal planes:* $(0001)_\alpha \parallel (11\bar{2}0)_{Mg_2Ca}$

The particular orientation relationship investigated in the previous section with the basal planes aligned parallel in both phases obviously favoured basal-to-basal slip transfer at the interface. To obtain some insights into the possibility of having such a slip transfer for other orientation relationships, we considered the OR $(0001)_\alpha \parallel \left(11\bar{2}0\right)_{Mg_2Ca}$, which is similar to the one observed in our experiments and in the literature [7]. In this configuration, the basal plane of the Mg phase is aligned parallel with a prismatic plane of the Mg_2Ca phase. The corresponding atomistic sample shown in Fig. 5a is composed of the Mg and Mg_2Ca phases separated by an interface normal to the Z-axis, and contains a total of 147,060 atoms. The phases are oriented as follows: X′-$\left[1\bar{1}00\right]$, Y′-[0001], Z′-$[11\bar{2}0]$ for Mg, and X″-$[1\bar{1}00]$, Y″-$[11\bar{2}0]$, Z″-[0001] for Mg_2Ca. The crystallographic directions Z′ and Z″ are aligned parallel with the box axis Z. The crystallographic directions Y′ and Y″ are parallel and have an angle of 45° with the Y axis. No periodic boundary conditions are used. Uniaxial compression is dynamically applied along the Y-axis: the sample is homogeneously scaled, and the compression is

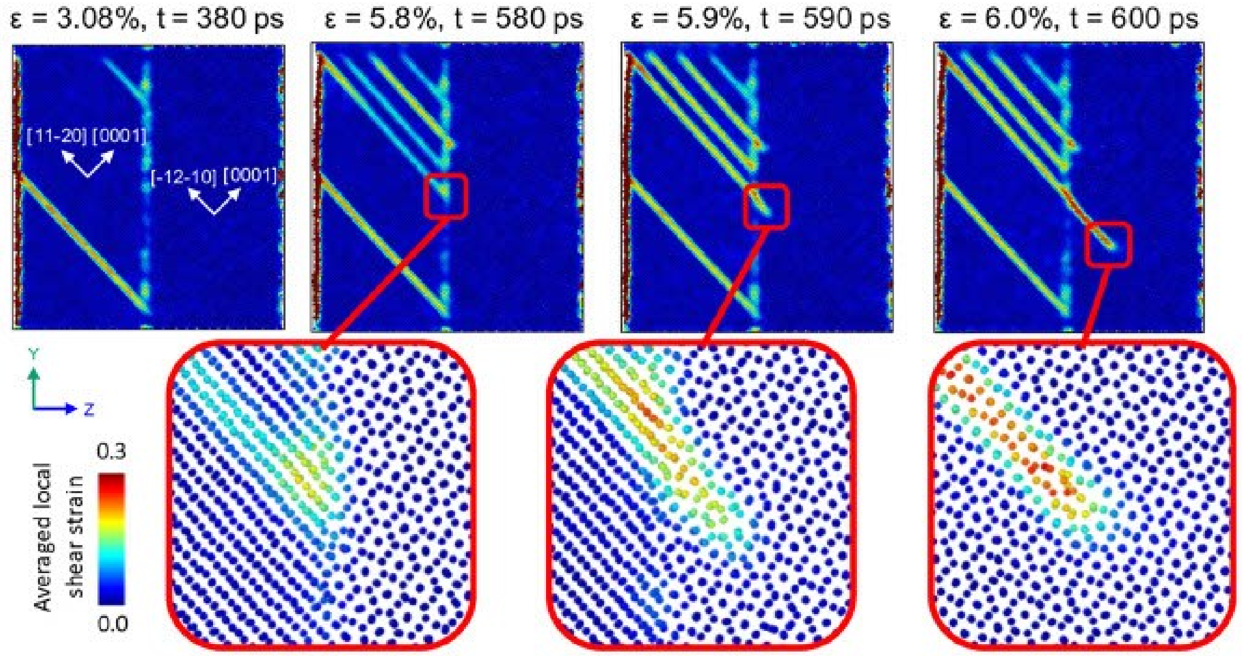

Fig. 4. Details of direct slip transfer at an Mg-Mg_2Ca interface $(0001)_\alpha \parallel (0001)_{Mg2Ca}$ during nanomechanical tensile tests at 500 K. Atoms are coloured according to their averaged local shear strain γ_{vM}. Insets show the details of the slip transfer at the interface.

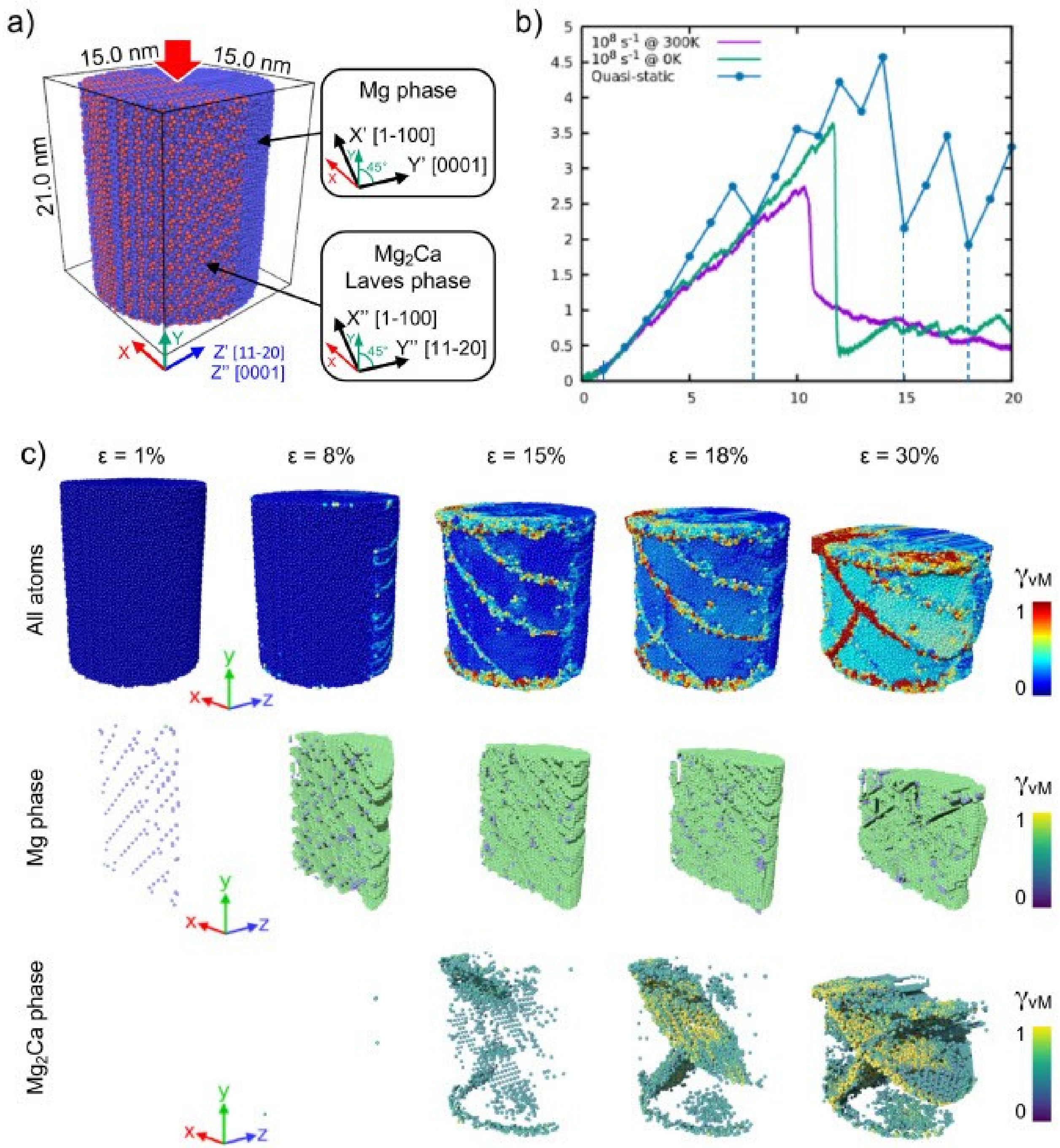

Fig. 5. Indirect slip transfer at the Mg-Mg_2Ca interface during nanomechanical compression tests. a) setup of the compression test simulation, with the orientation relationship $(0001)_\alpha \parallel \left(11\bar{2}0\right)_{Mg_2Ca}$. Red arrows indicate the compression direction. Atoms in blue (red) are Mg (Ca). b) stress-strain curves of the compression tests. The green and purple solid lines correspond to dynamic deformation at ≈50 K and 300 K. The dots of the blue line correspond to the relaxed states of the quasi-static deformation. Vertical dashed lines are guide for the eyes at strains 1%, 8%, 15% and 18% that correspond to the snapshots shown in c. c) snapshots of the quasi-static deformation test. First row: all atoms are shown. Second (third) row: only atoms of the Mg (Mg_2Ca) phase with an atomic shear strain γ_{vM} greater than 0.3 are shown. Atoms are coloured according to the atomic shear strain γ_{vM}. (For interpretation of the references to colour in this figure legend, the reader is referred to the web version of this article.)

maintained by means of a force wall defined by a harmonic potential. The quasi-static deformation test was performed by successive MS simulations. The deformation at T ≈ 50 K was performed within the microcanonical ensemble ($T_0 = 0$ K). A test at 300 K has been performed within the canonical ensemble. Both dynamic deformations were carried out at a strain rate of 10^8 s^{-1}.

Fig. 5b shows the stress-strain curves of the three compression tests. The quasi-static deformation shows a profile that is more staggered than the dynamic deformations, but all tests follow a similar trend. To describe the mechanisms in detail, we will focus on the quasi-static deformation. Fig. 5c shows sequences of snapshots of the quasi-static deformation from 1% to 30% compressive strain. The first row shows the entire sample during deformation, evidencing that slip traces form at the surface (See also Movie S2). The second and third rows show only those atoms that have an atomic von Mises shear invariant γ_{vM} larger than 0.3. In other words, slip activities are highlighted by hiding atoms that have not undergone significant shear. As a lot of events happened during the deformation, we split the sample in two parts to ease the visualization: the second and third rows show the Mg and Mg_2Ca phases only, respectively (see also Movies S3 and S4). Up to 8% strain, the deformation is purely elastic and no slip events are detected. At 8% strain, a slight drop of the stress occurred (first dashed vertical line in Fig. 5b) as the Mg phase shows a strong plastic activity with the nucleation of dislocations and the formation of twins. The Mg_2Ca phase is deformed elastically up to 15% strain as the Mg phase continues to deform plastically. At 15% strain, shear events are triggered in the Mg_2Ca phase, principally on two approximately orthogonal planes. The shear continues to increase while deforming the sample up to 30%. Note that while the Mg phase appears almost entirely twinned, most of the plastic shear in the Mg_2Ca phase is concentrated in the two planes initially activated at 15% strain.

A deeper insight in the onset of plasticity in the Mg_2Ca phase is given by the kinetics of the mechanism from the dynamic simulation, as shown in Fig. 6. Here, the Mg phase appears already largely twinned at a compressive strain of 15% and a time $t = 1.98$ ns. While maintaining the strain constant, the dynamics is simulated further (snapshots at $t = 2.38$ ns and $t = 3.43$ ns, Fig. 6a and Movie S5) and evidences the onset of slip at the Mg-Mg_2Ca interface in the centre of the pillar. As shown in Fig. 6b, the slip event at the interface can be characterized as a non-dissociated prismatic <a> dislocation (See also Movie S6 for the MD counterpart).

The driving force for the onset of plasticity in the Laves phase is unveiled in Fig. 7 showing sliced views normal to the glide planes at the onset of Laves phase plasticity. Fig. 7b-d represents the evolution of slip by the calculation of the local rigid-body rotation $\mathcal{R}_Z$ around the Z axis. Local rotation is especially useful to highlight twinning. Fig. 7e-g represents the evolution of to $\overline{S_{xy}}$, the averaged (over the neighbours within a sphere of 10 Å) local atomic shear stress. In particular, the nucleation of the dislocation in the Laves phase is revealed by an orange spot at the interface (Fig. 7c) and the fully propagated dislocation is clearly evidenced by the dark red band (Fig. 7d). Note that the nucleation of the dislocation in the Laves phase correlates to the propagation of one <a> partial dislocation in the Mg phase (Fig. 7b,c). The nucleation of the dislocation in the Laves phase is directly related to a stress concentration at the Mg-Mg_2Ca interface (Fig. 7f) that released the stress initially stored in the Mg phase (Fig. 7e). While releasing the global stress of the pillar (at 15% strain, as shown in Fig. 5b), the propagation of the dislocation in the Laves phase generates additional shear stresses in this phase of the order of 1 GPa (Fig. 7g), favouring the subsequent plasticity of the intermetallic phase.

3.2.3. Simple shear of dislocation pile-up

To gain detailed and well-defined insights into the mechanisms of interfacial plasticity, it is common to use carefully controlled two dimensional atomistic setups [36–38]. Such approaches include infinite

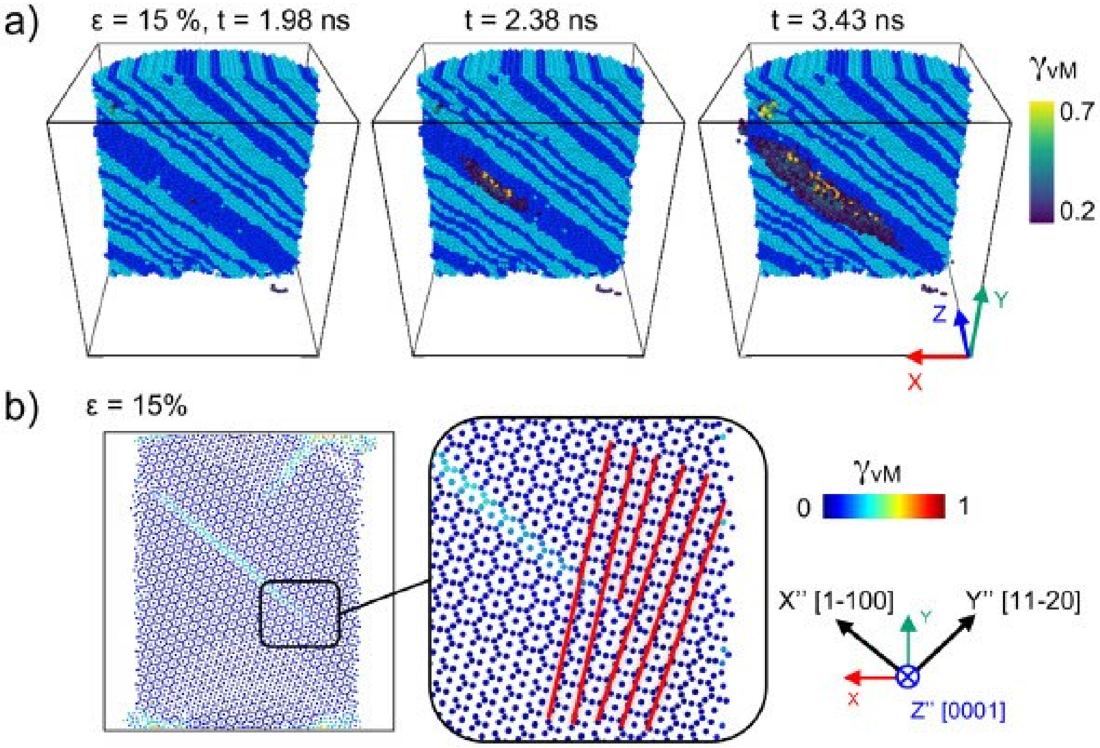

Fig. 6. a) snapshots of the dynamic deformation at ≈50 K showing the nucleation of a dislocation in the Laves phase from the interface. Mg phase: all atoms visible, coloured according to their crystal structure (HCP, light blue; FCC, dark blue). Mg_2Ca phase: only atoms with an atomic shear strain greater than 0.3 are visible. b) sliced view of the Mg_2Ca phase deformed to 15% during a quasi-static simulation. The inset highlights the non-dissociated core of the prismatic dislocation nucleated from the interface in b). Atoms are coloured according to the atomic shear strain.

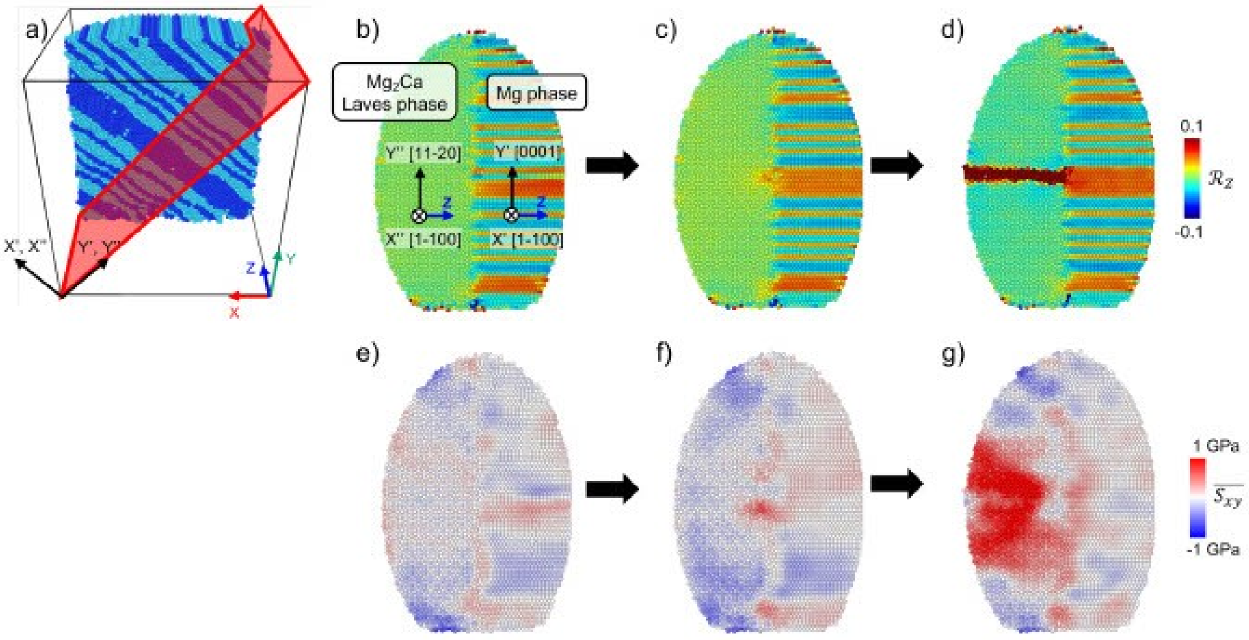

Fig. 7. Kinematics of the onset of plasticity at the Mg-Mg_2Ca interface during nanomechanical compression tests with the orientation relationship $(0001)_\alpha \parallel \left(11\bar{2}0\right)_{Mg_2Ca}$. a) perspective view similar to Fig. 6a, showing the plane visualized in b) to g). The atoms in the Laves phase are removed for clarity. b-g) sliced profile views of the onset of Laves phase plasticity, corresponding to the half-transparent red plane of the perspective view on the left. All atoms visible. b,c,d) atoms are coloured according to $\mathcal{R}_Z$, the local rigid-body rotation around the Z axis (arbitrary unit) highlighting dislocations and twins. e,f,g) atoms are coloured according to $\overline{S_{xy}}$, the averaged (over a sphere of 10 Å) local atomic shear stress (in GPa). (For interpretation of the references to colour in this figure legend, the reader is referred to the web version of this article.)

straight dislocations with controlled character, semi-infinite planar interfaces and controlled stress states. In our work, we consider a quasi-2D bi-crystal slab made of the Mg phase and the C14-Mg_2Ca phase with the OR $(0001)_\alpha \parallel (0001)_{Mg_2Ca}$ and the OR $(0001)_\alpha \parallel (11\bar{2}0)_{Mg_2Ca}$. Fig. 8a shows the Mg-$Mg_2Ca$ atomistic composite sample, with periodic boundary condition (BC) along the X and Y axes. The OR $(0001)_\alpha \parallel (11\bar{2}0)_{Mg_2Ca}$ is chosen as an example, but we observed identical results for the OR $(0001)_\alpha \parallel (0001)_{Mg_2Ca}$. 2D BC are applied along the Z axis (red layers in Fig. 8a). From 1 to 20 infinite straight basal edge dislocations are inserted in the centre of the simulation within the Mg phase. The dislocations are successively inserted by using Atomsk [30]. The system is relaxed by MS (see Section 3.1) and deformed by quasi-static simulations as described in the following. A strain ε_{yz} is applied on the sample by homogeneously displacing all the atoms, followed by a complete relaxation of the system by MS. To maintain the deformation during the minimization, a force F is applied in the Y direction on each atom that belong to the 2D BC, and defined by $F = \left(\varepsilon_{yz}.\overline{\mu^*}\right)/(S.N)$ with $\overline{\mu^*}$ being the average shear modulus of the sample for the particular orientations, S the surface area along the Z direction and N the number of atoms in the 2D BC.

A non-sheared relaxed sample containing four dislocations is shown in Fig. 8a. Two of the four dislocations are in contact with the interface. The stress-strain profile of the quasi-static deformation shown in Fig. 8b (purple line) exhibits a linear stress increase up to $\tau = 0.9$ GPa. This corresponds to the absorption of the first three Mg dislocations, as evidenced in Fig. 8c revealing a sequence of dislocation pile-ups interacting with the interface (left views highlight the crystallographic structure by CNA, right views evidence the local atomic shear stress). At an applied shear stress $\tau = 0.9$ GPa, the interface nucleates defects (Fig. 8c) that release not only the global stress (Fig. 8b) but also the stress induced into the Mg_2Ca phase by the dislocation absorbed at the interface (see Fig. 8c, snapshot 3 and 4). Due to this stress release, no defect is transmitted or formed in the Mg_2Ca phase. However, the nucleated interfacial defects continue to grow, while additional defects form and propagate into the Mg phase (Fig. 8c (5), dark blue bands). We conclude that the interface fails after the absorption of four dislocations. It is interesting to notice that during the linear stage of stress increase, the interface with absorbed dislocations undergoes significant local sliding (Fig. 8d, right vertical interface with a strong increase of local atomic strain γ_{VM}). On the contrary, the interface that did not absorb any dislocations from the pile-up shows negligible local sliding (Fig. 8d, left vertical interface with a low increase of local atomic strain γ_{VM}).

The behaviour we report above is independent of the size of the dislocation pile-up and of the orientation relationship. The maximum number of dislocations the interface can absorb is three. As an example, Fig. 8e shows a pile-up of 20 dislocations in front of a failed interface, 3 dislocations being already absorbed in the interface.

We investigated the influence of temperature on the behaviour we report above. The two dimensional set up with a pile-up of four dislocations has been deformed at finite temperatures within the canonical ensemble (NVT) at a shear rate of 10^8 s^{-1}. Fig. 8b shows the stress-strain curves of these deformation tests at 300 K and 700 K in green and light blue, respectively. Similar to the quasi-static simulations, the stress drops correspond to the nucleation of defects in the Mg phase or to the failure of the interface. No transfer of slip from the Mg to the Mg_2Ca phase is observed (See also Movie S7). The behaviour presented above appears thus independent of the temperature. A comprehensive investigation of the effect of the temperature on the brittle to ductile transition in such composite is however out of the scope of this work.

3.3. Discussion on the simulations

The numerical deformation tests we present in this work show slip transmission across the Mg-Mg_2Ca interface. We identified two regimes

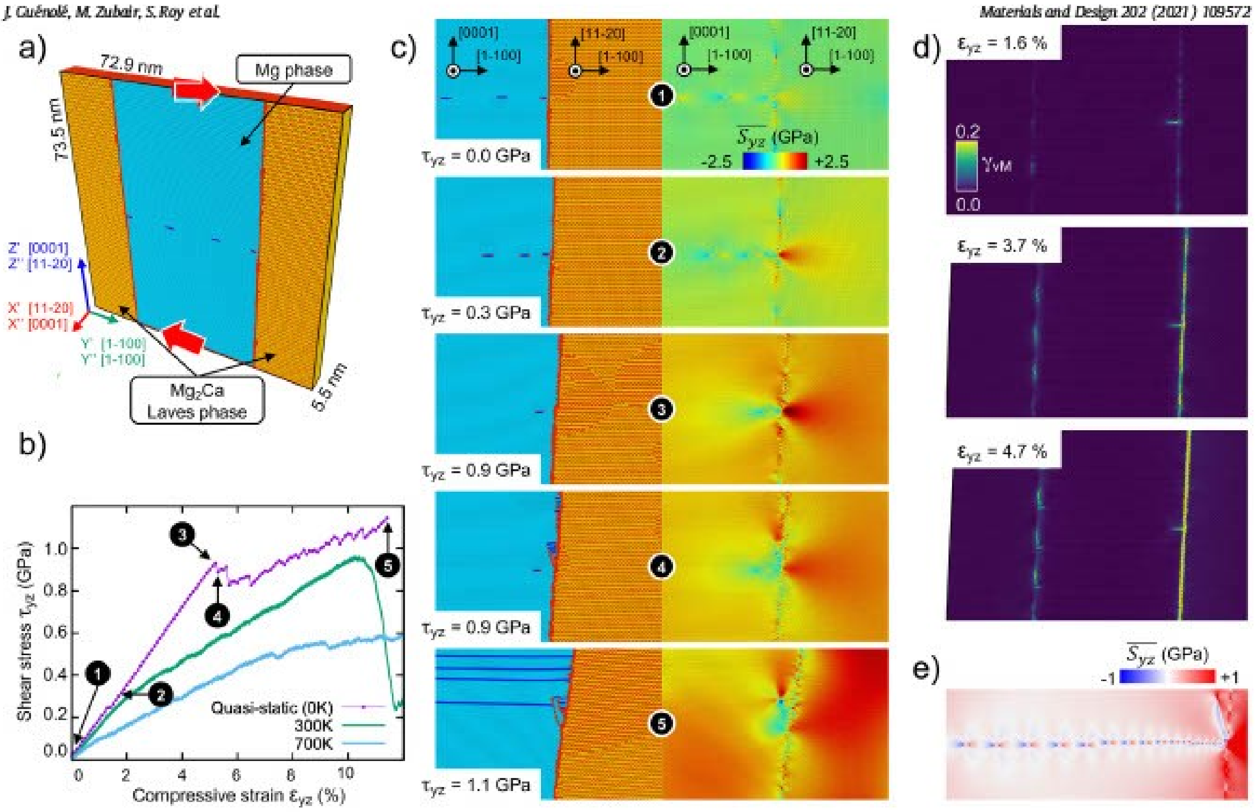

Fig. 8. Dislocation pile-up at the Mg-Mg_2Ca interface with orientation relationship $(0001)_\alpha \| \left(11\bar{2}0\right)_{Mg_2Ca}$. a) setup of the quasi-static simulations. Red arrows indicate the shear direction. Atoms are coloured according to the common neighbour analysis (CNA): perfect hexagonal crystal, light blue; stacking fault in hex, dark blue; C14 Laves phase, orange and red; other structure type, red only. b) stress-strain curves of the quasi-static (0 K) and finite temperature (300 K and 700 K) shear deformations. The numbers in the black circles refer to the snapshots in c). Each dot on the curve indicates a relaxed state. c) snapshots of the quasi-static deformation for different global shear stresses, τ, as referred in b). Left colouring: CNA. Right colouring: local shear stress $\overline{S_{yz}}$. d) interfacial sliding revealed by snapshots at different strain level during the linear regime. Colour according to the atomic shear strain γ_{vM}. e) pile-up of 20 dislocations at an applied shear stress of approximately 1 GPa, highlighted by the local shear stress $\overline{S_{yz}}$. (For interpretation of the references to colour in this figure legend, the reader is referred to the web version of this article.)

depending on the orientation relationship. When the basal planes of the matrix are aligned with the basal planes of the Laves phase, a direct slip transmission can occur. It consists of the accumulation of matrix <a> basal full dislocations at the interface, that directly trigger the nucleation of a partial dislocation on the basal planes of the Laves phase. The temperature dependency indicates that this mechanism is thermally activated, similar to the propagation of the synchroshear dislocation in bulk Laves phases [6,35,39]. Note that a synchroshear dislocation propagates by the synchronous glide of two ordinary Shockleys on adjacent parallel atomic planes, as described in detail elsewhere [6,39,40]. On the other hand, when the basal planes of the matrix are aligned with the prismatic planes of the Laves phase, an indirect transmission can occur. It consists of the local accumulation of shear stress within the interface plane, the resulting torsion indirectly triggering the nucleation of a full non-dissociated <a> dislocation on the prismatic plane of the Laves phase. This mechanism seems thus to be strongly facilitated by deformation twinning in the matrix. Note that the in-depth analysis of dislocation mechanisms in such complex atomistic structures requires novel technics that remain to be developed.

These two regimes for slip transmission can be, however, entirely inhibited by interfacial sliding. In particular, when the applied load favoured sliding within planes parallel to the interface plane, local sliding of the atoms at the interface appears to release sufficient internal stress to prevent the nucleation of dislocations in the Laves phase.

4. Discussion on experimental and simulation results

In this work, experimental and numerical approaches were combined to investigate the plasticity and co-deformation of Mg-Laves phase composites. As discussed in the previous sections, the stress required to activate plasticity in the Mg phase is significantly lower than that required in case of the Laves phases. Consequently, under the application of external loading, the Mg phase deforms first and then at the stress concentration points, three different events can take place: i) cracking in the Laves phase, ii) slip transfer from α-Mg to Laves phase and iii) interfacial sliding at the α-Mg-Laves phase interfaces. The details pertaining to each event are covered separately in the following sections.

4.1. Cracking in the Laves phase

The atomistic simulation results (Fig. 3) confirm that under application of tensile stress plasticity is first initiated in the α-Mg phase and then further straining results in the initiation of fracture in the Mg_2Ca phase especially at low temperatures, i.e. at 50 K. This happens preferably at places where basal slip lines in α-Mg matrix interacts with the interfaces. Due to limited ductility, experimental observations of pronounced deformation are largely limited to higher temperatures, but the same combination of cracking and slip events in the adjacent

Laves phase have indeed been found also in experiments after deformation at ≈170 °C (see Fig. 1 and [22]).

4.2. Slip transfer from α-Mg to Laves phase

Alternatively, simulations also confirm that, at the same stress concentration points (where basal slip lines in the α-Mg matrix interacts with the Laves phase), plasticity may be transmitted to the Laves phase, especially at elevated temperatures (500 K and 700 K, see Figs. 3 and 4). We further showed that the basal <a> slip in the α-Mg matrix activates plasticity in the Laves phase within the basal planes. Similar results were again also obtained in our experiments, where plasticity from the α-Mg phase can be seen transmitted to the basal planes of the Laves phase (Fig. 2) at the stress concentration points.

In some cases, as for our simulation setup with the orientation relationship $(0001)_\alpha \| \left(11\bar{2}0\right)_{Mg_2Ca}$, the slip event in the Mg_2Ca activated from the interface was based on non-dissociated prismatic <a> dislocations. In agreement with this, observations of prismatic slip during nano-indentation have also been made by Zehnder et al. [2]. In fact, the CRSS for 1st order prismatic slip (≈440 MPa) was reported to be lower compared with basal slip (≈520 MPa) at room temperature [2].

4.3. Interfacial sliding at the α-Mg-Laves phase interfaces

Our atomistic results suggest that interface sliding can prevent the transfer of matrix slip to the Laves phase. Interfacial sliding is primarily achieved by the absorption of dislocations at the interface. This is in agreement with earlier experimental observations, where interfacial sliding of Mg-Laves phase interfaces has been reported [22,41].

However, unfortunately we have not been able to provide an experimental correlation between slip transfer or local interfacial sliding and the local stress state and orientation relationship, as the number of events we observed remained limited. Nonetheless, our simulations show that the slip transfer mechanism depends on the interfacial orientation and can be inhibited for particular geometries, even at high temperature (see Fig. 8). This highlights the importance of considering local strain distributions and local interfacial geometries to predict slip transfer at phase boundaries. Experimentally, these insights may help guide future experiments to target specific orientation relationships and to investigate the thermal activation of interface-dominated deformation by nanomechanical testing. In this way, simulations and experiments will directly benefit from each other to unravel the co-deformation mechanisms of the two phases.

5. Conclusions

In this work, we combined experimental and numerical approaches to investigate the plasticity and co-deformation of Mg-Laves phase composites. From this work we conclude that:

- The mechanisms of co-deformation, namely cracking, slip transmission and interfacial sliding as a result of slip activity in the Mg phase, are observed in both simulation and experiment.
- For slip transfer, the Laves phase deforms on those planes identified previously in experiments and simulations, the prismatic and basal planes. The simulations suggest that this should occur by synchroshear on the basal plane and non-dissociated <a> dislocation on the prismatic plane.
- In the case of interfacial sliding, we found that dislocations are absorbed into the interface in the simulations. An insight that may be validated experimentally by targeted deformation and transmission electron microscopy in the future.
- Overall, our simulations reveal that the active co-deformation mechanism depends on the interfacial orientation. This highlights the importance of considering local strain distributions and local interfacial geometries to predict slip transfer at phase boundaries.

More work has to be performed to understand the full extent of slip transfer at such complex interfaces. In particular, our numerical results suggest that this transfer might be thermally activated, but this remains to be confirmed by dedicated experiments. The findings we present here on the transfer of slip across Laves phase interfaces in Mg alloys pave the way for in-depth investigations of the plasticity in such complex lightweight composite. More generally, understanding how the plasticity is transferred at phase boundaries opens up exploration paths for composites with tailored mechanical properties.

Supplementary data to this article can be found online at https://doi.org/10.1016/j.matdes.2021.109572.

Data availability

The raw/processed data required to reproduce these findings cannot be shared at this time as the data also forms part of an ongoing study.

Declaration of Competing Interest

The authors declare that they have no known competing financial interests or personal relationships that could have appeared to influence the work reported in this paper.

Acknowledgments

The authors acknowledge financial support by the Deutsche Forschungsgemeinschaft (DFG) through the projects A02, A03, A05, C01 and C02 of the SFB1394 Structural and Chemical Atomic Complexity – From Defect Phase Diagrams to Material Properties, project ID 409476157. Simulations were performed with computing resources granted by RWTH Aachen University (rwth0297, rwth0407, rwth0591 and prep0017) and by the GENCI-TGCC (grant 2020-A0080911390).

References

[1] M. Zubair, S. Sandlöbes, M.A. Wollenweber, C.F. Kusche, W. Hildebrandt, C. Broeckmann, S. Korte-Kerzel, On the role of Laves phases on the mechanical properties of Mg-Al-Ca alloys, Mater. Sci. Eng. A 756 (2019) 272–283, https://doi.org/10.1016/j.msea.2019.04.048.

[2] C. Zehnder, K. Czerwinski, K.D. Molodov, S. Sandlöbes-Haut, J.S.K.L. Gibson, S. Korte-Kerzel, Plastic deformation of single crystalline C14 Mg2Ca Laves phase at room temperature, Mater. Sci. Eng. A 759 (2019) 754–761, https://doi.org/10.1016/j.msea.2019.05.092.

[3] I. Polmear, D. StJohn, J.-F. Nie, M. Qian, Magnesium alloys, Light Alloy 1 (2017) 287–367, https://doi.org/10.1016/B978-0-08-099431-4.00006-3.

[4] Z.Q. Yang, M.F. Chisholm, B. Yang, X.L. Ma, Y.J. Wang, M.J. Zhuo, S.J. Pennycook, Role of crystal defects on brittleness of C15 Cr2Nb Laves phase, Acta Mater. 60 (2012) 2637–2646, https://doi.org/10.1016/J.ACTAMAT.2012.01.030.

[5] A.J. Knowles, A. Bhowmik, S. Purkayastha, N.G. Jones, F. Giuliani, W.J. Clegg, D. Dye, H.J. Stone, Laves phase intermetallic matrix composite in situ toughened by ductile precipitates, Scr. Mater. 140 (2017) 59–62, https://doi.org/10.1016/J.SCRIPTAMAT.2017.06.043.

[6] J. Guénolé, F.-Z. Mouhib, L. Huber, B. Grabowski, S. Korte-Kerzel, Basal slip in Laves phases: the synchroshear dislocation, Scr. Mater. 166 (2019) 134–138, https://doi.org/10.1016/j.scriptamat.2019.03.016.

[7] X. Di Li, H.T. Ma, Z.H. Dai, Y.C. Qian, L.J. Hu, Y.P. Xie, First-principles study of coherent interfaces of Laves-phase MgZn2and stability of thin MgZn2layers in Mg-Zn alloys, J. Alloys Compd. 696 (2017) 109–117, https://doi.org/10.1016/j.jallcom.2016.11.217.

[8] C.D. Rabadia, Y.J. Liu, L.Y. Chen, S.F. Jawed, L.Q. Wang, H. Sun, L.C. Zhang, Deformation and strength characteristics of Laves phases in titanium alloys, Mater. Des. 179 (2019) 107891, https://doi.org/10.1016/j.matdes.2019.107891.

[9] D. Amberger, P. Eisenlohr, M. Göken, Microstructural evolution during creep of Ca-containing AZ91, Mater. Sci. Eng. A 510–511 (2009) 398–402, https://doi.org/10.1016/j.msea.2008.04.115.

[10] S. Joseph, I. Bantounas, T.C. Lindley, D. Dye, Slip transfer and deformation structures resulting from the low cycle fatigue of near-alpha titanium alloy Ti-6242Si, Int. J. Plast. 100 (2018) 90–103, https://doi.org/10.1016/j.ijplas.2017.09.012.

[11] M. Luysberg, M. Heggen, K. Tillmann, FEI Tecnai G2 F20, J. Large Scale Res. Facil. 2 (2016) 77, https://doi.org/10.17815/jlsrf-2-138.

[12] Z.T. Li, X.D. Zhang, M.Y. Zheng, X.G. Qiao, K. Wu, C. Xu, S. Kamado, Effect of Ca/Al ratio on microstructure and mechanical properties of Mg-Al-Ca-Mn alloys, Mater. Sci. Eng. A 682 (2017) 423–432, https://doi.org/10.1016/j.msea.2016.11.026.

[13] L. Zhang, K. kun Deng, K. bo Nie, F. jun Xu, K. Su, W. Liang, Microstructures and mechanical properties of Mg-Al-Ca alloys affected by Ca/Al ratio, Mater. Sci. Eng. A 636 (2015) 279–288, https://doi.org/10.1016/j.msea.2015.03.100.

[14] H. Eibisch, A. Lohmüller, N. Kömpel, R.F. Singer, Effect of solidification microstructure and Ca additions on creep strength of magnesium alloy AZ91 processed by Thixomolding, Int. J. Mater. Res. 99 (2008) 56–66, https://doi.org/10.3139/146.101604.

[15] A. Suzuki, N.D. Saddock, J.W. Jones, T.M. Pollock, Solidification paths and eutectic intermetallic phases in mg-Al-Ca ternary alloys, Acta Mater. 53 (2005) 2823–2834, https://doi.org/10.1016/j.actamat.2005.03.001.

[16] A.A. Luo, B.R. Powell, M.P. Balogh, Creep and microstructure of magnesium-aluminum-calcium based alloys, Metall. Mater. Trans. A 33 (2002) 567–574, https://doi.org/10.1007/s11661-002-0118-1.

[17] H. Conrad, W.D. Robertson, Effect of temperature on the flow stress and strain-hardening coefficient of magnesium single crystals, JOM (1957) https://doi.org/10.1007/bf03397908.

[18] R.E. Reed-Hill, W.D. Robertson, Deformation of magnesium single crystals by nonbasal slip, JOM (1957) https://doi.org/10.1007/bf03397907.

[19] C.M. Byer, B. Li, B. Cao, K.T. Ramesh, Microcompression of single-crystal magnesium, Scr. Mater. (2010) https://doi.org/10.1016/j.scriptamat.2009.12.017.

[20] J.-Y. Wang, N. Li, R. Alizadeh, M.A. Monclús, Y.W. Cui, J.M. Molina-Aldareguía, J. LLorca, Effect of solute content and temperature on the deformation mechanisms and critical resolved shear stress in Mg-Al and Mg-Zn alloys, Acta Mater. 170 (2019) 155–165, https://doi.org/10.1016/j.actamat.2019.03.027.

[21] L.L. Rokhlin, T.V. Dobatkina, N.I. Nikitina, I.E. Tarytina, Calcium-alloyed magnesium alloys, Met. Sci. Heat Treat. (2009)https://doi.org/10.1007/s11041-009-9127-7.

[22] M. Zubair, S. Sandlöbes-Haut, M.A. Wollenweber, K. Bugelnig, C.F. Kusche, G. Requena, S. Korte-Kerzel, Strain heterogeneity and micro-damage nucleation under tensile stresses in an Mg–5Al–3Ca alloy with an intermetallic skeleton, Mater. Sci. Eng. A 767 (2019) 138414, https://doi.org/10.1016/j.msea.2019.138414.

[23] X.H. Feng, H.M. Jia, Y.T. Liu, Y.D. Li, W.R. Li, T. Zhang, Y.S. Yang, Effects of microstructures on the tensile properties and corrosion resistance of high-purity magnesium, Mater. Sci. Forum, Trans Tech Publications Ltd 2016, pp. 114–120, https://doi.org/10.4028/www.scientific.net/MSF.849.114.

[24] S. Plimpton, Fast parallel algorithms for short-range molecular dynamics, J. Comput. Phys. 117 (1995) 1–19, https://doi.org/10.1006/jcph.1995.1039.

[25] K.-H. Kim, J.B. Jeon, B.-J. Lee, Modified embedded-atom method interatomic potentials for Mg–X (X=Y, Sn, Ca) binary systems, Calphad 48 (2015) 27–34, https://doi.org/10.1016/j.calphad.2014.10.001.

[26] E. Polak, G. Ribiere, Note sur la convergence de méthodes de directions conjuguées, ESAIM Math. Model. Numer. Anal. 3 (1969) 35–43, https://doi.org/10.1051/m2an/196903R100351.

[27] E. Bitzek, P. Koskinen, F. Gähler, M. Moseler, P. Gumbsch, Structural relaxation made simple, Phys. Rev. Lett. 97 (2006) 1–4, https://doi.org/10.1103/PhysRevLett.97.170201.

[28] J. Guénolé, W.G. Nöhring, A. Vaid, F. Houllé, Z. Xie, A. Prakash, E. Bitzek, Assessment and optimization of the fast inertial relaxation engine (FIRE) for energy minimization in atomistic simulations and its implementation in LAMMPS, Comput. Mater. Sci. 175 (2020) 109584, https://doi.org/10.1016/j.commatsci.2020.109584.

[29] W.G. Hoover, Canonical dynamics : equilibrium phase-space distributions, Phys. Rev. A 31 (1985) 1695, https://doi.org/10.1103/PhysRevA.31.1695.

[30] P. Hirel, Atomsk: a tool for manipulating and converting atomic data files, Comput. Phys. Commun. 197 (2015) 212–219, https://doi.org/10.1016/j.cpc.2015.07.012.

[31] A. Stukowski, Visualization and analysis of atomistic simulation data with OVITO-the open visualization tool, Model. Simul. Mater. Sci. Eng. 18 (2010)https://doi.org/10.1088/0965-0393/18/1/015012.

[32] F. Shimizu, S. Ogata, J. Li, Theory of shear banding in metallic glasses and molecular dynamics calculations, Mater. Trans. 48 (2007) 2923–2927, https://doi.org/10.2320/matertrans.MJ200769.

[33] A. Stukowski, Visualization and analysis strategies for atomistic simulations, in: C.R. Weinberger, G.J. Tucker (Eds.), Multiscale Mater. Model. Nanomechanics, Springer International Publishing 2016, pp. 317–336, https://doi.org/10.1007/978-3-319-33480-6_10.

[34] J. Guénolé, J. Godet, S. Brochard, Plasticity in crystalline-amorphous core-shell Si nanowires controlled by native interface defects, Phys. Rev. B 87 (2013) 1–10, https://doi.org/10.1103/PhysRevB.87.045201.

[35] M.F. Chisholm, S. Kumar, P. Hazzledine, Dislocations in complex materials, Science (80-.) 307 (2005) 701–703, https://doi.org/10.1126/science.1105962.

[36] A. Prakash, J. Guénolé, J. Wang, J. Müller, E. Spiecker, M.J. Mills, I. Povstugar, P. Choi, D. Raabe, E. Bitzek, Atom probe informed simulations of dislocation-precipitate interactions reveal the importance of local interface curvature, Acta Mater. 92 (2015) 33–45, https://doi.org/10.1016/j.actamat.2015.03.050.

[37] M.A. Tschopp, D.L. McDowell, Dislocation nucleation in $\Sigma3$ asymmetric tilt grain boundaries, Int. J. Plast. 24 (2008) 191–217, https://doi.org/10.1016/j.ijplas.2007.02.010.

[38] M.A. Tschopp, S.P. Coleman, D.L. McDowell, Symmetric and asymmetric tilt grain boundary structure and energy in Cu and Al (and transferability to other fcc metals), Integr. Mater. Manuf. Innov. 4 (2015) 11, https://doi.org/10.1186/s40192-015-0040-1.

[39] O. Vedmedenko, F. Rösch, C. Elsässer, First-principles density functional theory study of phase transformations in (NbCr)2 and (TaCr)2, Acta Mater. 56 (2008) 4984–4992, https://doi.org/10.1016/j.actamat.2008.06.014.

[40] P.M. Hazzledine, K.S. Kumar, D.B. Miracle, A.G. Jackson, Synchroshear of Laves phases, MRS Proc. 288 (1992) 591, https://doi.org/10.1557/PROC-288-591.

[41] G. Zhang, K. Qiu, Q. Xiang, Y. Ren, Creep resistance of as-cast Mg-5Al-5Ca-2Sn alloy, China Found. 14 (2017) 265–271, https://doi.org/10.1007/s41230-017-7077-z.

Supplementary Material

Exploring the transfer of plasticity across Laves phase interfaces in a dual phase magnesium alloy

Julien Guénolé[a,b,c], Muhammad Zubair[a,d], Swagata Roy[a], Zhuocheng Xie[a], Marta Lipińska-Chwałek[e], Stefanie Sandlöbes-Haut[a], Sandra Korte-Kerzel[a]

[a] Institute of Physical Metallurgy and Materials Physics, RWTH Aachen University, D-52056 Aachen, Germany
[b] Université de Lorraine, CNRS, Arts et Métiers ParisTech, LEM3, F-57070 Metz, France
[c] Labex Damas, Université de Lorraine, F-57070 Metz, France
[d] Department of Metallurgical and Materials Engineering, G.T Road, UET Lahore, Pakistan
[e] Central Facility for Electron Microscopy, Ahornstraße 55, 52074 Aachen, Germany.
[f] Ernst Ruska-Centre for Microscopy and Spectroscopy with Electrons, Forschungszentrum Jülich GmbH, 52425 Jülich, Germany.

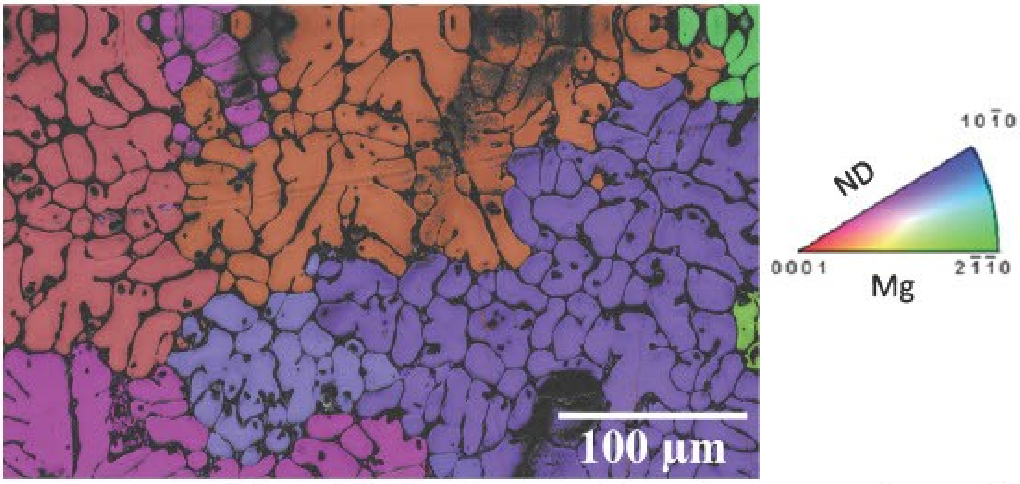

Figure SM1: inverse pole figure (IPF) and band contrast (BC) maps of as cast Mg-5.21Al-3.18Ca alloy captured using a step size of 0.25 µm. Shows that grain size of this alloy is way larger than the cell size or, in other words, that phase boundaries do not necessarily correspond to grain boundaries.

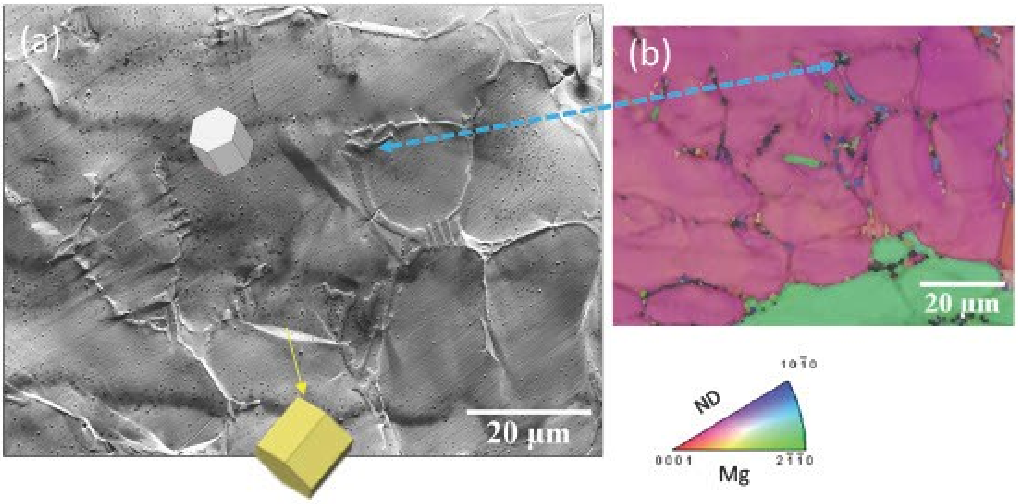

Figure SM2: (a) shows the same microstructural region in figure 1, (b) depict the IPF and BC maps superimposed on each other generated from EBSD using a step size of 0.35 µm. The blue arrows indicate the same region in both (a) and (b). This clearly shows that the area shown in figure 1 is made of only one grain. Phase boundaries do not correspond to grain boundaries. The tensile twin orientation is marked with yellow unit cell and highlighted using yellow arrow. The IPF map shown here is part of data that has been already published in our previous work [1].

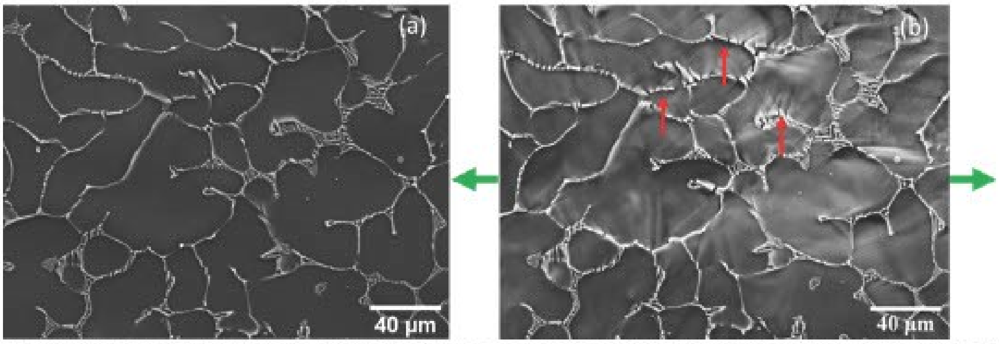

Figure SM3 (a) and (b): Microstructures of the as cast alloy before and after tensile deformation (up to a global strain of 6 %) at 170 °C. Morphology of Laves phase is largely unaffected with the increase in temperature. Cracks in the Laves phase are observed after deformation only (some of the cracks are highlighted with red arrows). Green arrows represent the tensile direction. Data represented in (a) has been already published in our previous work [1].

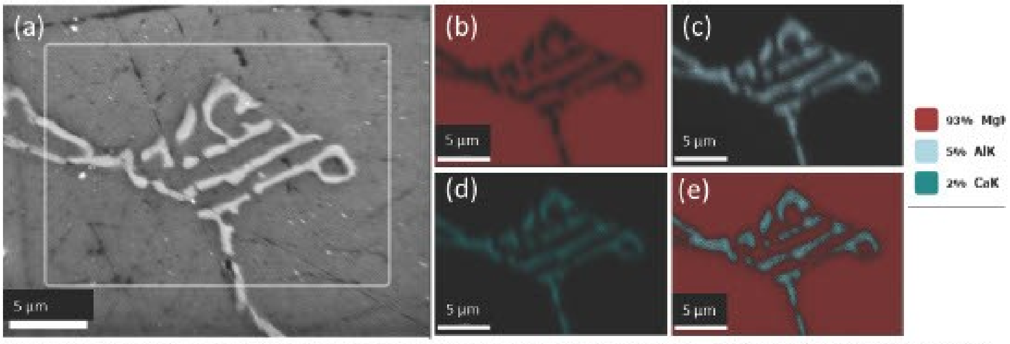

Figure SM4: a) SE image in the as-cast state from Mg-5.21Al-3.18Ca, white rectangle depicts the area investigated with EDS, b)-d) corresponding EDS signal distribution maps for Mg, Al and Ca, and e) cumulative EDS map for all three elements.

References

[1] M. Zubair, S. Sandlöbes-Haut, M.A. Wollenweber, K. Bugelnig, C.F. Kusche, G. Requena, S. Korte-Kerzel, Strain heterogeneity and micro-damage nucleation under tensile stresses in an Mg–5Al–3Ca alloy with an intermetallic skeleton, Mater. Sci. Eng. A. (2019). https://doi.org/10.1016/j.msea.2019.138414.

8. Research Publication 4 – Co-deformation Between the Metallic Matrix and Intermetallic Phases in a Creep-Resistant Mg-3.68Al-3.8Ca Alloy

M. Zubair, S. Sandlöbes-Haut, M. Lipińska-Chwałek, M. A. Wollenweber, C. Zehnder, S. Schröders, J. Mayer, J.S.K-L. Gibson, S. Korte-Kerzel, Co-deformation Between the Metallic Matrix and Intermetallic Phases in a Creep-Resistant Mg-3.68Al-3.8Ca Alloy, Materials and Design 210 (2021) 110113.

The paper elaborates the effect of orientation and the presence of Laves phases on the deformation behaviour of α-Mg matrix. Further, experimental evidence of co-deformation of metallic and intermetallic phases is presented and a strain transfer mechanism based on experimental results is proposed. The mechanical response of the individual microstructural constituents is also determined over a range of temperature varying from 23-170 °C. Micro- and nanoindentation in combination with SEM, EBSD and TEM are used for this purpose. This study answers the 4th, 5th and 6th research question raised in section 1.1.

Materials & Design 210 (2021) 110113

Contents lists available at ScienceDirect

Materials & Design

journal homepage: www.elsevier.com/locate/matdes

Co-deformation between the metallic matrix and intermetallic phases in a creep-resistant Mg-3.68Al-3.8Ca alloy

M. Zubair [a,b,*], S. Sandlöbes-Haut [a], M. Lipińska-Chwałek [c,d], M.A. Wollenweber [a], C. Zehnder [a], J. Mayer [c,d], J.S.K.-L. Gibson [a], S. Korte-Kerzel [a]

[a] *Institute for Physical Metallurgy and Materials Physics, Kopernikusstr. 14, RWTH Aachen University, 52074 Aachen, Germany*
[b] *Department of Metallurgical and Materials Engineering, G.T Road, UET Lahore, Pakistan*
[c] *Central Facility for Electron Microscopy, RWTH Aachen University, Ahornstraße 55, 52074 Aachen, Germany*
[d] *Ernst Ruska-Centre for Microscopy and Spectroscopy with Electrons (ER-C), Leo-Brandt-Str. 1, 52428 Forschungszentrum Jülich, Germany*

HIGHLIGHTS

- The C14 Mg_2Ca Laves phase retains its hardness up to at least 200 °C.
- Despite significant strength differences, slip transfers from α-Mg to the C36 phase.
- An orientation relationship between α-Mg and C36 basal planes exists at 82 ± 10°.
- Slip transfer into C36 Laves phase occurs along basal planes.
- The mechanism of co-deformation and possible future work directions are explained.

GRAPHICAL ABSTRACT

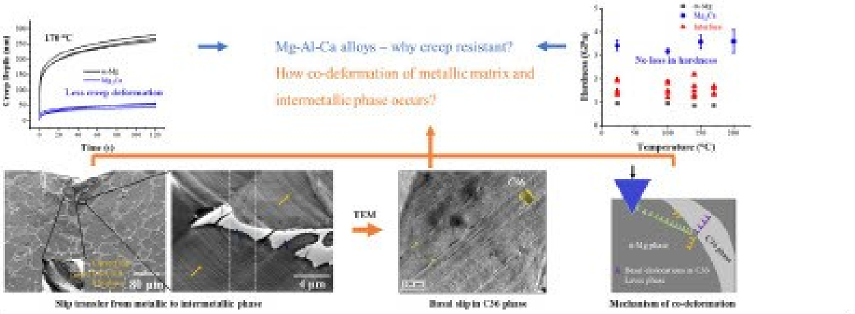

ARTICLE INFO

Article history:
Received 28 June 2021
Revised 22 August 2021
Accepted 12 September 2021
Available online 14 September 2021

Keywords:
Electron microscopy
Mg alloy
Mechanical properties
Micro-/nanoindentation
Co-deformation

ABSTRACT

The microstructure of Mg-Al-Ca alloys consists of a hard intra- and intergranular eutectic Laves phase network embedded in a soft α-Mg matrix. For such heterogeneous microstructures, the mechanical response and co-deformation of both phases under external load are not yet fully understood. We therefore used nano- and microindentation in combination with electron microscopy to study the deformation behaviour of an Mg-3.68Al-3.8Ca alloy.

We found that the hardness of the Mg_2Ca phase was significantly larger than the α-Mg phase and stays constant within the measured temperature range. The strain rate sensitivity of the softer α-Mg phase and of the interfaces increased while activation volume decreased with temperature. The creep deformation of the Mg_2Ca Laves phase was significantly lower than the α-Mg phase at 170 °C. Moreover, the deformation zone around and below microindents was dependant on the matrix orientation and was influenced by the presence of Laves phases. Most importantly, slip transfer from the α-Mg phase to the $(Mg,Al)_2Ca$ Laves phase occurred, carried by the basal planes. Based on the observed orientation relationship and active slip systems, a slip transfer mechanism from the soft α-Mg phase to the hard Laves phase is proposed. Further, we present implications for future alloy design strategies.

© 2021 The Authors. Published by Elsevier Ltd. This is an open access article under the CC BY-NC-ND license (http://creativecommons.org/licenses/by-nc-nd/4.0/).

---

* Corresponding author.
E-mail address: zubair@imm.rwth-aachen.de (M. Zubair).

https://doi.org/10.1016/j.matdes.2021.110113
0264-1275/© 2021 The Authors. Published by Elsevier Ltd.
This is an open access article under the CC BY-NC-ND license (http://creativecommons.org/licenses/by-nc-nd/4.0/).

1. Introduction

Increased fuel economy and the reduction of harmful emissions are the key factors behind a growing interest in the use of magnesium alloys for automotive applications [1–3]. Mg-Al-Ca alloys are among the most important alloys proposed for elevated- to high-temperature automotive applications (125–200 °C) such as powertrains [4]. They are well-known for their low weight, good creep resistance [5–8], and thermal stability [9] while maintaining good specific strength [4,10].

Mg-Al-Ca alloys consist of a dual-phase microstructure: a soft α-Mg matrix reinforced with hard intermetallic Laves phases in the form of an interconnected network. Laves phases are a prominent class of intermetallic compounds with an AB_2 stoichiometry and a fairly complex crystal structure [11,12]. Three types of Laves phases are known in Mg-Al-Ca alloys: Al_2Ca (C15), $(Mg,Al)_2Ca$ (C36) and Mg_2Ca (C14), which form during solidification as a result of the eutectic reactions: L → α-Mg + C36 and L → α-Mg + C14 (~514 °C, transformation temperature) [13]. The Ca/Al ratio controls the type(s) of Laves phase(s) formed in the microstructure [14–16]. In alloys with a high Ca/Al ratio (~1), the Laves phases formed in the as-cast microstructure are either $(Mg,Al)_2Ca$ + Mg_2Ca (as in the present work) or Mg_2Ca (if the ratio is significantly higher than ~ 1). At room temperature (RT), the critical resolved shear stress (CRSS) for basal slip in Mg amounts to < 1 MPa [17], while the CRSS are < 10 MPa for tensile twinning [18,19], ≈ 39 MPa for prismatic slip [20] and ≈ 40–44 MPa for pyramidal slip [21,22]. These values change with temperature and composition (addition of alloying elements) [19,20,23–27]. The CRSS values of basal, prismatic and pyramidal slip in Laves phases are well above the values of pure and alloyed Mg; e.g. for the Mg_2Ca phase, the CRSS for basal slip has been reported based on micro-compression experiments to amount to ≈0.52 GPa, for prismatic slip ≈0.44 GPa and ≈0.53 GPa for 1st order pyramidal slip [28]. The hardness (related to the resistance to dislocation glide) of the other Laves phases in the Mg-Al-Ca system is even higher than that of the Mg_2Ca Laves phase [29]. The difference, therefore, between the CRSS required to activate basal, prismatic, or pyramidal slip in both phases amounts to at least two orders of magnitude (see Fig. SM 1). Under external loading, it is then expected that the soft α-Mg matrix will deform first. The Laves phase skeleton is also expected to restrict the dislocation movement in the matrix and will correspondingly affect the deformation occurring in the soft phase.

In order to improve the alloys' deformation and failure behaviour in application, it is essential to understand the co-deformation behaviour of the two, mechanically very different phases (soft α-Mg and hard Laves phases) under external loading at different temperatures and time scales.

Therefore, the present study addresses the following key aspects related to the deformation behaviour of a dual phase Mg-3.68Al-3.8Ca alloy:

1. Mechanical properties of the individual phases and thermally activated deformation mechanisms, determined over a temperature range spanning from room temperature to an application temperature of 170 °C,
2. The effects of matrix orientation and presence of Laves phases on the deformation of the α-Mg matrix,
3. Slip transfer from the soft α-Mg phase to the hard intermetallic Laves phase.

All these aspects were studied using a combination of nano and microindentation, scanning electron microscopy (SEM), electron backscatter diffraction (EBSD) and transmission electron microscopy (TEM).

2. Experimental methods

A permanent mould cast Mg-3.68Al-3.8Ca (referred to as AX44 throughout the paper) and a master alloy Mg-30Ca consisting of large areas of Mg_2Ca Laves phase (both in wt.%, here and below) were investigated in this study. The melting and casting procedures of alloy AX44 are described in [30], the master alloy was investigated in its as-received state. Separate disc-shaped specimens (~12.5 mm diameter, ~1 mm thickness) for nano- and microindentation testing were machined from the as-cast block and the master alloy by electric discharge machining. The specimen preparation routine used to prepare samples for microscopy, nano- and microindentation are described in [30,31].

The micro-/nano-mechanical behaviour of the alloy AX44 was investigated by nanoindentation (Nanomechanics InSEM-III) using a diamond Berkovich indenter tip (Synton MDP, Switzerland) and a continuous stiffness measurement (CSM) unit. The diamond area function (DAF) and frame stiffness were calibrated on a standard fused SiO_2 sample at room temperature according to the Oliver and Pharr method [32]. The indenter tip and specimen were heated separately to minimise thermal drift, which was stabilised below 0.1 nm/s. Nanoindentation testing was carried out within the temperature range from RT to 170 °C. Three different types of nanoindentation tests were performed on alloy AX44: i) constant strain rate (CSR) tests, ii) strain rate jump (SRJ) tests and iii) nanoindentation creep (relaxation) tests. All the nanoindentation tests on the AX44 alloy were performed on the same sample in a way that the sample was first heated up to a temperature of 170 °C using an in-situ nanoindenter and then all three types of tests were performed. Afterwards the temperature was decreased to 140 °C, and the same tests were done on a different location. Further tests at 100 °C and room temperature were carried out subsequently. As incorporation of Al, as evidenced by a reduction in lattice parameters and the presence of C15 stacking faults was reported for the C36 Laves phase at high temperature and after 100 or more hours [33,34], we performed the experiments all on the same sample with descending temperature to minimize the effect of this change in the C36 Laves phase on the deformation behaviour at different temperatures. Due to the increased size of the indents in the nanoindentation creep tests, these were also performed separately on the Mg_2Ca Laves phase present in the Mg-30Ca master alloy (Fig. SM 2). Besides that, CSR tests were also performed on the Mg-30Ca master alloy to determine the hardness of the Mg_2Ca phase over a range of temperature. High temperature CSR tests on Mg_2Ca phase were also conducted in a similar manner as mentioned for the AX44 alloy. The hardness obtained for the Mg_2Ca phase is an average of three different orientations. As these were the only tests performed on this sample, unless otherwise stated, the results presented here refer to the AX44 material.

CSR tests were carried out at a strain rate of 0.2 s^{-1} to a maximum load of 45 mN. The load was held constant at maximum load for one second before unloading. CSR, SRJ, and nanoindentation creep tests were performed at RT, 100 °C, 140 °C and 170 °C. During the SRJ tests, the strain rate was varied between 0.1 s^{-1} and 0.001 s^{-1} in two jumps between indentation depths of 500–800 nm. The creep tests were performed at a load of 16 mN, applied at a rate of 160 mN/s, which was then held constant for 120 s before unloading.

Microhardness tests were carried out using a Vickers hardness tester at a force of 0.5, 5 and 10 N at room temperature (RT) on alloy AX44. The holding time at maximum load for all micro indents was 15 s. The deformed regions below the indents were studied using the bonding-interface technique [35–37]. Flat, rectangular specimens (~7 × ~4 × ~3 mm, machined and metallographically prepared in the same way as mentioned for disc specimens) were used for this purpose. The polished surfaces of two flat specimens were glued together (using Crystal bond) and then the indents were made at the interface. The samples were then placed in acetone in order to dissolve the glue.

Microstructure characterisation was performed using secondary electron (SE) and back-scattered electron (BSE) imaging at 10–20 kV in a scanning electron microscope (SEM) (FEI Helios Nanolab 600i and Zeiss LEO1530). Electron backscatter diffraction (EBSD, FEI Helios Nanolab 600i) was carried out at an acceleration voltage of 20 kV.

Site specific preparation of the electron transparent samples for transmission electron microscopy (TEM) was performed with the aid of focused ion beam milling (FEI Helios Nanolab 600i). The FIB lamellas were prepared in such a way that the viewing direction was perpendicular to the indentation direction (the top of the lamellas is shown outlined in Fig. 6 and Fig. 9). TEM observations were performed at 200 kV (FEI Tecnai G2 F20) [38].

3. Results

3.1. Microstructure of the as-cast alloy

The as-cast microstructure of alloy AX44 is presented in Fig. 1 (a) and (b) with the aid of SEM-BSE images. The interconnected network of intermetallic Laves phases has been studied using SEM, TEM and energy dispersive X-ray spectroscopy (EDS) by other researchers [13,39,40] and found to consist of a mixture of two different morphologies in similar alloy systems (having comparable Ca/Al ratios). These correspond to two different Laves phases: i) coarse eutectic $(Mg,Al)_2Ca$ and ii) fine eutectic Mg_2Ca. In addition to intermetallic network, thin needle like Al_2Ca precipitates were also observed in the as-cast alloy in line with the previous work [41–43]. The EDS analysis and further details about the microstructural constituents of alloy AX44 are presented in a previous paper [30].

3.2. Nanoindentation

3.2.1. CSR tests

3.2.1.1. Hardness variation of all three microstructural constituents with temperature. Fig. 2 (a) shows the average hardness (at a depth of ~ 500 nm) of the α-Mg and Mg_2Ca phases from RT up to 170 °C and 200 °C, respectively. The scatter from averaging the values of the α-Mg phase at all temperatures is so small that it is hardly visible in Fig. 2 (a) (also given in Table 1). The hardnesses of a few randomly-selected indents at the interface are also represented in Fig. 2 (a) as red triangles. As the volume fractions vary for indents placed at the interface (see Fig. SM 3), individual data points are shown rather than an average and its deviation. The hardness of α-Mg phase decreases slightly while that of Mg_2Ca phase stays constant with temperature. The hardness at the interfaces is significantly higher than the hardness of the α-Mg matrix at all test temperatures. A small indentation size effect is apparent in the deformation of the α-Mg matrix at all temperatures, i.e, the hardness of the α-Mg matrix decreases with increasing depth (until ~ 1000 nm) (see Fig. 2 (b)). The indentation size effect (i.e. a decreasing hardness with increasing depth) is a well-known phenomenon in the indentation of crystalline materials and is attributed to the strain gradients produced beneath indents and the related density of geometrically necessary dislocations [44–46]. For the indents in the magnesium matrix, there is a slight increase in the mean hardness after a depth of ~ 1000 nm was reached because of the hardening effect from interfaces (Fig. 2 (b)).

3.2.1.2. Hardening from interfaces. Load-depth and hardness-depth curves of two different indents made at RT are given in Fig. 2 (c and d). The blue curves are from an indent made some distance away from a Laves phase, the red curves from an indent close to one. The hardness of both indents is nearly the same between 500 and 1000 nm, beyond which there is an increase in hardness for the indent made closer to the α-Mg/Laves phase interface (shown red). This increase in hardness is assumed to be because the interface blocks dislocation motion.

3.2.2. SRJ tests

Nanoindentation SRJ tests were performed to determine the strain rate sensitivity (SRS) of individual phases and other microstructural features, such as interfacial areas, in order to gain a deeper understanding of the thermally activated deformation mechanisms taking place in these regions. The strain rate sensitivity, m, was calculated according to [47–49]

$$m = \frac{\partial \ln H}{\partial \ln \dot{\varepsilon}} \tag{1}$$

where H is the hardness and $\dot{\varepsilon}$ is the indentation strain rate. $\dot{\varepsilon}$ can be determined using the true strain rate concept using [47,50]:

$$\dot{\varepsilon} = \left(\frac{1}{h}\right)\left(\frac{dh}{dt}\right) = \frac{\dot{h}}{h} = \frac{1}{2}\left(\frac{\dot{P}}{P} - \frac{\dot{H}}{H}\right) \approx \frac{1}{2}\frac{\dot{P}}{P} \tag{2}$$

where h is the contact depth, and P is the applied load. $\dot{h}$, $\dot{P}$ and $\dot{H}$ are the respective rates (with respect to time) of depth, load, and hardness.

The activation volumes, V^*, were calculated using [47,48,51–54]

$$V^* = 3\sqrt{3}kT\left(\frac{\partial \ln \dot{\varepsilon}}{\partial H}\right) \tag{3}$$

where k is the Boltzman constant and T is the absolute temperature.

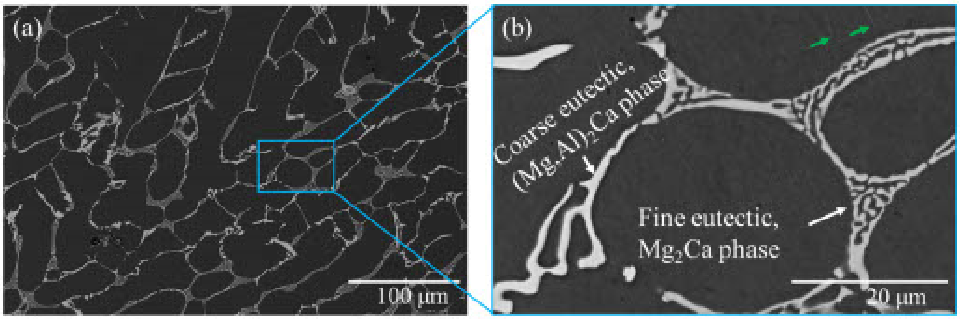

Fig. 1. Microstructure (SEM-BSE) of as-cast AX44 showing an interconnected Laves phase network consisting of coarse eutectic $(Mg,Al)_2Ca$ and fine eutectic Mg_2Ca. White arrows depict the intermetallic Laves phase while green arrows show the presence of Al_2Ca precipitates within the α-Mg matrix.

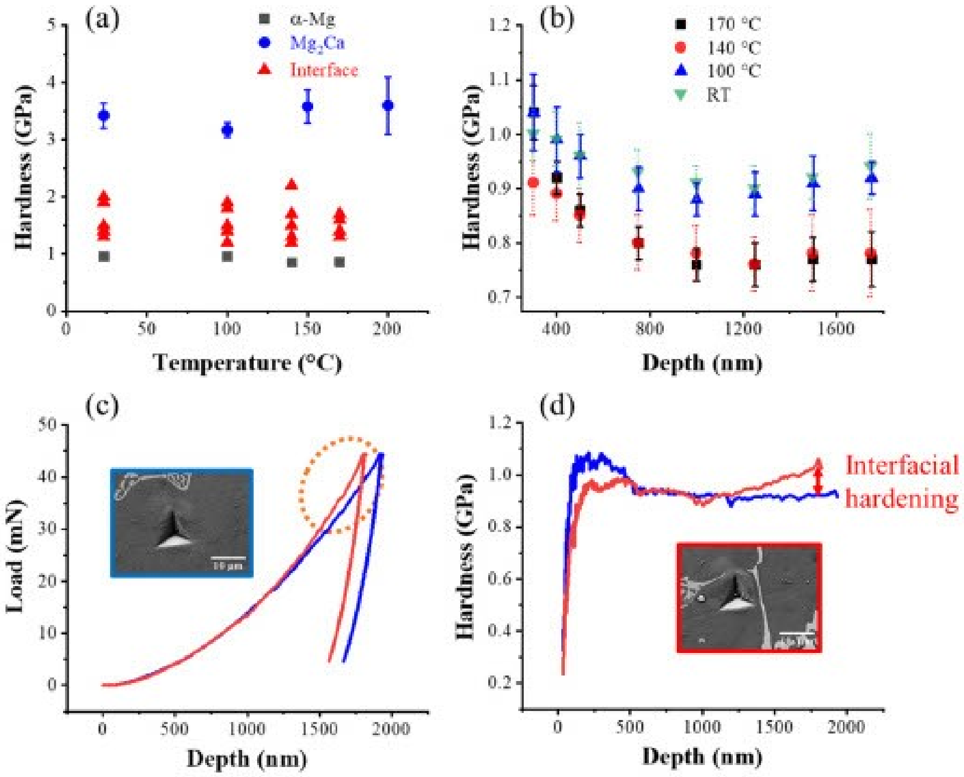

Fig. 2. (a) Average hardness of the α-Mg phase, Mg_2Ca phase and at the interface up to a temperature of 170 °C (for Mg_2Ca until 200 °C), (b) dependence of the hardness on the indentation depth for α-Mg matrix at all test temperatures, (c) load-depth, and (d) hardness-depth curves (at RT) highlighting the effect of interfaces on the depth dependent hardness. Hardness of the Mg_2Ca phase at RT was taken from [28].

Table 1
Hardness at a depth of 500 nm, m and V* values of the α-Mg phase and α-Mg/Laves phase interfaces at different temperatures.

Temp (°C)	Hardness (α-Mg), [GPa]	Strain rate sensitivity, m α-Mg phase	Interface	Activation volume, V* [nm^3 (b^3)] α-Mg phase nm^3 [b^3]	Interface [nm^3]
RT	0.96 ± 0.06	0.004 ± 0.002	0.006 ± 0.001	7.66 ± 3.70 (232 ± 112)	3.35 ± 0.91
100	0.96 ± 0.04	0.013 ± 0.006	0.016 ± 0.007	2.84 ± 1.12 (86 ± 34)	1.48 ± 0.82
140	0.85 ± 0.05	0.016 ± 0.006	0.020 ± 0.006	2.63 ± 1.18 (79 ± 36)	1.27 ± 0.40
170	0.86 ± 0.03	0.023 ± 0.009	0.024 ± 0.008	2.31 ± 0.87 (70 ± 26)	1.46 ± 0.54

The hardness-depth and modulus-depth curves are shown in Fig. 3 (a) and (b), for two representative indents performed at 170 °C within the α-Mg phase and at the α-Mg/Laves phase interface, respectively. Both microstructural regions showed an indentation size effect below 1000 nm, therefore, linear fitting was carried out for each strain rate jump in the hardness-depth curve. The instantaneous hardness values (measured right before (H($\dot{\varepsilon}_1$)) and after the strain rate jump (H($\dot{\varepsilon}_2$)) as depicted in the magnified region of Fig. 3 (a)) were then used to calculate *m* and *V** as suggested by Maier et al. [45] and Wu et al. [55].

The magnitude of the hardness change with strain rate in the α-Mg phase increased with temperature. Consequently, the value of *m* also increased and amounts to 0.004 at RT and 0.023 at 170 °C (details in Table 1). The indents made across α-Mg-Laves phase interfaces revealed that this microstructural region exhibits a similar strain rate sensitivity as that of the α-Mg phase at all testing temperatures, despite the significantly increased hardness. The values of the strain rate sensitivity were calculated from a minimum of eight indents at all testing temperatures (except RT, where six indents were used to calculate *m*). A size effect in *m* was observed for the α-Mg phase (see Fig. SM 4) and the *m* values given in Table 1 are average values at all strain rate jumps in between 500 and 900 nm.

Table 1 lists the values of the activation volume, *V**, for the α-Mg phase and α-Mg/Laves phase interfaces in nm^3 and b^3, respectively, when considering the <a> Burgers vector of Mg (3.21×10^{-10} m) [54,56] at various temperatures. There is a significant decrease in V* from RT to 100 °C, but with a further increase in temperature up to 170 °C it remains relatively constant (within the measurement noise) for both the α-Mg phase and α-Mg/Laves phase interfaces. In general, however, the α-Mg/Laves phase interfacial regions possessed lower activation volumes than the α-Mg phase at all testing temperatures. Several researchers [51,57,58] have used modulus compensated hardness to calculate activation energies, however, in this work the modulus decreased at the nearly same rate as the hardness which precludes the calculation of the activation energy and thermally activated mechanisms in this manner. We therefore rely solely on the activation volumes determined at each temperature.

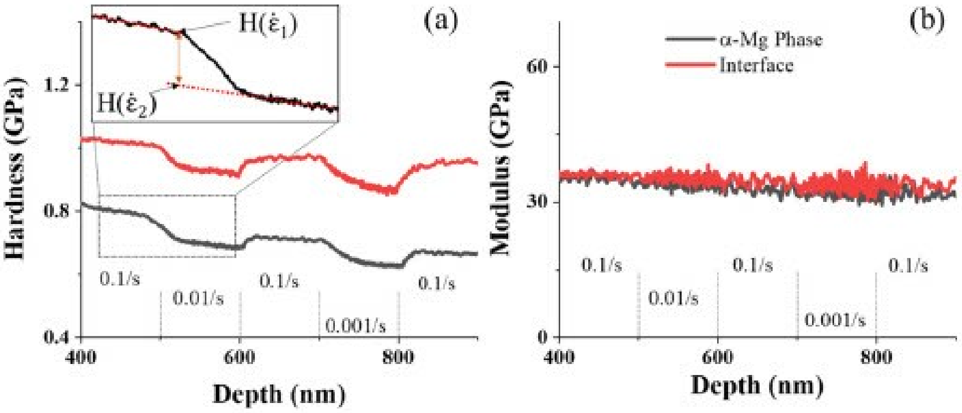

Fig. 3. a) Variation of hardness with strain rate of the α-Mg phase and α-Mg/Laves phase interfaces at 170 °C and b) modulus vs depth curves with strain rate for the α-Mg phase and α-Mg/Laves phase interfaces at the same temperature. H($\dot{\varepsilon}_1$) is the value of hardness before the strain rate jump and H($\dot{\varepsilon}_2$) represents the value of hardness directly after the strain rate jump, found by extrapolating the hardness-depth curve backwards once the transient had stabilised.

3.2.3. Nanoindentation creep testing

As the investigated alloys are designed for elevated-temperature applications, nanoindentation creep tests were also performed on alloy AX44 and the Mg-30Ca master alloy (consisting of large areas of Mg_2Ca Laves phase) at room temperature, 100 °C, 140 °C and 170 °C. Fig. 4 shows the fitted creep curves of the α-Mg phase (present in alloy AX44) at various temperatures. The creep rate in indentation creep testing can be related to the nominal pressure (p_{nom} = P/A, where P is the applied load and A is the contact area of indentation) or hardness according to Eq. (4) [59,60]

$$\dot{\varepsilon} = \left(\frac{1}{h}\right)\left(\frac{dh}{dt}\right) = B(p_{nom})^N \tag{4}$$

with h being the indentation depth, B a material constant, and N the stress exponent obtained from nanoindentation.

The creep depth increased, and the stress exponent decreased with increasing temperature, Fig. 4 (a) and (b), respectively. The nanoindentation stress exponent of this alloy was nearly four times higher than the stress exponent obtained previously from uniaxial tensile testing (n = 5.42) at the same temperature of 170 °C [30]. This discrepancy between (nano)indentation creep and macroscopic creep tests is relatively common [61,62], and can largely be explained by the fact that the stress and strain levels in nanoindentation using a Berkovich indenter are significantly higher than that during macroscopic uniaxial tensile testing. Accordingly, it is generally assumed that the hardness resulting from a Berkovich indenter corresponds to a flow stress at 8% strain [57,63]. A similar difference between the stress exponents obtained from nanoindentation creep tests and macroscopic creep tests was also observed by Wu et al. [61].

Nevertheless, the indentation creep tests allowed a comparison between the α-Mg (present in the AX44 alloy) and Mg_2Ca (present in the Mg-30Ca master alloy) phases at the same load (16 mN) and temperature (170 °C) (Fig. 5 (a and b)), showing that creep deformation was nearly 4.5 times lower in the Mg_2Ca phase than in the α-Mg phase. Moreover, the hardness of the Mg_2Ca phase is significantly higher than that of the α-Mg phase. There exists an elegant numerical agreement between creep depth and hardness of both phases. However, caution must be taken while using short term hardness tests as a proxy for more laborious indentation creep testing, at least for determining relative behaviour between phases. This is because sometimes the rate of hardness loss changes with increasing or decreasing strain rate as evident in Fig. SM 5 and as reported by Mathur et al. [57] while working with $Mg_{17}Al_{12}$ phase.

3.3. Microindentation

The microhardness of the as-cast AX44 at 5 N was determined as 61.2 ± 3.5 HV. In line with previous work [30], cracks in the Laves

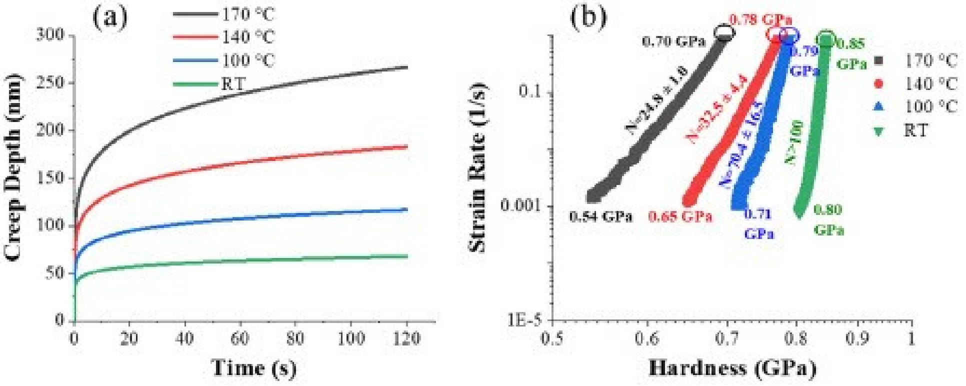

Fig. 4. (a) Creep depth as a function of temperature of the α-Mg phase (present in alloy AX44); (b) strain rate vs hardness of the α-Mg phase at various temperatures, the first data point in the graph is highlighted by open circles.

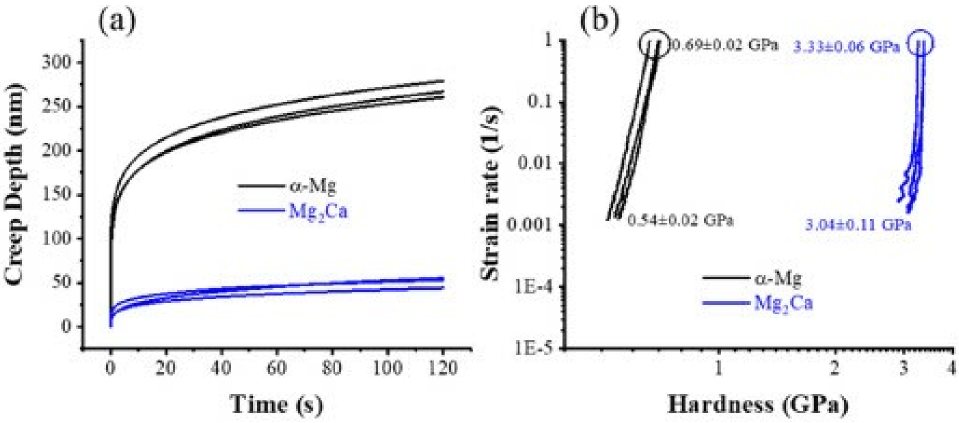

Fig. 5. (a) Nanoindention creep curves for the α-Mg phase and the Mg_2Ca phase (present in the Mg-30Ca master alloy), (b) Strain rate-hardness curve for α-Mg and the Mg_2Ca phase, the first data points are highlighted with open circles.

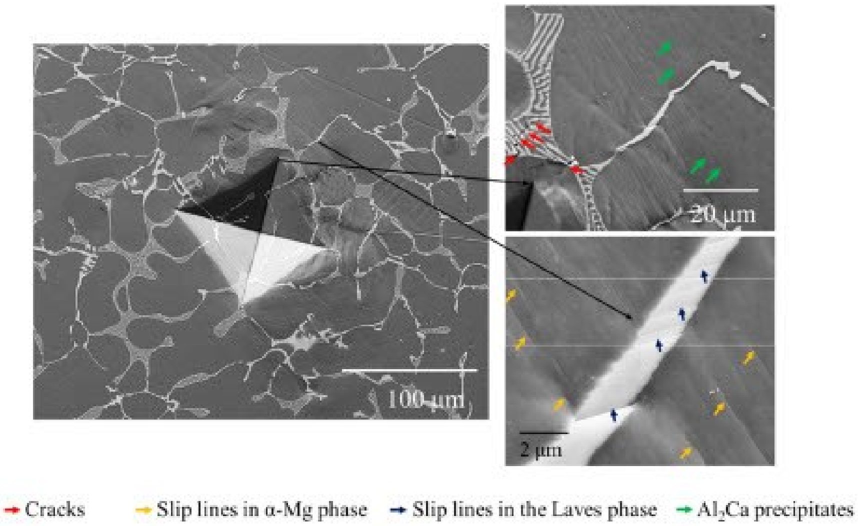

Fig. 6. SEM (SE) images of a microindent at 5 N performed on alloy AX44. The magnified regions are shown as insets. The red arrows indicate cracks in the Mg_2Ca and $(Mg,Al)_2Ca$ Laves phases, green arrows highlight Al_2Ca precipitates, orange arrows show slip lines in the α-Mg phase and blue arrows depict slip lines in the $(Mg,Al)_2Ca$ Laves phase. The dotted white rectangle indicates the region of the FIB lamella cut.

phase were observed within the direct proximity of the indents. In addition, parallel slip lines were observed on the sample surface around the indent (Fig. 6). Coincident positions of the slip lines at the interface between the α-Mg matrix and the $(Mg,Al)_2Ca$ phase (see Fig. 6) indicate that co-deformation of both phases has occurred.

As is expected from a hexagonal metal, the deformation zone in the α-Mg phase is strongly orientation-dependent, i.e. the presence of twins and slip lines around indents are significantly affected by the orientation of the α-Mg phase. Fig. 7 shows an inverse pole figure (IPF) map superimposed with band contrast (BC) map (also known as pattern quality) together with the corresponding SE micrographs of microindents in alloy AX44. It can be seen in Fig. 7 (a-d) that the appearance of the area around the microindents is orientation dependent. Further, formation of cracks in the Laves phase was observed at places where slip lines in the α-Mg phase intersect with the Laves phase, as indicated in Fig. 7 (e) and (f), which is in line with observations reported in previous work [31], where cracks were observed at similar regions in macroscopic uniaxial tensile deformation.

The presence of Laves phases further modifies the shape of the deformation zone. Fig. 8 (a) shows superimposed IPF and BC maps of the alloy AX44, with microindents placed at two different locations within the same grain: near the $(Mg,Al)_2Ca$ Laves phase (Fig. 8 (b)) and away from the Laves phase network (Fig. 8 (c)). The indentation-induced deformation twinning of the α-Mg matrix, (as confirmed by post-deformation EBSD) was observed around the indent (indicated with a dashed ellipse in Fig. 8 c),) in the Laves-phase-free area, but deformation twinning was suppressed in the vicinity of the hard Laves phase despite the same crystal orientation and the same relative position to the indent (see Fig. 8 (b)). This demonstrates the importance of co-deformation studies, as there is a clear effect of the intermetallic skeleton.

Finally, it was observed that in addition to the previously shown co-deformation resulting from dislocation slip in the α-Mg phase (Fig. 6), similar co-deformation can be introduced from other deformation structures, as indicated by the green arrow in Fig. 8 (d). Here, the deformation mechanism in the α-Mg is most likely

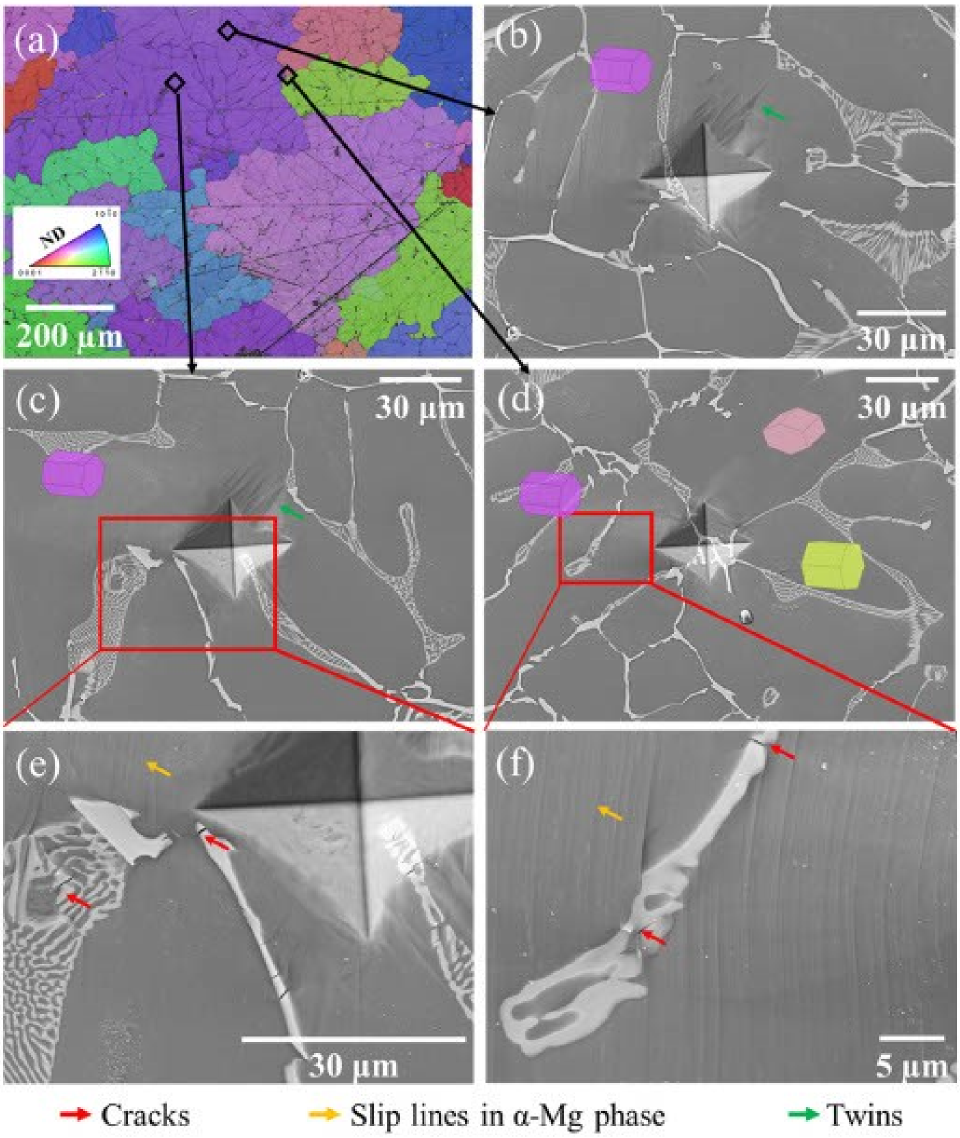

Fig. 7. Microstructure and deformation behaviour in alloy AX44. (a) Inverse pole figure (IPF) and band contrast (BC) maps superimposed on each other (black arrows indicate positions of the indents presented in detail in (b)-(d)), (b) and (c) SE images of 500 mN indents in one grain with twin formation around the indentations, (d) SE image of an indent made at a grain triple point. (e) and (f) show magnified images of the regions indicated in (c) and (d), respectively.

deformation twinning (only one small twin like region is present, assumed from visual analysis as it was not possible to confirm this as a twin by EBSD, as compared to multiple twins present in Fig. 8 (c)), but it is nevertheless present adjacent to slip lines in the Laves phase.

Having demonstrated the effect of crystal orientation and Laves phases on the deformation microstructure visible around the indents at the indented sample surface (Fig. 7 and Fig. 8), the sub-surface deformation is now presented. These studies are intended to determine whether the deformation observed in the presence of a free surface are representative for the mechanisms that occur in the bulk.

Fig. 9 (a-d) shows SE images of the deformed sub-surface regions of the indents, produced at 5 (a,b) and 10 N (c,d)). Fig. 9 (a) and (b) highlight dislocation slip (orange arrows) in the α-Mg phase as well as cracking in the Laves phase (red arrows). The curved slip lines, as indicated in the magnified inset in micrograph (c), are indicative of multiple active slip systems in the α-Mg phase. Fig. 9 (d) demonstrates co-deformation of the α-Mg and the Laves phases, evident from the parallel slip lines in the Laves phase (blue arrows) coincident with the slip lines in the matrix phase (orange arrows). Overall, the observed surface deformation around the indents (Fig. 6, Fig. 7 and Fig. 8), including the mix of co-deformation and cracking in the Laves phase, do indeed appear to be representative for deformation of the bulk material.

Cracks and slip transmission events from the α-Mg phase into the C36 Laves phase were observed under all three loading conditions (Fig. 6, Fig. 8 and Fig. 9). However, higher and more frequent instances of slip transmission were detected under higher loading, i.e. 10 N (see Fig. 9 and Fig. SM 6). In the sub surface analysis presented in Fig. SM 6, more instances of slip transfer are evident for the indent made at 10 N when compared to the indent made at 5 N.

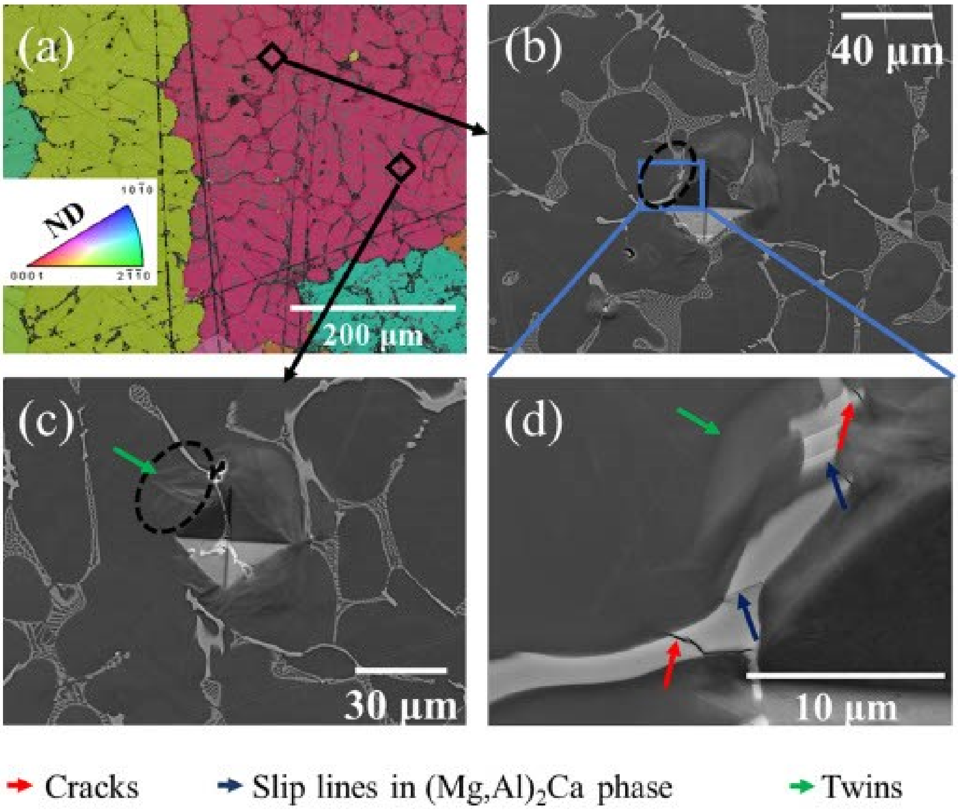

Fig. 8. (a) Superimposed IPF and BC maps of a grain containing two microindents. The position of the indents in the grain is highlighted by black squares and arrows in (a); (b) and (c) show the SE images of the two indents (made at 500 mN). The black dotted ellipses highlight differences in deformation behaviour. (d) Shows the magnified region highlighted by the box in (b). Twins in the α-Mg phase are represented by green arrows, red arrows depict cracks and blue arrows show slip lines in the $(Mg,Al)_2Ca$ Laves phase.

This is because the higher force in indentation generally results in high plastic strain across a larger volume, the plastic zone, causing the aggregation of high-densities of dislocations at the Mg/Laves phase interface. Therefore, higher loads seem to promote more slip transmission from the α-Mg to the C36 Laves phase.

3.4. TEM

Fig. 10 shows bright field (BF) TEM and corresponding selected area electron diffraction (SAED) images of the microstructure observed in a FIB lamella cut from the surface as indicated in Fig. 6 by a white dotted rectangle (located aside the indent - FIB cut plane parallel to the indentation direction and perpendicular to the sample surface). The slightly curved volume of C36 Laves phase in the lamella is surrounded by a single Mg matrix (α-Mg) grain.

The crystallographic orientation of both phases was determined using SAED. The Mg matrix located on either side of the C36 belongs to the same matrix grain exhibiting, accordingly, almost the same orientation (see Fig. 10 (a)), with negligible variation (below 2° across the lamella) related mainly to the bending of thin samples. The C36 phase grain also exhibits the same crystallographic orientation across the FIB lamella (<2.5° misorientation). Analysis of the relative crystallographic orientation of both phases based on corresponding SAED data (see Fig. 10 (b) and (c)), revealed an almost perpendicular orientation (within ± 3°) of their basal planes. In particular, $\angle[1\bar{2}10]_{C36}, [0001]_{\alpha-Mg} = 3^\circ$ and $[10\bar{1}0]_{C36} \parallel [3\bar{4}10]_{\alpha-Mg}$. BF images in Fig. 10 (a) and (d), show the microstructure observed with the electron beam direction $B \parallel [10\bar{1}0]_{\alpha-Mg}$. Stacking faults (SFs) in the α-Mg phase are observed in (a) and (d) along (or very close to) $[10\bar{1}0]_{\alpha-Mg}$. The crystallographic direction in an edge-on orientation (with the SF habit plane perpendicular to the image plane and parallel to the viewing/beam direction), reveals dark, thin, and straight lines (indicated by yellow arrows). Identification of SFs in the overview (a) is rather difficult due to strong diffraction contrast present in the Mg grain (dark, blurry appearance), resulting from the in-axis grain orientation (i.e. observation condition with exact $B \parallel [10\bar{1}0]_{\alpha-Mg}$). Accordingly, a better presentation of the edge-on SFs in the Mg matrix is shown in the magnified BF image presented in (d), where diffraction contrast is lowered by slight sample tilt (~2° away from the diffraction condition $B \parallel [10\bar{1}0]_{\alpha-Mg}$). The corresponding SAED pattern for the Mg grain in the orientation presented in (a) is shown in (b), while the SAED pattern for the $[10\bar{1}0]_{\alpha-Mg}$ condition, i.e. close to the observation conditions applied in (d) is shown in (e). Fig. 10 (f) presents an SAED pattern of the other main zone axis of the hexagonal Mg $[11\bar{2}0]_{\alpha-Mg}$, acquired with the sample tilted 30° away from the orientation conditions applied in (d).

The presence of dislocations on a non-basal plane was also observed in the α-Mg matrix (e.g. curved dark lines, indicated in Fig. 10 (d) with blue arrows), evidencing the activation of a non-basal deformation system within the Mg matrix of the composite material. Within the C36 grain, dislocation contrast confined within defined slip planes was also observed (indicated by blue arrows in Fig. 10 (a)). Due to an unfavorable orientation of the slip planes almost parallel to the lamella plane, an edge-on observation and unambiguous confirmation of the crystallographic orientation

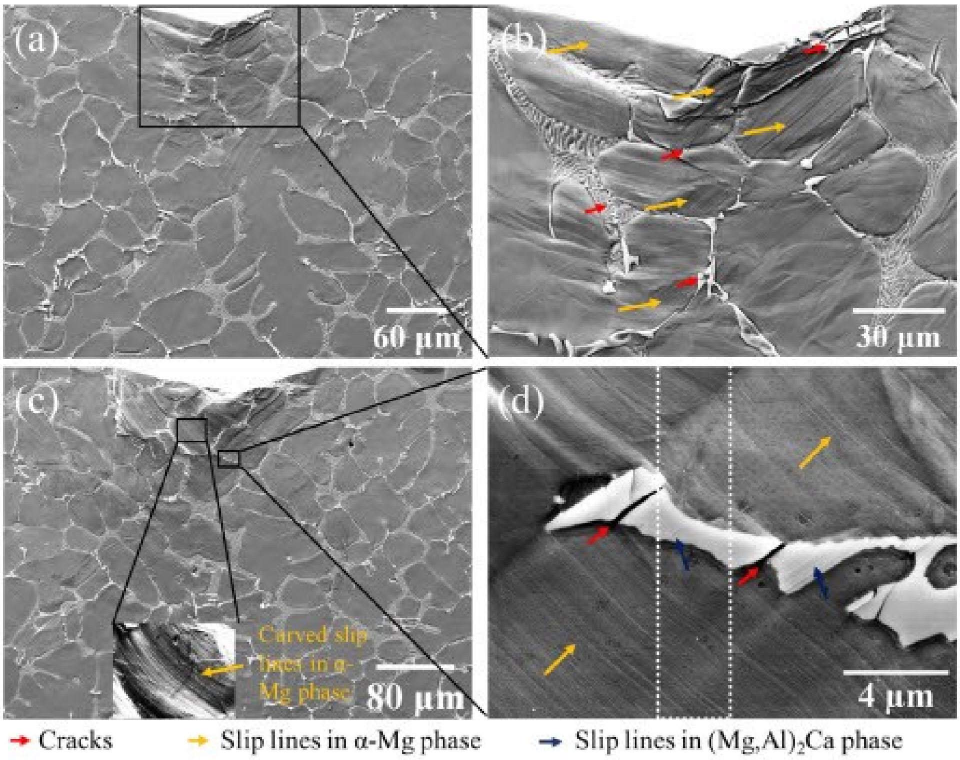

Fig. 9. SEM (SE) micrographs of the sub-surface region of indents at 5 N (a-b) and 10 N (c-d). Overview of the sub-surface features from an indent made at 5 N (a). (b) Represents the magnified image of the area highlighted with a black rectangle in (a). Overview of similar sub-surface features from an indent made at 10 N (c). Inset in (c) highlights the curved slip lines observed in the α-Mg matrix. (d) Reveals co-deformation of the α-Mg matrix and the Laves phases. Orange and blue arrows indicate the slip lines in α-Mg and Laves phases, respectively, while cracks are highlighted by red arrows. The white dotted rectangle shows the region from where the TEM lamella was lifted out.

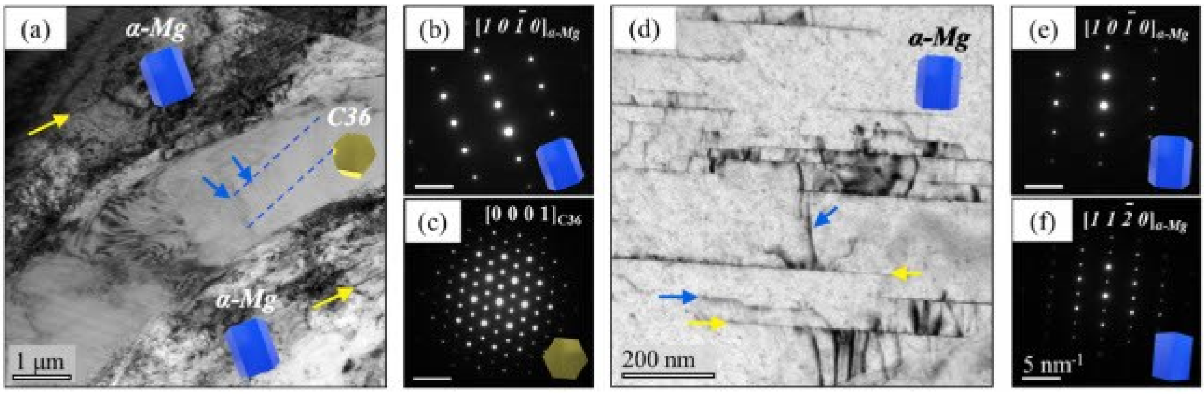

Fig. 10. Composite microstructure of the lamella as observed in TEM: a) BF overview image acquired with lamella orientation $B\|[10\bar{1}0]_{\alpha-Mg}$ with corresponding SAED of Mg matrix given in (b). c) SAED of the C36 grain shown in (a), observed in orientation $B\|[0001]_{C36}$. d) Magnified BF appearance of the Mg matrix structure with edge-on basal-plane SFs (yellow arrows) and non-basal dislocations (blue arrows). e) - f) SAED images of the Mg matrix shown in (d), acquired with sample orientation $B\|[10\bar{1}0]_{\alpha-Mg}$ and $B\|[11\bar{2}0]_{\alpha-Mg}$. Matrix and C36 orientation are visualised by blue and yellow hexagons, respectively. Images in (d-f) contain a 45° clockwise relative sample rotation with respect to those in (a-c).

of the habit plane was not possible in this sample. Nonetheless, a basal-slip co-deformation was postulated for the composite Laves phase taking into account the crystallographic orientation of the C36 grain, with $[0001]_{C36}$ tilted 17° away from the lamella plane normal (corresponding SAED is shown in Fig. 10 (c)), as well as the line direction of the intersections of the C36-dislocation slip habit planes with the lamella surface (indicated in Fig. 10 (a) with blue dashed lines).

Further insights into the crystallographic orientation of the related slip system were obtained with analysis of a second FIB lamella cut from the sample volume indicated in Fig. 9 with a white dotted rectangle, i.e. within the material volume located beneath the indent and parallel to the indentation direction but perpendicular to both the sample surface and the deformation sub-surface. The composite microstructure present in the lamella is shown in Fig. 11 (a). Again, matrix regions located on either side of the Laves phase belong to the same Mg grain, exhibiting accordingly the same crystallographic orientation. The C36 Laves phase consisted also of a single grain across the lamella. The local orientation relationship between the Mg matrix and the Laves phase identified was very similar as found for the lamella cut from the surface (Fig. 10). Basal planes of both hexagonal phases exhibited again almost perpendicular relative orientation, with $\angle[0001]_{C36}, [10\bar{1}0]_{\alpha-Mg} = 3^\circ$ and $[1\bar{2}10]_{C36} \| [\bar{1}2\bar{1}0]_{\alpha-Mg}$. A similar orientation relationship, specifically $\angle[0001]_{C36}, [0001]_{\alpha-Mg} = 82^\circ \pm 10^\circ$, was also observed in several other FIB lamellae from alloys having slightly different compositions but similar microstructures, as shown in [64] and in Fig. SM 7. The presence of basal slip traces was identified in the Mg matrix as well as in the C36 phase. Fig. 11 (b) and (c) show magnified BF images of the Mg matrix and C36 phase, at the extreme sample tilt conditions, corresponding to $B \| [\,1120]_{\alpha-Mg}$ (in (b)) and $B \| [10\bar{1}0]_{C36}$(in (c)). Basal-plane stacking faults of both phases are observed in the respective images in edge-on orientations (indicated in (b) and (c) with yellow arrows). Corresponding SAED patterns are presented in (d) and (e). It is important to note that BF images of planar defects in their edge-on orientations were acquired at extreme α and β tilt values of the TEM sample holder ->80° apart from each other (at the very limits of the TEM holder tilt capabilities). Accordingly, the projection thickness of the FIB lamella was exceptionally high, resulting in a relatively poor quality of the BF TEM images. Nonetheless, the presence of dislocations evidencing the activation of a non-basal deformation system within the α-Mg matrix was also observed here. Sets of dislocations piled-up at the α-Mg/Laves phase interface, confined within non-basal slip planes of the α-Mg grain are indicated in Fig. 11 (b) with blue arrows, while the line directions of the intersection of their slip planes with the lamella surface are approximately indicated by blue dashed lines.

4. Discussion

4.1. Nanoindentation studies

4.1.1. CSR tests

The RT hardness measured across α-Mg-Laves phase interface regions is higher than that of the α-Mg phase (which amounts to ≈ 0.95 GPa, see Fig. 2). In the case of indents specifically at the interface, the higher measured hardness is largely attributed to the higher hardness of the Laves phase when compared to the soft α-Mg phase, i.e. it occurs from a rule-of-mixtures effect, rather than strengthening resulting from the interfaces inhibiting dislocation motion. However, due to the complex microstructure and three-dimensional stress field from indentation, it is not possible to determine the specific volume fractions of each phase deformed by each indent and examine this phenomenon in more detail.

Specifically, the hardness of the Mg_2Ca phase was measured to be ≈ 3.42 GPa at RT [28], nearly 3.5 times higher than that of the α-Mg phase (≈ 0.95 GPa at RT). No drop in hardness of the Mg_2Ca phase was observed until 200 °C (see Fig. 2 (a)). This is somewhat consistent with the results of Kirsten et al. [65], who also reported only slight loss in the Brinell hardness with temperature for the Mg_2Ca phase up to the ductile-to-brittle-transition temperature ($0.59\,T_m$, where T_m is the melting temperature). The hardness measured across the α-Mg/Laves phase interfaces has the similar level at RT and at 170 °C. This clearly indicates that the Laves phase retains its hardness at least until 170 °C during the short interval CSR testing.

However, as expected, the hardness of the α-Mg phase decreases with temperature (see Table 1). It is therefore assumed that the superior creep properties of Mg-Al-Ca alloys when compared to conventional Mg-Al-Mn or AZ91 alloys [5–7] is caused by the fact that the Laves phases maintain their hardness with temperature up to at least 200 °C.

Moreover, it is clear from Fig. 2 (a and b) that the hardness of the α-Mg matrix decreases with temperature and also that an apparent indentation size effect (at depths below 1000 nm) is observed for the α-Mg matrix at all test temperatures. The indentation size effect is attributed to the density of GNDs generated due to the strain gradient underneath the indenter [44]. The effect is more pronounced at low depths, which are usually encountered in nanoindentation [44,46]. However, since the indentation size effect is not the focus of this study, it is not further discussed here. It can also be seen in Fig. 2 (b-d), that there is a slight but noticeable increase in mean hardness for the α-Mg phase after an indentation depth of ~ 1000 nm was reached. This is assumed to be caused by the back stress work hardening associated with the pile-up of dislocations at α-Mg/Laves phase interfaces surrounding the indent location at a greater distance.

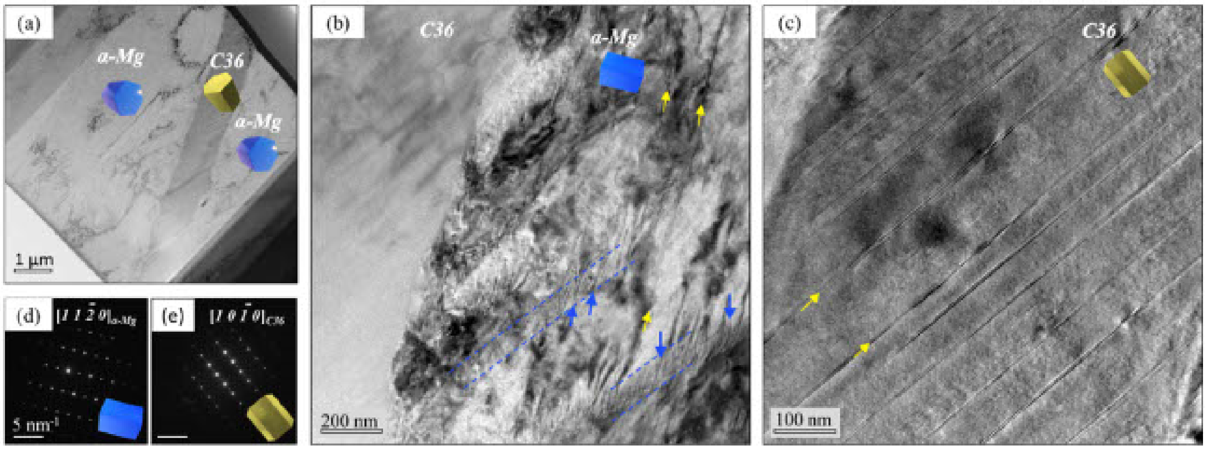

Fig. 11. Composite microstructure of the FIB lamella, observed in TEM: (a) BF overview image in the initial lamellae orientation (without any sample tilt). b) Magnified BF appearance of deformed α-Mg matrix in the lamella orientation $B \| [11\bar{2}0]_{\alpha-Mg}$. Basal-plane SFs (edge-on) and non-basal dislocations of the Mg matrix are indicated in (b) with yellow and blue arrows, respectively. c) Basal-slip SFs in C36 Laves phase (yellow arrows), observed in edge-on orientation at $B \| [10\bar{1}0]_{C36}$. d)-e) SAED patterns corresponding to the Mg matrix at $B \| [11\bar{2}0]_{\alpha-Mg}$ and Laves phase at $B \| [10\bar{1}0]_{C36}$, as presented in (b) and (c), respectively.

4.1.2. SRJ and creep tests

The strain rate sensitivity and activation volume are two important parameters that are connected to the deformation mechanisms of metallic materials [66]. Materials with a high strain rate sensitivity have a smaller activation volume and hence a higher probability of thermal activation of plasticity mechanisms [51,67]. The activation volume of fine-grained Mg alloys at room temperature was calculated to be within the range of 20–80 b^3 by Somekawa et al. [67], who concluded that the rate controlling mechanism was most likely dislocation cross-slip. Somekawa et al. [54] also carried out nanoindentation studies on coarse grained (~100 µm) pure Mg and Mg-0.3 at.% (Al, Li, Y and Zn) alloys at room temperature. They calculated activation volumes in the range of 45–105 b^3 depending on the different compositions. In these coarse grained Mg alloys, deformation twins were visible in the regions around indents, and it was assumed that these deformation twins play a similar role in coarse grained materials as grain boundaries in fine grained materials: acting as obstacles for dislocations [54]. Table 2 summarizes activation volumes and the associated mechanisms of different Mg alloys reported in the literature.

In the present study, the strain rate sensitivity of the α-Mg phase marginally increased from 0.013 ± 0.06 to 0.023 ± 0.009 and the activation volume slightly decreased from 86 ± 34 b^3 to 70 ± 26 b^3, when the temperature was increased from 100 °C to 170 °C. The values calculated in the present work are close to the values reported by Somekawa et al. [54,67] for fine and coarse grained Mg alloys. As mentioned, the plastic deformation of Mg is facilitated by deformation twinning and dislocation slip. Deformation twinning is not a thermally activated process but is important for the deformation of Mg alloys [54,69,70]. However, the strain rate sensitivity and activation volume values obtained from nanoindentation reveal thermal activation of the α-Mg phase. This means that in addition to the observed deformation twinning, thermally-activated deformation mechanisms are also active in the α-Mg phase. The V^* values obtained from nanoindentation SRJ tests are below 100 b^3 (at temperature ≥ 100 °C) indicating thermally activated dislocation cross-slip in the α-Mg phase similar to what has been reported by Somekawa et al. [54,67].

The activation volume of α-Mg/Laves phase ($(Mg,Al)_2Ca$ and Mg_2Ca) interfaces was slightly lower than that of the α-Mg phase at all testing temperatures (100, 140 and 170 °C, see Table 1). The hardness of the Mg_2Ca phase stays constant at least till 200 °C, which indicates negligible thermal activation in the temperature range investigated for this phase. However, a lower activation volume of α-Mg-Laves interfaces indicates that thermally activated mechanisms like interfacial sliding may be active to some extent in these interfacial regions. The interfacial sliding in this alloy system has been reported earlier [30,31,71].

It is evident from Fig. SM 5 that the N value for the Mg_2Ca phase appears to change at low strain rates (~ ≤ 0.01/s, i.e. in the creep experiments) and a temperature of 170 °C. The N value for the Mg_2Ca phase (at low strain rates) is nearly the same as that of the α-Mg phase. Further, a loss in hardness with holding time is also observed at low strain rate for the Mg_2Ca phase. This is consistent with the results published by Rokhlin et al. [29], who reported a loss in microhardness with increasing holding time at temperatures ≥ 150 °C. Unfortunately, our data for the Mg_2Ca phase (as can be seen in the Fig. SM 5) is affected by thermal drift. Therefore, we did not attempt to derive thermally activated mechanisms active in the Mg_2Ca phase based on these experiments.

Similar to what was observed during microindentation (Fig. 6 and Fig. 9), parallel slip lines on the surface of Laves phases (particularly in $(Mg,Al)_2Ca$) were also observed in the regions around nanoindents, indicating that deformation is confined to particular and equivalent crystallographic planes.

4.2. Co-deformation mechanisms

The CRSS values of all available slip systems differ highly for the α-Mg matrix and the Laves phases (see Fig. SM 1). It therefore might be expected that the probability of slip transfer from one phase to another is low. However, slip transfer from the soft α-Mg phase to Laves phase is exactly what is observed in this work.

Generally, this unexpected slip transfer can be attributed to two main reasons. Firstly, the slip behaviour observed from individual single crystal experiments cannot truly account for polycrystalline alloys. Specifically, in the case of polycrystalline Mg alloys, the presence of grain boundaries [72,73], alloying elements [74] and precipitates [75,76] dramatically affects the deformation behaviour and activation of non-basal slip systems. Moreover, the CRSS ratio between non-basal and basal slip systems estimated in polycrystalline Mg alloys is quite low (~2–3) in comparison to the estimates deduced from single crystal testing (~80–100) (Fig. SM 1). Therefore, non-basal slip is also readily observed at room temperature in several Mg alloys [77–79].

Secondly, stress concentrations caused by the pile-up of dislocations at the phase boundaries between the soft matrix and the hard Laves phases can promote slip transfer. Consequently, it is assumed that during indentation, basal dislocations in the α-Mg matrix start to glide first (see Fig. 6 and Fig. 7, where basal slip lines are readily evident around indents). However, their movement is blocked at the (C36) Laves phase boundaries due to the different CRSS, crystal structure, nature of dislocations and crystal orienta-

Table 2
Activation volumes and associated deformation mechanisms of pure Mg and Mg alloys.

Testing method	Material	Grain size	Activation volume (b^3)	Proposed mechanisms
Compression [68]	Pure Mg	120 µm	409	Forest dislocation activity
Compression [68]	Pure Mg	400 nm	42	Twinning
Compression [68]	Pure Mg	60 nm	12	Grain boundary sliding
Nanoindentation [67]	Pure Mg	~2–3 µm	25.3	Cross-slip
Nanoindentation [67]	Mg-0.31at% Al	~2–3 µm	80.8	Cross-slip
Nanoindentation [67]	Mg- 0.3at% Ca	~2–3 µm	80.8	Cross-slip
Nanoindentation [54]	Pure Mg	101.9 µm	45	Cross-slip
Nanoindentation [54]	Mg-0.3 at.% Al	83 µm	105	Cross-slip
Nanoindentation [54]	Mg-0.3at.%Zn	90.3 µm	93	Cross-slip
Nanoindentation SRJ [53]	ZK 60 (Mg-5.5Zn-0.5Zr)	~20 µm (25%) ~1–1.5 µm (75%)*	7.38	Grain boundary sliding
Tensile [69]	Pure Mg	2.1 µm	9.8 at < 10^{-4}/s & 15.2 at > 10^{-4}/s	Grain boundary sliding at < 10^{-4}/s and cross-slip at > 10^{-4}/s
Tensile [69]	Pure Mg	18.5 µm	20.1 at < 10^{-4}/s & 23.9 at > 10^{-4}/s	Cross-slip and multiple-slip

*Extruded alloy which was subjected to high pressure torsion resulting in a bi-modal grain size distribution.

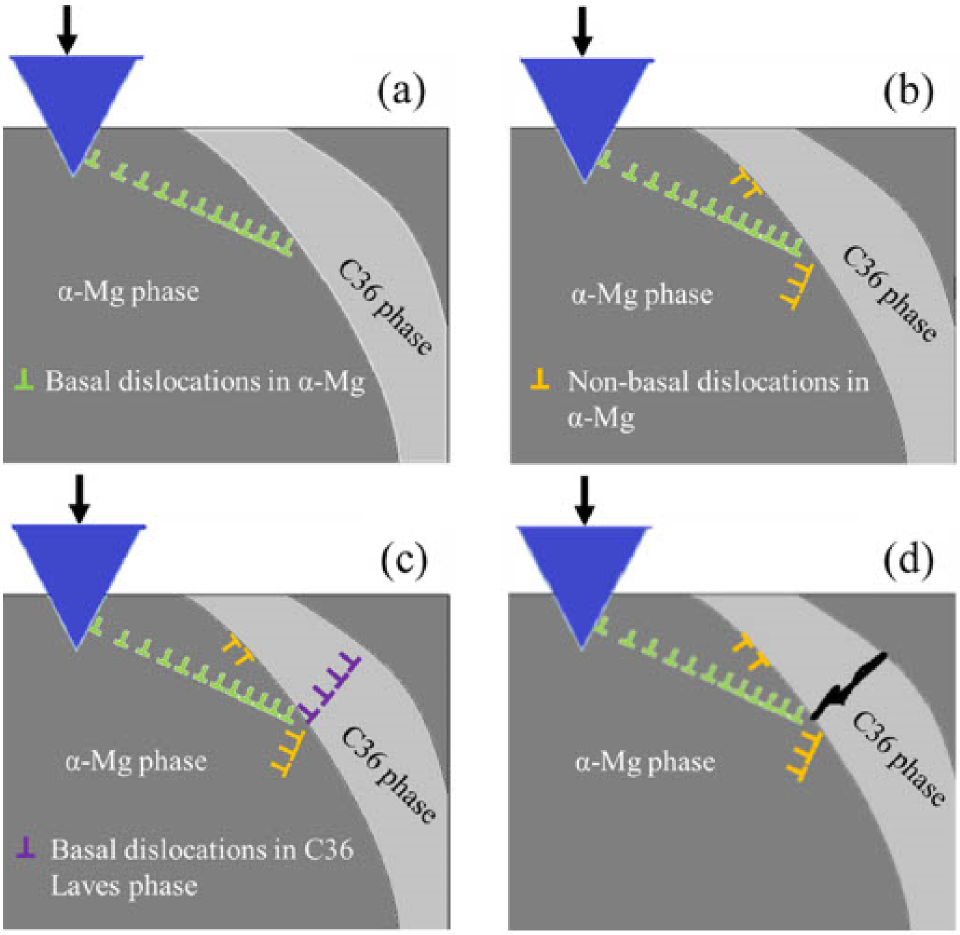

Fig. 12. Co-deformation mechanisms of soft α-Mg matrix with hard Laves phase, (a) basal slip in the α-Mg matrix and pile-up of dislocations at an α-Mg/Laves phase interface, (b) activation and generation of non-basal dislocations in the matrix close to the phase boundary, (c) deformation by basal slip in Laves phase or (d) cracking of the Laves phase at stress concentration points. (d) might occur after (c).

tion (see Fig. 10 and Fig. 11) of (C36) Laves phase and the α-Mg matrix. The blocking of dislocations creates pile-ups of dislocations at the phase boundaries and an associated strain gradient, shown by the increasing hardness of deep indents (Fig. 2 (b)) [80,81]. Phase boundaries are generally considered to be stronger obstacles to dislocation movement than grain boundaries [82–84]. This is because the transmission of dislocations across phase boundaries requires in most cases the nucleation of new dislocations due to the different crystal structures, crystal orientations and lattice parameters of both phases [82–84]. The pile up of dislocations will then create back stress work hardening in the α-Mg matrix. The compatibility and hardening effect by the dislocations pile ups can then activate several favourably orientated non-basal dislocations sources in the α-Mg matrix and at the phase boundaries. The pile up of non-basal dislocations at the α-Mg/Laves phase boundary is marked by blue arrows in Fig. 11 (b).

In addition to back stress work hardening of the soft phase, the pile up of basal and non-basal dislocations at the interface will create forward stresses in the C36 Laves phase [80,81]. The magnitude of the forward stress in the intermetallic phase can be several times higher than the applied stress and is usually calculated as

$$n \cdot \tau_a \quad (5)$$

where τ_a is the applied shear stress and n is the number of dislocations in the pile-up [81,85]. A high stress concentration can then trigger the activation of basal dislocations in the C36 Laves phase to release the stress concentration at the phase boundaries. A recent study by Guénolé et al. [64] presents the slip transfer mechanisms from the α-Mg phase to the Mg_2Ca Laves phase in a situation where both phases are aligned perpendicular to each other. They [64] found that under the application of a compressive stress, plasticity is nucleated in the α-Mg matrix and then the local stress concentrations at the α-Mg/Laves phase interface can induce the nucleation of prismatic < a > dislocation from the interface. The present work reports a similar orientation relationship between the α-Mg phase and the C36 Laves phase (see Fig. 10 and Fig. 11). However, in this work, basal slip, rather than prismatic slip, was observed in the C36 Laves phase.

The role of non-basal dislocations seems to be important for the activation of basal dislocation slip in the C36 Laves phase because of geometrical reasons. One is the very simple geometric compatibility factor widely used to estimate the ease of slip transfer. This Luster-Morris parameter, m', suggested by Luster and Morris, is calculated as (Eq. (6)) [86]:

$$m' = cos\phi . cos\kappa \quad (6)$$

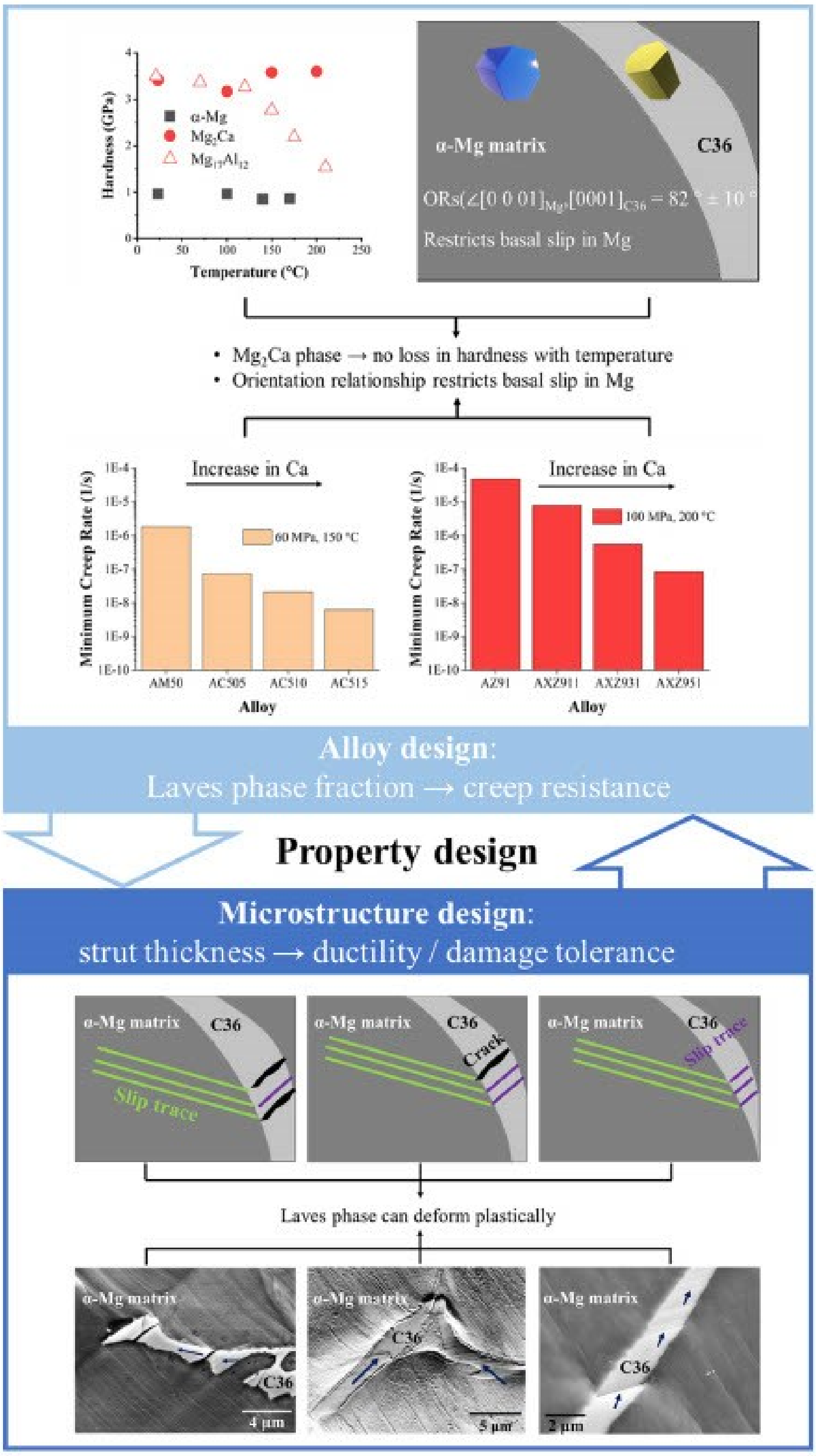

Fig. 13. Significance of the present work and possible future work directions. Average hardness of $Mg_{17}Al_{12}$ at different temperatures were drawn out from [57]. Values of minimum creep rates for AM50, AC505, AC510 and AC 515 alloys were extracted from [10], while for AZ91, AXZ911, AXZ931 and AXZ 951 alloys from [6].

where ϕ and κ are the angle between the slip plane normals and the slip directions in two neighbouring grains or phases, respectively. An m' value close to 1 indicates that the slip systems are crystallographically aligned and highly favourable for slip transmission, while for $m' = 0$ the slip systems are completely incompatible. When applying this criterion to α-Mg/Laves phase interfaces, it is highly unlikely that basal slip in the α-Mg matrix will trigger basal slip in the C36 phase. This is because the basal plane normals of both phases, ϕ, are at an angle of ~ 90°, causing a low m' value. However, the pile-up of non-basal dislocations can create relatively favourable stress concentrations at the α-Mg/Laves phase interface, which can trigger the activation of basal slip sources in the C36 phase. The proposed mechanism is shown schematically in Fig. 12. Zhu et al. [76] also reported the presence of non-basal geometrically necessary dislocations (GNDs) in the Mg phase around Al_2Ca Laves phase precipitates. They also reported slip on {111} planes in the Al_2Ca phase.

In addition to slip transfer, crack formation in the Laves phase is another way of releasing stress concentrations at the phase boundary. The observed different plastic behaviour such as dislocation slip or crack formation in the Laves phase is assumed to occur because of the following three reasons when considering the observed orientation relationship:

1. The orientation of the cracks (see Fig. 9 d) in the Laves phase is often parallel to the basal plane indicating that the crack might have formed after some plastic deformation on the basal plane [64]. For the crystallographically related μ-phase, similar decohesion along planes with high dislocation density after plastic deformation was observed in deformed micropillars by TEM [87].
2. Due to the preferred orientation relationship between the α-Mg matrix and the C36 Laves phase, the activation of non-basal slip in the α-Mg phase seems critical for initiating slip in the Laves phase. Therefore, α-Mg grains having a high Schmid (or Taylor) factor for non-basal slip systems can facilitate slip transmission from Mg into the Laves phases. Crack formation in the Laves phase would then be more pronounced, when non-basal slip in the α-Mg phase cannot be activated.
3. The only mode of plastic deformation of the Laves phase was basal, therefore, the Schmid factor for basal slip in the C36 Laves phase is also of significant importance. A C36 Laves phase loaded having a low Schmid factor for basal slip will have low chances to undergo plastic deformation and will be prone to crack formation.

Due to the complex stress state associated with indentation, however, the Schmid factors for several slip systems in this work could not be computed. The critical resolved shear stresses for activating slip in the C36 Laves through co-deformation could be obtained using micro-pillar compression in a future study.

Unfortunately, synthesis of a corresponding sample with large enough, single phase C36 grains for nanomechanical testing proved unsuccessful during this work and we therefore compare our results with the better known and structurally very similar hexagonal C14 phase. With suitable bulk C36 Laves phase material, nanomechanical tests could also be performed over a range of temperature to analyse the effect of temperature on its hardness and deformation behavior and to potentially separate this from any effects of changing composition and stacking fault density in the presence of a matrix phase. A similar challenge exists in simulations, where the availability of a ternary Mg-Al-Ca interatomic potential limits the use of MD simulations that could shed further light on dislocation mechanisms in the C36 phase and at the Mg-C36 interface. Until now, such computational work has been limited to the Mg-C14 system and therefore both experiments and simulations will benefit from progress in synthesis and empirical potentials to further reveal and separate the mechanisms we observe here.

4.3. Implications of the present work for alloy design

As described in the previous sections, the Laves phase is much harder and requires significantly higher stresses than the α-Mg matrix for plastic deformation. The presence of the Laves phase, therefore, significantly restricts the deformation occurring in the α-Mg matrix as is evident around the microindents (Fig. 8). Further, it is clear from this study that the Mg_2Ca phase does not lose hardness with temperature. This means the Laves phase can provide strengthening to the α-Mg matrix at elevated temperatures that are usually encountered during creep loading of automotive components, like powertrains [4,88], and is most probably the reason for the good creep properties of these alloys.

There are also a few interesting prospects owing to the nature of co-deformation of the Laves phases in the metallic matrix, namely that they are apparently non-shearable obstacles to dislocations but at the same time can relieve the stress of dislocation pile-ups by nucleation and motion of dislocations inside the intermetallic phase itself. Zhu et al. [76] have recently used the non-shearable yet deformable nature of Al_2Ca precipitates to design a Mg-6Al-1Ca alloy with significant ductility. They attributed the high work hardening capacity of the alloy to the increased density of geometrically necessary dislocations nucleated and accumulated around Al_2Ca precipitates. Similarly, we also observed plastic deformation in the $(Mg,Al)_2Ca$ phase itself and non-basal dislocations around interfaces in this work.

As with the case of lean Ca alloys [76], in alloys with relatively high Ca content the deformable nature of the $(Mg,Al)_2Ca$ phase can then also be used as a tool to design creep resistant alloys that also exhibit sufficient ductility and work hardening capacity. Since the small size of the microstructure enables plasticity in the Laves phase [28,89], there is additional scope for alloy design in terms of its microstructural length scales. Different alloys with varying thicknesses of intermetallic Laves phase struts (by alloying additions or cooling rate adjustments) can be produced and then the Laves phase thickness effects on slip transfer and mechanical properties can be studied and ultimately used to fine tune the alloy composition. These thoughts are summarised in the Fig. 13.

5. Conclusions

The goal of this work was to study the co-deformation behaviour of hard Laves phases in a soft magnesium matrix. In particular, it was necessary to determine the mechanical properties of the individual phases and thermally activated deformation mechanisms, elucidate the effects of orientation and Laves phase on the deformation of the α-Mg matrix, and study slip transfer from the soft α-Mg phase to the hard intermetallic Laves phase. Based on the results of nano- and microindentation experiments on alloys AX44 and Mg-30Ca, along with post-deformation SEM and TEM studies, the following conclusions can be drawn:

i) The hardness of the α-Mg phase decreases slightly from 0.96 GPa to 0.86 GPa when the temperature increases from RT to 170 °C, while the hardness of the Mg_2Ca phase stays approximately constant. The hardness across α-Mg-Laves phase interfaces was higher than that observed for the α-Mg phase at all testing temperatures.

ii) The strain rate sensitivity of the α-Mg phase slightly increases from 0.013 ± 0.006 at 100 °C to 0.023 ± 0.009 at 170 °C while its activation volume decreases from 2.84 nm^3 (86 ± 34 b^3) to 2.31 nm^3 (70 ± 26 b^3). These activation volumes indicate that deformation is dominated by dislocation cross-slip.

iii) The activation volume at α-Mg/Laves phase interfaces is smaller than that of the α-Mg phase suggesting that thermally activated mechanisms, like interfacial sliding, are active in the interfacial regions.

iv) The creep deformation of the Mg_2Ca Laves phase at the same load and a temperature of 170 °C is significantly lower than that of the α-Mg phase.
v) The deformation zone around and below indents in the α-Mg matrix is both orientation-dependent and strongly influenced by adjacent Laves phases. Sub-surface deformation mechanisms are well-represented by deformation around indents at the surface.
vi) Co-deformation of the Laves phase and the α-Mg matrix occurs, despite the Laves phase being significantly harder than the α-Mg phase. This is evidenced by slip lines in the Laves phase being observed in regions where slip lines or twins in the α-Mg matrix intersect with the Laves phase.
vii) A preferential orientation relationship, with basal (0001) planes of the constituent phases being almost perpendicular to each other, was revealed in the AX44 dual-phase material investigated by TEM.
viii) Deformation of the α-Mg phase occurs via mechanical twinning, basal and non-basal slip. However, basal slip was observed to be predominant. The C36 Laves phase deforms mainly by basal slip as was identified by TEM analysis.

Data availability

The raw/processed data required to reproduce these findings cannot be shared at this time as the data also forms part of an ongoing study.

Declaration of Competing Interest

The authors declare that they have no known competing financial interests or personal relationships that could have appeared to influence the work reported in this paper.

Acknowledgments

The authors are immensely grateful for the financial support provided by the Deutsche Forschungsgemeinschaft (DFG), under Collaborative Research Centre (CRC) 1394, project ID 409476157 within projects A03, A05, C01 and C02. We are also thankful to Dr. Risheng Pei for his help and support in analysing EBSD data. Further, we also gratefully acknowledge the help received from our colleagues, Mr. David Beckers, Mr. Maximilian Kruth, Mr. Gerhard Schutz and Mr. Arndt Ziemons (in alphabetical order), at various steps in this study.

Appendix A. Supplementary material

Supplementary data to this article can be found online at https://doi.org/10.1016/j.matdes.2021.110113.

References

[1] S.-Q. Yang, C.-B. Li, J. Du, Y.-J. Zhao, Theoretical study of active Ca element on grain refining of carbon-inoculated Mg-Al alloy, Mater. Des. 192 (2020) 108664.
[2] C. Zhang, L. Wu, G.-S. Huang, G.-G. Wang, B. Jiang, F.-S. Pan, Microstructure and corrosion properties of Mg–0.5Zn–0.2Ca–0.2Ce alloy with different processing conditions, Rare Met. 40 (7) (2021) 1924–1931.
[3] P.K. Mallick, Chapter 1 - Overview, in: P.K. Mallick (Ed.), Materials, Design and Manufacturing for Lightweight Vehicles (Second Edition), Woodhead Publishing2021, pp. 1-36
[4] M.O. Pekguleryuz, A.A. Kaya, Creep resistant magnesium alloys for powertrain applications, Adv. Eng. Mater. 5 (12) (2003) 866–878.
[5] B. Kondori, R. Mahmudi, Effect of Ca additions on the microstructure and creep properties of a cast Mg–Al–Mn magnesium alloy, Mater. Sci. Eng., A 700 (2017) 438–447.
[6] D. Amberger, P. Eisenlohr, M. Göken, Microstructural evolution during creep of Ca-containing AZ91, Mater. Sci. Eng., A 510–511 (2009) 398–402.
[7] Y. Terada, R. Sota, N. Ishimatsu, T. Sato, K. Ohori, A thousandfold creep strengthening by Ca addition in die-cast AM50 magnesium alloy, Metallurgical and Materials Transactions A 35 (9) (2004) 3029–3032.
[8] D. Amberger, P. Eisenlohr, M. Göken, On the importance of a connected hard-phase skeleton for the creep resistance of Mg alloys, Acta Mater. 60 (5) (2012) 2277–2289.
[9] B. Kondori, R. Mahmudi, Effect of Ca additions on the microstructure, thermal stability and mechanical properties of a cast AM60 magnesium alloy, Mater. Sci. Eng., A 527 (7) (2010) 2014–2021.
[10] Y. Nakaura, A. Watanabe, K. Ohori, Effects of Ca, Sr additions on properties of Mg-Al based alloys, Mater. Trans. 47 (4) (2006) 1031–1039.
[11] N. Takata, H. Ghassemi-Armaki, M. Takeyama, S. Kumar, Nanoindentation study on solid solution softening of Fe-rich Fe_2Nb Laves phase by Ni in Fe–Nb–Ni ternary alloys, Intermetallics 70 (2016) 7–16.
[12] Q. Yang, S. Lv, P. Qin, F. Meng, X. Qiu, X. Hua, K. Guan, W. Sun, X. Liu, J. Meng, Interphase boundary segregation induced phase transformation in a high-pressure die casting Mg-Al-La-Ca-Mn alloy, Mater. Des. 190 (2020) 108566.
[13] A. Suzuki, N.D. Saddock, J.W. Jones, T.M. Pollock, Solidification paths and eutectic intermetallic phases in Mg–Al–Ca ternary alloys, Acta Mater. 53 (9) (2005) 2823–2834.
[14] L. Zhang, K.-K. Deng, K.-B. Nie, F.-J. Xu, K. Su, W. Liang, Microstructures and mechanical properties of Mg–Al–Ca alloys affected by Ca/Al ratio, Mater. Sci. Eng., A 636 (2015) 279–288.
[15] H.A. Elamami, A. Incesu, K. Korgiopoulos, M. Pekguleryuz, A. Gungor, Phase selection and mechanical properties of permanent-mold cast Mg-Al-Ca-Mn alloys and the role of Ca/Al ratio, J. Alloy. Compd. 764 (2018) 216–225.
[16] S. Sanyal, M. Paliwal, T.K. Bandyopadhyay, S. Mandal, Evolution of microstructure, phases and mechanical properties in lean as-cast Mg–Al–Ca–Mn alloys under the influence of a wide range of Ca/Al ratio, Mater. Sci. Eng., A 800 (2021) 140322.
[17] H. Conrad, W.D. Robertson, Effect of temperature on the flow stress and strain-hardening coefficient of magnesium single crystals, JOM 9 (4) (1957) 503–512.
[18] Q. Yu, J. Zhang, Y. Jiang, Direct observation of twinning–detwinning–retwinning on magnesium single crystal subjected to strain-controlled cyclic tension–compression in [0 0 0 1] direction, Philos. Mag. Lett. 91 (12) (2011) 757–765.
[19] A. Chapuis, J.H. Driver, Temperature dependency of slip and twinning in plane strain compressed magnesium single crystals, Acta Mater. 59 (5) (2011) 1986–1994.
[20] R.E. Reed-Hill, W.D. Robertson, Deformation of magnesium single crystals by nonbasal slip, JOM 9 (4) (1957) 496–502.
[21] C.M. Byer, B. Li, B. Cao, K.T. Ramesh, Microcompression of single-crystal magnesium, Scr. Mater. 62 (8) (2010) 536–539.
[22] T. Obara, H. Yoshinga, S. Morozumi, 11221123 Slip system in magnesium, Acta Metall. 21 (7) (1973) 845–853.
[23] A. Akhtar, E. Teghtsoonian, Substitutional solution hardening of magnesium single crystals, Philos. Magazine: A J. Theor. Exp. Appl. Phys. 25 (4) (1972) 897–916.
[24] A. Akhtar, E. Teghtsoonian, Solid solution strengthening of magnesium single crystals—I alloying behaviour in basal slip, Acta Metall. 17 (11) (1969) 1339–1349.
[25] A. Akhtar, E. Teghtsoonian, Solid solution strengthening of magnesium single crystals—ii the effect of solute on the ease of prismatic slip, Acta Metall. 17 (11) (1969) 1351–1356.
[26] S. Miura, S. Yamamoto, K. Ohkubo, T. Mohri, Deformation behavior of Mg alloy single crystals at various temperatures, Mater. Sci. Forum 350-351 (2000) 183–190.
[27] N. Stanford, M.R. Barnett, Solute strengthening of prismatic slip, basal slip and twinning in Mg and Mg–Zn binary alloys, Int. J. Plast. 47 (2013) 165–181.
[28] C. Zehnder, K. Czerwinski, K.D. Molodov, S. Sandlöbes-Haut, J.S.K.L. Gibson, S. Korte-Kerzel, Plastic deformation of single crystalline C14 Mg_2Ca Laves phase at room temperature, Mater. Sci. Eng., A 759 (2019) 754–761.
[29] L.L. Rokhlin, T.V. Dobatkina, N.I. Nikitina, I.E. Tarytina, Calcium-alloyed magnesium alloys, Met. Sci. Heat Treat. 51 (3-4) (2009) 164–169.
[30] M. Zubair, S. Sandlöbes, M.A. Wollenweber, C.F. Kusche, W. Hildebrandt, C. Broeckmann, S. Korte-Kerzel, On the role of Laves phases on the mechanical properties of Mg-Al-Ca alloys, Mater. Sci. Eng., A 756 (2019) 272–283.
[31] M. Zubair, S. Sandlöbes-Haut, M.A. Wollenweber, K. Bugelnig, C.F. Kusche, G. Requena, S. Korte-Kerzel, Strain heterogeneity and micro-damage nucleation under tensile stresses in an Mg–5Al–3Ca alloy with an intermetallic skeleton, Mater. Sci. Eng., A 767 (2019) 138414, https://doi.org/10.1016/j.msea.2019.138414.
[32] W.C. Oliver, G.M. Pharr, Measurement of hardness and elastic modulus by instrumented indentation: Advances in understanding and refinements to methodology, J. Mater. Res. 19 (1) (2004) 3–20.
[33] Q. Yang, X. Qiu, S. Lv, F. Meng, K. Guan, B. Li, D. Zhang, Y. Zhang, X. Liu, J. Meng, Deteriorated tensile creep resistance of a high-pressure die-cast Mg–4Al–4RE–0.3Mn alloy induced by substituting part RE with Ca, Mater. Sci. Eng., A 716 (2018) 120–128.
[34] A. Suzuki, N.D. Saddock, J.W. Jones, T.M. Pollock, Structure and transition of eutectic (Mg, Al)2Ca Laves phase in a die-cast Mg–Al–Ca base alloy, Scr. Mater. 51 (10) (2004) 1005–1010.
[35] C.D. Rabadia, Y.J. Liu, L.Y. Chen, S.F. Jawed, L.Q. Wang, H. Sun, L.C. Zhang, Deformation and strength characteristics of Laves phases in titanium alloys,

Mater. Des. 179 (2019) 107891, https://doi.org/10.1016/j.matdes.2019.107891.

[36] U. Ramamurty, S. Jana, Y. Kawamura, K. Chattopadhyay, Hardness and plastic deformation in a bulk metallic glass, Acta Mater. 53 (3) (2005) 705–717.

[37] H. Zhang, X. Jing, G. Subhash, L.J. Kecskes, R.J. Dowding, Investigation of shear band evolution in amorphous alloys beneath a Vickers indentation, Acta Mater. 53 (14) (2005) 3849–3859.

[38] M. Luysberg, M. Heggen, K. Tillmann, FEI Tecnai G2 F20, J. Large-scale Research Facilities JLSRF 2 (2016).

[39] S.W. Xu, N. Matsumoto, K. Yamamoto, S. Kamado, T. Honma, Y. Kojima, High temperature tensile properties of as-cast Mg–Al–Ca alloys, Mater. Sci. Eng., A 509 (1) (2009) 105–110.

[40] Z.T. Li, X.D. Zhang, M.Y. Zheng, X.G. Qiao, K. Wu, C. Xu, S. Kamado, Effect of Ca/Al ratio on microstructure and mechanical properties of Mg-Al-Ca-Mn alloys, Mater. Sci. Eng., A 682 (2017) 423–432.

[41] P.-F. Qin, Q. Yang, Y.-Y. He, J.-H. Zhang, J.-S. Xie, X.-R. Hua, K. Guan, J. Meng, Microstructure and mechanical properties of high-strength high-pressure die-cast Mg–4Al–3La–1Ca–0.3Mn alloy, Rare Met. 40 (10) (2021) 2956–2963.

[42] A. Suzuki, N.D. Saddock, J.R. TerBush, B.R. Powell, J.W. Jones, T.M. Pollock, Precipitation strengthening of a Mg-Al-Ca–based AXJ530 die-cast alloy, Metall. Mater. Trans. A 39 (3) (2008) 696–702.

[43] N.D. Saddock, A. Suzuki, J.W. Jones, T.M. Pollock, Grain-scale creep processes in Mg–Al–Ca base alloys: Implications for alloy design, Scr. Mater. 63 (7) (2010) 692–697.

[44] W.D. Nix, H. Gao, Indentation size effects in crystalline materials: A law for strain gradient plasticity, J. Mech. Phys. Solids 46 (3) (1998) 411–425.

[45] V. Maier, C. Schunk, M. Göken, K. Durst, Microstructure-dependent deformation behaviour of bcc-metals – indentation size effect and strain rate sensitivity, Phil. Mag. 95 (16-18) (2015) 1766–1779.

[46] O. Franke, J.C. Trenkle, C.A. Schuh, Temperature dependence of the indentation size effect, J. Mater. Res. 25 (7) (2010) 1225–1229.

[47] V. Maier, K. Durst, J. Mueller, B. Backes, H.W. Höppel, M. Göken, Nanoindentation strain-rate jump tests for determining the local strain-rate sensitivity in nanocrystalline Ni and ultrafine-grained Al, J. Mater. Res. 26 (11) (2011) 1421–1430.

[48] V. Maier, B. Merle, M. Göken, K. Durst, An improved long-term nanoindentation creep testing approach for studying the local deformation processes in nanocrystalline metals at room and elevated temperatures, J. Mater. Res. 28 (9) (2013) 1177–1188.

[49] M.J. Mayo, W.D. Nix, A micro-indentation study of superplasticity in Pb, Sn, and Sn-38 wt% Pb, Acta Metall. 36 (8) (1988) 2183–2192.

[50] B.N. Lucas, W.C. Oliver, Indentation power-law creep of high-purity indium, Metall. Mater. Trans. A 30 (3) (1999) 601–610.

[51] J.M. Wheeler, V. Maier, K. Durst, M. Göken, J. Michler, Activation parameters for deformation of ultrafine-grained aluminium as determined by indentation strain rate jumps at elevated temperature, Mater. Sci. Eng., A 585 (2013) 108–113.

[52] I.-C. Choi, Y.-J. Kim, B. Ahn, M. Kawasaki, T.G. Langdon, J.-i. Jang, Evolution of plasticity, strain-rate sensitivity and the underlying deformation mechanism in Zn–22% Al during high-pressure torsion, Scr. Mater. 75 (2014) 102–105.

[53] I.-C. Choi, D.-H. Lee, B. Ahn, K. Durst, M. Kawasaki, T.G. Langdon, J.-i. Jang, Enhancement of strain-rate sensitivity and shear yield strength of a magnesium alloy processed by high-pressure torsion, Scr. Mater. 94 (2015) 44–47.

[54] H. Somekawa, C.A. Schuh, Nanoindentation behavior and deformed microstructures in coarse-grained magnesium alloys, Scr. Mater. 68 (6) (2013) 416–419.

[55] Z. Wu, S. Sandlöbes, J. Rao, J.-L. Gibson, B. Berkels, S. Korte-Kerzel, Local mechanical properties and plasticity mechanisms in a Zn-Al eutectic alloy, Mater. Des. 157 (2018) 337–350.

[56] H.J. Frost, M.F. Ashby, Deformation-mechanism map, Pergaman Press, Oxford, 1982.

[57] H.N. Mathur, V. Maier-Kiener, S. Korte-Kerzel, Deformation in the γ-Mg$_{17}$Al$_{12}$ phase at 25–278 °C, Acta Mater. 113 (2016) 221–229.

[58] J. Kappacher, A. Leitner, D. Kiener, H. Clemens, V. Maier-Kiener, Thermally activated deformation mechanisms and solid solution softening in W-Re alloys investigated via high temperature nanoindentation, Mater. Des. 189 (2020) 108499.

[59] C. Su, E.G. Herbert, S. Sohn, J.A. LaManna, W.C. Oliver, G.M. Pharr, Measurement of power-law creep parameters by instrumented indentation methods, J. Mech. Phys. Solids 61 (2) (2013) 517–536.

[60] P.S. Phani, W.C. Oliver, A direct comparison of high temperature nanoindentation creep and uniaxial creep measurements for commercial purity aluminum, Acta Mater. 111 (2016) 31–38.

[61] Z. Wu, S. Sandlöbes, Y. Wang, J.S.K.L. Gibson, S. Korte-Kerzel, Creep behaviour of eutectic Zn-Al-Cu-Mg alloys, Mater. Sci. Eng., A 724 (2018) 80–94.

[62] R. Goodall, T.W. Clyne, A critical appraisal of the extraction of creep parameters from nanoindentation data obtained at room temperature, Acta Mater. 54 (20) (2006) 5489–5499.

[63] D. Tabor, The Hardness of Metals, Oxford University Press, 2000.

[64] J. Guénolé, M. Zubair, S. Roy, Z. Xie, M. Lipińska-Chwałek, S. Sandlöbes-Haut, S. Korte-Kerzel, Exploring the transfer of plasticity across Laves phase interfaces in a dual phase magnesium alloy, Mater. Des. 202 (2021) 109572.

[65] C. Kirsten, P. Paufler, G.E.R. Schulze, Zur plastischen Verformung intermetallischer Verbindungen, Monatsberichte der Deutschen Akademie der Wissenschaften 6 (2) (1964) 140–147.

[66] Y. Wang, Y. Liu, J.T. Wang, Investigation on activation volume and strain-rate sensitivity in ultrafine-grained tantalum, Mater. Sci. Eng., A 635 (2015) 86–93.

[67] H. Somekawa, C.A. Schuh, Effect of solid solution elements on nanoindentation hardness, rate dependence, and incipient plasticity in fine grained magnesium alloys, Acta Mater. 59 (20) (2011) 7554–7563.

[68] H.J. Choi, Y. Kim, J.H. Shin, D.H. Bae, Deformation behavior of magnesium in the grain size spectrum from nano- to micrometer, Mater. Sci. Eng., A 527 (6) (2010) 1565–1570.

[69] H. Somekawa, T. Mukai, Hall-Petch breakdown in fine-grained pure magnesium at low strain rates, Metall. Mater. Trans. A 46 (2) (2015) 894–902.

[70] J.W. Christian, S. Mahajan, Deformation twinning, Prog. Mater. Sci. 39 (1-2) (1995) 1–157.

[71] G. Zhang, K.-Q. Qiu, Q.-C. Xiang, Y.-L. Ren, Creep resistance of as-cast Mg-5Al-5Ca-2Sn alloy, China Foundry 14 (4) (2017) 265–271.

[72] J. Koike, T. Kobayashi, T. Mukai, H. Watanabe, M. Suzuki, K. Maruyama, K. Higashi, The activity of non-basal slip systems and dynamic recovery at room temperature in fine-grained AZ31B magnesium alloys, Acta Mater. 51 (7) (2003) 2055–2065.

[73] J. Koike, Enhanced deformation mechanisms by anisotropic plasticity in polycrystalline Mg alloys at room temperature, Metall. Mater. Trans. A 36 (7) (2005) 1689–1696.

[74] H. Somekawa, D.A. Basha, A. Singh, T. Tsuru, M. Yamaguchi, Non-basal dislocation nucleation site of solid solution magnesium alloy, Mater. Trans. 61 (6) (2020) 1172–1175.

[75] Z. Huang, C. Yang, J.E. Allison, L. Qi, A. Misra, Dislocation cross-slip in precipitation hardened Mg–Nd alloys, J. Alloy. Compd. 859 (2021) 157858.

[76] G. Zhu, L. Wang, J. Wang, J. Wang, J.-S. Park, X. Zeng, Highly deformable Mg–Al–Ca alloy with Al$_2$Ca precipitates, Acta Mater. 200 (2020) 236–245.

[77] J. Koike, R. Ohyama, Geometrical criterion for the activation of prismatic slip in AZ61 Mg alloy sheets deformed at room temperature, Acta Mater. 53 (7) (2005) 1963–1972.

[78] S.R. Agnew, Ö. Duygulu, Plastic anisotropy and the role of non-basal slip in magnesium alloy AZ31B, Int. J. Plast. 21 (6) (2005) 1161–1193.

[79] G. Zhu, L. Wang, H. Zhou, J. Wang, Y. Shen, P. Tu, H. Zhu, W. Liu, P. Jin, X. Zeng, Improving ductility of a Mg alloy via non-basal <a> slip induced by Ca addition, Int. J. Plast. 120 (2019) 164–179.

[80] X. Wu, Y. Zhu, Heterogeneous materials: a new class of materials with unprecedented mechanical properties, Mater. Res. Lett. 5 (8) (2017) 527–532.

[81] Y. Zhu, X. Wu, Perspective on hetero-deformation induced (HDI) hardening and back stress, Mater. Res. Lett. 7 (10) (2019) 393–398.

[82] J.R. Seal, M.A. Crimp, T.R. Bieler, C.J. Boehlert, Analysis of slip transfer and deformation behavior across the α/β interface in Ti–5Al–2.5Sn (wt.%) with an equiaxed microstructure, Mater. Sci. Eng., A 552 (2012) 61–68.

[83] H. Pan, Y. He, X. Zhang, Interactions between Dislocations and Boundaries during Deformation, Materials (Basel) 14(4) (2021) 1012.

[84] M. Guziewski, S.P. Coleman, C.R. Weinberger, Atomistic investigation into interfacial effects on the plastic response and deformation mechanisms of the pearlitic microstructure, Acta Mater. 180 (2019) 287–300.

[85] D. Hull, D.J. Bacon, Chapter 9 - Dislocation Arrays and Crystal Boundaries, in: D. Hull, D.J. Bacon (Eds.), Introduction to Dislocations (Fifth Edition), Butterworth-Heinemann, Oxford, 2011, pp. 171–204.

[86] J. Luster, M.A. Morris, Compatibility of deformation in two-phase Ti-Al alloys: Dependence on microstructure and orientation relationships, Metall. Mater. Trans. A 26 (7) (1995) 1745–1756.

[87] S. Schröders, S. Sandlöbes, C. Birke, M. Loeck, L. Peters, C. Tromas, S. Korte-Kerzel, Room temperature deformation in the Fe$_7$Mo$_6$ μ-phase, Int. J. Plast. 108 (2018) 125–143.

[88] B.R. Powell, P.E. Krajewski, A.A. Luo, Chapter 4 - Magnesium alloys for lightweight powertrains and automotive structures, in: P.K. Mallick (Ed.), Materials, Design and Manufacturing for Lightweight Vehicles (Second Edition), Woodhead Publishing2021, pp. 125-186

[89] N. Takata, H. Ghassemi Armaki, Y. Terada, M. Takeyama, K.S. Kumar, Plastic deformation of the C14 Laves phase (Fe, Ni)$_2$Nb, Scr. Mater. 68 (8) (2013) 615–618.

Supplementary Material

Co-deformation Between the Metallic Matrix and Intermetallic Phases in a Creep-Resistant Mg-3.68Al-3.8Ca Alloy

M. Zubair[1,2], S. Sandlöbes-Haut[1], M. Lipińska-Chwałek[3,4], M. A. Wollenweber[1], C. Zehnder[1], J. Mayer[3,4], J.S.K-L. Gibson[1], S. Korte-Kerzel[1]

[1]Institute for Physical Metallurgy and Materials Physics, Kopernikusstr. 14, RWTH Aachen University, 52074 Aachen, Germany.
[2]Department of Metallurgical and Materials Engineering, G.T Road, UET Lahore, Pakistan.
[3]Central Facility for Electron Microscopy, RWTH Aachen University, Ahornstraße 55, 52074 Aachen, Germany.

[4]Ernst Ruska-Centre for Microscopy and Spectroscopy with Electrons (ER-C), Leo-Brandt-Str. 1 52428 Forschungszentrum Jülich, Germany.

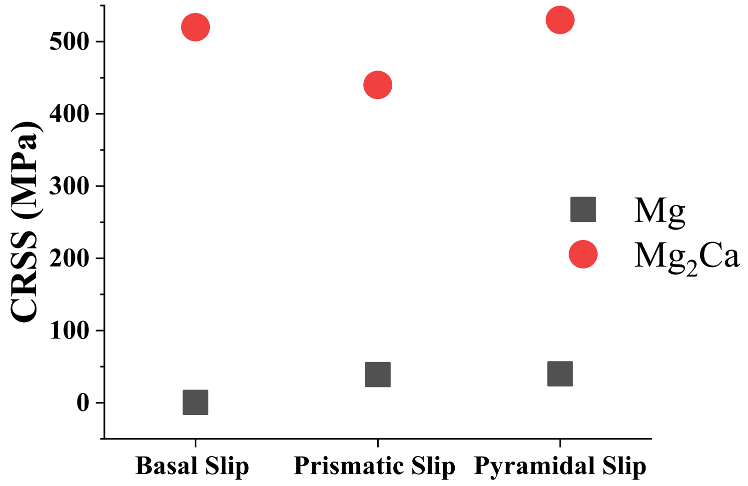

Fig. SM 1: Difference between the CRSS values for basal slip, prismatic slip and pyramidal slip in α-Mg and the Mg_2Ca Laves phase. The values shown are extracted from [1-4].

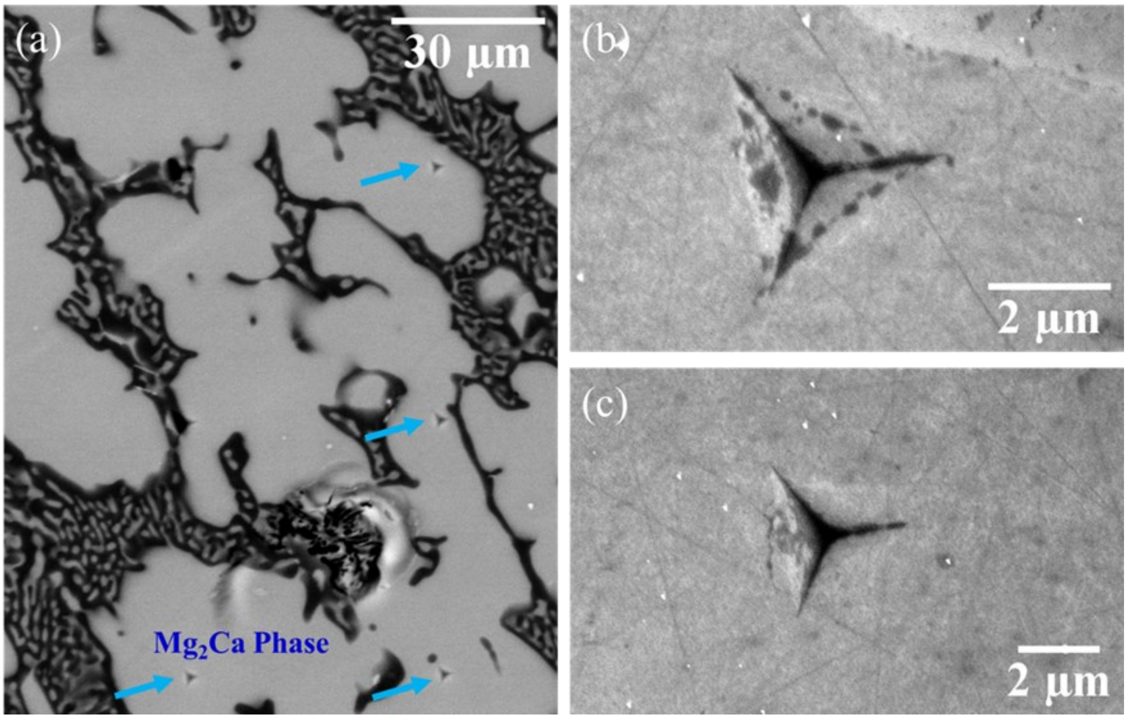

Fig. SM 2: (a): BSE image of creep indents made in the Mg_2Ca phase (bright phase) in an Mg-30Ca master alloy; the creep indents are highlighted using blue arrows, (b) and (c) are the high magnification SE images of the creep indents in the Mg_2Ca phase. This phase has been characterised as Mg_2Ca phase based on SADP in TEM and by EDS and EBSD in SEM in the earlier work by Zehnder et al. [4].

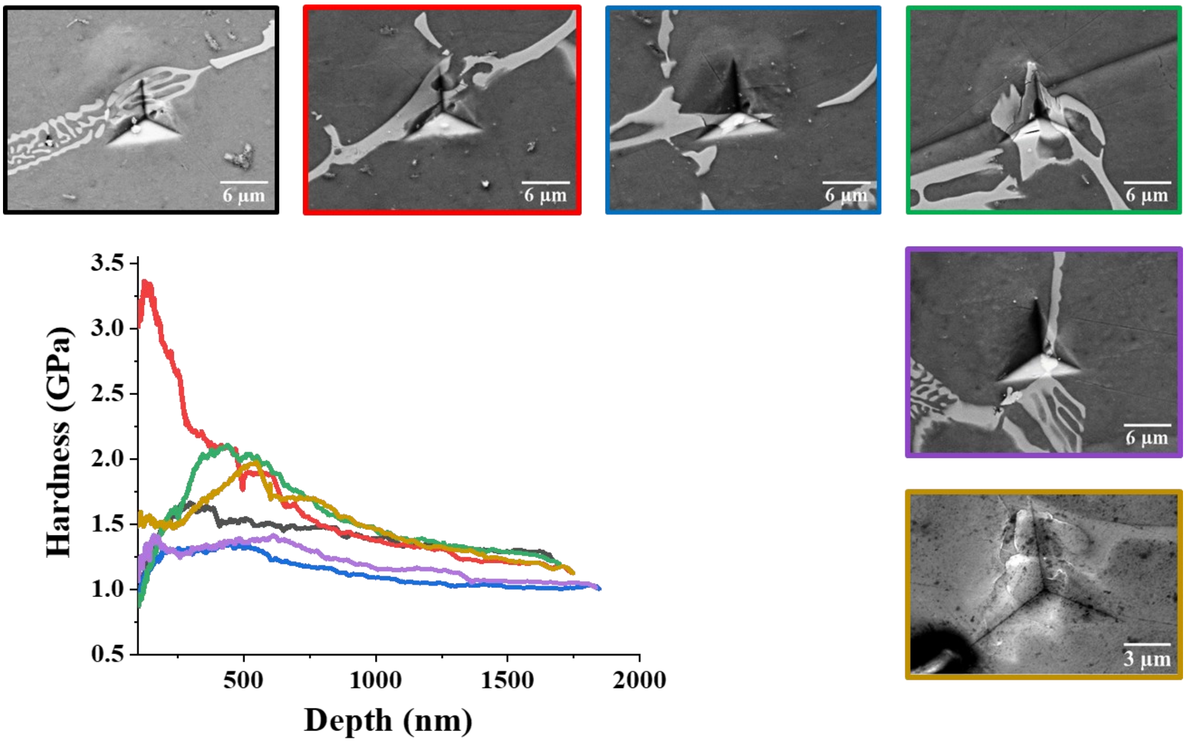

Fig. SM 3: Hardness-depth curves of various indents at α-Mg/Laves phase interfaces. At higher depths, the contribution of the α-Mg phase increases.

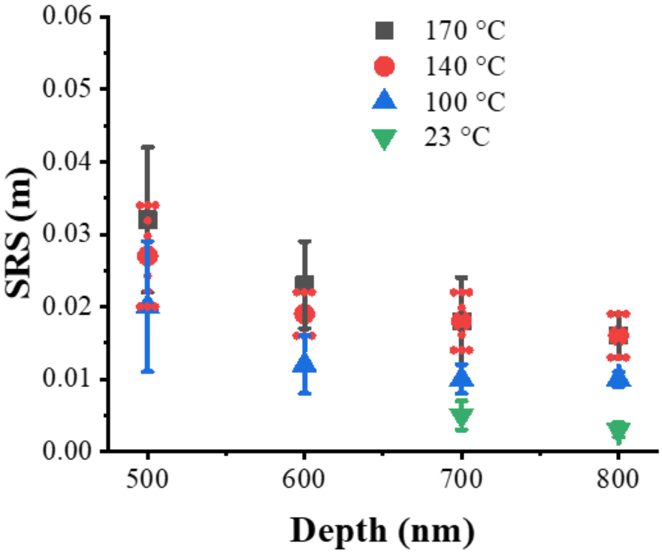

Fig. SM 4: Variation in m with depth for α-Mg phase at all test temperatures

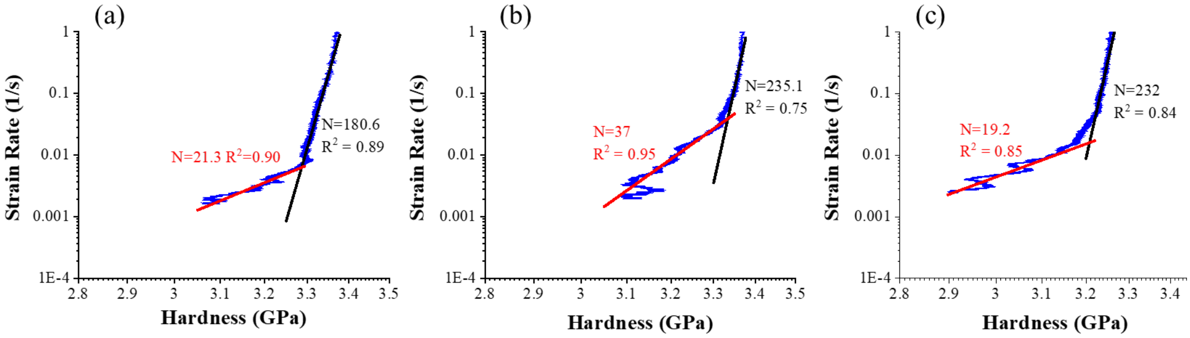

Fig. SM 5: (a-c): Strain rate vs hardness variation of the Mg_2Ca phase for three different indents made at 170 °C.

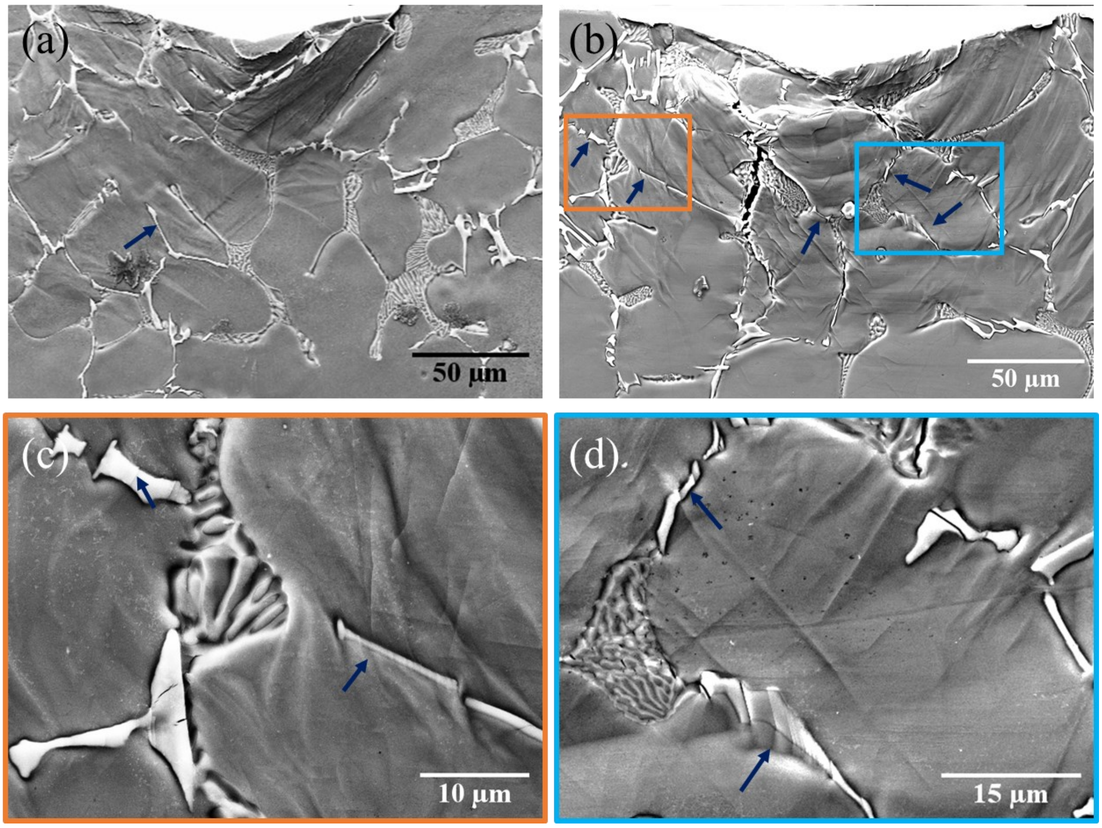

Fig. SM 6: SE images of the sub-surface regions of indents made at 5 N (a) and 10 N (b). (c) and (d) are higher magnification SE images of the regions enclosed by orange and light blue rectangles in (b). Dark blue arrows indicate the slip in the C36 Laves phase.

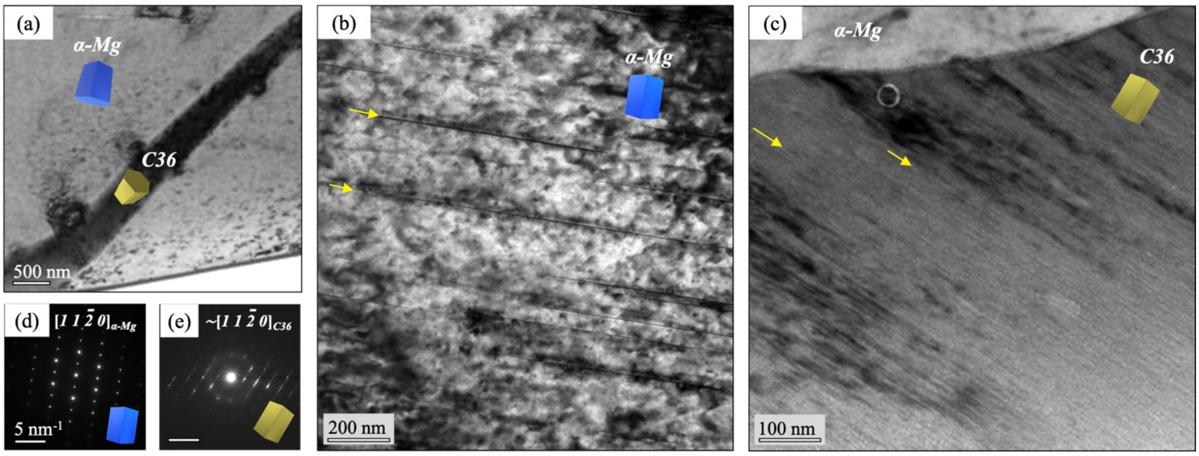

Fig. SM 7: Composite microstructure observed with TEM in FIB lamella lifted out from an alloy with slightly different composition (*Mg-3.94Al-3.83Ca, wt.%)* but similar microstructure, almost perpendicular relative orientation of the constituent phases $\measuredangle[1\,1\,\bar{2}\,0]_{C36}, [0\,0\,0\,1]_{\alpha\text{-}Mg} = \sim 3°$. *(a) BF overview image. b) and c) Magnified BF images of deformation str*ucture in *α-Mg matrix and* C36 Laves phase, as observed *in orientations corresponding to* $B \parallel [1\,1\,\bar{2}\,0]_{\alpha\text{-}Mg}$ (b) *and* close to $B \parallel [1\,1\,\bar{2}\,0]_{C36}$ (c). *Basal-plane SFs in edge-on* orientation are indicated with yellow arrows. *d)-e) SAED patterns of the* α-Mg *matrix and C36 Laves phase* corresponding to real space images *presented in (b) and (c), respectively. Note* that *BF images (b) and (c) were acquired at extreme α and β tilt values of the TEM sample holder (*condition $B \parallel [1\,1\,\bar{2}\,0]_{C36}$ was out of the tilt range). *Accordingly, very high projection thickness of the FIB lamella results in poor quality of the BF TEM images in (b) and (c).*

References

[1] H. Conrad, W.D. Robertson, Effect of temperature on the flow stress and strain-hardening coefficient of magnesium single crystals, JOM 9(4) (1957) 503-512.
[2] R.E. Reed-Hill, W.D. Robertson, Deformation of magnesium single crystals by nonbasal slip, JOM 9(4) (1957) 496-502.
[3] T. Obara, H. Yoshinga, S. Morozumi, $\{11\bar{2}2\}$ $\langle\bar{1}\bar{1}23\rangle$ Slip system in magnesium, Acta Metallurgica 21(7) (1973) 845-853.
[4] C. Zehnder, K. Czerwinski, K.D. Molodov, S. Sandlöbes-Haut, J.S.K.L. Gibson, S. Korte-Kerzel, Plastic deformation of single crystalline C14 Mg_2Ca Laves phase at room temperature, Materials Science and Engineering: A 759 (2019) 754-761.